Inaugural dissertation
for
obtaining the doctoral degree
of the
Combined Faculty of Mathematics, Engineering and Natural Sciences
of the
Ruprecht - Karls - University
Heidelberg

Presented by

M.Sc. Aline Tschanz
born in: Zürich, Switzerland
Oral examination: 10th July, 2023

A nanoscopic reconstruction of clathrin coat remodeling during mammalian endocytosis

Referees: Prof. Dr. Ulrich S. Schwarz
Dr. Alba Diz-Muñoz

„Anything goes.“

Paul Feyerabend

The main content of this thesis has been published

Mund, M.*, **Tschanz, A.***, Wu, Y.-L., Frey, F., Mehl, J. L., Kaksonen, M., Avinoam, O., Schwarz, U. S., Ries, J. 2023. Clathrin coats partially preassemble and subsequently bend during endocytosis. *Journal of Cell Biology* **222(3)**: e202206038.

*Authors contributed equally to this paper

Further publications were partially based on work presented in this thesis

Wu, Y.-L.*, **Tschanz, A.***, Krupnik, L.*, Ries, J. 2020. Quantitative Data Analysis in Single-Molecule Localization Microscopy. *Trends in Cell Biology* **30**: 837–851.

*Authors contributed equally to this paper

Lardon, N., Wang, L., **Tschanz, A.**, Hoess, P., Tran, M., D'Este, E., Ries, J., and Johnsson K. 2021. Systematic Tuning of Rhodamine Spirocyclization for Super-resolution Microscopy. *Journal of the American Chemical Society* **143(36)**: 14592–14600

Diekmann, R., Deschamps, J., Li, Y., Deguchi, T., **Tschanz, A.,**, Kahnwald, M., Matti, U., Ries, J. 2022. Photon-free (s)CMOS camera characterization for artifact reduction in high- and super-resolution microscopy. *Nature Communications* **13**: 3362.

Wu, Y.-L., Hoess, P., **Tschanz, A.**, Matti, U., Mund, M., Ries, J. 2023. Maximum-likelihood model fitting for quantitative analysis of SMLM data. *Nature Methods* **20(1)**: 139–148.

Ewa Sitarska, E., Almeida, S. D., Beckwith, M. S., Stopp, J., Czuchnowski, J., Siggel, M., Roessner, R., **Tschanz, A.**, Ejsing, C., Schwab, Y., Kosinski, J., Sixt, M., Kreshuk, A., Erzberger, A., and Diz-Muñoz, A. 2023. Sensing their plasma membrane curvature allows migrating cells to circumvent obstacles. *Nature Communications*, *Accepted*.

This work was carried out at the European Molecular Biology Laboratory in Heidelberg from October 2018 to May 2023 under the supervision of Dr. Jonas Ries.

Abstract

Clathrin-mediated endocytosis is an essential pathway by which eukaryotic cells take up extracellular compounds. It is characterized by the formation of a clathrin coat at the inner leaflet of the plasma membrane, which drives the invagination of the membrane to form a spherical vesicle.

While the static ultrastructure and the interactome of the clathrin coat are well-studied, the molecular mechanisms and dynamics of the structural rearrangements that reshape the underlying membrane remain controversial. Convergence toward a detailed mechanistic understanding has been difficult due to the small size, molecular complexity, and relatively fast dynamics of the endocytic process.

In this work, I present a superresolution microscopy approach that allowed me to dynamically reconstruct the 3D architecture of clathrin coats *in situ*. To robustly determine the geometry of these structures, I employed the model-fitting framework LocMoFit, which approximates each clathrin coat as a spherical cap. The parameters extracted with this approach accurately describe geometric quantities such as coat curvature and surface area and enable the sorting of structures along their endocytic progression. The reconstruction of changes in clathrin coat geometry showed that these structures initially pre-assemble on a flat membrane, initiating curvature once approximately half the final coat area has been accumulated. Curvature then increases while clathrin polymerization continues until the final vesicular coat is formed. Based on these findings, we formulated the cooperative curvature model, which is based on positive feedback for curvature generation. This model accurately describes the experimental data retrieved from three cell lines, thus likely conceptualizing a general, physiologically relevant pathway of membrane bending by the clathrin coat.

Geometric changes in the clathrin coat are a result of the cumulative contributions of over 50 endocytic components involved in this process. Concurrently visualizing multiple components of the endocytic machinery could elucidate the detailed interplay of the involved proteins. As proof of principle, I visualized the dynamic recruitment of dynamin-2 and adaptor protein-2 complex relative to the developing clathrin coat using dual-color imaging. Based on the spatiotemporal distribution of these proteins, their functional role within the larger endocytic machinery could be confirmed.

Taken together, the superresolution microscopy approach I present in this work allows the reliable dynamic reconstruction of clathrin coat remodeling at the nanoscale. The resulting observations informed a new clathrin coat growth model, allowing for further mechanistic insights into the process. Future endeavors will focus on the application of this approach to reconstruct the temporal rearrangement of other components to the endocytic site, progressing towards a structural model of the entire endocytic machinery at the nanoscale. This pipeline further offers a means to test for structural adaptations of the endocytic machinery in response to changing environmental conditions.

Zusammenfassung

Die Clathrin-vermittelte Endozytose ist ein essentieller zellulärer Vorgang, über den eukaryotische Zellen extrazelluläre Moleküle aufnehmen können. Der Prozess ist durch die Bildung einer Clathrin-Hülle an der inneren Plasmamembran gekennzeichnet, die eine Einstülpung der Membran und die Bildung eines kugelförmigen Vesikels vermittelt.

Während die statische Ultrastruktur und das Interaktom der Clathrin-Hülle weitreichend bekannt sind, sind die molekularen Mechanismen und die Dynamik der strukturellen Veränderungen, welche die darunter liegende Membran umformen, weitgehend umstritten. Die geringe Größe, molekulare Komplexität, und die Geschwindigkeit der Endozytose erschweren die detaillierte Darstellung dieses zellulären Vorgangs.

In dieser Arbeit stelle ich eine hochauflösende Mikroskopie-Methode vor, die es mir ermöglicht hat, die dynamischen Veränderungen der 3D-Architektur von Clathrin-Hüllen *in situ* zu rekonstruieren. Um die Geometrie dieser Strukturen robust zu bestimmen, habe ich das Modell-Fitting-Framework LocMoFit verwendet, welches jede Clathrin-Hülle als eine kugelförmige Haube approximiert. Die mit diesem Ansatz extrahierten Parameter beschreiben geometrische Größen wie Radius und Oberfläche des Mantels genau und ermöglichen die Sortierung von Strukturen entsprechend ihrer Einordnung in den Verlauf der Endozytose. Die rekonstruierten Veränderungen in der Geometrie von Clathrin-Hüllen zeigt, dass diese Strukturen sich zu Beginn des Prozesses flach auf der Plasmamembran bilden, um dann Krümmung zu initiieren sobald circa die Hälfte der Oberfläche der finalen vesikulären Hülle bedeckt ist. Die Krümmung der Hülle nimmt danach zu, während Clathrin weiterhin polymerisiert, bis das finale Vesikel gebildet wird. Basierend auf diesen Erkenntnissen haben wir das kooperative Krümmungs-Modell formuliert, das auf positivem Feedback zur Erzeugung der Krümmung basiert. Dieses Modell stimmt mit experimentellen Daten von drei verschiedenen Zelllinien überein und beschreibt daher einen allgemeinen, physiologisch relevanten Mechanismus der Membranbiegung durch Clathrin.

Geometrische Veränderungen in der Clathrin-Hülle sind das Ergebnis der kumulierten Beiträge von über 50 an diesem Prozess beteiligten Proteine. Die gleichzeitige Visualisierung mehrerer Proteine der endozytären Maschinerie könnte deren detailliertes Zusammenspiel aufklären. Um dies zu veranschaulichen, visualisierte ich die dynamische Rekrutierung von Dynamin-2 und dem Adapterprotein 2-Komplex relativ zur Clathrin-Hülle mittels zweifarbiger hochauflösender Mikroskopie. Basierend auf der räumlich-zeitlichen Verteilung dieser Proteine kann ihre funktionelle Rolle innerhalb der größeren endozytären Maschinerie bestätigt werden.

Zusammengefasst ermöglicht die von mir in dieser Arbeit vorgestellte hochauflösende Mikroskopie-Methode die dynamischen Veränderungen der Clathrin-Hülle im Nanometer-Bereich zuverlässig zu rekonstruieren. Die dadurch erzeugten Erkenntnisse ermöglichten es uns, ein neues Wachstumsmodell der Clathrin-Hülle zu formulieren,

welches weitere mechanistische Einblicke in den Prozess erlaubt. Zukünftige Bemühungen werden sich auf die Anwendung dieses Ansatzes fokussieren, um die zeitlichen Veränderungen weiterer Proteine innerhalb der endozytischen Maschinerie zu rekonstruieren und so ein strukturelles Modell der gesamten Maschinerie im Nanomaßstab zu erreichen. Diese Methode bietet darüber hinaus die Möglichkeit, strukturelle Anpassungen der endozytischen Maschinerie als Reaktion auf veränderte Bedingungen im Umfeld der Zelle zu testen.

Acknowledgments

The European Molecular Biology Laboratory is an amazing place to do research at. I cannot even begin to explain what it meant to me to work in such an environment, and how lucky I feel to have spent my time alongside such great scientists, many of which I am grateful to now call friends.

Thus I wish to express this gratitude here as well as I can, starting with you **Jonas**. It has been a pleasure to do my PhD in your group. You have created an incredibly supportive, respectful, and creative environment, and I have greatly enjoyed being a part of it. I thank you for the incredible support and patience you have always shown me, and your quite literal interpretation of 'open-door policy'. While my scientific journey has had its ups and downs, your excitement and curiosity for the research we did together were always motivating and helped me stay passionate about what I do.

I further want to thank you, **Ulrich**, for our fruitful and productive collaboration. It was inspiring to work with you, and I have learned so much from our meetings and discussions. The work that you and **Felix** did significantly contributed to my own project, and the story we were ultimately able to tell together.

Thank you, **Alba**, for all the insightful conversations and advice that long surpassed your duties as my TAC committee member. I am grateful for all the different collaborative projects we embarked on.

I want to further thank **Maria** for her insightful contributions during my TAC meetings, and **Michael Knop** for agreeing to participate in my defense. And thank you, **Gautam**, for jumping in as a (very) last-minute committee member replacement.

The Ries lab has grown very dear to my heart, and I am grateful for all the work colleagues turned friends of current and past **Rieslings**.

Special thanks to **Yu-le** and **Markus**, for their contributions to this project, input on my thesis, and their friendship. Thank you **Yu-Le**, for countering my temporary frustrations by calmly fixing the bugs I created in the first place. Thank you for your patience, insights, and kindness. Thank you, **Markus**, for your guidance from the very start. Thank you, for involving me in this project which ultimately became the most important part of my PhD thesis. Thank you for your optimism, the slightly hungover, definitely too-early runs, and for making sure the fun never gets lost in the work.

Thank you, **Anindita** and **Maurice**, for all the banter and GeoGuessers. Gurl, I still miss our Saturday work days. Thank you **Joran**, for all your support throughout the year, your unparalleled patience when I once again forgot to put in the mirror correctly, and for always finding the exact right amount of sarcasm. And Thank you, **Nika**, for continuing the jokes in Jorans absence.

Thank you, **Philipp**, for always having an ear for my questions, even when I figured the answer out halfway through asking. Thanks for the bike rides, skiing holidays, secretary duties, patience, scientific advice, and for letting me win that one time in GeoGuessr! Thank you, **Ulf**, for giving us our first table. And our first chairs. And the cheesecakes. And the tools. And the car. The lab has yet to recover from your leaving. Thank you **Yiming**, **Robin**, and **Jervis**, for welcoming me to the Lab with open arms. Thank you, **Tomas**, **Angie**, **Sheng**, and **Lucas**, for some unforgettable retreats. Thank you, **Michal**, for your kindness and enthusiasm, and your input on my thesis. Thank you to all the interns that made the Ries lab always so fun: Thank you **Eva**, **Lisa** and **Lisa**, **Jonas** the younger one, **Andreas**, **Franzi**, and **Lukas**. And special thanks to **Jan-Niklas** and **Arnas**, for sticking with me as my first students.

A big thank you to all the current members of the Ries lab, and their support especially through my thesis writing phase. Thank you to **Takahiro**, for being the best office mate, and for your valuable input on my thesis. Thank you **Soheil**, **Nestor**, **Sara**, **Nick** and **Chris**, the exciting and weird-in-the-best-way lunch-break conversations, your kind words of support during thesis writing, and the unforgettable Ries-Leggings-day! Thank you, **Timon**, for your honest interest in my project, your input on my thesis, and awesome scientific and not-so-scientific discussions. Thank you, to my thesis-writing buddy **Marc**, for sharing my desperation. Few more weeks, hang in there!

Thank you to all pre- and postdocs that made EMBL such a lovely place. I am grateful to all the Bad-movie-nights, SOLA 2019, 2022, 2023, and 2024(!), parties, brunches, and MarioKarites. Thank you, **Marina**, **Martina**, **Franzi**, **Nikita**, **Karel**, **Manu**, **Lucia**, **Matteo**, **Agata**, **Javi**, **Andrea**, **Anusha**, **Guillermo**, **Philipp**, **Kevin**, **Lea**, **Charlie**, **Maxime**, **Hari**, **Chris**. Thank you, **Ale** & **Vale** the tire-d kids. And Gruezi **Fynn**, thanks for your last-minute latex help.

Thanks to my sporty friends, who made sure EMBL cantine wouldn't get to me too much. Thank you, **Dewi**, for our therapeutic venting sessions on the Boulderhaus mats! They kept me sane during thesis writing. And thanks for always keeping it competitive to making me climb better, and rage (cage) more. Thanks to the boys, **Luca** and **Thorsten**, for making lock-down a lot less boring, and for the culinary exchange ranging from protein powder to six-course menus. Thank you, **Danai**, for all the training sessions. Looking forward to the bike rides! And speaking of bikes, thank you, **Danila**, for our cycling adventures! Thank you, **Ana**, for our repeatedly failed attempts at committing to a healthier commute. And for your friendship and support throughout these last four-and-a-half years. Thank you, **Paul** and **Prachiti**, for bad-movie nights and hikes, a great stay in Cambridge, and hopefully more trips as soon as I wrap up this thesis. And thank you to the beautiful beach people, **Anna**, **Alex**, and **Wolfi**. Let's find one with sand next time.

Thank you, **Elisa**, for your friendship. I am so glad I could do this journey with you, from start to finish, and for the first brunch where it all began. I am looking forward to many more years of brunches, hikes, and hour-long talks! Thank you, **Kai**, for making my Grandma a very happy woman.

Thank you, **Fergus**, for your honesty that helped me chose the amazing lab I ended up in. Thank you, **Wolfi**, for your kindness behind all the jokes. Thank you, **Gilberto**, for Yoshi, my reliable writing companion. Thank you, **Jesus**, for the long walks and philosophical discussions. I will vote for you! And thank you **Hendrik** for all the delicious dinners. Thank you to my writing buddy **Karolina**. I was sad when you left, but lucky me you came back to the library on the last day. Thank you, **Alberto**, for a pretty cool conference! Not the one in Dresden though, the other one... Thanks, **George**, for the sweets that supported my writing, and thanks **Clement** for the unexpected shared journey from Utrecht to Heidelberg. Thank you, **Ewa** and **Kuba**, for introducing me to the right kind of Vodka and the right kind of board games. Thank you, **Leanne**, for your help with my project and patience with all my questions.

Thanks to my friends back home, **Glenn**, **Ana**, **Dara**, and **Liga**! I love you guys, thank you so much for staying in touch over the distance, and putting up with my lack of texting skills. Thanks for the hikes, the parties, and helping me chose that Pineapple I liked.

Danke, and die **Franks** und **Gervautzs**, für all die wunderschönen Neujahrsfeiern, und die Buchstäbliche Stütze während dem Schreiben meiner Arbeit.

And thank you to my family. **Mami**, **Papi**, ich wär nie so wiit cho wenn ihr nöd immer und ohni Zwiifel a mich glaubt hättet. Merci für eui Geduld, für alles wonir mir biibrocht hend und eui Liebi. Mami, merci für dini Creativität und Stärchi, wo mi immer inspiriert. Papi, merci, dass du mir mini Neugier fürd Wüsseschaft geh hesch und all dini Ratschläg. Danke, a di coolste zwei Mensche woni kenn: Danke **Michelle**, für dini Geduld und dass du immer für mich, und alli andere da bisch. Merci **Leonie**, für dini Neugier und dini Freud, und dini Liebi allem und jedem gegenüber. Und danke, **Gotti**, für di wunderschöne Glücksbringer zum Arbeit schriibe.

Danke **Mima**, honorary EMBL member. Vil zwiit weg bisch, und Linzertorte sind nur en schwache Troscht, egal wie guet's sind. Danke, das du mi nie vergesse lohsch woni aneghör. Danke **Pipa**. Das tuet so weh z schriibe, so gern hätt ich dir die Arbeit zeigt. Ich han vo dir mini Liebi zu de Berge gerbt, und hoffentli es bizli au de Humor. Han immer Heiweh.

Und merci **Max**. I am not sure I can find the right words to express this, oder die richtige Sprache dafür. Your support means the world to me. You mean the world to me. If I say I couldn't have done it without you I mean it very literally. I wouldn't even have applied to EMBL if it weren't for your encouragement. Thank you for all the adventures, can't wait for what comes next.

Table of Contents

Abstract ix

Zusammenfassung xi

Acknowledgments xiii

Table of Contents xvii

List of Figures xxi

List of Tables xxiii

List of Abbreviations xxv

0 Preamble 1

1 Introduction 3

1.1 Membrane trafficking . . . 3
1.2 Endocytosis: Table manners of a cell . . . 6
1.3 Clathrin-mediated endocytosis . . . 7
1.3.1 Structural investigation of the clathrin coat . . . 9
1.3.2 Imaging the dynamics of clathrin-mediated endocytosis . . . 13
1.3.3 The complex roles of endocytic components . . . 14
1.4 Membrane bending and the clathrin coat . . . 16
1.4.1 Explaining the structural diversity of clathrin lattices in cells . 18
1.4.2 The remodeling of the clathrin coat . . . 19
1.5 Superresolution microscopy . . . 22
1.5.1 The optical resolution limit . . . 23
1.5.2 Principle of single-molecule localization microscopy . . . 24
1.5.2.1 Three-dimensional single-molecule localization microscopy . . . 27
1.5.2.2 Multi-color single-molecule localization microscopy . 28
1.5.3 Updated definition of resolution . . . 30
1.5.4 Illuminating the nanoscale: Choosing the appropriate label . . 31
1.5.4.1 Organic dyes . . . 32

1.5.4.2 Fluorescent proteins 35
1.5.5 Delivering labels to biological structures 36
1.5.5.1 Considerations for the choice of labeling strategy . . . 36
1.5.5.2 Different labeling strategies 37
1.5.6 Quantitative Data Analysis in Single-Molecule Localization Microscopy 39
1.5.6.1 General patterns in localization data 40
1.5.6.2 Describing individual clusters of localizations 40
1.5.6.3 Understanding the geometries of individual structures 40

2 Aims of the study **43**

3 Results **45**
3.1 Imaging clathrin-coated structures with single-molecule localization microscopy 45
3.1.1 Experimental considerations for successful clathrin coat labeling 46
3.1.2 Resolving the 3D geometry of clathrin coats 47
3.2 From qualitative to quantitative: Capturing the geometric diversity of clathrin coats 50
3.2.1 Segmentation and curation of single clathrin-coated structures 50
3.2.2 LocMoFit: Maximum-likelihood model fitting for quantitative analysis of single-molecule localization data 51
3.2.3 Sorting clathrin coats along their endocytic progression 54
3.2.4 Clathrin coats simultaneously grow and bend during endocytosis 57
3.2.5 Additional parameters that reflect changes in clathrin coat geometry 58
3.2.6 Golgi-originated clathrin coats grow distinct from endocytic sites 59
3.2.7 Comparing current clathrin coat growth models with experimental data 61
3.3 Cooperative curvature model: an updated model for clathrin coat remodeling 63
3.3.1 Model assumptions, analytical solution and fit to data 63
3.3.2 Linkage error and potential effects on model fit 69
3.3.3 Cell-line specific adaptations of the clathrin coat remodeling mechanism 71
3.4 Clathrin coat remodeling over pseudotime 78
3.4.1 Reconstructing the pseudo-timeline of clathrin coat remodeling 78
3.4.2 Generating high-resolution averages of clathrin coats at distinct endocytic stages 81
3.5 Towards a reconstruction of the entire endocytic machinery 84
3.5.1 Using the clathrin coat as a structural and temporal reference . 84
3.5.2 Dynamin-2 recruitment to the developing clathrin coat 85
3.5.3 AP-2 recruitment to the developing clathrin coat 87

3.6 Contributions 90

4 Discussion **91**
4.1 Investigating geometric changes of the clathrin coat 92
4.2 Clathrin coat growth models 92
4.3 Membrane bending according to the cooperative curvature model . . . 93
4.4 Flat clathrin pre-assembly 94
4.5 Abortive events 95
4.6 Further mechanistic interpretations of the cooperative curvature model 96
4.7 Cellular consequences of the cooperative curvature model 97
4.8 Limitations of the cooperative curvature model 98
4.8.1 Other endocytic components 98
4.8.2 Assumption of a single endocytic pathway 99
4.9 Comparison with live-cell data 100

***5* Future outlook** **103**

6 Materials & Methods **107**
6.1 Materials 107
6.1.1 Chemicals 107
6.1.2 Consumables 109
6.1.3 Buffers, solutions, and media 110
6.1.4 Equipment 113
6.1.4.1 Microscope for localization microscopy 113
6.2 Methods 116
6.2.1 Antibody conjugation 116
6.2.2 Cell culture 116
6.2.2.1 SK-MEL-2 human melanoma cells 117
6.2.2.2 3T3 mouse fibroblasts 117
6.2.2.3 U-2 OS human bone osteosarcoma 117
6.2.2.4 Transfection of 3T3 mouse fibroblasts 117
6.2.3 Sample preparation 118
6.2.3.1 Coverslip preparation 118
6.2.3.2 Fluorescent bead sample preparation 118
6.2.3.3 Fluorescent dye sandwich preparation 119
6.2.3.4 Biological sample preparation 119
6.2.4 Microscopy 120
6.2.4.1 Sample mounting 120
6.2.4.2 Biological sample image acquisition in single-color . . 121
6.2.4.3 Biological sample image acquisition in dual-color . . . 122
6.2.4.4 Acquisition of 3D bead stacks 122
6.2.4.5 Imaging of a dye sandwich 122
6.2.5 Processing of microscope images 122

6.2.5.1 Localization of fluorescence signal 123
6.2.5.2 Generation of an experimental PSF model 124
6.2.5.3 Rendering and filtering 124
6.2.5.4 Drift correction 124
6.2.5.5 Image resolution 124
6.2.5.6 Color assigmnent 125
6.2.6 Geometric model fitting 126
6.2.6.1 Segmentation 126
6.2.6.2 Curation 126
6.2.6.3 LocMoFit analysis 126
6.2.6.4 Rotational averages over pseudotime 127
6.2.6.5 Simulations 128
6.2.7 Further data analysis 129
6.2.7.1 Data manipulation 129
6.2.7.2 Clathrin coat growth model fitting 130
6.2.8 Data availability 130

Bibliography **133**

List of Figures

1.1 Intracellular pathways of vesicular trafficking 5
1.2 First descriptions of what will be known as 'clathrin-coated vesicles' . . 7
1.3 Clathrin-coated structures adopt a variety of different curvatures *in situ* 10
1.4 Triskelia form the basic assembly unit of the clathrin lattice 11
1.5 Ultrastructure of assembled clathrin 12
1.6 Morphological differences of clathrin-coated structures across cell types 13
1.7 Modular pathway of clathrin-mediated endocytosis in mammalian cells 15
1.8 Clathrin coat remodeling according to different growth models 18
1.9 Point spread functions of single point emitters 25
1.10 Principle of single-molecule localization microscopy 27
1.11 Three-dimensional single-molecule localization microscopy 28
1.12 Ratiometric approach to acquire multicolor images in single-molecule localization microscopy 30
1.13 Blinking mechanism of Cy5 32
1.14 Fluorescence of Cy5 33
1.15 Enzyme-based imaging buffer for single-molecule localization microsocpy 34
1.16 Activation mechanisms of fluorescent proteins 36
1.17 Labeling strategies for single-molecule localization microscopy 39
1.18 Geometric analysis of a microtubule resolved using single-molecule localization microscopy 41
1.19 LocMoFit: Maximum-likelihood model fitting for quantitative analysis of single-molecule localization microscopy data 42

3.1 Single-molecule localization microscopy of clathrin 48
3.2 3D visualization of a clathrin coat 49
3.3 Exploring the diversity of clathrin-coated structures 50
3.4 Examples of clustered clathrin-coated structures 51
3.5 Quantitative description of the clathrin coat 52
3.6 Examples of clathrin-coated structures analyzed with LocMoFit . . . 53
3.7 Theta as a proxy for endocytic progression 54
3.8 Robustness of closing angle θ estimation 55

3.9 Distribution of clathrin coat geometries 56
3.10 Inhomogeneous labeling of clathrin-coated structures 56
3.11 Examples of vesicular structures 57
3.12 Changes in curvature and surface area of clathrin coats during endocytosis 58
3.13 Distribution and propagation of the projected area A_p and edge length ε of clathrin coats 59
3.14 Population of non-endocytic clathrin-coated structures 60
3.15 Population of non-endocytic clathrin-coated structures 61
3.16 Contradiction of current models with geometric data on clathrin coats 62
3.17 The cooperative curvature model describes clathrin coat remodeling during endocytosis 65
3.18 Impact of linkage error on geometric model fit 70
3.19 Clathrin-coated structures imaged in 3T3 mouse fibroblasts 72
3.20 Clathrin-coated structures imaged in U-2 OS human bone osteosarcoma 73
3.21 Distributions of clathrin coat geometries in different cell lines 74
3.22 Clathrin coat remodeling in different cell lines 75
3.23 Dynamic interpretation of the clathrin coat closing angle θ in SK-MEL-2 cells 79
3.24 Clathrin coat remodeling over pseudotime in SK-MEL-2 cells 80
3.25 Clathrin coat remodeling over pseudotime in 3T3 and U2OS cells . . 81
3.26 High-resolution averages of clathrin coat remodeling in three different cell lines 83
3.27 Simulation and analysis of U-shaped clathrin coats 84
3.28 Analysis of dynamin-2 recruitment to the developing clathrin coat . . 86
3.29 Dynamin-2 is increasingly recruited at enriched endocytic stages . . . 87
3.30 Localization precision determined for AF647 and CF680 88
3.31 Analysis of AP-2 recruitment to the developing clathrin coat 89

5.1 Investigating the role of actin in clathrin-mediated endocytosis 104

List of Tables

3.1 Equations to describe clathrin coat growth according to distinct models . 63
3.2 Bayesian information criterion (BIC) to compare different clathrin coat growth model fits 66
3.3 Summary of clathrin coat growth model fits in SK-MEL-2 cells 68
3.4 Summary of clathrin coat growth model fits in 3T3 cells 76
3.5 Summary of clathrin coat growth model fits in U-2 OS cells 77

6.1 List of chemicals used in this work 107
6.2 List of consumables used in this work 109
6.3 Microscope components 114
6.4 Equipment used in this work 115
6.5 Geometric descriptions of a spherical cap 129

List of Abbreviations

AP-2	Adaptor protein-2 complex
ATP	Adenosine triphosphate
BAR	Bin/Amphiphysin/Rvs
BFP	Back focal plane
BIC	Bayesian information criterion
CALM	Clathrin assembly lymphoid myeloid leukemia protein
CAM	Constant area model
EM-CCD	Electron multiplying charge-coupled device
CCM	Constant curvature model
CLIC	Clathrin- and dynamin-independent carriers
GEEC	Glycosyl phosphatidylinositol-anchored protein-enriched early endosomal compartments
CLTA	Clathrin light chain-A
CME	Clathrin-mediated endocytosis
DBSCAN	Density-based spatial clustering of applications with noise
DMSO	Dimethyl sulfoxide
DNA	Deoxyribonucleic acid
DOL	Degree of labeling
DONALD	Direct optical nanoscopy with axially localized detection
EM	Electron microsocpy
EMBL	European molecular biology laboratory
EMU	Easier microscope user-interface
FWHM	Full-width half maximum
GFP	Green fluorescent protein
GLOX	Glucose oxidase
IC	Internal conversion
ISC	Inter-system crossing
LDL	Low-density lipoprotein
LUT	Look-up table
MLE	Maximum-likelihood estimation
NA	Numerical aperture
NPC	Nuclear pore complex

PA-GFP	Photoactivatable green fluorescent protein
PAINT	Point accumulation for imaging in nanoscale topography
PALM	Photoactivated localization microscopy
PBS	Phosphate-buffered saline
PDF	Probability density function
PERPL	Pattern extraction from relative positions of localizations
PIP_2	phosphatidylinositol-4,5-bisphosphate
PSF	Point spread funtion
QPD	Quadrant photodiode
RFP	Red fluorescent protein
RNA	Ribonucleic acid
ROI	Region of interest
ROS	Reactive oxygen species
RT	Room temperature
SALM	Supercritical angle localization microscopy
SIM	Structured illumination microscopy
SMAP	Super-resolution microscopy analysis platform
SMLM	Single-molecule localization microscopy
STED	Stimulated emission depletion
STORM	Stochastic optical reconstruction microscopy
TIFF	Tagged image file format
TIRF	Total internal reflection fluorescence
UV	Ultraviolet light
3D	Three-dimensional

To my parents - Sabine & Marcel

0 | Preamble

I thought a lot about how best to start this first chapter of my doctoral thesis. It is well known that, while of course, mostly fascinating and intriguing, scientific text can be a bit dry at times. So I hoped to reward whoever attempts to read this work and offer an entertaining and light introduction to the introduction. I thought to write about the explorative spirit of human nature, how we look for meaning and reason from the emptiness of space to the packed and crowded environment within a single cell. I wanted to draw this analogy between astronomy and cell biology and point out how connected the development of microscopes and telescopes are. Even today, these fields inspire one another. The adaptive optics many of my colleagues implement in their microscopes were first developed to correct for distortions caused by the earth's atmosphere when peering into the vast universe (Booth, 2014; Beckers, 1993). I thought that would be quite poetic. Apart from it being a bit of a brag, I hoped it would explain to my family and friends outside the scientific field, why I devoted such a significant portion of my life to sitting in a dark room, staring at images of rather similar-looking bright dots, over and over and over again. I wanted to bring across a sense of wonder, that balances out these four years of complaining they had to endure. I aimed to say: This is it! This is why I did it, why I keep doing it, and why I can only wish to be doing it for much longer. It is really cool, just like Star Wars! 'Wissenschaft'. Although to me, generating knowledge always seemed more of an afterthought. Most of the time I generated confusion.

So here we are, I hope whoever reads this preamble can envision what I truly wanted to say. Just imagine something really smart and science-y.

The focus of this work itself is held in a much smaller scope than drawing analogies between science and Star Wars. What I actually sought to research are the table manners of individual human cells. Much like us, these tiny building blocks that make up our bodies need to eat and take up essential nutrients. Without a mouth, stomach, and intestine, they have to do it a little bit differently. Whenever they receive the signal for dinner time, they wrap themselves around their food, until they completely engulf and internalize it. Thus, whatever was outside, becomes inside, in a rather dramatic fashion, and can be digested to fuel the cell's function.

This spectacle is called clathrin-mediated endocytosis, and this is all I will talk about for the next 50 pages or so.

1 | Introduction

1.1 Membrane trafficking

Cells of all living organisms are surrounded by a thin layer called the plasma membrane. One of the main functions of the plasma membrane is that of a barrier, separating the extracellular from the intracellular space, thereby defining the entity of an individual cell, as well as the surface by which any cell interacts with its immediate environment.

However, this barrier is not absolute. It is, in fact, crucial for cellular function that it is not. Cells must constantly communicate with their environment to sense and relay extracellular cues, internalize and secrete components, and promote physical interactions. The plasma membrane allows certain molecules to diffuse freely across it but keeps out others entirely, which then require channels for facilitated diffusion or energy for active transport. Thus, the plasma membrane fulfills the complex balancing act between maintaining its structural integrity as a barrier and, at the same time, selectively enabling the exchange of components and information with the extracellular space.

To accomplish these tasks, cells constantly adapt the composition of their plasma membrane. The plasma membrane consists of phospholipids, which give rise to its basic bilayer architecture, but also harbors a vast diversity of proteins and other molecules. By modulating both its lipid composition as well as the population of membrane proteins like receptors, channels, and transporters presented at the surface, cells can dramatically change the characteristics of the plasma membrane.

While all cells are surrounded by an outer membrane, cells of eukaryotes also feature an intricate system of intracellular membranes and membraneous compartments. Their outer plasma membrane and internal membranes are in a state of continuous flux and exchange of molecules and information. Eukaryotes have evolved to take advantage of this wide membrane network to quickly respond to extra- and intracellular cues by adding and removing parts of the plasma membrane and exchanging any embedded material with other membranous compartments - a process that is generally referred to as membrane trafficking.

Membrane trafficking processes have traditionally been separated by their directionality. During a process called exocytosis, proteins, lipids, and carbohydrates are delivered

outwards to the plasma membrane or the extracellular space along the secretory pathway. In reverse, a process called endocytosis facilitates the internalization of the plasma membrane surface. Apart from retrieving membrane components themselves, endocytosis further enables the uptake of extracellular materials, specific substances, and in certain cases, even entire cells.

Mechanistically, during endocytosis, any material destined for internalization becomes locally engulfed by a small portion of the plasma membrane, which is eventually pinched off to form a small compartment called a vesicle containing that material. Generally, vesicles such as those generated during endocytosis act as carriers for the transport of cargo between different membranous compartments, from which they bud off or with which they fuse. The transport of molecules via vesicles is commonly called vesicular trafficking and represents a highly organized and specialized process.

During vesicular trafficking, proteins and other cargo can be transported across the cell, without ever having to pass the membrane. The endocytic route starts at the plasma membrane and transports extracellular cargo to the endosome and, ultimately the lysosome. In reverse, the secretory transport route generally passes vesicles from the endoplasmic reticulum to the plasma membrane and the extracellular space, via the Golgi Apparatus. However, these are not unidirectional pathways. For example, the secretory pathway can side-route via the lysosome, or endocytosed particles can escape the lysosome and be re-routed back to the plasma membrane. Thus balancing the influx and efflux of membrane elements allows cells to maintain their cell surface area while allowing for the exchange and reorganization of lipids and cargo, as shown in Figure 1.1 (Alberts *et al.*, 2008).

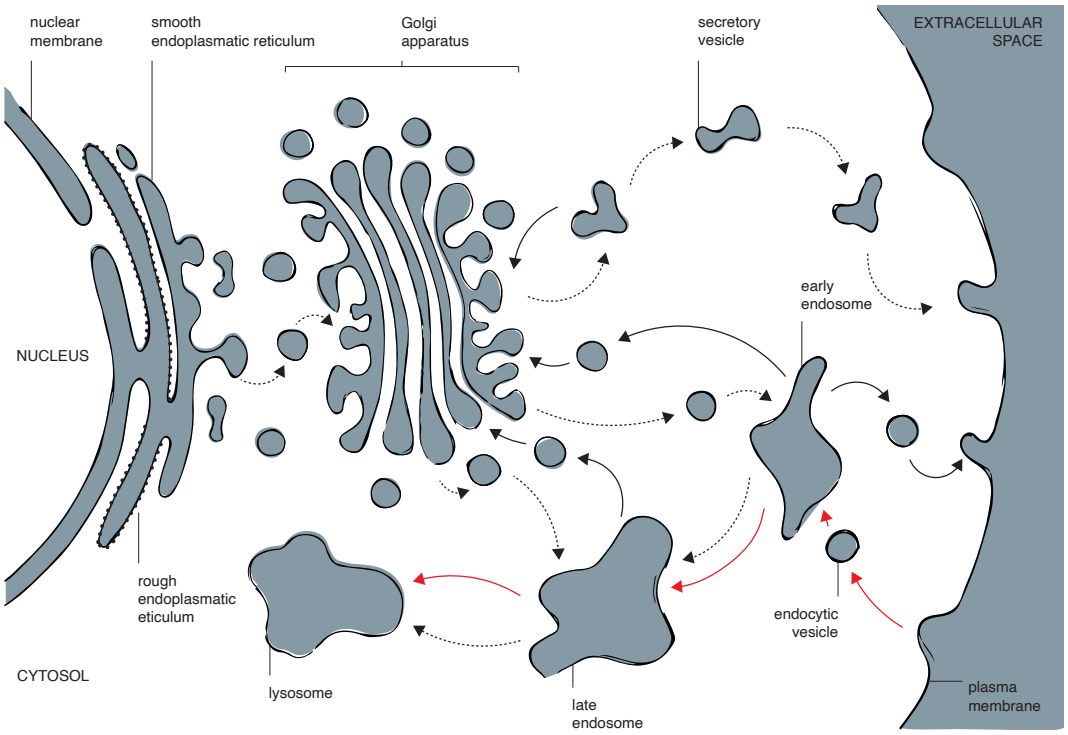


Figure 1.1 | Intracellular pathways of vesicular trafficking. Membraneous compartments within the cell are in constant exchange with the plasma membrane. Through endocytosis, small spherical compartments, called vesicles, are budding off of the plasma membrane, thus transporting membrane-bound and extracellular components into the cell *(red arrows)*. These endocytic vesicles fuse with early endosomes, which mature into late endosomes, which by fusing with a lysosome, ultimately leads to the degradation of endocytosed material into usable anabolic components. Certain components, such as trans-membrane receptors, can escape this degradation via vesicular transport from the early endosome back to the plasma membrane. Such recycling pathways *(black arrows)* can also transport material from the early endosome or secretory vesicles back to the trans-Golgi network. To ensure constant surface area of all membraneous compartments, the endocytic influx of membrane material is balanced out by efflux via the secretory pathway *(dotted arrows)*. This pathway transports components from the smooth endoplasmic reticulum connected to the nuclear membrane to the cis-Golgi network. The cis- and trans- Golgi networks are interconnected by vesicular transport in both directions. From the trans-Golgi network, budding vesicles can form secretory vesicles, fusing with the plasma membrane and transporting material to the extracellular space via a process called exocytosis. They can also fuse with the early endosome, targeting material to the lysosome. Throughout this process, the topology of the vesicular lumen stays constant across the lumen of other membranous compartments and the extracellular space *(grey)*. Thus membrane-bound components do not have to cross the membrane to be transported across the cell. *Figure generated by Aline Tschanz, with input from Alberts* et al., *2008.*

Vesicle formation and trafficking must be highly selective to ensure the specialized function of each compartment. The cell thus developed different molecular mechanisms, ensuring the formation of vesicles enriched for a specific cargo. The endocytic pathway alone summarizes a multitude of different mechanisms by which extracellular components can be packaged into vesicles and internalized (Mayor and Pagano, 2007; Thottacherry *et al.*, 2019).

1.2 Endocytosis: Table manners of a cell

The umbrella term 'Endocytosis' describes an array of mechanisms by which cells "eat and drink". Phagocytosis, from the Greek 'phagos' (to eat) and 'cyte' (cell) is characterized by the uptake of large particles including microbial pathogens and in specialized cases even other cells. It was first described by Ilya Metchnikoff in 1883, who discovered this process in starfish larvae (Tauber, 2003; Metchnikoff, 1883; Metschnikoff, 1887). Pinocytosis, from the Greek 'pinean' (to drink) and 'cyte' (cell) was described a few decades later by Warren H. Lewis, a pioneer in time-lapse cine photography of cells (Lewis, 1937). He observed membrane ruffles continuously engulfing large droplets of fluids and suggested this to be a process by which cells can take up large amounts of liquids and nutritional solutes. In the following decades of research, aided by the development of more powerful electron microscopy techniques, an intricate network of membranous compartments was described, connected by many endocytic pathways that differ in morphology and mechanics (Schmid *et al.*, 2014; Mayor and Pagano, 2007; Thottacherry *et al.*, 2019).

A seminal study by Thomas Roth and Keith Porter in 1964 described the first endocytic pathway dedicated to the selective uptake of cargo, which we know today as clathrin-mediated endocytosis. They observed the presence of protein-coated vesicles in mosquito-derived oocytes and argued that these protein coats could provide mechanical support in vesicle formation (see Figure 1.2). As the protein coat was present at shallow and progressively curved invagination sites, they argued that these protein structures could promote curvature throughout invagination. They further suggested a potential role of this ≈100 nm big coat in guiding the selective uptake of, in the case of their study, yolk protein at increased efficiency (Roth and Porter, 1964). Toku Kanaseki and Ken Kadota studied the structural details of this protein coat in 1969, and described it as a vesicular basket with polygonal faces (Kanaseki, 1969, see Figure 1.2b). Their notion, that a rearrangement of hexagonal to pentagonal faces could be the mechanical basis of vesicle formation, was later supported by Barbara Pearse, who, in 1975, finally coined the term 'clathrin' for the molecules that make up these vesicular baskets (Pearse, 1975). Around that time, in 1976 and 1977, Michael Brown and Joseph Goldstein described the selective uptake of low-density lipoprotein (LDL) via the same coated vesicles, coining the term 'receptor-mediated endocytosis' (Brown and Goldstein, 1976; Anderson *et al.*, 1977). Thus, by the end of the 1970s, clathrin-mediated endocytosis was described as an endocytic pathway mechanistically promoted by the characteristic arrangement of clathrin molecules into a polygonal lattice, allowing for the selective uptake of, among others, LDL particles (Robinson, 2015).

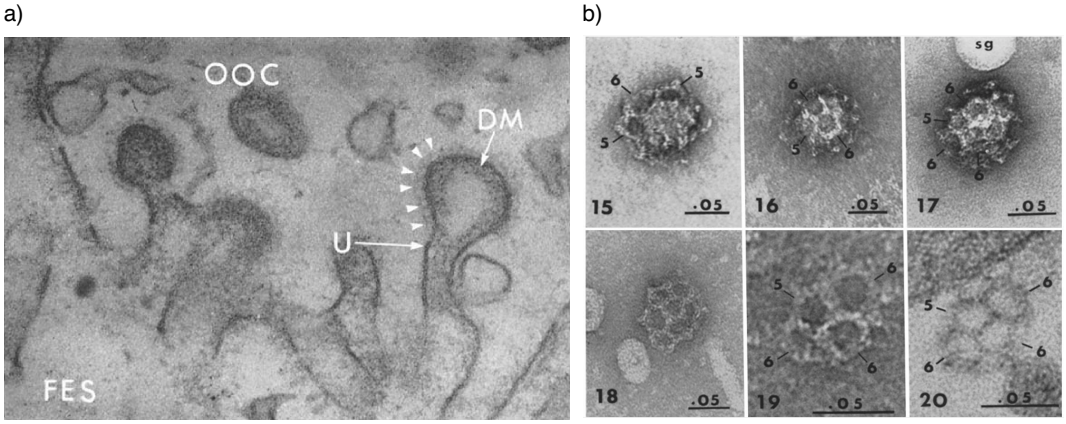


Figure 1.2 | First descriptions of what would later be known as 'clathrin-coated vesicles'. a) Electron micrographs generated by Thomas Roth and Keith Porter in 1964. They observed the formation of pits through the invagination of oocyte cell (OOC) membranes. A uniform layer of dense material can be seen to adhere to the 74 Å unit membrane (U) at the interface between oocyte and follicular epithelium (FES). On the cytoplasmic side of the pit 200 Å bristles (arrows) radiate inwards. The image was 106,000 times magnified. **b)** In 1969, Toku Kanaseki and Ken Kadota described the structural details of these bristles in isolated vesicular structures. They showed 'basketed vesicles' using negative-stain electron microscopy (panel 15 - 19), resolving the hexagonal (6) and pentagonal (5) faces of the coat lattice. Each polygon has a diameter of ≈240 Å. Panel 20 represents OsO_2-glutaraldehyde-fixed and thin-sectioned electron micrograph. Scale bars: 50 nm. *Figures adapted from a), Roth and Porter, 1964; b), Kanaseki, 1969, according to journal guidelines.*

To date, clathrin-mediated endocytosis has become one of the most thoroughly studied endocytic pathways of eukaryotic cells (Kaksonen and Roux, 2018). In addition, many other pathways have been since described, including macropinocytosis, caveolae-dependent endocytosis, cholesterol-sensitive clathrin- and caveolae-independent pathways, and large capacity CLIC/GEEC (clathrin- and dynamin-independent carriers/glycosyl phosphatidylinositol-anchored protein-enriched early endosomal compartments) pathways (Thottacherry *et al.*, 2019).

1.3 Clathrin-mediated endocytosis

The pathway of clathrin-mediated endocytosis starts at the plasma membrane, where a roughly spherically shaped vesicle is generated. This process occurs via the assembly of a protein coat on the inner leaflet of the membrane, which fulfills two functions: Sequestering and sorting cargo destined for internalization, and mechanical reshaping of the underlying membrane (Traub and Bonifacino, 2013; Chen and Schmid, 2020).

The major component of the clathrin coat is clathrin itself (Pearse, 1975). Each subunit comprises three clathrin heavy and three clathrin light chains, which assemble into a structure called a clathrin triskelion. Interactions of multiple triskelia result in the characteristic polygonal lattice. The regularity and rigidity of this coat structure are thought to contribute most of the mechanical forces that lead to reshaping the underlying plasma membrane (Royle, 2006).

Although clathrin can assemble into rigid coat structures, it binds neither to the membrane nor to cargo molecules. Thus, clathrin requires adaptor proteins to allow for membrane recruitment and the selection of specific cargo. These adaptor proteins, such as adaptor protein-2, enable the recognition of sites at the plasma membrane destined for internalization. They further recruit scaffolding units, including clathrin, to this endocytic site, ultimately crosslinking cargoes and membranes to the surrounding coat (Popova *et al.*, 2013; Mettlen *et al.*, 2010; Kovtun *et al.*, 2020; Lizarrondo *et al.*, 2021; Smith and Smith, 2022.

During clathrin-mediated endocytosis, the interplay between protein coat components has to successfully counteract the plasma membrane's resistance to deformation. This requires force, locally pulling the plasma membrane inside the cell. As clathrin-mediated endocytosis is highly conserved across different organisms, cell types, and mechanical environments, it becomes clear that this machinery has evolved to ensure robust uptake of plasma membrane against such opposing forces, including membrane tension (Hassinger *et al.*, 2017; Liu *et al.*, 2010b; Lacy *et al.*, 2018; Jin *et al.*, 2022).

While most of the remodeling mechanics are attributed to clathrin itself, actin and its regulatory proteins are thought to also contribute to the force required when invaginating the plasma membrane. This notion is strongly supported by studies using budding yeast as a model organism for endocytosis (Skruzny, 2022). These studies have spearheaded the investigation of clathrin-mediated endocytosis and revealed many aspects of endocytic dynamics and function. In yeast, actin is essential when forming membrane invaginations. In contrast to mammalian cells, yeast cells are surrounded by a rigid cell wall. High intracellular pressure, called turgor, causes the plasma membrane to be pressed against this cell wall, resulting in much greater forces required to invaginate it (Basu *et al.*, 2014). Thus, these cells require the involvement of actin, which provides this additional force and counteracts the high turgor pressure (Kukulski *et al.*, 2012). Compared to yeast, mammalian cells have to counteract a much smaller intracellular pressure, and actin is thought to occupy a more ambivalent role in force generation (Merrifield *et al.*, 2005; Fujimoto *et al.*, 2000; Aghamohammadzadeh and Ayscough, 2009). Analogous to its force-generating role in yeast, actin becomes essential when increasing the membrane tension, and thus the force requirement, in mammalian cells (Boulant *et al.*, 2011). As cells can exhibit variable membrane tension, depending on their environment or cell type, actin could therefore represent an essential adaptation mechanism of the endocytic machinery, responding to changing requirements by the cell (Sitarska and Diz-Muñoz, 2020). Recent studies highlight the possible mechanisms by which actin can contribute to clathrin-mediated endocytosis in mammalian cells (Kessels and Qualmann, 2021; Jin *et al.*, 2022; Kaplan *et al.*, 2022; Akamatsu *et al.*, 2020).

The release of a finalized clathrin coat into the cytosol is mediated by additional factors recruited to the developing vesicle neck. These include curvature sensing, stabilizing, and promoting proteins, which in turn enable the large GTPase dynamin to be recruited to the neck region. Dynamin then pinches off the vesicle during a process called scission.

Ultimately, the protein coat has to be removed from the now fully formed vesicle. This uncoating allows the recycling of coat material to form new endocytic sites while at the same time allowing the exposed vesicular membrane to fuse with the membrane of the target organelle (reviews of the general mechanism of clathrin-mediated endocytosis: Kaksonen and Roux, 2018; Skruzny, 2022; Smith and Smith, 2022).

1.3.1 Structural investigation of the clathrin coat

The structural characterization of clathrin is closely linked to advances in electron microscopy. From the earliest description of the protein coat and its polygonal arrangement to the high-resolution imaging of individual clathrin molecules within this lattice, improvement of electron microscopy over the past decades has revealed increasingly more structural details of clathrin-coated structures (Picco and Kaksonen, 2018; Schmid *et al.*, 2014).

The honeycomb lattices formed by clathrin were first clearly appreciated in the work of John Heuser in 1980. Using deep-etch electron microscopy, he removed most intracellular content obstructing the view on these structures *in situ*, resulting in unprecedented images of clathrin at the inside of the plasma membrane. He described the structural versatility of the observed clathrin coats, ranging from large shallow patches to dome-shaped structures and spherical coats (Heuser, 1980, see Figure 1.3). Advances in this imaging technology, also called 'unroofing,' combined with platinum replicate electron microscopy, continue to provide remarkable images and insights into the structural aspects of the clathrin lattice (Sochacki *et al.*, 2021; Sochacki *et al.*, 2017; Collins *et al.*, 2011).

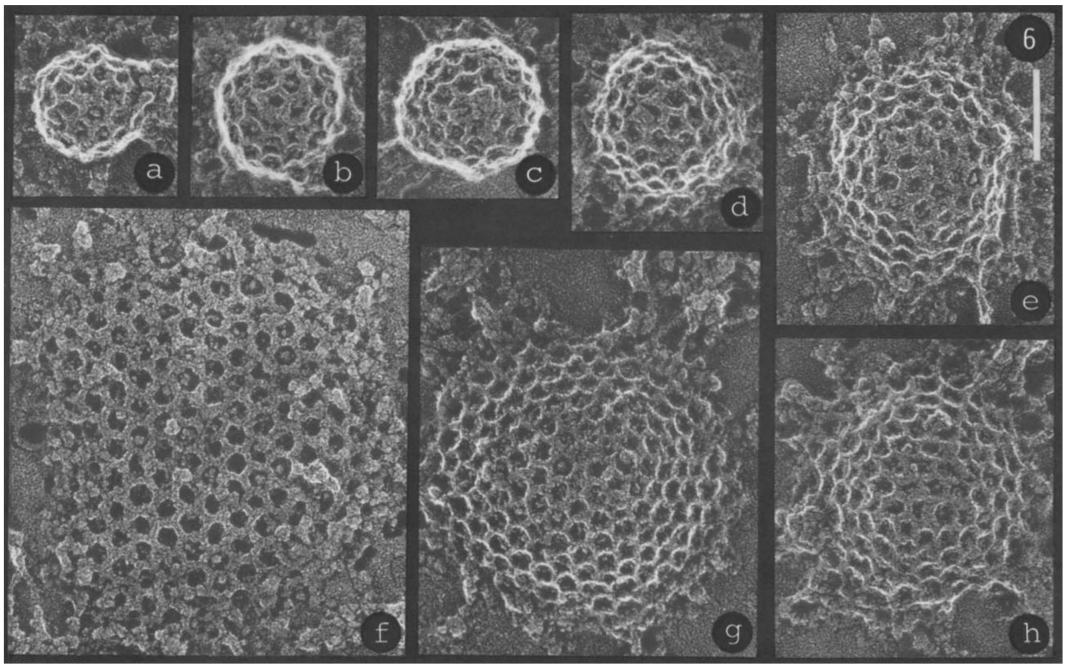


Figure 1.3 | Clathrin-coated structures adopt a variety of different curvatures *in situ*. In 1980, John Heuser described the architecture of clathrin-coated structures in fibroblasts using quick-freeze, deep-etch, and rotary-replication electron-microscopy. Selected example structures were arranged in decreasing (a-e) and increasing curvature (f-h). Scale bar: 0.1 µm. *Figure adapted from Heuser, 1980, according to journal guidelines*.

As previously mentioned (see Section 1.3), the main components of the clathrin coat are clathrin molecules themselves, called triskelia. To understand how clathrin-coated structures can arise, it is paramount to investigate the structural properties of triskelia themselves. The interactions between these molecules are responsible for forming the polygonal faces in the clathrin lattice visible in Figure 1.3. First described in 1981 by Ernst Ungewickell and Daniel Branton using rotary shadowing and transmission electron microscopy, the trimeric structure of a triskelion could be appreciated. All clathrin subunits comprise three identical clathrin-heavy chains, each ≈ 190 kDa, and three smaller units of clathrin-light chains, each ≈ 25 kDa (Ungewickell and Branton, 1981). The interactions between the heavy chains 'legs' of multiple triskelia results in the formation of pentagons and hexagons, forming the structural backbone of the clathrin coat (Paraan *et al.*, 2020).

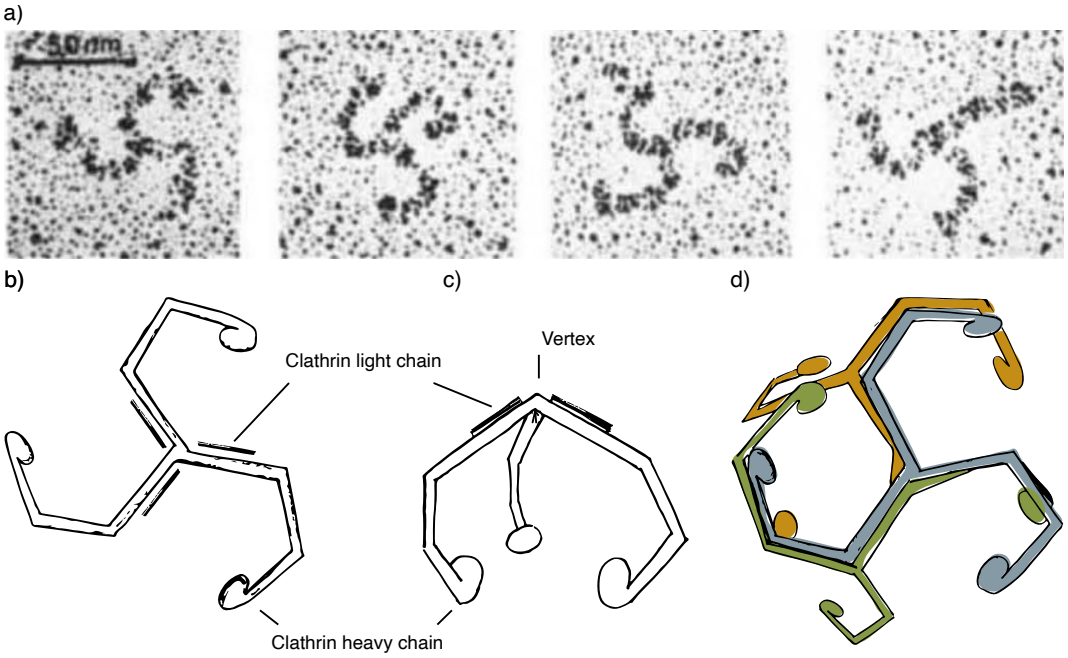


Figure 1.4 | Triskelia form the basic assembly unit of the clathrin lattice. a) First described by Ernst Ungewickell and Daniel Branton in 1981, clathrin assembles into a trimeric structure called a 'triskelion'. **b)** A single triskelion is formed by three heavy and three light chains. **c)** When assembled, a triskelion comprises an intrinsic 'pucker' angle. **d)** Multiple triskelia interact to form a clathrin lattice. *a), Figure adapted from Ungewickell and Branton, 1981, according to journal guidelines; b-d) Figure generated by Aline Tschanz, original structure can be found at PDB ID 1XI4 (Fotin* et al.*, 2004).*

Advances in structural resolution both on reconstructed clathrin cages (Kanaseki, 1969; Vigers *et al.*, 1986; Smith *et al.*, 1998; Edeling *et al.*, 2006) and well as on single clathrin particles (using X-ray crystallography, Ybe *et al.*, 1999; Haar *et al.*, 1998) allowed the structural investigation of clathrin heavy and light chain interactions directly within a coat. Ultimately, Fotin and colleagues were able to combine X-ray crystallography-derived ultrastructures of clathrin subunits with electron densities determined by cryogenic electron microscopy, resolving the clathrin coat assembly *in vitro* at ≈8 Å (Fotin *et al.*, 2004). This provided a detailed molecular understanding of how clathrin molecules can assemble into a polygonal lattice (see Figure 1.5).

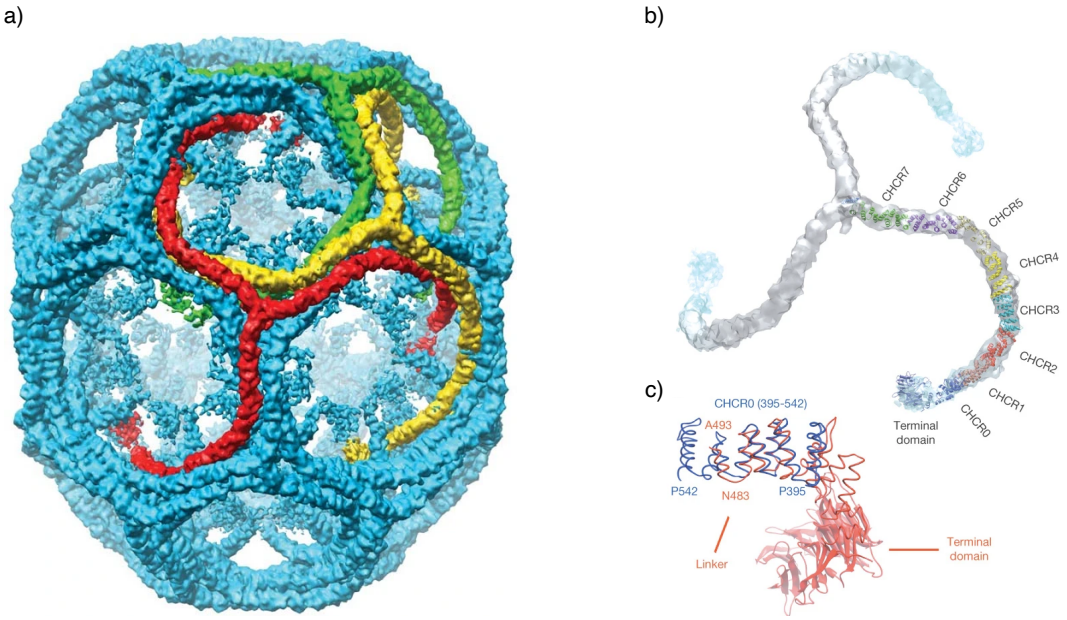


Figure 1.5 | Ultrastructure of assembled clathrin. a) Cryogenic electron microscopy allowed the reconstruction of a clathrin hexagonal barrel at 7.9 Å resolution. Here, only clathrin-heavy chains are shown. **b)** Combination of structures and homology models resulted in atomic models for each segment of a clathrin leg. **c)** Superimposed homology model for CHCR0 *(blue)* superimposed with the crystallographically derived model for the terminal domain and linker *(red)*. *Figure adapted from Fotin* et al.*, 2004, with permission from the authors.*

These studies highlighted the clathrin triskelia arrangement around a central hub, or vertex, from which three heavy chain 'legs' protrude outwards. The heavy chains are considered the 'back-bone' of these structures, with the much smaller light chains embedded on top. Through their many interaction points, the legs of the heavy chains can interact with each other to form pentagonal or hexagonal faces. As suggested early on, the integration of pentagonal faces is essential for forming spherical structures, indicated by local curvatures next to pentagonal faces. 12 pentagons are thought to be required to reshape a flat clathrin lattice into a spherical vesicular basket (Heuser, 1980; Kanaseki, 1969).

Coats assembled *in vitro* and resolved by cryogenic electron microscopy are generally made up of 12 pentagons and 8 hexagons, commonly referred to as barrels (Fotin *et al.*, 2004). However, clathrin structures can adopt a wide variety of different conformations, often cell-type specific (see Figure 1.6). While clathrin-coated structures in neurons are generally small, similar to the *in vitro* reconstructed clathrin barrels (Cheng *et al.*, 2007; Pechstein *et al.*, 2010), fibroblasts exhibit larger vesicular coats (Bretscher *et al.*, 1980; see Section 3.3.3). Additionally, clathrin can shape larger, flat patches referred to as plaques, which can serve as hot spots for vesicle generation. An additional function of flat clathrin structures, especially in muscle cells or migrating cells is adhesion to the cellular environment (Leyton-Puig *et al.*, 2017). Plaques can sequester proteins involved in adhesion, such as integrins, which can mediate their interaction with the surrounding extracellular matrix (Almeida-Souza *et al.*, 2018. Further, disrupting the balance between

clathrin sequestered to endocytic sites for vesicle generation and clathrin sequestered to adhesive structures in muscle cells can have severe implications for the function of these cell types and ultimately the health of the entire organism (Moulay *et al.*, 2020).

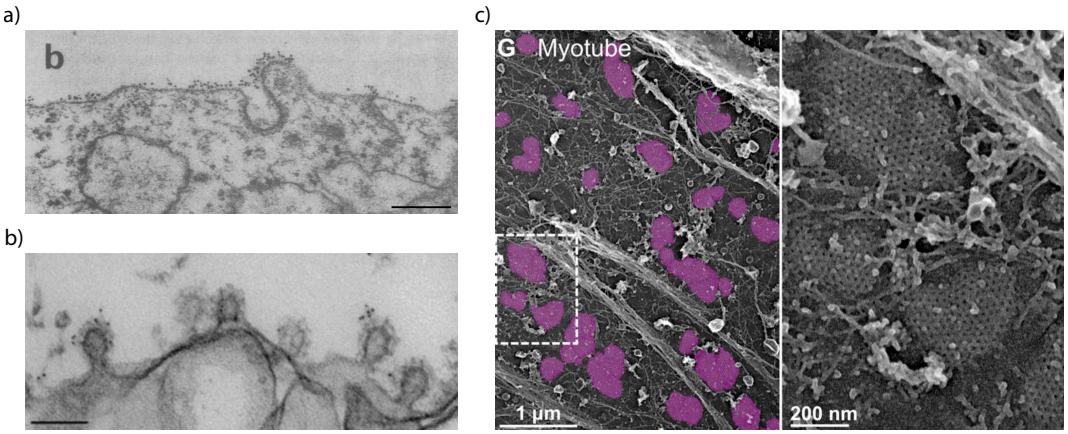


Figure 1.6 | Morphological differences of clathrin-coated structures across cell types. a) Mouse fibroblasts generate clathirn-coated structures at a diameter of ≈153 nm. **b)** Structures at stimulated Lamprey synapses are on average 84 nm in size. c) Human myotube muscle cells exhibit large flat clathrin patches. Scale bars: a), 0.2 µm; b), 0.2 µm; c), 1 µm (left) and 200 nm (right). *Figure adapted from a), Bretscher* et al.*, 1980; b), Pechstein* et al.*, 2010; c), Moulay* et al.*, 2020, according to journal guidelines.*

1.3.2 Imaging the dynamics of clathrin-mediated endocytosis

Advances in our understanding of clathrin-mediated endocytosis are closely linked to the development of techniques for visualizing this complex cellular mechanism. Electron microscopy has proven to be an essential tool for resolving membranous compartments, revealing the vesicular connections between organelles and the protein coats that facilitate their formation. Nevertheless, endocytosis is a dynamic process, and while electron microscopy provides excellent spatial resolution, it lacks temporal information, making it challenging to study the dynamics of this process in living cells and organisms. To address this, fluorescence microscopy has emerged as a cornerstone in the visualization of clathrin-mediated endocytosis, enabling researchers to study the temporal aspects of this process.

Since the discovery and widespread application of green fluorescent protein (GFP) and its derivatives, fluorescence microscopy has become an indispensable tool for visualizing cellular processes in living cells (Tsien, 1998; Remington, 2011). GFP and other fluorescent proteins make it possible to directly label a protein of interest with high molecular specificity. By generating chimeric gene sequences of both target and fluorescent proteins, these fusion proteins can be expressed in mammalian or other systems and visualized using light. As light is minimally invasive to the cell, the target molecules can thus be followed live, at sub-second temporal resolution (Rodriguez *et al.*, 2017).

Live-cell studies employing fluorescence microscopy have identified new endocytic components, resolved the sequential order in which they are recruited to the maturing

clathrin coat, and measured their movement and lifetime during endocytosis (Taylor *et al.*, 2011; Gaidarov *et al.*, 1999; Engqvist-Goldstein *et al.*, 2001; Rappoport and Simon, 2003; Merrifield *et al.*, 2002; Kaksonen *et al.*, 2003; Ehrlich, 2004; Sirotkin *et al.*, 2010; Loerke *et al.*, 2011; Aguet *et al.*, 2013). These tools have painted a comprehensive picture of when which proteins arrive at the endocytic site and for how long they remain. By carefully calibrating the fluorescence intensity detected, it is further possible to estimate the number of proteins involved and quantify their abundance. Thus, the functional roles of endocytic components could be inferred from their study in living cells (Picco and Kaksonen, 2018; Keyel *et al.*, 2004; Cocucci *et al.*, 2012).

1.3.3 The complex roles of endocytic components

To date, over 50 proteins with suggested roles during clathrin-mediated endocytosis have been identified. Functional studies performed either *in vitro* or *in situ* have elucidated a complex network of interactions and redundancies between these endocytic components (Traub, 2011; Weinberg and Drubin, 2012).

Most of these studies were performed in the model organism budding yeast. Clathrin-mediated endocytosis is largely conserved across eukaryotic species. The budding yeast *Saccharomyces cerevisiae* has human homologs for ≈90% of its endocytic machinery. Studies in yeast came with considerable practical and experimental advantages, thus greatly complementing our understanding of the endocytic process in mammalian cells. The yeast endocytic machinery is considerably less complex, with fewer auxiliary, redundant, and cell-type-specific proteins involved. They are easier to genetically manipulate than mammalian cells, with a much more regular endocytic process (McMahon and Boucrot, 2011; Skruzny, 2022).

Insights gained from both model systems highlight the modular character of clathrin-mediated endocytosis. The proteins are involved at the endocytic site in a highly regular manner, arriving and leaving in an organized sequence. On the basis of their role in the process, proteins can thus be categorized into functional modules. The functional and structural interactions of proteins in each module ensure the propagation, regulation, and orchestration of the entire endocytic pathway (see Figure 1.7).

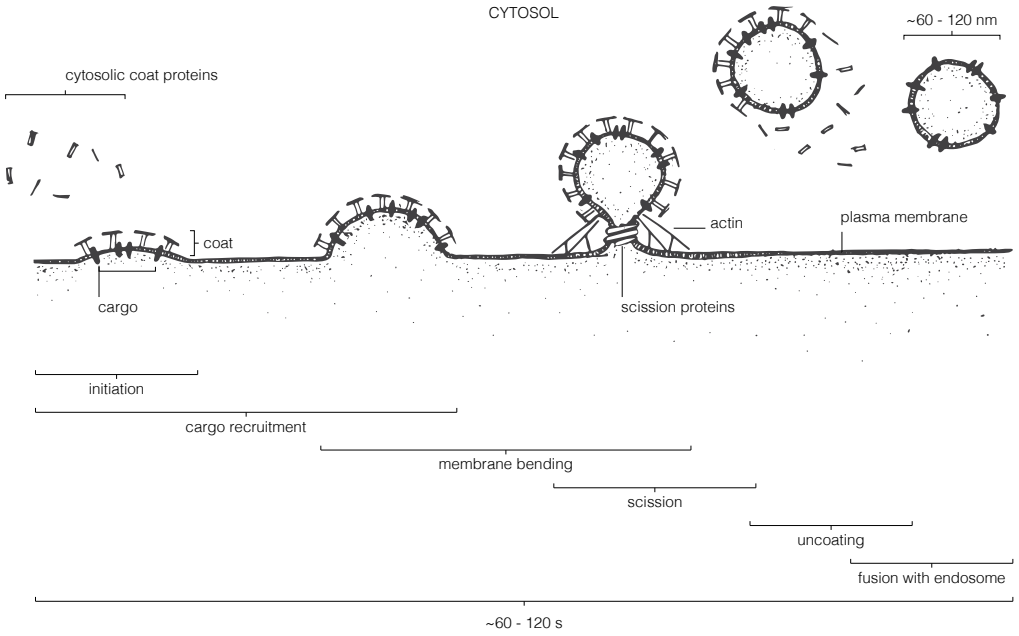


Figure 1.7 | Modular pathway of clathrin-mediated endocytosis in mammalian cells. During mammalian endocytosis, cargo molecules are sequestered at the plasma membrane, and a protein coat is initiated at its inner leaflet. Next, further cargo is recruited to the endocytic site which matures and reshapes the underlying plasma membrane into a spherical vesicle. This vesicle is released into the cytosol via scission, where it quickly becomes uncoated, thus freeing it for subsequent fusion with endosomes. Released coat proteins can be recycled back to the membrane for new endocytic events. This entire process takes approximately 60 to 120 seconds and generates vesicles ranging from a diameter of 60 to 120 nm. *Figure generated by Aline Tschanz.*

Clathrin-mediated endocytosis starts with the initiation of the endocytic site, to which then cargo is recruited. Next, the membrane has to be re-shaped into an invagination, which is ultimately released from the plasma membrane during scission. The final uncoating step ensures the release of coat proteins back to the cytosol, and the release of the vesicle for further trafficking.

During the initial nucleation, extracellular and transmembrane cargo is selected and sorted into early endocytic sites. Certain cargoes are constitutively taken up (transferrin receptors, TfR; low-density lipoprotein receptors, LDLR), while others are only taken up upon ligand binding (epidermal growth factor receptors, EGFR; G protein–coupled receptors, GPCR). Cargoes are recognized by particular amino acid sequences and architecture (motifs) in their cytoplasmic domain. This recognition is mediated by adaptor proteins such as adaptor protein-2 complex AP-2. AP-2, in turn, also recognizes specific membrane domains (phosphatidylinositol-4,5-bisphosphate, PIP_2) and other components of the endocytic machinery. Together with F-BAR domain only protein 1 and 2 complex (FCHO1/2) and clathrin assembly lymphoid myeloid leukemia protein (CALM), it forms the connection between cargo, plasma membrane, and scaffolding proteins of the initial endocytic site.

Nucleating proteins allow scaffolding proteins such as clathrin, epsin, intersectin, epidermal growth factor receptor substrate 15 (EPS15), and epidermal growth factor receptor substrate 15-like 1 (EPS15L1) to accumulate where cargo is sequestered. This results in the clustering of these pioneering molecules forming the initial clathrin-coated pit.

Next, actin and its regulatory components are recruited. The branched actin network at clathrin-coated pits is nucleated by the actin-related proteins-2/3 (ARP2/3) complex, which is promoted via proteins of the Wiskott–Aldrich syndrome protein (WASP) family.

Once the spherical invagination has formed, the neck of the budding vesicles becomes more and more restricted through an assembly of curvature-sensing, stabilizing, and inducing bin-amphiphysin-rvs (BAR) proteins, including endophilins and amphiphysins. Their recruit the large GTPase dynamin recruits to the neck of the budding vesicle, where it mediates scission and the final release into the cytosol.

Auxilin and ATP-bound Heat shock cognate 71 kDa protein (HSC70) promote the final uncoating step.

These functional modules paint a highly complex network of interactions between different endocytic components. The fact that many of these components can be removed without severe consequences highlights the essentiality of this process for cell function, and the redundancies in place to ensure the stability of the endocytic process (Kaksonen and Roux, 2018; Traub, 2009; Mettlen *et al.*, 2018; Chen and Schmid, 2020).

1.4 Membrane bending and the clathrin coat

Cell membranes generally prefer to be flat, lacking any spontaneous curvature generation. However, during clathrin-mediated endocytosis, the plasma membrane becomes continuously invaginated to form a spherical vesicle. Thus, the endocytic machinery has to be able to counteract any resistance to deformation by the plasma membrane, such as membrane tension. This requires force (Sitarska and Diz-Muñoz, 2020). In mammalian cells, this force is thought to be provided in large parts by the assembly of the clathrin coat. However, the mechanism by which this force is generated remains elusive.

There have been two models proposed to conceptualize the mechanism underlying membrane bending by the clathrin coat. The 'constant curvature model' and the 'constant area model', both of which are supported by different experimental studies (see Figure 1.8).

According to the constant area model, clathrin is first accumulated into a flat structure, which provides the necessary force for membrane invagination through structural rearrangements within the clathrin lattice. This flat-to-curved transition was suggested based on the observations of the large diversity of curvatures present at mammalian membranes *in situ* (Heuser, 1980; Kanaseki, 1969). Assuming that all clathrin structures detected belong to the same endocytic pathway, it was assumed that more shallow structures

represent precursors to curved and spherical clathrin-coated structures. Following this pathway, shallow structures had to have the capability of remodeling into spherical coats, generating a spherical vesicle from a flat membrane in the process. As an enrichment of pentagonal faces was observed in curved compared to flat structures, the transformation of hexagons into pentagons was suggested as the driving force behind membrane bending.

However, in the years that followed, *in vitro* studies on clathrin assembly started to paint a different picture. First, these studies showed that clathrin spontaneously arranges into an empty basket, either under low-salt and -pH conditions (Woodward and Roth, 1978) or in the presence of AP-2 (Zaremba and Keen, 1983; Pearse and Robinson, 1984). This observation suggested that clathrin preferably arranges itself into spherical structures, showing a preference for high curvatures. Later experiments on membranes showed that clathrin, together with AP-2, represents the minimal endocytic machinery required to generate vesicles from membranes (Ford, 2001; Dannhauser and Ungewickell, 2012). Under these considerations, the initially proposed mechanism of a flat-to-curved transition seemed unlikely. The suggested rearrangement within the clathrin lattice was considered energetically unfavorable, as it would require the modification of numerous bonds between already arranged triskelia (Kirchhausen, 1993; Nossal, 2001). Therefore, it was proposed that clathrin directly polymerizes into a bent lattice. The invagination of the plasma membrane was thus considered the result of the continuous addition of clathrin to small coats, consistently invaginating the membrane with each accumulated molecule. This clathrin coat growth mode is nowadays referred to as the constant curvature model.

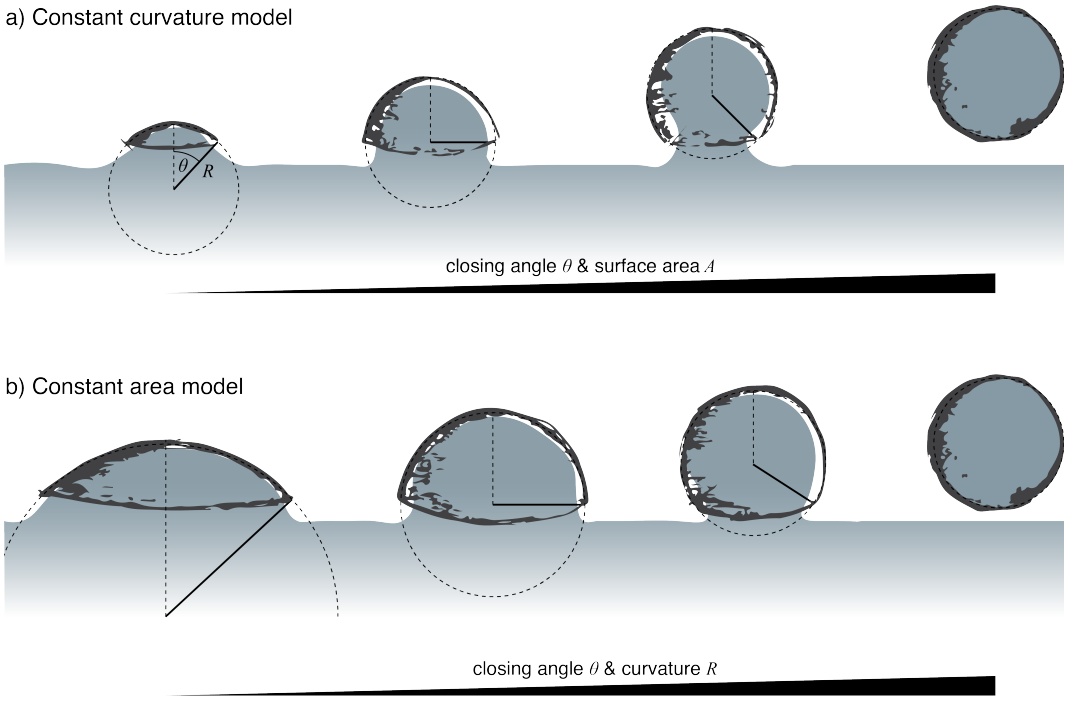


Figure 1.8 | Clathrin coat remodeling according to different growth models. a) The constant curvature model suggests an increase of surface area A through the gradual polymerization of clathrin triskelia. **b)** The constant area model proposes curvature initiation after the final coat area has been accumulated on a flat membrane. The subsequent increase in curvature leads to continuous invagination of the membrane until a vesicle is formed. For both models, the closing angle θ increases while a flat membrane is reshaped into a spherical vesicle. *Figure generated by Aline Tschanz.*

1.4.1 Explaining the structural diversity of clathrin lattices in cells

Both, the constant area and the constant curvature model have gained support from different experimental studies. The constant area model is mainly supported by studies *in situ*, where a high diversity in coat curvatures was observed. Under the assumption that all these structures belong to the same endocytic pathway, membrane bending was suggested to occur via the remodeling of shallow coats into spherical vesicles. Thus, according to the constant area model, flat clathrin structures have the ability to gain curvature during endocytosis.

However, *in vitro* studies have found that clathrin has the ability to spontaneously generate curvature. Thus, the constant curvature model suggests that the preferred curvature of clathrin molecules ensures that the polymerization of triskelia provides sufficient force for membrane bending.

How come that clathrin behaves so differently in these contexts? While *in vitro* experiments were generally performed with a minimal set of endocytic components (clathrin and adaptor proteins), endocytosis in cells is known to involve many more factors (see Section 1.3.3).

These factors could provide additional modulation of curvature generation, resulting in a larger diversity of sizes and topologies of clathrin-coated structures *in vivo*.

As an example, curvature sensing, stabilizing, and promoting proteins including CALM (clathrin assembly lymphoid myeloid leukemia protein) or proteins of the BAR family are known to increase local membrane curvatures during endocytosis (Miller, 2015; Qualmann *et al.*, 2011). Their involvement could facilitate membrane bending by the clathrin coat and distribute the desired curvature over the coat area (Kaksonen and Roux, 2018). This modulation of coat curvature could further depend on the location of these curvature-generating proteins relative to the clathrin coat (Sochacki *et al.*, 2017). The crowding of molecules at the edge of the lattice for example could modulate the tension, further promoting curvature generation, especially at later stages of endocytosis (Frey and Schwarz, 2020).

Additionally, curvature built up could be the result of increased rigidity of the clathrin coat itself. This rigidity could be modulated by additional endocytic components present *in vivo*. For example, clathrin light chains have been shown to modulate the triskelia structure, rigidifying the clathrin lattice and in turn regulating coat curvature (Dannhauser, 2015; Obashi *et al.*, 2023; Maib *et al.*, 2018).

Lastly, the clathrin coat could exhibit a flexibility *in vivo* that facilitates remodeling and curvature generation. This flexibility could be ensured by the exchange of clathrin material throughout the lattice, which has been shown previously (Avinoam *et al.*, 2015; Loerke *et al.*, 2005; Wu, 2001). As mentioned above, clathrin light chains are thought to provide the clathrin lattice with rigidity, which in turn modulates the curvatures of clathrin coats. The turnover of these proteins during endocytosis could thus provide the lattice with the necessary flexibility to transform hexagonal structures into pentagons, generating the local curvature needed for membrane bending. This flexibility of the clathrin coat could be further ensured through vacancies, which represent positions within the lattice that are not occupied by a triskelion (Frey *et al.*, 2020; Sochacki *et al.*, 2021).

These examples highlight the impact of cellular complexity and offer an explanation as to why clathrin exhibits a larger structural diversity in living cells compared to structures generated *in vitro*. The network of proteins involved during endocytosis can modulate the size and curvature of clathrin coats via the promotion of local membrane curvatures (CALM or BAR domain proteins), an increase of tension at the lattice edge, or an increase of rigidity of the clathrin lattice itself. Additionally, the flexibility of clathrin-coated structures offers the potential for structural remodeling, theoretically allowing the transformation of hexagonal into pentagonal faces.

1.4.2 The remodeling of the clathrin coat

To truly understand the mechanism behind membrane bending, it is paramount to visualize clathrin coats *in vivo*, where the cumulative effect of many endocytic components results in the characteristic maturation of the clathrin coat.

However, there is no simple approach available that would allow the simultaneous visualization of clathrin coat dynamics and spatial organization. The small size (≈80 nm) and fast dynamics (≈80 s) of the process make it difficult to record the necessary resolution in both the spatial as well as temporal dimensions. In the following paragraph, I will summarize current studies that aim to overcome this technical limitation using various different approaches.

In 2015, Avionam and colleagues set out to visualize clathrin-coated structures *in situ*. Their aim was to describe the 3D organization of a larger number of structures using correlative fluorescence and electron microscopy. Using direct 3D information, they sought to precisely characterize the geometries of all 233 structures in their data set, and investigate their potential remodeling during endocytosis. By manually tracing the profiles of each structure and analyzing them computationally, they could extract the curvature as well as the angle between the adherent plasma membrane and the invaginating segment. The invagination angle served as an estimate for endocytic progression, which allowed the sorting of clathrin-coated structures along the endocytic progression.

According to the constant curvature model, curvature values were expected to be distributed along a mean value, without any correlation along endocytic progression. Instead, the authors observed a strong relationship between curvature and invagination angle, which suggested that curvature increases during endocytosis. These observations agreed with the constant area model, which predicted a remodeling of the clathrin coat from a shallow to a curved structure (Avinoam *et al.*, 2015).

However, a significant drawback of this approach is the lack of direct temporal information. While the strong correlation between curvature and invagination angle suggested a mechanistically similar pathway for all structures involved, sorting along the invagination angle might still result in confounding temporal information. Delia Bucher and colleagues, therefore, complemented their electron microscopy approach with fluorescent markers for coat assembly to better fine-tune the temporal information content in static images. By using carefully calibrated fluorescence intensity as a marker for accumulated coat material, they were able to pinpoint the moment of curvature initiation, which they estimated at 70% of the final coat assembly (Bucher *et al.*, 2018). Contrary to Avinoam et al., they thus suggest a less stringent interpretation of the constant are model, with curvature being generated before the entire structure is accumulated on a flat membrane. A similar finding was reported by Aiko Yoshida and colleagues using high-speed atomic force microscopy in living cells (Yoshida *et al.*, 2018).

According to Bucher and Avinoam, all structures they visualized follow the same mechanistic pathway. However, without any direct temporal information, dynamic and potentially mechanistic variabilities between individual endocytic events are difficult to characterize. Brandon Scott and colleagues, therefore, took a different approach to the same question. To investigate the remodeling of individual clathrin coats *in vivo*, they applied a polarized total-internal reflection (TIRF) microscopy approach, which allows

them to record direct temporal information. With this technique, Scott et al. were able to investigate the structural reorganization based on the ratio between the signal illuminated parallel versus perpendicular to the coverslip. Depending on the changes in this ratio, they could estimate the degree of curvature being generated. As they observed a strong site-to-site variability, they concluded the co-existence of multiple pathways of curvature generation. Some structures seem to generate curvature instantly, whilst others show a flat pre-assembly and subsequent bending of the coat (Scott *et al.*, 2018). A similar strategy was presented recently by Tomasz Nawara and colleagues, who employed a TIRF-based method called simultaneous two-wavelength axial ratiometry (STAR) (Stabley *et al.*, 2015). Using STAR, Nawara et al. were able to record the dynamics of individual clathrin coats, while simultaneously inferring their invagination depths. They report similar results to Scott et al, suggesting the presence of various different coat growth mechanisms within a single cell (Nawara *et al.*, 2022).

While Scott et al. and Nawara et al. used technologies with excellent temporal resolution, they did not directly record the 3D organization of clathrin coats. Formulating a conceptualized model for clathrin coat maturation without sufficient structural detail can be misleading. Thus, Kem Sochacki and colleagues employ an approach that combines cell unroofing with 2D platinum replica electron microscopy. This technology offers a large field of view, resulting in many endocytic structures being captured in a single image. Thus, Sochacki et al. were able to probe the structural diversity of clathrin coats across many different cell lines. They observed the presence of many shallow structures, and while the measured surface area for clathrin coats seemed largely constant across different cell lines, they observed an increase of curvature, supporting the constant area model (Sochacki *et al.*, 2021).

The excellent throughput of 2D platinum replica electron microscopy allowed a systematic investigation of clathrin coat curvature. By generating large data sets of hundreds of clathrin coats, the endocytic pathway could be densely sampled and reconstructed. However, as this approach is limited to 2D information, the 3D architecture of the clathrin-coated structures had to be roughly categorized into flat, domed, and spherical structures. In order to confidently reconstruct the process of curvature generation from high-resolution snapshots of clathrin coats, it is paramount to record the direct 3D information.

With the arrival of superresolution microscopy, clathrin-mediated endocytosis has received new attention (Mund *et al.*, 2018; Arasada *et al.*, 2018; Sochacki *et al.*, 2017; Willy *et al.*, 2021). The advantage of superresolution microscopy methods is the high molecular specificity at a high signal-to-noise ratio inherent to all fluorescence-based imaging methods. Additionally, due to their increased spatial resolution, these methods allow the detailed structural investigation of subcellular machinery at a much higher throughput than electron microscopy-based approaches.

Thus, superresolution microscopy offers the ideal combination of information to investigate the remodeling of the clathrin coat, applicable across many cell types.

1.5 Superresolution microscopy

Advances in cell biology are tightly connected to advances in technologies that allow scientists to visualize cells and subcellular structures. Due to their small and complex nature, it is difficult to understand the temporal and structural relationships between cellular components. The tools available to visualize these relationships determine the information and understanding we can derive from them (Combs and Shroff, 2017). Thus, advances in visualization methods have frequently resulted in advances in cell biology.

Clathrin-mediated endocytosis presents a perfect example of this relationship, where increasingly detailed and resolved information on this process has increased our understanding thereof (see Section 1.3).

While electron microscopy has been particularly essential in the early days of clathrin-mediated endocytosis research (see Section 1.3.1), cell biology, in general, began with the light microscope (Hooke and Jo. Martyn and Ja. Allestry., 1665; Zuylen, 1981). In recent decades, optical microscopy has become a cornerstone of cell biological research, largely owing to the development of specific labeling applied in fluorescence microscopy (Morris and Payne, 2019; Giepmans *et al.*, 2006). Using fluorescent dyes, cellular constituents can be targeted at high molecular specificity and signal-to-noise contrast. Thus, the 3D architecture and relationship of these components can be reconstructed *in situ*. An additional advantage of optical microscopy is the minimal invasiveness of light. By tagging specific cellular components with fluorescent labels in living cells, their dynamics and interactions over time can be studied *in vivo*, at low phototoxicity. However, conventional fluorescence microscopy is limited to a spatial resolution of ≈250 nm (Schermelleh *et al.*, 2019). Thus, visualization at the molecular scale used to be reserved for structural methods such as cryogenic electron microscopy, X-ray crystallography, and nuclear magnetic resonance (Bai *et al.*, 2015).

Several imaging modalities have been developed to improve this optical resolution limit, promising increasingly detailed information on cellular processes. For example, as mentioned in Section 1.3.2, TIRF microscopy has proven to be an essential imaging technology when studying clathrin-mediated endocytosis dynamics (Taylor *et al.*, 2011). Here, the signal-to-noise is greatly enhanced by eliminating a large fraction of background fluorescence, dramatically improving image quality. In TIRF microscopy, the excitation and detection of fluorophores are restricted to a thin region of the specimen, thus excluding fluorophores located outside the focal plane. This technique exploits the unique property of an induced evanescent field, adjacent to the interface between a specimen and a glass coverslip. The penetration depth of this evanescent field usually ranges from 60 to 200 nm, thus in the example of clathrin-mediated endocytosis exciting only labeled

structures at the bottom membrane of a cell cultured on a glass coverslip (Axelrod, 2001). By removing the background caused by intracellular signal, the image quality could be greatly improved and the duration or 'lifetime' of individual endocytic traces could be studied (Taylor *et al.*, 2011).

While methods such as TIRF microscopy could improve image quality and effective spatial resolution, optical microscopy methods were long thought to be fundamentally limited by the laws of diffraction. This limit in spatial resolution of optical microscopes is called the 'diffraction barrier'.

1.5.1 The optical resolution limit

In an optical microscope, light travels through a system of lenses to generate a magnified image of a much smaller object. In the case of fluorescence microscopy, this object can be thought of as a collection of individual point sources such as fluorophores emitting light. The emitted light is then captured by the objective lens and focused onto the image plane, where it is projected onto a detector, such as a camera chip.

The imaging process of a single point source involves the propagation of light waves through an optical setup. As the waves encounter an aperture, such as a lens, they are diffracted and bent, leading to interference. Thus, instead of generating a focused image of the original point source, constructive interference results in a Gaussian intensity distribution of the signal, known as the point spread function (PSF). The width of the PSF is proportional to the wavelength of the light and the angle at which the light is collected by the objective lens. In the absence of aberrations, the PSF is an 'Airy disc' pattern, where constructive and destructive interference of light waves results in a central disc, surrounded by a series of dimmer diffraction rings (Airy, 1835). Thus, the resolution of an optical setup can be described as the radius of the Airy disk, as was first described by Ernst Abbe according to Equation 1.1 (Abbe, 1873).

$$R \approx \frac{\lambda}{2n \sin \alpha} \approx \frac{\lambda}{2\mathrm{NA}} \tag{1.1}$$

Here, r described the smallest resolvable distance or 'resolution limit' between two points. Any structural feature smaller than r is not resolvable. λ is the wavelength of the imaging light, n the refractive index of the imaging medium, and α the aperture angle. The expression $n \sin \alpha$ describes the numerical aperture NA of an objective lens. Thus, when imaging with light at a wavelength of λ = 600 nm and a commonly used objective lens (NA= 1.40, oil immersion), this results in a lateral resolution limit of ≈ 200 nm. Any points located closer than 200 nm will be challenging to resolve.

Using the mathematical expression of the PSF, John W. S. Rayleigh advanced Abbe's resolution criterion (see Equation 1.2), stating that two point sources are resolvable as long as the distance between them is greater than the distance between the maximum of

the central Airy disk to the first minimum of the Airy pattern. Should the maximum and minimum overlap, two point sources are not readily distinguishable (Rayleigh, 1879.

$$R \approx \frac{0.61\lambda}{\mathrm{NA}} \tag{1.2}$$

In the axial dimension, the PSF is more elongated, resulting in a resolution commonly 2-3 times worse in comparison to the lateral resolution. The conditions mentioned above that resulted in a lateral resolution limit of 200 nm would thus result in an axial resolution limit of ≈ 500 nm (Abbe, 1873).

1.5.2 Principle of single-molecule localization microscopy

The superresolution microscopy method called single-molecule localization microscopy (SMLM) aims to break the diffraction barrier by evaluating the fluorescence images of individual molecules.

As discussed above, when fluorescent molecules are spatially close, they can only be resolved as individual point sources if they are separated at least by the size of their PSF (generally measured at their full-width half maximum, FWHM, see Figure 1.9a-b). However, if only a single emitter is considered, its PSF in the resulting image is well-isolated and does not overlap with any other signal. In this case, the original position of the fluorophore at the center of the PSF can be determined with greater precision than the resolution limit (see Figure 1.9)c-e.

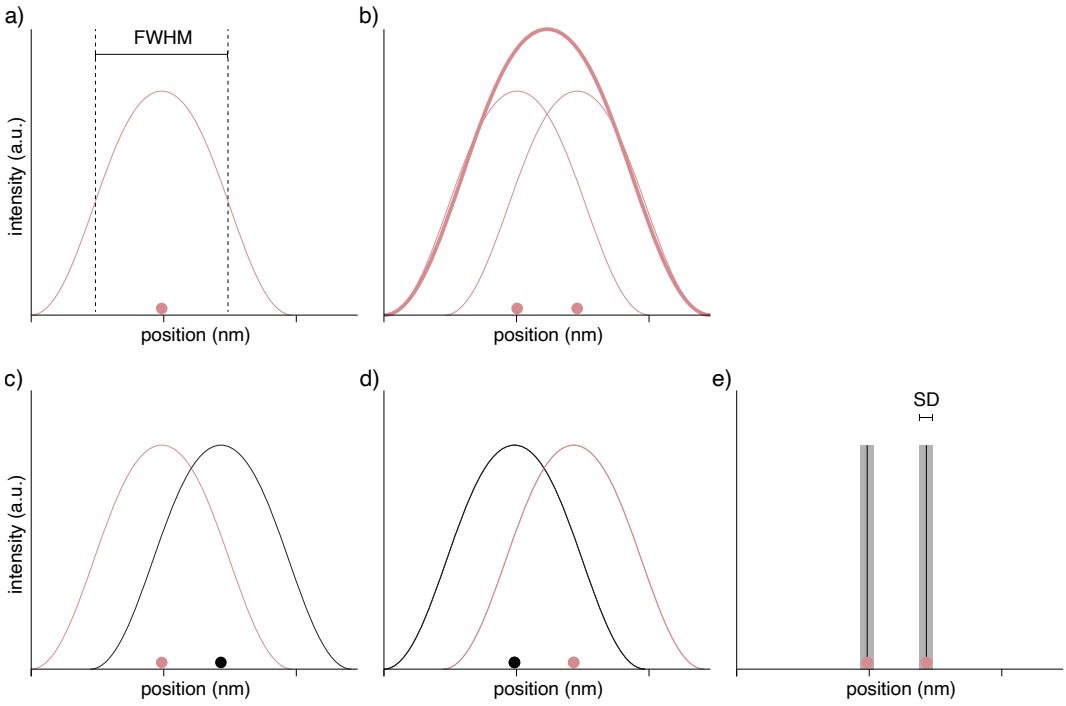


Figure 1.9 | Point spread functions of single point emitters. a) The intensity profile of an imaged single point emitter, such as a fluorophore *(pink dot)*, can be described by the point spread function PSF *(pink curve)*. The size of a PSF is usually measured at its full-width-half-maximum (FWHM). **b)** The size of a PSF determines the resolution limit of an optical microscope, as two points located closer than their respective FWHM become indistinguishable. **c-d** However, by selectively activating only a single emitter at a time, the coordinate of that fluorophore can be determined at much higher precision (smaller standard deviation SD). **e)** Thus, the coordinates of two point emitters located close in space can be traced back. Scale bar: 200 nm. *Figure generated by Aline Tschanz.*

A two-dimensional PSF can be well approximated with a Gaussian distribution, for which a centroid can be calculated. By fitting a Gaussian to an experimental PSF and determining its centroid, the original coordinates of the fluorescent molecule can be localized at high precision (Thompson *et al.*, 2002). The precision $\sigma_{x,y}$ of this localization improves with the number of photons N detected, as the more photons are emitted, the more information on the original position of the fluorophore can be collected, and scales with the size of the PSF σ_{PSF} (in the case of a Gaussian PSF, the σ_{PSF} corresponds to the standard deviation).

$$\sigma_{x,y} \approx \frac{\sigma_{\text{PSF}}}{\sqrt{N}} \tag{1.3}$$

This approximation is only possible for isolated PSFs of single emitters. SMLM takes advantage of this principle, separating individual fluorophores in time and space by stochastically activating only a sparse subset of fluorophores for a single image (see Figure 1.10). Thus, the PSF of these emitters are well separated, and their original position can be localized at a much higher precision than the original size of the PSF. Considering Equation 1.3, a fluorescent point source emitting ≈ 600 photons, previously imaged at a

diffraction-limited resolution of 250 nm can now be localized at a precision of 10 nm. This theoretical localization precision represents the best-case scenario, as it neglects factors such as background fluorescence.

By constantly activating a small subset of emitters over 1,000 to 100,000 of camera frames, the spatial coordinates of all fluorophores in the sample can be recorded. In its simplest form, the output of SMLM is a list of millions of these coordinates, including their respective localization precision, brightness, the number of the frame in which they were recorded, and, in the case of multi-color imaging, the channel in which they were detected (Rust *et al.*, 2006; Heilemann *et al.*, 2008, see Figure 1.10).

To reconstruct and visualize these data, their coordinates are combined and rendered as a pixelated image. Individual localizations are often rendered with Gaussian blur, scaled to the precision of their detection. Additionally, mapping pixel intensities representing a pixel-wise number of localizations to a color gradient gives an even more intuitive understanding of the underlying data.

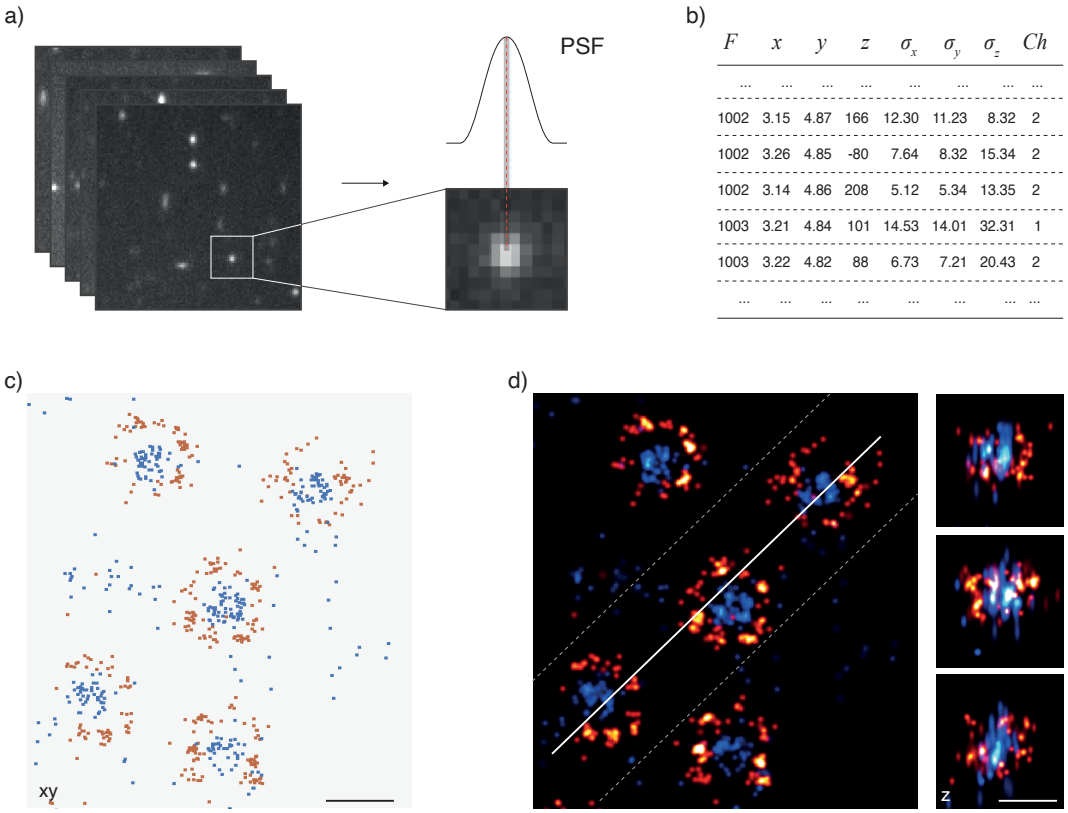


Figure 1.10 | Principle of single-molecule localization microscopy. a) During single-molecule localization microscopy, a movie of stochastically activated fluorophores is acquired. The well-separated signal emitted by each fluorophore in each frame is then localized by fitting a model of the point-spread function (e.g. a 2D Gaussian or an experimentally derived model). **b)** By repeating this localization step for all fluorophores detected in 10,000 s to 100,000 s of frames (F), a comprehensive list of the determined fluorophore coordinates (x, y, z), the respective precision at which they were localized (σ_x, σ_y, σ_z), as well as additional information such as color assignment (*Ch* for color channel) is obtained. **c)** These data can be visualized by rendering the localizations in a single super-resolution image. **d)** For a more intuitive visualization, localization can be rendered as a Gaussian with a size corresponding to the localization precision (*left*: top view, *right*: side view). *Red*: Nup96-AF647, *blue*: wheat germ agglutinin-CF680 (protocol available in Thevathasan *et al.*, 2019). Scale bars: 100 nm. *Figure generated by Aline Tschanz for previously published review Wu* et al., *2020*.

1.5.2.1 Three-dimensional single-molecule localization microscopy

As biological structures are three-dimensional, extension to 3D imaging represents an essential step in the biological applicability of SMLM. While there are a variety of approaches to capture the z-position of a fluorophore, the approach applied in this work is generally referred to as 'PSF engineering'. The main principle of this method is to encode the axial coordinate directly into the shape of the PSF (Sage *et al.*, 2019).

In 3D space, a PSF represents a symmetric distribution above and below the focal plane. The further out-of-focus it is captured, the larger its representing image. However, due to this symmetry, it is impossible to tell whether an image was taken above or below the focal point. One approach to break this symmetry and generate z-specific distractions is to introduce a cylindrical lens into the emission path (see Figure 1.11). This results in the

PSF being elongated in x above the focal point, and elongated in y below the focal point, for example. The extent of this elongation encodes the position of the emitter relative to the focal plane of the microscope (Huang *et al.*, 2008).

To decode this position, an empirical PSF model can be built from imaging stacks of fluorescent beads, immobilized on the coverslip. Each bead produces a single PSF, and by taking snapshots at equal step sizes above and below the focal point, one can sample and reconstruct the average PSF. This 3D model can then be used instead of a Gaussian fit to approximate the PSFs generated by fluorophores in the sample at varying heights, extracting not only the lateral position of the distribution's centroid but also the axial coordinate (Li *et al.*, 2018). Apart from PSF engineering (Huang *et al.*, 2008; Pavani *et al.*, 2009; Baddeley *et al.*, 2011; Shechtman *et al.*, 2014), various other approaches have been applied to record 3D information, including supercritical angle localization microscopy (SALM, Deschamps *et al.*, 2014; Dasgupta *et al.*, 2021) or Direct optical nanoscopy with axially localized detection (DONALD, Bourg *et al.*, 2015); dual-objective SMLM [interferometric PALM (iPALM) or 4Pi single-molecule switching microscopy (4Pi-SMS), Aquino *et al.*, 2011; Shtengel *et al.*, 2009; Huang *et al.*, 2016]; and Biplane SMLM (Juette *et al.*, 2008).

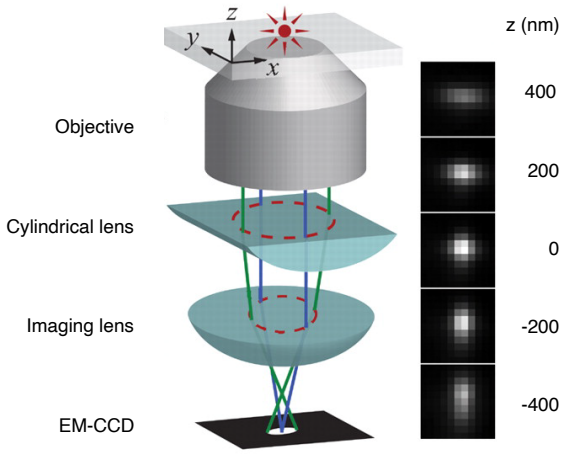


Figure 1.11 | Three-dimensional single-molecule localization microscopy. The symmetric blurring of the point-spread function can be broken through the addition of a cylindrical lens into the emission beam path. This results in a z-specific distortion of the point emitter imaged onto the camera (electron multiplying charge-coupled device, EM-CCD). Fluorophores imaged below the focal point (0 to -400 nm) are elongated in y, while fluorophores imaged above the focal point (0 to 400 nm) are elongated in x. *Figure adapted from Huang* et al., *2008, with permission from the journal.*

1.5.2.2 Multi-color single-molecule localization microscopy

A last principle to introduce here regards the extension of SMLM to multicolor imaging. This is an essential aspect of SMLM, as it exploits the high molecular specificity inherent to fluorescence microscopy to study the relative organization and interaction of distinct molecules.

Analog to multicolor imaging performed in conventional fluorescent microscopy, spectrally well-separated fluorophores can be imaged simultaneously on distinct camera channels or sequentially on the same camera. Equally analog to traditional methods, this approach has certain limitations. First, it requires the accurate registration of the two color channels. This becomes difficult with fluorophores with well-separated spectra. As light specific for both fluorophores passes through the same optical setup, chromatic aberrations caused by dispersion result in their focal points being slightly shifted relative to each other. This can create a spatial shift between the two images, resulting in registration inaccuracies between the two image channels and inaccuracies when relating the position of two different targets (Dempsey *et al.*, 2011). Further, it becomes increasingly difficult to find imaging conditions such as buffer compositions that suit both fluorophores.

The multicolor approach applied in this work is called ratiometric imaging and circumvents many of these limitations by using fluorophores with highly overlapping spectra (see Figure 1.12). These fluorophores are simultaneously excited at the same wavelength. Their emitted light is split by a dichroic mirror placed in the emission path and projected onto separate areas on the camera chip. Due to the large overlap between the two fluorophores, their emission is not well separated, and signals from an emitter of either species will result in an image on both channels.

However, the intensity ratio between the two channels is specific for a particular fluorescent species. Thus, by plotting the intensity collected for signals in channel 1 against the intensity of signals collected in channel 2, distinct populations of localizations can be made out (see Figure 1.12c). The identity of each fluorescent species can then be assigned based on these distinct populations (Schoen *et al.*, 2017; Zhang *et al.*, 2020.

Generally, the localizations from both channels have to be combined to ensure a high precision (Li *et al.*, 2022). In this work, the signal is split less far in the red wavelength. Thus, only the signal from the significantly brighter channel is used for localization. This has the advantage that registration of the two images only has to be performed at the precision of the diffraction-limited resolution and can thus be considered trivial. This avoids registration errors between two distinct color channels. Additionally, as the fluorescent species are spectrally close, chromatic aberrations are minimal.

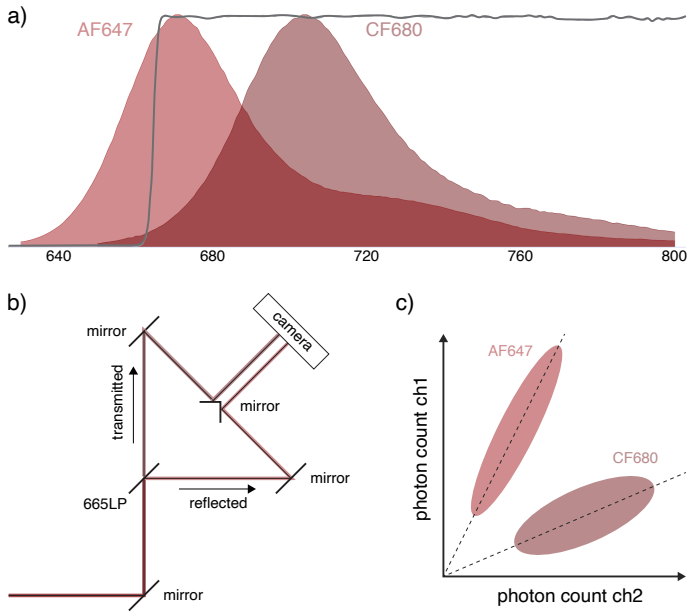


Figure 1.12 | Ratiometric approach to acquire multicolor images in single-molecule localization microscopy. a) Overlapping emission spectra of the two example fluorophores AF647 and CF680. **b)** Simplified diagram of the beam path. 665LP beamsplitter is used to separate the emission of both fluorophores as indicated by the grey line in a). The transmitted and reflected beam path is then projected onto different fields on the camera, imaging the signal in two different channels. **c)** By plotting the signal intensity (photon count) detected in each channel (ch1, ch2), two distinct populations of fluorophores can be made out. Thus, each localization can be assigned a specific color based on which population they belong to. *Figure generated by Aline Tschanz; a) panel generated using FPbase spectral viewer, Lambert, 2019.*

1.5.3 Updated definition of resolution

According to Abbe, only spatial features that are larger than diffraction-limited resolution can be resolved in a fluorescence microscopy image (Abbe, 1873). In the case of SMLM, where the position of the fluorophore can be resolved to a discrete spot on a continuous structure of interest, this definition of resolution needs to be updated, as the criterion is not applicable for sparsely labeled structures.

It is insufficient to think of the localization precision σ as a measure of resolution. Instead, we have to consider the density of the labels as well. As defined by the Nyquist-Shannon sampling theorem, to accurately reconstruct a continuous signal from its sampled representation, the sampling rate must be at least twice the frequency of the highest frequency component in the signal (Shannon, 1949). Applied to SMLM, this theorem states that the resolution of the final image cannot be better than twice the average distance between the localized molecules in the image (see Equation 1.4.

$$R_{\mathrm{Nyq}} = \frac{2}{\rho^{\frac{1}{d}}} \tag{1.4}$$

Here, R_{Nyq} is the resolution limit according to Nyquist; d is the spatial dimension (d = 1, 2, 3); and ρ is the density of localization described as N/a, with N being the number

of recorded localization within the area of interest *a* (Shroff *et al.*, 2008). However, this only holds true for localizations with minimal errors, where localization precision is much smaller than the spacing between the detected molecules ($\sigma \ll R_{\mathrm{Nyq}}$). For cases, where this does not hold true, an additional approximation has been proposed (see Equation 1.5).

$$R = \sqrt{\sigma^2 + R_{\mathrm{Nyq}}^2} \tag{1.5}$$

Here, the image resolution R depends on the localization precision σ and the resolution limit defined by Nyquist Resolution R_{Nyq} from Equation 1.4 (Shim *et al.*, 2012; Legant *et al.*, 2016).

These theoretical considerations neglect certain practical limitations. For example, even under optimal labeling conditions, the fluorophore itself will not be uniformly placed as assumed by the abovementioned theorem. Therefore, in practice, a sampling rate at five-fold the Nyquist sampling is considered more appropriate (Legant *et al.*, 2016).

The resolution of SMLM depends strongly on imaging conditions, target structure, and choice of label and labeling strategy. Ultimately, in the work presented here, the achievable resolution ranged from 10 nm lateral, to 30 nm axial (see 6.2.5.5).

1.5.4 Illuminating the nanoscale: Choosing the appropriate label

The definition of resolution applicable to SMLM puts strong restraints on the choice of labels and their delivery strategy. These approaches must fulfill the requirements of precise localization (small σ) and a dense distribution close to the original structure of interest (five-fold Nyquist sampling at minor linkage errors).

Thus, developing appropriate labels and labeling strategies is just as crucial as developing the microscopy approach itself. This is reflected in the Chemistry Nobel Prize awarded for superresolution microscopy. Apart from Stefan W. Hell, who received this award for the development of STED microscopy, William E. Moerner and Eric Betzig shared theirs for their work in SMLM (Van Noorden, 2014). The formulation of this microscopy approach and its first application by Eric Betzig (Betzig, 1995; Betzig *et al.*, 2006) would not have been possible without the first observation of single-molecules in a solid (Moerner and Kador, 1989), and the later description of a spontaneously blinking green fluorescent protein (GFP, Dickson *et al.*, 1997).

Today, a broad palette of different labels is available (Li and Vaughan, 2018). While these molecules differ in activation mechanisms, they all have to fulfill certain requirements for their application in SMLM.

First, only a small subset of fluorophores must emit light at any given time, resulting in well-separated PSFs on a single camera frame (see Section 1.5.2). Thus, these molecules should be able to switch between a bright on- and a dark off-state, also referred to as

'blinking'. The contrast between these states should be strong, as single fluorophores in the on-state must be detectable against the background of thousands of dark molecules. Additionally, the duty cycle of the fluorophores should be low, such that they spend most of their time in the dark off-state.

Second, as we know from Equation 1.3, the localization precision scales with the number of photons detected. Thus, the fluorophores should be bright, as the number of photons emitted during their on-state, directly determines localization precision.

Fluorescent probes for SMLM can be roughly categorized into synthesized organic dyes and fluorescent proteins.

1.5.4.1 Organic dyes

The first application of a localization microscopy approach called stochastic optical reconstruction microscopy (STORM), used the cyanine Cy5 (Rust *et al.*, 2006). Under reducing buffer conditions, these synthesized organic dye can be switched to a long-lived non-fluorescent dark state, from which it can be recovered by illumination with shorter wavelengths (see Figure 1.13). These shorter wavelengths were either provided by direct illumination with visible light (Heilemann *et al.*, 2005) or by exciting a second molecule, Cy3, which was placed in close proximity (1-2 nm) to Cy5 and is able to promote the Cy5 recovery to the on-state (Bates *et al.*, 2005). The photoswitching of these molecules is achieved in the presence of a primary thiol and an enzymatic oxygen-scavenging buffer. Upon illumination with light at its absorption peak wavelength (≈650 nm), thiolated anions disrupted the conjugation of Cy5 by covalently binding to the Cy5-bridge. Thus, the absorption is shifted to the ultraviolet range (≈405 nm). This bond is broken again by irradiating with ultraviolet light, and the molecule is recovered to an activatable on-state. This switching mechanism is shared among the structural relatives of Cy5, including Cy7, Alexa Fluor 750, and the very popular Alexa Fluor 647 (AF647) (Dempsey *et al.*, 2011).

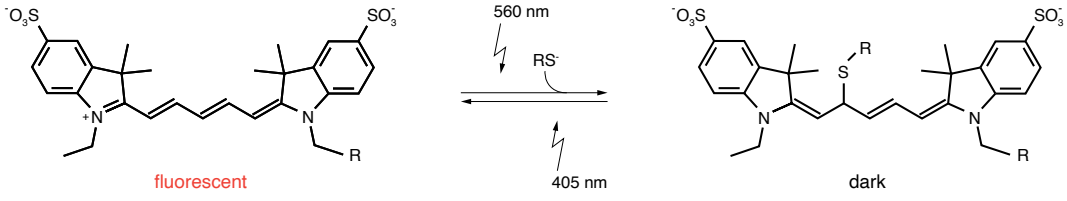


Figure 1.13 | Blinking mechanism of Cy5. Cy5 can be switched from an excitable state (fluorescent) to a non-excitable state (dark). In its fluorescent state, it can be excited by irradiation at 650 nm wavelength. From this excited state, it can either return to a ground state by emitting photons or react with thiolated anions (RS^-). Reaction with RD^- results in the switching to a dark state where irradiation at 650 nm will not result in a fluorescent signal. It can be retrieved to the fluorescent state by irradiation with ultraviolet light at 405 nm wavelength. Thus Cy5 switching can be actively controlled, resulting in 'blinking' behavior suitable for single-molecule localization microscopy. *Figure generated by Aline Tschanz.*

When a fluorescent molecule absorbs light, the energy transitions it undergoes can be described by a Jablonski diagram (see Figure 1.14). For Cy5, the light at 650 nm wavelength is absorbed, which transitions the fluorophore from its S_0 ground state to an excited electronic state, typically a higher vibrational state than S_1. Within a few picoseconds, internal conversion results in the transfer to the excited state S_1, while energy is typically dissipated as heat. From this S_1 state, molecules transition back to the ground state S_0, during which excess energy is dissipated as emitted fluorescent light. The small loss of energy to heat is the reason why this emitted light contains less energy than the absorbed one, resulting in a shift to longer wavelengths than the excitation light (Stokes shift). A molecule can transition through an alternative relaxation pathway via intersystem crossing from the S_1 to the triplet state T_1. This transition is considered 'forbidden', thus occurring at much slower rates than S_1 to S_0. The relaxation from T_1 to S_0 is promoted by oxygen, thus oxygen can also function as a triplet-state quencher. Alternatively, in reducing conditions under the presence of thiol, the molecule can further transition to form a long-lived radical. The recovery from this long-lived dark state can be again promoted by oxygen or irradiation with ultraviolet light (≈405 nm). Further, high-energy states such as the triplet state or long-lived radicals are prone to bleaching. Bleaching is described as the permanent loss of fluorescent capabilities and is promoted via reactive oxygen species (Dempsey *et al.*, 2009; Linde *et al.*, 2010).

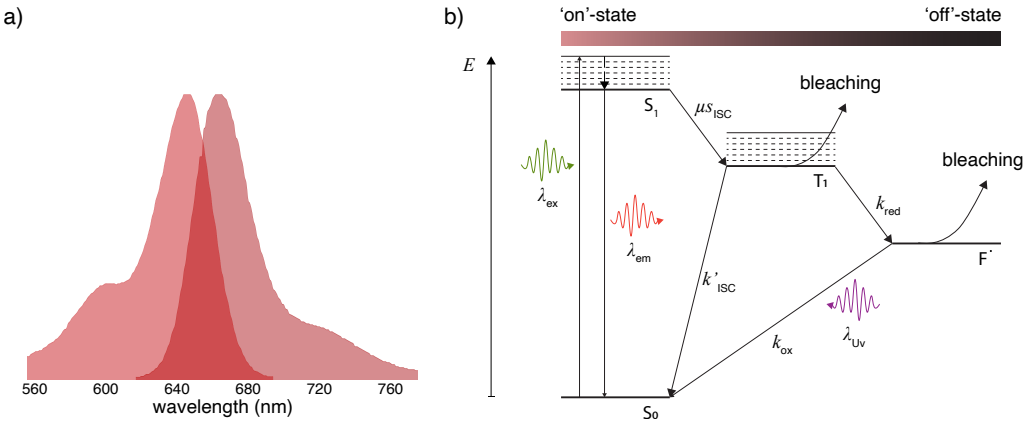


Figure 1.14 | Fluorescence of Cy5. a) Absorption and emission spectra for Cy5. **b)** Greatly simplified Jablonski diagram of Cy5. Excitation at 650 nm wavelength (λ_{ex}) excites Cy5 from the ground state S_0 to an elevated energetic E state (femtoseconds), after which it relaxes at the rate K_{IC} (picoseconds) through internal conversion to the excited state S_1. From S_1, the molecule returns to the ground state S_0 (nanoseconds), emitting light at 665 nm wavelength (λ_{em}). An alternative path, occurring at a much lower rate k_{ISC}, transfers the molecule to a triplet state T_1. From T_1 it can either return to the ground at the rate k'_{ISC} (microseconds) or be reduced to the radical state $F^{\bullet}$ at the rate K_{red}. The return to the S_0 ground state can be sped up through 'triplet-quenchers' such as oxygen. The transition to the radical state can be mediated by the presence of thiol in the buffer. The rate K_{ox} (microseconds to minutes) at which molecules are returned from $F^{\bullet}$ to S_0 can be mediated by oxygen. It can be further sped up via irradiation at ultraviolet 405 nm wavelength (λ_{uv}). Higher energetic states are prone to bleaching, which is mediated by oxygen and completely removes Cy5 from the pool of fluorescent molecules. *Figure generated by Aline Tschanz, a) panel generated using FPbase spectral viewer, Lambert, 2019.*

As mentioned above, we require fluorophores to spend the majority of their time in a dark off-state. Thus, modifying imaging buffers to shift the equilibrium of energy transitions to the long-lived dark state is preferable. Adding thiol (such as β-mercaptoethanolamin) results in the preferred transition to this state. By additionally reducing the oxygen level of the buffer, we achieve two things: we reduce triplet-quenching, thus increasing the transition to and duration in the dark state, and we reduce photobleaching, which is also mediated by oxygen. There are different buffer compositions developed for this purpose. An oxygen-scavenging buffer based on the enzymatic activity of glucose oxidase and catalase is probably the most widely used (Heilemann *et al.*, 2005, see Figure 1.15). Here, the glucose oxidase catalyzes the reaction of molecular oxygen with glucose, generating hydrogen peroxide and gluconolactone. As hydrogen peroxide to the production of reactive oxygen species (ROS), causing photobleaching and phototoxicity, it is detoxified by the catalase enzyme to water and oxygen. Two cycles through this process remove one oxygen from the buffer. However, as gluconolactone further hydrolyzes into glucuronic acid, each cycle acidifies the buffer. Over long imaging times, this leads to a significant drop in pH, which in turn can unfavorably affect the photophysics of fluorophores. It is therefore recommended to seal the buffer chamber to increase imaging time to reduce oxygen influx. Additional buffer compositions have been developed to prolong imaging times by reducing the acidification when removing oxygen from the imaging buffer (Nahidiazar *et al.*, 2016; Aitken *et al.*, 2008; Swoboda *et al.*, 2012).

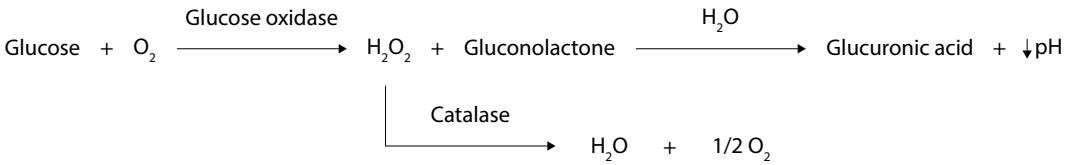


Figure 1.15 | Enzyme-based imaging buffer for single-molecule localization microsocpy. Oxygen (O_2) influences the bleaching as well as oxidation rate of fluorescent molecules such as Cy5. Thus, the removal of O_2 is preferred. An approach to achieve this is by adding glucose together with the enzyme glucose oxidase to imaging buffers. Thus, O_2 gets removed from the solution, generating hydrogen peroxide (H_2O_2) and gluconolactone. Since H_2O_2 can severely damage the sample, it is decomposed to water and oxygen, catalyzed by the enzyme catalase. Gluconolacetone, in the presence of water (H_2O) further reacts to glucuronic acid, acidifying the buffer (decrease in pH). As changes in pH can severely alter the photophysical properties of fluorescent molecules, it is generally recommended to limit influx of O_2 into the buffer by e.g. sealing the imaging chamber. *Figure generated by Aline Tschanz.*

To summarize, by reducing oxygen in the imaging buffer and adding thiols, the equilibrium of energetic transitions through which a fluorophore cycles is shifted to a long-lived dark state. It can be recovered from this dark state through irradiation with ultraviolet light. By modulating the intensity of this irradiation, we can control the density of molecules in the bright on-state, recovering more and more molecules through the imaging process until they have been either detected or permanently bleached away. This method of controlling the activation density of fluorescent molecules in the sample is called direct stochastic optical reconstruction microscopy, or short, dSTORM (Heilemann *et al.*, 2009;

Heilemann *et al.*, 2008), and, combined with the fluorophore AF647 is the method of choice in this work.

Next to the above-described photoswitching, organic dyes can achieve sparse activation also through other mechanisms. These include photoactivation (Michie *et al.*, 2017) and photoconversion (Lackner *et al.*, 2020), which are mechanisms discussed in the next section in the context of fluorescent proteins.

Additionally, rhodamin-based spontaneously blinking dyes have been reported. These molecules exploit a reversible chemical reaction, enabling SMLM at defined pH without the necessity of complex imaging buffers (Lardon *et al.*, 2021). Apart from the high photon yield, these fluorophores are partially membrane permeable, facilitating staining protocols and enabling live-cell experiments. In this case, blinking kinetics are purely dependent on the chemical environment (e.g. pH) of the buffer (reviewed in Li and Vaughan, 2018; Lelek *et al.*, 2021).

1.5.4.2 Fluorescent proteins

Apart from organic dyes, fluorescence can also be provided by proteins (see Figure 1.16). While these proteins provide less photon yield compared to organic dyes, they have the advantage of being live-cell compatible (see Section 1.5.5).

Such proteins include PA-GFP and are used during for example photoactivated localization microscopy (PALM, Patterson and Lippincott-Schwartz, 2002; Betzig *et al.*, 2006). **Photoactivation** occurs when a non-fluorescent molecule is irradiated with light in the violet spectrum. The resulting decarboxylation shifts the equilibrium of these proteins in the sample to a fluorescent on-state, which can be imaged by irradiation at longer wavelengths (e.g. 488 nm for PA-GFP). By modulating the intensity of the initial irradiation laser, the density of activated molecules can be controlled. Additional blinking mechanisms of fluorescent proteins include photoconversion (mEos2, McKinney *et al.*, 2009) or photoswitching (Dronpa, Ando *et al.*, 2004).

Photoconversion describes the process where the emission spectrum of a fluorescent protein is changed. Thus, the initial green emission maximum for mEOS2 at 506 nm is shifted to the red 573 nm maximum upon irradiation with 405 nm UV. Similar to PA-GFP, the density of activated fluorescent proteins can be modulated by the intensity of the UV laser. However, this is an irreversible process, and after activation and excitation, fluorescent proteins such as mEOS2 are bleached.

10.1073/pnas.0911073107 described a reversible process. Here, irradiation at 405 nm shifts the protein to a fluorescent on-state, where it can be excited at, for example, 503 nm. After emitting light, the protein is returned to its off-state. This makes it possible to reactivate a single fluorophore multiple times, increasing the information content for the thus recorded coordinate.

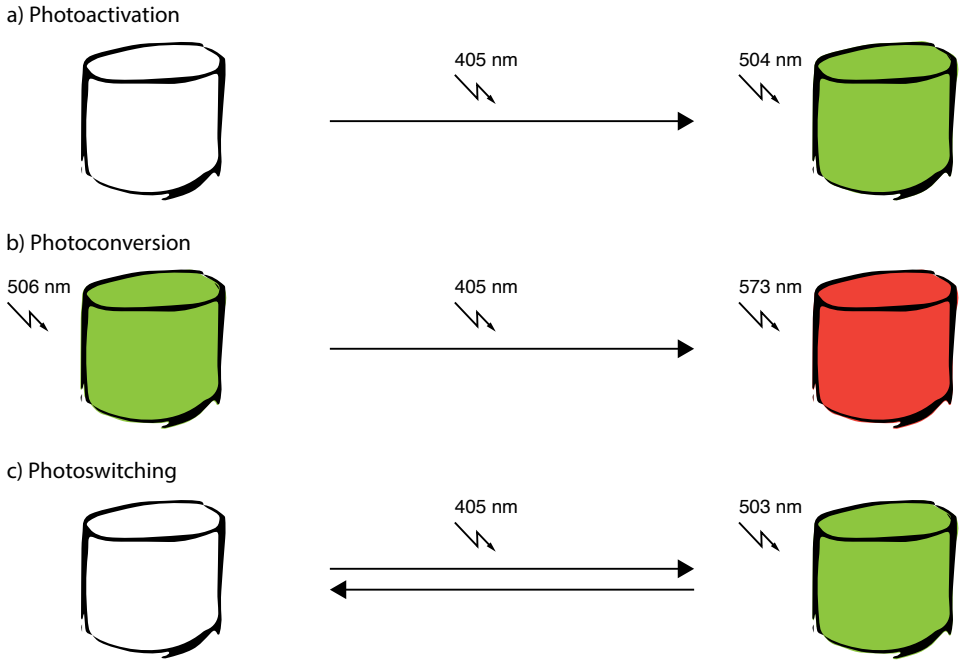


Figure 1.16 | Activation mechanisms of fluorescent proteins. a) Proteins including the photoactivatable green fluorescent protein (PA-GFP) can be modulated in their fluorescence activity by irradiation with ultraviolet light at 405 nm wavelength, which shifts their absorption spectra to 488 nm. Thus, the activation density of these proteins can be controlled through the intensity of the 405 nm laser used. **b)** Similarly, photoconversion shifts the absorption maximum of proteins including mEOS2 from the green spectra (e.g. 488 nm) to the red (e.g. 540 nm) upon irradiation with 405 nm. **c)** While photoactivation is an irreversible process, whereupon emission of the fluorophore is bleached away, photoswitching describes a process where an activated fluorescent molecule returns to the non-activated state upon emitting a signal. Thus, a single fluorophore can be cycled through multiple activation processes, increasing the chance of detection. Proteins *Figure generated by Aline Tschanz.*

1.5.5 Delivering labels to biological structures

As mentioned in Section 1.5.3, apart from the optimal choice of a fluorescent label, the arrangement of this label at the biological structure is essential for high-resolution imaging. Depending on the type of label, different approaches have been implemented to deliver this probe to the desired structure (Liu *et al.*, 2022, see Figure 1.17). The selection of the appropriate labeling strategy tends to optimize for multiple features that strongly depend on the type of information required from the imaging results. Generally, compromises between linkage error, live-cell compatibility, and labeling efficiency are made.

1.5.5.1 Considerations for the choice of labeling strategy

Live-cell compatibility is required to study real-time dynamic processes inside a cell. While live-cell imaging is where conventional fluorescence microscopy techniques excel (see Section 1.3.2), especially for SMLM, it represents a challenge. This is due to the high laser powers required to create fluorophore blinking as well as the long acquisition times usually needed. High laser power leads to increased phototoxicity, disturbing and

disrupting cells. As we are additionally spreading our fluorescence information over time by sequentially recording only a small subset of fluorophores at a time, live SMLM is limited to studying biological processes that take place on a timescale of minutes or longer. Thus, dynamics that occur at smaller time scales are difficult to capture with this approach. Clathrin-mediated endocytosis occurs on a timescale of seconds to minutes, which places it outside of the applicable time domain of live SMLM. We, therefore, resorted to a different approach to reconstruct dynamic information (see 3.4.1).

Efforts to speed up SMLM and thus improve its live-cell compatibility have been made, including developing fitting algorithms to retain high localization precision for highly overlapping PSF signals. By increasing the density of localizations per imaging frame, fewer frames have to be acquired to adequately sample the underlying structure, thus speeding up the imaging process. By applying this approach, dynamics in the Golgi Apparatus and the Endoplasmic Reticulum could be observed via live-cell SMLM (Speiser *et al.*, 2021).

Linkage error describes the distance between the structure of interest and the position of the localized fluorophore. Commonly used indirect immunolabeling strategies (see below) result in an average displacement of the fluorophore from the original structure by 10 - 15 nm. At defined orientations of the antibody, linkage errors result in a systematic offset between label and target leading to an inaccurate representation of the structure. The flexibility and random attachments inherent to antibodies lead to a spread of the measured label position, resulting in imprecision when resolving the underlying structure. Thus, minimal linkage errors are preferred to accurately and precisely determine the position and structure of the target (Früh *et al.*, 2021).

Labeling efficiency is a measure that describes the fraction of target proteins within a sample that is ultimately detected via a usable localization. In an ideal case, every protein in a structure would be labeled with exactly one fluorophore, and all fluorophores on these proteins are detected. In practice, labeling efficiency is always less than 100%. This can be caused by imperfect conjugation efficiencies between dye and ligand, bleaching of the fluorophore during initial off-switching, or nonfunctioning fluorophores. While this parameter is typically not crucial for conventional fluorescent imaging, as the overlapping signals generate a certain redundancy, for SMLM, high labeling efficiency is paramount to detect structural features (Thevathasan *et al.*, 2019; Shivanandan *et al.*, 2014; Baddeley and Bewersdorf, 2018).

1.5.5.2 Different labeling strategies

Immunolabeling using a primary antibody to detect epitopes on the structure of interest, and a secondary antibody conjugated to a fluorophore to deliver the label, represents a widely applied strategy. This approach has the advantage of amplifying labeling efficiency, especially in combination with polyclonal antibodies, as a single protein can be detected by multiple antibodies at a time, increasing the chance of detection of at least one of them.

For these considerations, it was the labeling approach of choice presented in this work. However, this method comes with critical limitations. First, it results in a robust linkage error, displacing the label up to 20 nm from the protein due to the size of antibodies (10 - 15 nm, 150 kDA). This error can be removed by directly labeling the primary antibody, which is an additional experimental effort, and still results in a linkage error up to 13 nm. Additionally, as antibodies are not cell membrane permeable, the method is not live-cell compatible, and one needs to perform this labeling in fixed cells.

Further options include the use of much smaller immunolabels such as Fab fragments (antigen-binding domains of regular immunoglobulin G antibodies, Holliger and Hudson, 2005) or nanobodies (single-domain antibodies, 15 kDa, 2 nm), directly labeling the target of interest or a fusion tag such as GFP (Ries *et al.*, 2012). Further, short and inert peptide tags can be used, including BC2- or spot-tag (1.4 kDa, Virant *et al.*, 2018) or ALFA-tag (1.9 kDa, Götzke *et al.*, 2019).

Fusion proteins comprising the target protein and a photoswitchable protein (e.g., PA-GFP) or self-labeling enzymes represent an alternative approach. These much smaller molecules, which include SNAP- (Keppler *et al.*, 2004, HALO- (Los *et al.*, 2008, or CLIP-tag (Gautier *et al.*, 2008), are covalently linked to the structure of interest resulting in a linkage error of only 2 - 3 nm. Additionally, as they can be endogenously expressed, they are mostly live-cell compatible (except for most SNAP ligands, which are either toxic or non-permeable) and result in stoichiometric labeling. They are more prone to deficiency in labeling efficiency, as only one label per protein of interest is present.

Non-antibody based molecules including aptamers (single-stranded DNA or RNA oligonucleotides, 13–15 kDa, Opazo *et al.*, 2012) or affirmers (polypeptide, 10–12 kDa, Carrington *et al.*, 2019), can be targeted specifically to proteins. Labeled toxins, including paclitaxel or phalloidin, are frequently used to label microtubules and filamentous actin respectively (Wulf *et al.*, 1979; Barasoain *et al.*, 2010).

DNA-PAINT employs freely diffusing, fluorescently labeled single-stranded DNA probes. By labeling the target structure with the complementary DNA 'docking' strand, the binding and subsequent immobilization of the labeled 'imager' strand appears shortly as a bright spot that can be localized. The kinetics of this binding can be modified by straightforward adjustments of the DNA sequence used. Optimizations of this approach lead to a decrease in background signal and an increased number of photons per blink. The relative robustness to bleaching due to an excess of imager strands results in excellent localization precision, and sequential imaging with different DNA probes allows high multiplexed multicolor imaging without requiring multiple fluorophores. Ultimately, virtually any fluorophore could be used to label the 'imager' strand, as the blinking is in this case not dependent on photophysics, but solely on the binding kinetics of the DNA probes, making DNA-PAINT a versatile and easy-to-use method (Schnitzbauer *et al.*, 2017).

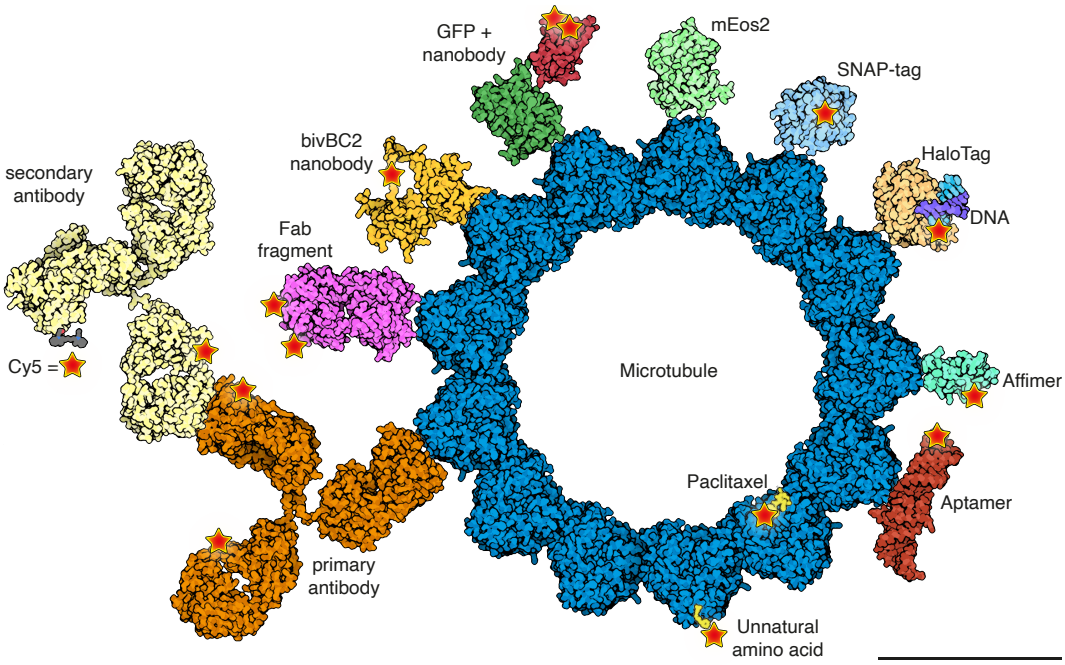


Figure 1.17 | Labeling strategies for single-molecule localization microscopy. Different labeling strategies are showcased on an example microtubule structure (β-tubulin, pDB ID 5SYF) in *blue*. Classical immunolabeling with primary (*orange*; PDB ID 1IGT) and secondary (*light yellow*; PDB ID 1IGT) antibodies introduces the biggest linkage error of the approaches shown. Alternative strategies involve Fab fragments (*purple*; PDB ID 3QNZ); nanobodies binding to the native target (*yellow*; PDB ID 5IVN); and nanobodies binding to GFP (*green*, nanobody in *red*; PDB ID 3OGO). Endogenous tags can be used to directly target fluorescent proteins such as mEOS (*light green*; PDB ID 3S05); or self-labeling enzymes such as HaloTag (*yellow*; PDB ID 6Y7A) or SNAP-tag (*light blue*; PDB ID 3KZY) to the microtubule. Self-labeling enzymes can then be labeled with a palette of different organic dyes or single-stranded DNA for DNA-PAINT (eight base pairs shown in *purple* and *turquoise* attached to the HaloTag; PDB ID 1BNA). Affimers (*light green*; PDB ID 4N6T), similar to RNA-based aptamers (*dark red*; PDB ID 5OB3) directly bind to the target. Toxins such as paclitaxel can further be used (*yellow*, displayed on top instead of buried within the protein for visualization; PDB ID 5SYF). The introduction of unnatural amino acids directly into the sequence of the target structure leads to minimal linkage error (*yellow*; PDB ID 6AAO). *Figure generated by Dr. Philipp Hoess, published in Liu* et al.*, 2022, adapted with permission from the authors.*

1.5.6 Quantitative Data Analysis in Single-Molecule Localization Microscopy

While SMLM can depict biological structures at nanometer resolution, its power goes beyond generating high-resolution images. Using quantitative analyses, parameters describing the connections between individual localizations can be extracted and related to relevant biological information.

Different approaches are available which strive to describe the pointillist data underlying an SMLM image in terms of their overall patterning and geometric features. These methods are generally applied directly to the localization data, circumventing the reconstruction of these data into a pixelated image, harnessing the entire information available, and avoiding obscuring effects caused by rendering (Baddeley *et al.*, 2010).

1.5.6.1 General patterns in localization data

A general investigation of SMLM data is to determine whether there is a non-random pattern present in the first place. Or in other words, do localizations cluster into higher-density regions, that could describe specific biological structures? To distinguish between randomly dispersed and clustered data, spatial descriptive analyses such as the pair correlation function (Sengupta *et al.*, 2011), Ripley's K function (Owen *et al.*, 2010), or PERPL (pattern extraction from relative positions of localizations, Curd *et al.*, 2021) are employed. These approaches offer general information on the average size and density of the clusters that can be extracted and are useful tools to investigate the relationship between the distribution of molecules and their biological function. Thus, the connection between the oligomerization state of receptors and their functional activation could be investigated (Pageon *et al.*, 2016).

These calculations yield an overall measure and description of the general degree of clustering within one field of view. If, instead, more descriptive information on individual clusters is desired, including the number, size, or shape of each region, different approaches must be used.

1.5.6.2 Describing individual clusters of localizations

Segmentation and cluster analyses are performed to investigate differences across individual clusters of localizations. With this approach, a more detailed description is achieved, extracting information such as size, shape, and density for each region. Segmentation has to fulfill three main tasks: calculate the density of localizations, threshold this density, and assign localizations to specific clusters. Example tools that perform segmentation on SMLM data include DBSCAN (density-based spatial clustering of ap- plications with noise, Endesfelder *et al.*, 2013) and ToMATo (topological mode analysis tool, pike topo 2020). Such segmentation tools are useful to investigate the spatial organization and density of biological targets. Thus, the molecular density of, for example, RNA polymerase clusters in *Escherichia coli* could be connected with nutrient content in the media (Endesfelder *et al.*, 2013).

1.5.6.3 Understanding the geometries of individual structures

A general approach to extracting descriptive parameters on the distribution of localizations within a single cluster is to postulate an underlying geometry of the labeled structure. The parameterization of these geometries is usually based on observations of the imaged structures and/or a certain degree of prior knowledge of the structure itself, often provided by complementary imaging methods such as electron microscopy. A simple implementation of this is to approximate short segments on a microtubule using a line profile. By manually aligning this profile with the imaged microtubule, the localizations along this linear model can be collected. Their distribution across the line

profile can then be fitted with a double Gaussian, and the diameter of the structure can be extracted based on the peak distance (see Figure 1.18, Dempsey *et al.*, 2011).

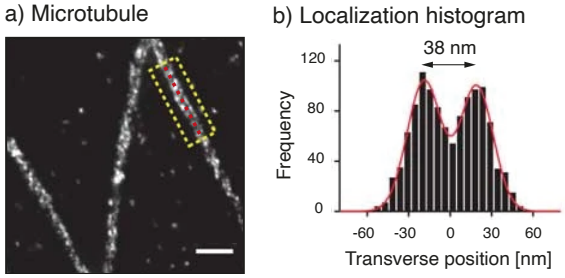


Figure 1.18 | Geometric analysis of a microtubule structure resolved using single-molecule localization microscopy. a) Microtubules were immunolabeled with AF647. **b)** Transverse profiles of localizations as indicated in a). By fitting a double-Gaussian to the localization distribution *red*, the diameter of the structure can be estimated through the distance between both peaks. Scale bar: 250 nm. *Adapted from Dempsey* et al.*, 2011, according to journal guidelines*.

More complex shapes, such as the double-ring structure of nuclear pore complexes (NPC) can still be approximated with simple geometric quantities in certain cases. For instance, the radii of multiple NPCs can be extracted by fitting a circular model to the localization coordinates in the top view.

The high resolution of SMLM (≈10 nm lateral, ≈30 nm axial in this work) opens up the possibility of the detailed structural description of many macromolecular machines. In the case of a clathrin-coated structure, a simple ring or line profile does not suffice to approximate its true geometry. However, as pointed out in Section 1.3, electron microscopy studies have already provided extensive information on the architecture of these structures. From these studies, we have learned of the spherical shapes diverse clathrin lattices can adopt, ranging from shallow pits to Experimental studies have supported both proposed models for understanding membrane bending by the clathrin coat. Thus, this information can be used to inform the model to approximate the data, selecting the most likely geometry to extract the desired structural features. To be able to translate this information into a model and fit it directly to the underlying data, Dr. Yu-Le Wu has developed a maximum-likelihood-based approach called LocMoFit (Wu *et al.*, 2023). This framework allows the fit of a specified geometric model directly to the localization coordinates, taking into account additional information such as localization precision (see Figure 1.19).

In the case of clathrin-mediated endocytosis, prior knowledge would commend to approximate these structures with a sphere, extracting the diameter for every coat. Together, Dr. Yu-Le Wu and I tested and developed the application of this model-fitting framework to SMLM data of clathrin-coated structures. We were able to describe these complex and dynamic subcellular machineries in terms of their radii and closing angle θ, which allowed us to reconstruct the dynamic remodeling of the clathrin coat at the nanoscale.

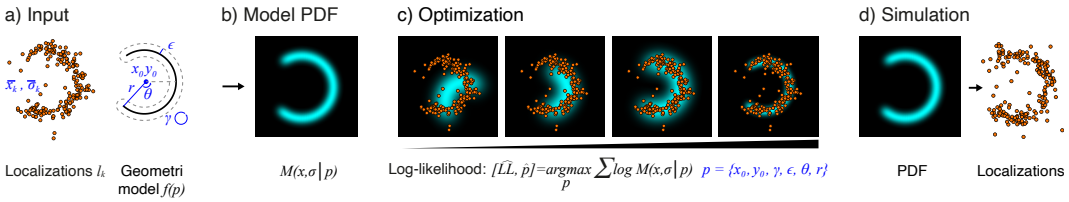


Figure 1.19 | LocMoFit: Maximum-likelihood model fitting for quantitative analysis of single-molecule localization microscopy data. a) LocMoFit uses the spatial coordinates $\vec{x}_k$ and their respective localization precision $\vec{\sigma}_k$, as well as a geometric model f parameterized by p as input. **b)** The input model is then used to construct the probability density function (PDF) $M(\vec{x}_k, \vec{\sigma}_k|p)$. **c)** The log-likelihood of the model describing the data is calculated. The maximum likelihood estimation maximizes the log-likelihood to find parameter values that best describe the input data. The example shows the application of a 2D arc model *(cyan)*, parametrized by its position x_0, y_0, z_0; its rotational angle γ; extra uncertainty $\mathscr{E}$; arc closing angle θ; and radius r. This model is fitted to the localization data *(orange)*. **d)** Among other features, LocMoFit contains a simulation engine that can be used for validation of the model fit. By simulating the underlying localization data using experimentally and/or user-defined parameters, the robustness of the model can be estimated. *Figure adapted from Wu* et al., *2023, with permission from the authors.*

2 | Aims of the study

Today, almost six decades after the first description of clathrin-coated structures, clathrin-mediated endocytosis is one of the most thoroughly studied endocytic pathways. However, while the static ultrastructure and the interactome of clathrin are well understood, the molecular mechanism that drives the dynamic remodeling of the underlying plasma membrane remains elusive.

To conceptualize this mechanism, two clathrin coat growth models are commonly discussed: The constant curvature and the constant area model. Both of these models come with their own geometric prediction for clathrin coat organization and are supported by the literature. The reason why it has been difficult to converge to a single descriptive model is the small size, molecular complexity, and fast dynamics of the process. So far, no single imaging technique can capture all necessary information at sufficient resolution.

However, by applying the superresolution microscopy approach I propose in this work, I could address this question through the combination of nanoscale spatial resolution, thorough sampling of the endocytic trajectory, and reliable dynamic reconstruction of the process. Specifically, the aim of this study was to employ single-molecule localization microscopy (SMLM) to directly visualize the 3D architecture of clathrin-coated structures at the bottom membrane of mammalian cells.

SMLM is a relatively slow technique, requiring up to two hours of imaging time for a single acquisition in this context. Compared to clathrin-mediated endocytosis, which only takes a few seconds to minutes, this approach is too slow to capture direct temporal information and has to be performed in fixed cells. The second aim of this study was, therefore, to retrieve some of this temporal information in order to reconstruct the dynamic changes in clathrin coat geometry from static images.

To this end, I set out to optimize the model-fitting framework LocMoFit for its application to SMLM clathrin data. Using a spherical cap model, I could extract descriptive parameters for each structure, which allowed me to not only characterize their geometries but also sort each snapshot along their endocytic progression.

Ultimately, I here present a superresolution microscopy pipeline that, in combination with computational model fitting, allowed the investigation of the dynamic remodeling of the plasma membrane by the maturing clathrin coat. While I did not capture any

direct temporal information, the high throughput at which this approach samples the distribution of clathrin-coated structures *in situ* allowed for a reliable reconstruction of the average geometric trajectory over pseudotime.

3 | Results

In this work, I sought to investigate how protein assemblies formed during clathrin-mediated endocytosis can reshape the underlying membrane. The aim was to integrate both structural and temporal information in sufficient detail to resolve the underlying mechanism of this process. To achieve this goal, I developed a superresolution microscopy pipeline that allowed for the direct visualization and quantification of the precise geometries of thousands of clathrin-coated structures. The resulting data highlights a complex mechanism of membrane remodeling based on the intricate cooperation of multiple clathrin triskelia.

In the first part of this chapter, I outline the details of the imaging approach, followed by a geometric analysis of highly resolved clathrin-coated structures. The results of this analysis enabled the three-dimensional (3D) description of the clathrin coat geometry and allowed the investigations of their changes during endocytosis. My findings challenged current models for coat remodeling, which motivated the formulation of a new clathrin coat growth model called 'the cooperative curvature model'. I further confirmed the generalizability of this model across three different cell lines. The density of endocytic stages, represented by static snapshots of clathrin coats, allowed me to reconstruct a pseudotime and investigate the dynamics of curvature generation during endocytosis. Finally, I could highlight the potential of the here described pipeline to investigate the dynamic recruitment of additional endocytic components using dual-color imaging.

3.1 Imaging clathrin-coated structures with single-molecule localization microscopy

To resolve clathrin-coated structures at nanometer resolution, I applied a single-molecule localization microscopy (SMLM) approach to visualize their 3D architecture. Careful experimental considerations are required to generate images of high quality. In the following sections, I will outline these considerations and describe the general imaging approach.

3.1.1 Experimental considerations for successful clathrin coat labeling

In living cells, the duration of clathrin-mediated endocytosis is on the order of seconds to a few minutes (Kaksonen and Roux, 2018). As mentioned previously (see Section 1.5), SMLM has inherent limits to acquisition speed, scaling with the number of fluorescent molecules that must be sequentially detected to sample the underlying structure sufficiently. Since thorough and dense labeling of the clathrin coat is crucial for the subsequent analysis (see Section 3.2), it takes up to two hours to capture sufficiently many localizations in a single acquisition. Thus, the temporal resolution of this imaging approach was much too low to capture any dynamics of the relatively fast endocytic process directly. Instead, imaging was performed in chemically fixed cells to achieve the highest spatial resolution possible.

Apart from an increased spatial resolution, the advantage of working with fixed cells is the permeabilization of the plasma membrane during sample preparation. This increases the variety of labeling strategies employable, including indirect immunofluorescence and cytotoxic or membrane-impermeable dyes (see Section 1.5.4 & 1.5.5).

Dr. Markus Mund developed an antibody-based labeling protocol to deliver the fluorophore Alexa Fluor 647 (AF647) to the clathrin coat. He used the combination of primary antibodies against clathrin heavy and light chain, recognized by a secondary antibody conjugated to AF647. By applying and optimizing his protocol, I achieved thorough and dense labeling of the clathrin coat. It is important to note that all antibodies used are polyclonal, recognizing multiple distinct epitopes within the same protein target. This is essential for subsequent analyses, as it increases labeling efficiency and provides signal amplification necessary for a thorough and dense coverage of the clathrin coat.

Most of the data presented in the next sections were generated in SK-MEL-2 cells, generously gifted to the group by Prof. Dr. David Drubin (UC Berkeley, described in Doyon *et al.*, 2011). This cell line has been extensively studied in the context of mammalian clathrin-mediated endocytosis, which facilitated the integrations of my findings with the available literature (Doyon *et al.*, 2011; Aguet *et al.*, 2013; Avinoam *et al.*, 2015; Kaplan *et al.*, 2022, see Section 4). As these cells additionally expressed endogenous clathrin light chain A tagged with RFP (CLTA-RFP), I could directly control the specificity of the immunolabeling approach. A GFP tag on the endogenous dynamin-2 (DNM2-GFP) protein further allowed me to generate dual-color images by additionally labeling my samples with an anti-GFP nanobody (see Section 3.5.2).

In summary, I employed an indirect immunolabeling approach to label clathrin-coated structures in chemically fixed SK-MEL-2 CLTA-RFP DNM2-GFP cells. All SK-MEL-2-derived data presented in this work was originally generated by joint imaging efforts of Dr. Markus Mund, Dr. Johanna L. Mehl, and me.

3.1.2 Resolving the 3D geometry of clathrin coats

Following the immunolabeling of clathrin-coated structures with AF647, I could next visualize them using SMLM. While a detailed description of the sample preparation and microscope setup can be found in Section 6, I will here focus on imaging considerations specific to the SMLM approach presented in this work.

An important step when taking microscopy images is to decide on the appropriate region of interest. For this pipeline, it was essential to choose regions enriched for clathrin-coated structures, while simultaneously ensuring high image quality by reducing background signal as much as possible.

By focusing on the adhesive bottom membrane of the cell, the number of resolvable structures within one image could be increased. As this part of the cellular membrane aligns with the underlying coverslip, a large fraction of clathrin-coated structures were captured within one focal plane. Additionally, by staying close to the coverslip, light-scattering effects caused by mismatches between the refractive index of the imaging buffer and immersion oil could be reduced, resulting in higher image quality than at elevated imaging depth.

Increasing image quality can be further achieved by minimizing background noise caused by out-of-focus signals. Apart from non-specifically bound antibodies, there are several sources for out-of-focus signals, including cytosolic clathrin, clathrin sequestered to the Golgi apparatus for vesicle formation (see Section 1.1), and clathrin at endocytic sites at other parts of the plasma membrane (e.g. at the upper, non-adhesive plasma membrane). These sources are enriched in the soma, which contains most of the cytosolic volume, the Golgi, and plasma membrane regions at the top of the cell, far out of focus. Thus, imaging at protrusions at the cell's periphery is preferred, excluding most of these background-causing sources (see Figure 3.1a).

To understand the 3D architecture of clathrin-coated structures, I employed astigmatism-based 3D imaging (see Section 1.5.2). Fluorophores were localized with high precision by fitting each detected signal with an experimentally determined PSF model (Li *et al.*, 2018). For the particular data described here, this precision relates to ≈10 nm laterally, and ≈30 nm axially (see Section 6.2.5.5). Additionally, for the subsequent analyses and dynamic reconstruction, it was essential to acquire images at high throughput. By using an automated set-up for both the activation of fluorophores as well as the simultaneous acquisition of multiple regions of interest, I could acquire up to 10 cells in one imaging session. Within each cell, an average of ≈150 individual clathrin-coated structures could be captured.

Figure 3.1 shows an example image of a clathrin-labeled cell acquired with the above-mentioned considerations. As mentioned in Section 3.1.1, the presence of an endogenous tag (CLTA-RFP) allowed the estimation of labeling specificity. The clear overlap of the

diffraction-limited RFP with the superresolved AF647 signal demonstrates the high specificity achieved with this approach (see Figure 3.1d & g).

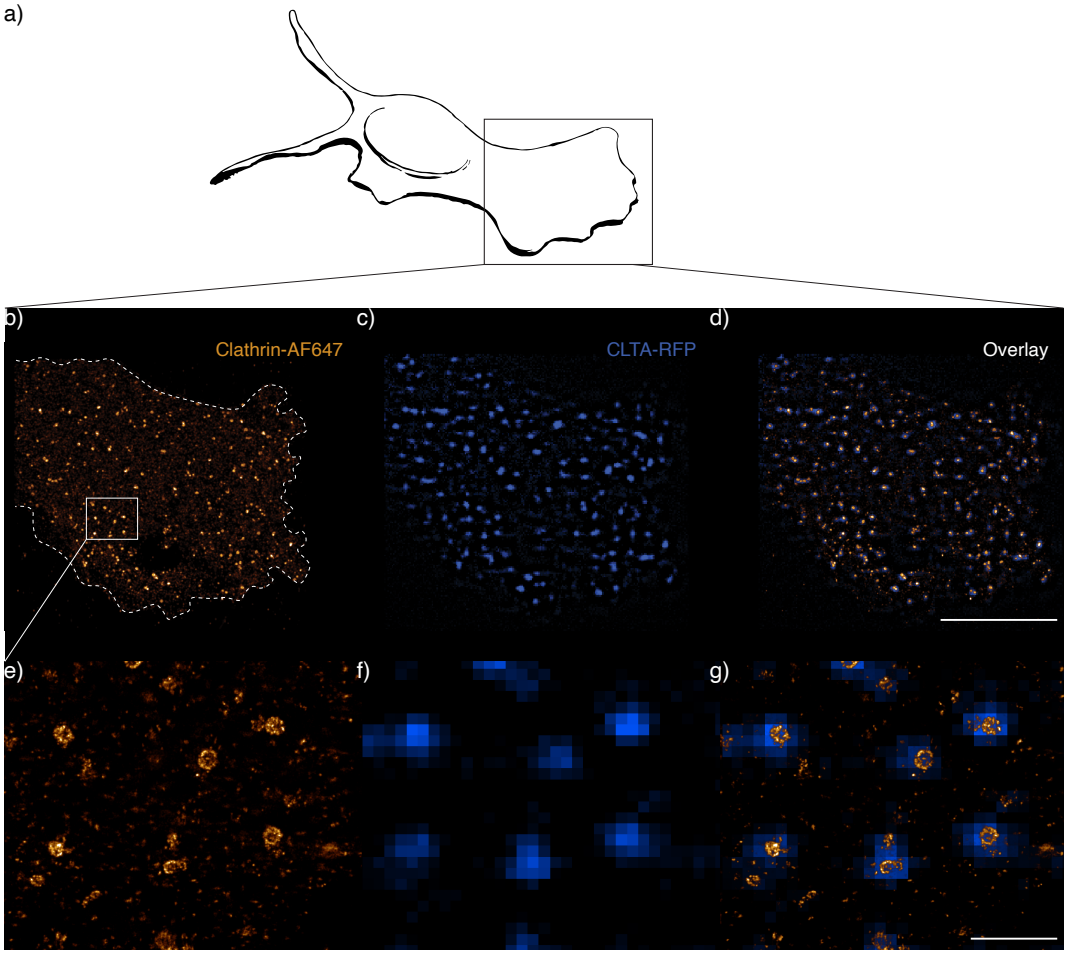


Figure 3.1 | Single-molecule localization microscopy of clathrin. a) To minimize the background caused by intracellular clathrin signal, cellular protrusions are selected as region-of-interests for imaging. **b)** By focusing on the bottom membrane clathrin-coated structures labeled with AF647 can be visualized. The color inenstiy scales with number of localizations per pixel and a Gaussian blur is applied scaled to the precision of each localization. **c)** A diffraction-limited image of the endogenous clathrin light chain A-RFP functions as an internal control for the specificity of the antibody-based labeling strategy. **d)** The clear correlation between both signals in the overlay image confirms the high specificity of the labeling approach. **e-g)** Enlarged images of the boxed-out region in b-d). Scale bars: b-d), 10 µm; e-g) 1 µm. *Data and figure generated by Aline Tschanz.*

Figure 3.2 shows the 3D architecture of the imaged structures, where each localization is colored based on its z-position. The clusters of localizations were clearly discernible from their surroundings represent individual clathrin coats. An enlarged example structure can be seen in Figure 3.2c-f, depicted in different orientations and representations to highlight the dome-shaped nature of this particular structure.

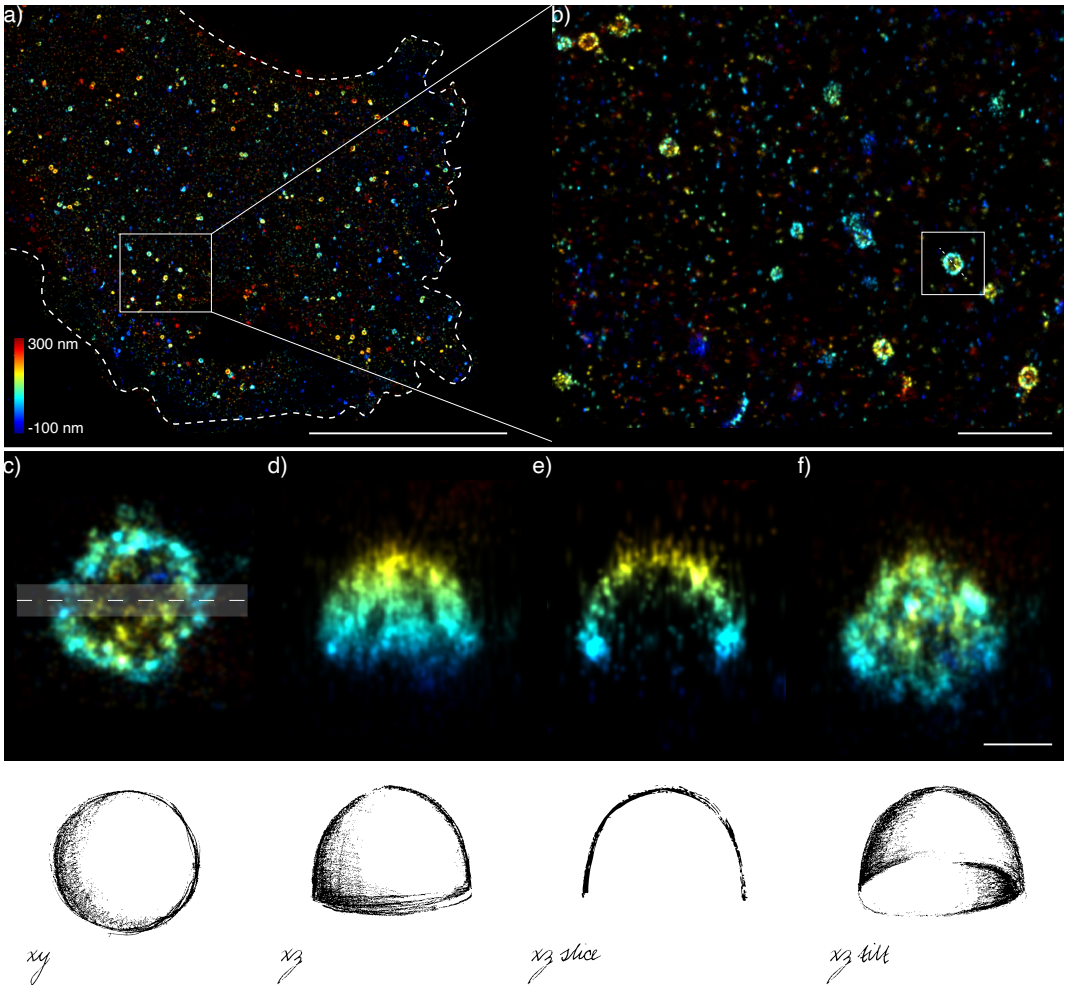


Figure 3.2 | 3D visualization of a clathrin coat. The localizations first presented in Figure 3.1 are colored based on their relative z position. **a)** Clathrin-coated structures, labeled with AF647, are located at variable heights within a range of 400 nm. **b)** Enlarged image of the region boxed out in a). **c)** To explore an individual structure in more detail, an exemplary structure highlighted in b) is shown, and oriented along the dotted line. The shaded area indicates a width of 50 nm. **d)** 90° rotation of the structure shown in c) shows the side view of a half-domed structure. **e)** A xz-slice of the shaded region indicated in c) clearly visualizes the dome-shaped structure of this clathrin coat. **f)** 45° rotation of the structure shown in c). Illustrations are included to depict the orientation of the data. Scale bars: a), 10 µm; b), 10 µm; f), 100 nm. *Data and figure generated by Aline Tschanz.*

While the microscopy approach presented here did not resolve the characteristic hexagonal pattern of the clathrin lattice, the spatial resolution of the data suffices to determine the overall geometry of the coat. As highlighted in Figure 3.3, this geometry is highly variable across the many structures captured in this cell. Coats ranged from flat, to domed, and spherical shapes.

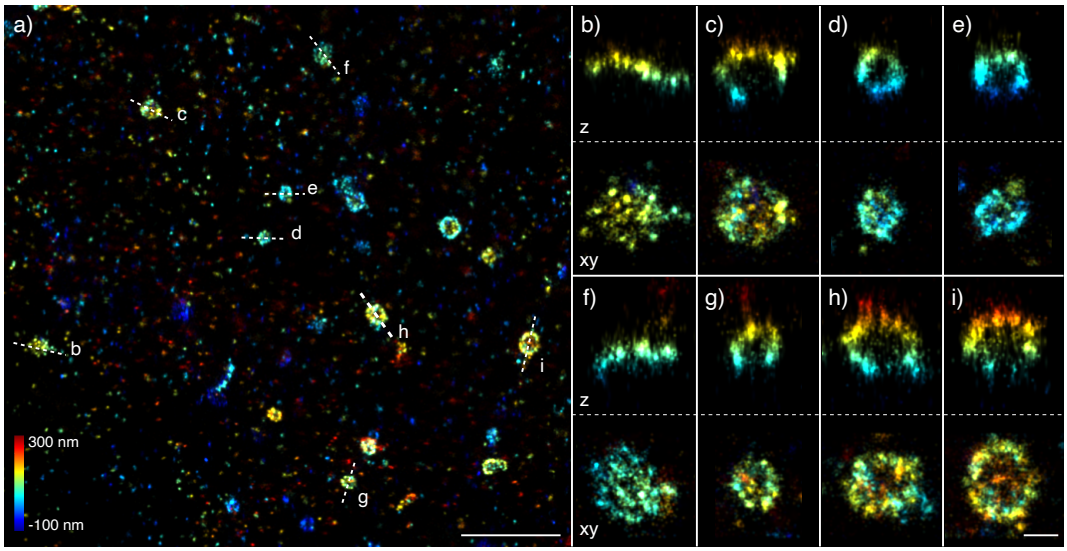


Figure 3.3 | Exploring the diversity of clathrin-coated structures. Clathrin-coated structures were labeled with AF647 and color-coded based on the relative z-position of the localizations. **a)** Example structures were selected from the same data shown in Figure 3.2. **b-i)** 50 nm wide xz-slices and corresponding xy-projections are shown to provide a closer look at the geometric variability in the data. Both views are oriented along the dotted lines shown in a). Scale bars: a), 1 µm; b-i), 100 nm. *Data and figure generated by Aline Tschanz.*

The fact that I detected such a diverse set of structures within a single cell suggests that the chemical sample fixation indeed arrested the endocytic process at random time points. If each captured structure represents a different time point of the overall endocytic process, acquiring a large number of structures should give a more comprehensive understanding of the entire clathrin coat remodeling process.

3.2 From qualitative to quantitative: Capturing the geometric diversity of clathrin coats

The data set described in the following sections was acquired by Dr. Markus Mund, Dr. Johanna L. Mehl, and me, and comprises images of 13 SK-MEL-2 cells, resulting in approximately 2000 snapshots of clathrin-coated structures. To understand at which relative time point each of these structures was arrested during fixation, I next segmented each structure and quantified their geometries using LocMoFit.

3.2.1 Segmentation and curation of single clathrin-coated structures

Semi-automated segmentation of 13 cells resulted in a data set containing ≈2193 sites of interest. The majority (82%) of all segmented structures had similar geometries as shown in Figure 3.3, representing well-isolated sites ranging from flat to dome-shaped, to spherical structures. The remaining 18% had to be excluded due to an upside-down orientation, or due to clustering with other structures such as large flat plaques or other clathrin coats (see Figure 3.4). Distinct physical properties of the plasma membrane could influence the force required for its deformation into a vesicular structure (Wood

and Smith, 2021). This could lead to changes in clathrin coat architecture, that represent structural adaptations to distinct mechanical environments (Ferguson *et al.*, 2017, see Section 5). To generate an average trajectory of clathrin coat remodeling, I, therefore, aim to include structures that likely followed the same mechanistic principles, as they satisfy similar force requirements. Thus, I exclude upside-down structures oriented structures, as they originate from a non-adhesive membrane with distinct composition and physical properties compared to adhesive membranes. Similarly, clathrin coat formation could be influenced by the connection to larger flat clathrin arrangements called plaques and was therefore excluded as well (Leyton-Puig *et al.*, 2017). After considering these exclusion criteria, the final data set comprised 1798 structures. All of these structures are available as rotating movies in the online repository BioStudies (https://www.ebi.ac.uk/biostudies/) under accession number S-BIAD566.

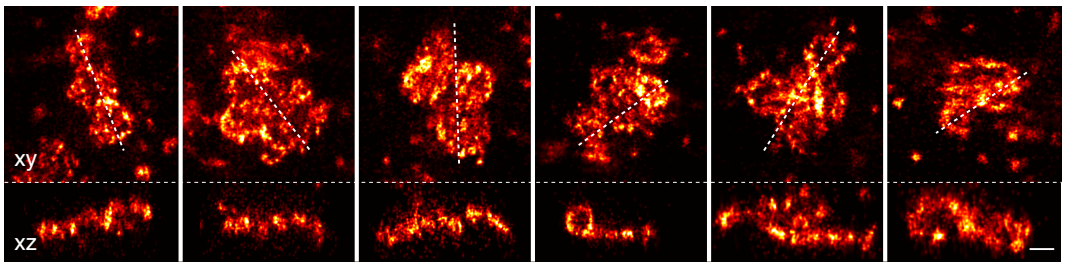


Figure 3.4 | Examples of clustered clathrin-coated structures. These large, asymmetric clusters of clathrin-coated structures were excluded from any subsequent analysis. Vesicular structures budding at such large patches most likely do not follow the same endocytic pathway as well-isolated sites. The dotted line in xy indicates the 50 nm wide cross-section, visualized in xz below. Scale bar: 100 nm. *Data generated by Dr. Markus Mund, Dr. Johanna L. Mehl, and Aline Tschanz, figure generated by Aline Tschanz.*

3.2.2 LocMoFit: Maximum-likelihood model fitting for quantitative analysis of single-molecule localization data

Next, the size and shape of these 1798 manually curated clathrin-coated structures were quantified. To this end, I used a geometric model-fitting framework LocMoFit developed by Dr. Yu-Le Wu, which we jointly optimized for its application to this data (Wu *et al.*, 2023). Here, we used the model of a spherical cap, defined by two main parameters: the radius R and the closing angle θ, as illustrated in Figure 3.5a. Additional parameters included the location (x_0, y_0, z_0) of the model and the relative orientation of the opening of the spherical cap. This model was converted to a probability density function describing the distribution of labeled molecules, and fit directly to the localization data. By maximizing the likelihood of the localizations being sampled from the probability density function, LocMoFit determined the parameter estimates that minimize the difference between the model and all localizations of the segmented structure. This approach circumvents the need to reconstruct the data as a pixelated image (Wu *et al.*, 2020). We could therefore include information such as the localization precision, which was used to weigh the optimization of the model fit. This resulted in a robust approximation of individual clathrin coats and closely matched the geometrical

features of most structures. Figure 3.5b shows example structures and their corresponding model fit results. The good overlap between the model and the underlying data is clearly visible, indicating that this approach could appropriately approximate all clathrin coats independent of their curvature.

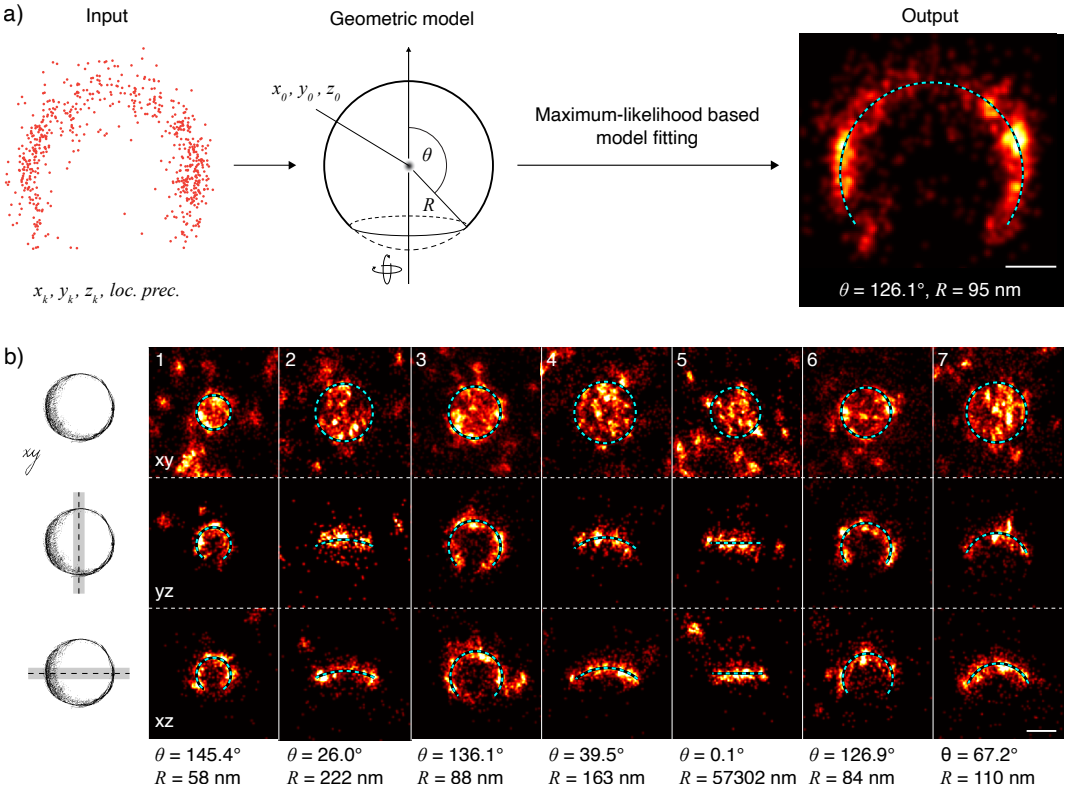


Figure 3.5 | Quantitative description of the clathrin coat. LocMoFit allows for the approximation of clathrin coat geometries. **a)** Principle of the geometric model fitting. The model of a spherical cap was fit to the localization-based input data using the maximum-likelihood-based LocMoFit framework (Wu *et al.*, 2023). The geometric model is described by two main parameters, the closing angle θ and the radius R. Additionally, the model is described by its position x_0, y_0, z_0, and orientation. This model was then fitted to the coordinates x_k, y_k, z_k of all localizations k within the structure, minimizing its distance to each localization, weighted by their respective localization precision σ. This analysis outputs descriptive parameters including θ and R for each clathrin coat. **b)** Example structures analyzed by LocMoFit and depicted as illustrated in the leftmost column. The top row shows the xy view of each structure. The lower two rows show an xz- and yz-slice, respectively, of 30 nm thickness. Scale bars: a), 50 nm; b), 100 nm. *Data and figure generated by Aline Tschanz.*

Whilst the spherical cap is a good approximation for most clathrin coats, certain structures show slight deformations that are less well captured by the model. Figure 3.6a shows a selection of structures representative of the majority of the data set. 3.6b showcases examples of deformations and asymmetries where the spherical model falls short. These variations are currently not quantified. However, investigating the origins and implications of such structural diversity can be an exciting avenue for future inspection of this data. As extending the geometric model with additional parameters is possible, features such as the eccentricity of clathrin coats can be explored with this approach (see Section 5).

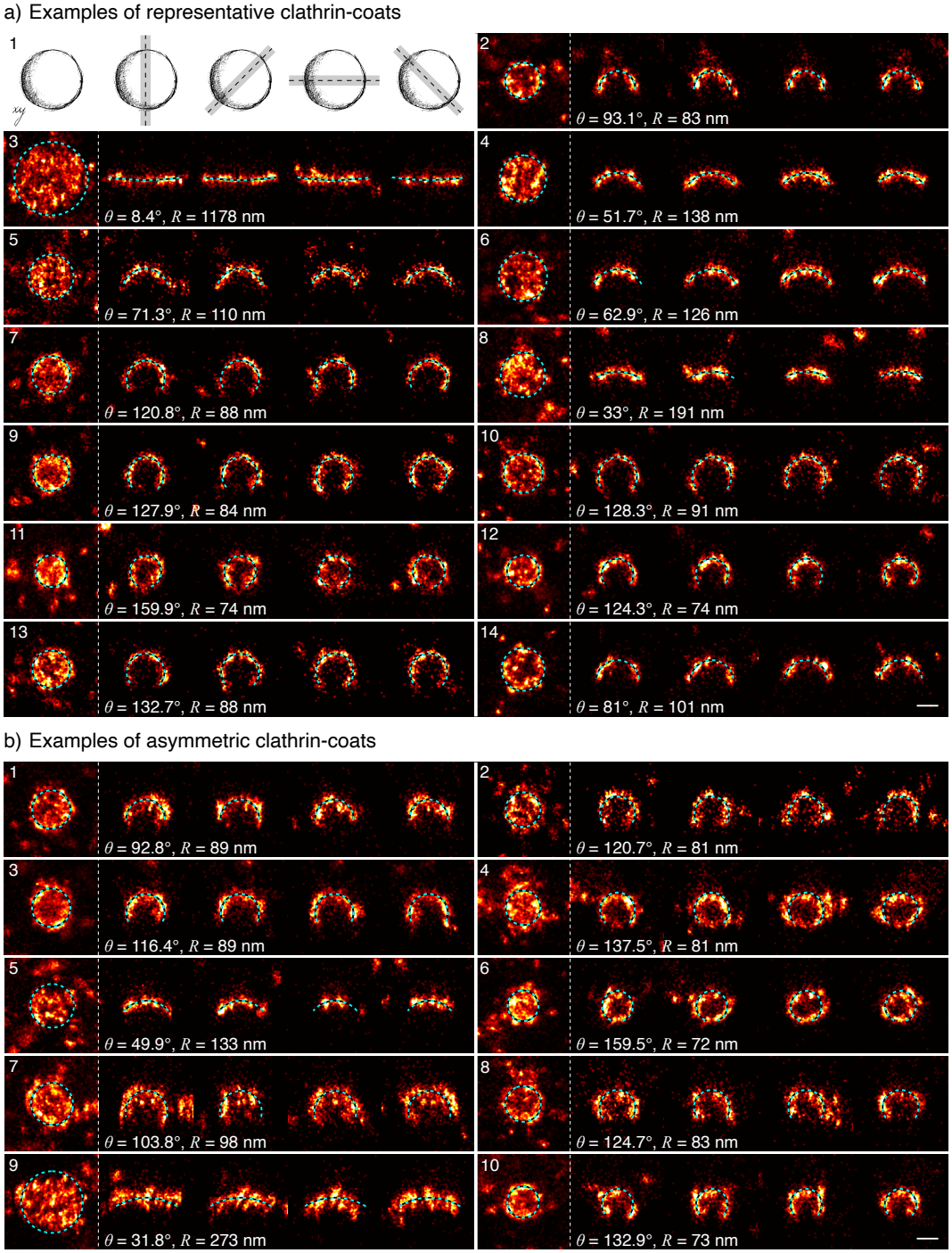


Figure 3.6 | Examples of clathrin-coated structures analyzed with LocMoFit. 1) Each structure is shown as a top view projection on the left, followed by 30 nm thick z-slices at angles 0°, 45°, 90°, and 135°. *2-24)* Localizations are depicted with a Gaussian blur of 3 nm and the red-hot color scale indicates localization density per pixel. The outline of the spherical cap model is depicted in cyan and plotted on top of the data. *2-14)* Randomly selected example sites from a larger data set of 1798 individual structures, resulting from 13 imaged cells. *14-24)* Specific selection of sites that show asymmetries and other deviations from a spherical model. Scale bars: 100 nm. *Data generated by Dr. Markus Mund, Dr. Johanna L. Mehl, and Aline Tschanz, figure generated by Aline Tschanz.*

3.2.3 Sorting clathrin coats along their endocytic progression

All data presented thus far were generated in chemically fixed cells, resulting in static snapshots of the dynamic clathrin coat remodeling process. To understand at which relative time point in the process each structure was fixed, I needed a parameter that would allow me to sort all of my structures along their endocytic progression. This topic was also addressed in work by Dr. Ori Avinoam and colleagues, who sorted their electron tomography images using the closing angle θ as a proxy for endocytic progression (REF to Avinoam). One can assume θ increases monotonously while a flat membrane ($\theta = 0°$) is being remodeled into a spherical, clathrin-coated vesicle ($\theta = 180°$). Thus, by sorting all structures along their quantified θ value, they were in fact sorted along their endocytic trajectory (see Figure 3.7).

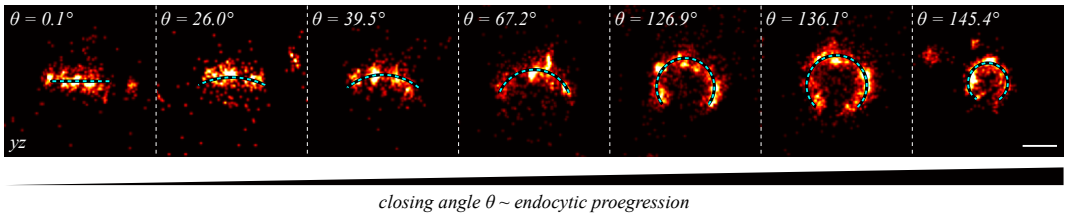


Figure 3.7 | Theta as a proxy for endocytic progression. The same example structures as in Figure 3.5 are shown, after they were sorted along their endocytic progression in θ. Scale bar: 100 nm. *Data and figure generated by Aline Tschanz.*

However, before continuing to analyze all 1789 sorted structures, we wanted to ensure the estimation of the closing angle θ parameter is accurate and consistent. With Dr. Yu-Le Wu's help, we tested the robustness of this analysis using simulated clathrin coats. For simulation parameters such as background, localization precision, labeling efficiency, and linkage error, Dr. Yu-Le Wu used estimations directly from the experimental imaging data I acquired. However, certain assumptions for the clathrin coat geometry had to be made. As we wanted to estimate the accuracy of our model in extracting θ at any endocytic stage, we equally sampled θ values from 0° to 180°. The relationship between θ and the corresponding radius R for each simulated structure was then assumed to be based on the cooperative curvature model, described as $R(\theta) = 1/R_0(\tanh(R_0\gamma\theta))$, which is introduced in Section 3.3.

With these geometric assumptions, we next simulated localization data for individual clathrin coats, fitted them with our spherical cap model, and compared the result with the ground truth of the simulation. This results in a strong linear correlation between the fitted θ values and their respective ground truth (Figure 3.8a), with minimal errors. This indicates a high accuracy of our estimation across the entire θ space. However, a slight decrease in fit accuracy could be observed for small closing angle values ($\theta < 20°$), where the structures are assumed to be almost perfectly flat (see Section 3.2.4). This is not surprising, as in these cases a spherical model was used to approximate flat, 2D structures, which is not the optimal choice of model. Thus, slightly larger fitting errors were obtained

for small θ values. Further, a slight decrease in fit accuracy was observed for large closing angle values ($\theta > 170°$). During fit optimization, the model aimed to estimate the location and size of the spherical cap opening, identifiable as a sudden decrease in localization density. These openings, visible as holes or discontinuities in the labeled clathrin coat, represent the neck region of the budding vesicles. My labeling approach targets discrete positions on the clathrin coat, as the antibodies recognize specific clathrin heavy and light chain epitopes. This means that even in a fully closed, coated, and perfectly labeled vesicle, there would be holes with a minimal size of the distance between two labels, which could still be detected by the model. It could be thus reasonably assumed that this explains the model fitting inaccuracy for larger θ, with a tendency to underestimate $\theta = 180°$ (see Figure 3.8b).

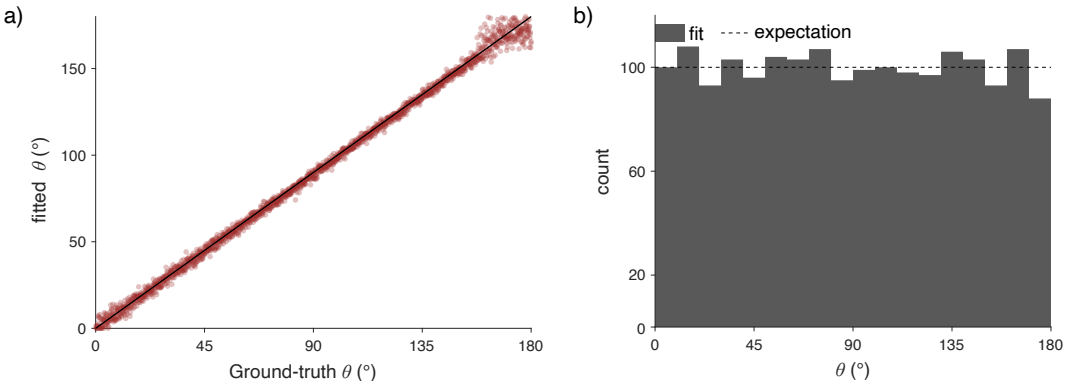


Figure 3.8 | Robustness of closing angle θ estimation. Localization data for $N = 1800$ clathrin-coated structures were simulated using LocMoFit. θ values are sampled from a uniform distribution from $\theta = 0°$ to $\theta = 180°$. R values were calculated based on their $R(\theta) = 1/R_0(\tanh(R_0\gamma\theta))$ relationship. Additional simulation parameters were extracted from experimental data (see Methods). **a)** Correlation between fitted θ and simulation ground truth shows a linear relationship, with slight inaccuracies at low and high angles. **b)** The distribution of θ values shows a slight underestimation of $\theta = 180°$ and is otherwise unbiased. *Data, analysis, and figure generated by Dr. Yu-Le Wu, adapted by Aline Tschanz*

Taken together, the analysis of simulated data using LocMoFit confirmed the accurate estimation of the closing angle θ, with slight but negligible biases for completely closed clathrin coats. Thus, I returned to the experimental data and investigated the distribution of θ for all structures (see Figure 3.9a). It was immediately clear that θ is not uniformly distributed in this data. Instead, some endocytic stages were overrepresented compared to others, indicated by enrichment at $\theta \approx 70°$, and an even stronger peak at $\theta \approx 135°$. As the endocytic process was homogeneously sampled with my approach, a higher prevalence of certain endocytic stages could be interpreted as prolonged phases of the overall process, with long-lived states being overrepresented, and transient stages being more rarely captured (see Section 3.4).

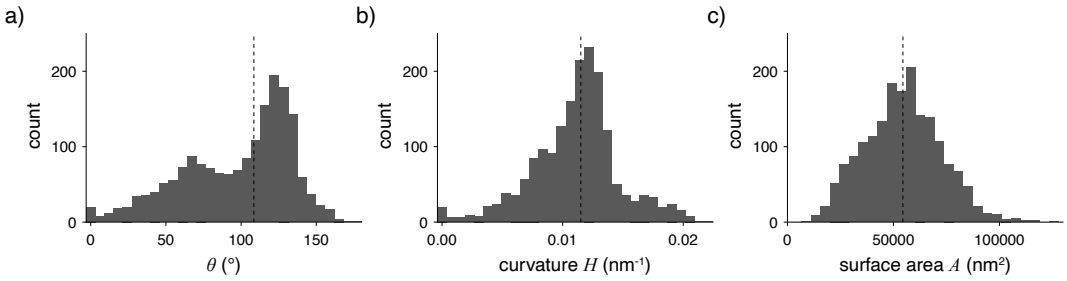


Figure 3.9 | Distribution of clathrin coat geometries. In this data set, n = 1798 clathrin-coated structures, imaged in N = 13 SK-MEL-2 cells, were segmented and analyzed with LocMoFit to determine their geometries. **a)** The closing angle θ was distributed non-uniformly within a range of $\theta = 0°$ to $\theta = 177°$, with a median of $\theta = 108°$. **b)** Curvatures H of clathrin-coats ranged from completely flat ($H = 0\,\mathrm{nm}^{-1}$) to highly curved ($H = 0.022\,\mathrm{nm}^{-1}$) structures, with a median of $H = 0.011\,\mathrm{nm}^{-1}$. **c)** The surface area A calculated for all structures ranged from $A = 9{,}177\,\mathrm{nm}^2$ to $A = 141{,}172\,\mathrm{nm}^2$ with a median of $A = 54{,}478\,\mathrm{nm}^2$. Median values are indicated as dotted lines. *Data generated by Dr. Markus Mund, Dr. Johanna L. Mehl, and Aline Tschanz, analysis and figure generated by Aline Tschanz.*

Additionally, the absence of structures at $\theta = 180°$ was puzzling. As mentioned in the previous paragraph, the model fit is more prone to errors at higher values of θ and sensitive to slight discontinuities in the coat labeling of fully closed vesicles. Contrary to the simulated data in figure 3.8, experimental clathrin coat data comprises less uniformly labeled structures, with more discontinuities and variable labeling densities (see Figure 3.10). Apart from the fact that discrete points on the continuous clathrin coat are labeled, this is due to an imperfect labeling efficiency inherent to the microscopy approach applied here (see Section 1.5.5).

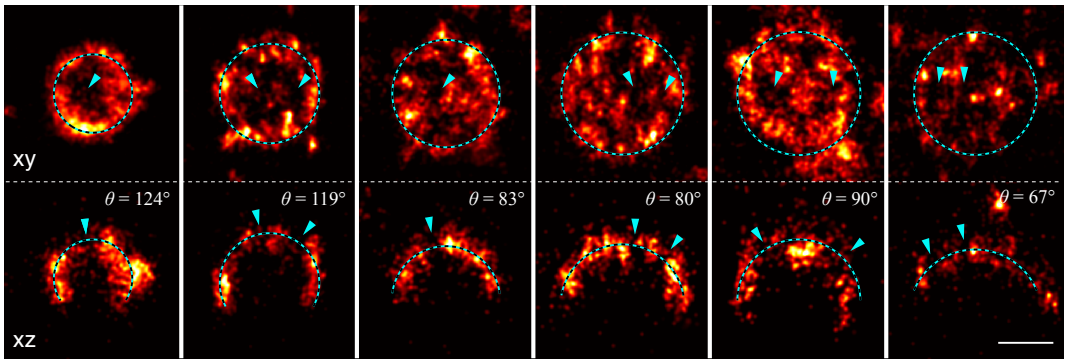


Figure 3.10 | Inhomogeneous labeling of clathrin-coated structures. As an antibody-based strategy was applied to visualize clathrin using single-molecule localization microscopy, discrete positions on the continuous protein coat were labeled. With imperfect labeling efficiency, this results in small holes in the visualized coat, indicated by blue arrows. The model fit result is plotted as a dotted line in cyan. Estimated closing angles θ are indicated for each structure. Scale bar: 100 nm. *Data generated by Dr. Markus Mund, Dr. Johanna L. Mehl, and Aline Tschanz, analysis and figure generated by Aline Tschanz.*

Therefore, the closing angle θ of fully formed vesicles is likely underestimated. This notion was confirmed when clathrin coats at $\theta \approx 170°$ were inspected. In some cases, the structure could be clearly categorized as a closed vesicle, yet the model identifies

slight discontinuities in localization densities as openings, underestimating the actual θ (see Figure 3.11)). Ultimately, this model bias might have resulted in a redistribution of $\theta = 180°$ to slightly lower values. However, it did not explain the drastic decrease after $\theta \approx 130°$. A much more plausible explanation for this observation was the low prevalence of fully formed vesicles in the first place. Possible reasons why these structures might be rarely captured in the data set include shearing off of fully formed, unattached vesicles during sample fixation, the fast nature of scission and uncoating processes in the cell, or fast transport of vesicles out of focus.

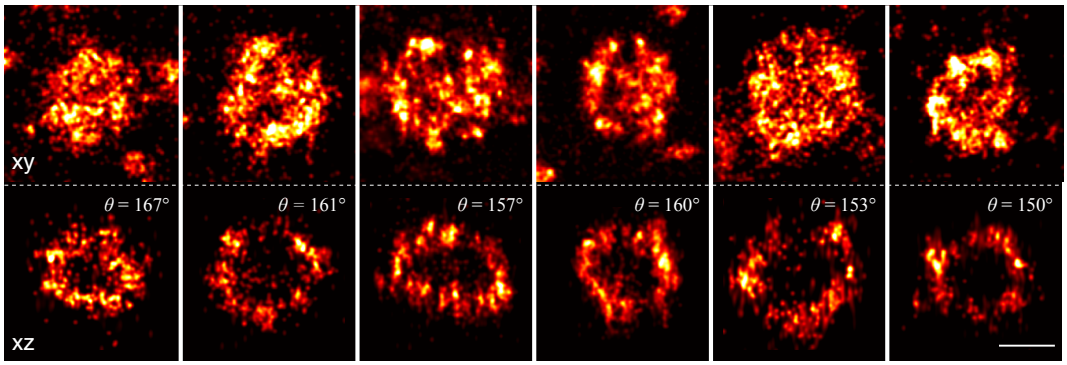


Figure 3.11 | Examples of vesicular structures. Visual inspection indicates a fully formed clathrin coat. However, the geometric model fitting with LocMoFit estimated closing angle values $\theta < 180°$. This is likely due to inhomogeneous labeling, as the model identifies small discontinuities in the coat as openings. Scale bar: 100 nm. *Data generated by Dr. Markus Mund, Dr. Johanna L. Mehl, and Aline Tschanz, analysis and figure generated by Aline Tschanz.*

In summary, I robustly determined the closing angle θ for all structures in this data and used it as a temporal marker to sort randomly arrested clathrin-coated structures along their endocytic progression. I observed a non-uniform distribution of endocytic stages in my data set, indicating a strong variability in the dynamics of clathrin coat formation over time.

3.2.4 Clathrin coats simultaneously grow and bend during endocytosis

Using θ to sort all clathrin-coated structures along endocytic progression, I could next investigate their geometric remodeling during this process. To this end, the curvature $H = 1/R$ and surface area $A = 2\pi R^2(1 - \cos\theta)$ were derived from the closing angle θ and radius R for each structure (see Figure 3.9b-c). By plotting the curvature H and surface area A against their respective closing angle θ, the average progression of these quantities during endocytosis could be reconstructed.

As shown in Figure 3.12, curvature H and θ strongly correlate. The earliest structures in the data set were clearly shallow at a curvature of $H = 0.003\,\text{nm}^{-1}$ ($R = 333$ nm), while the latest structures were highly curved with $H = 0.015\,\text{nm}^{-1}$ ($R = 67$ nm). Here, the median curvature of the 5th and 95th percentile of theta was calculated, representing clathrin coats with the lowest and highest θ value respectively. Also the surface area

A showed an increase during endocytic progression, ranging from $A = 32{,}000\,\mathrm{nm}^2$ to $A = 50{,}000\,\mathrm{nm}^2$ for the earliest and latest 5% of all structures, respectively.

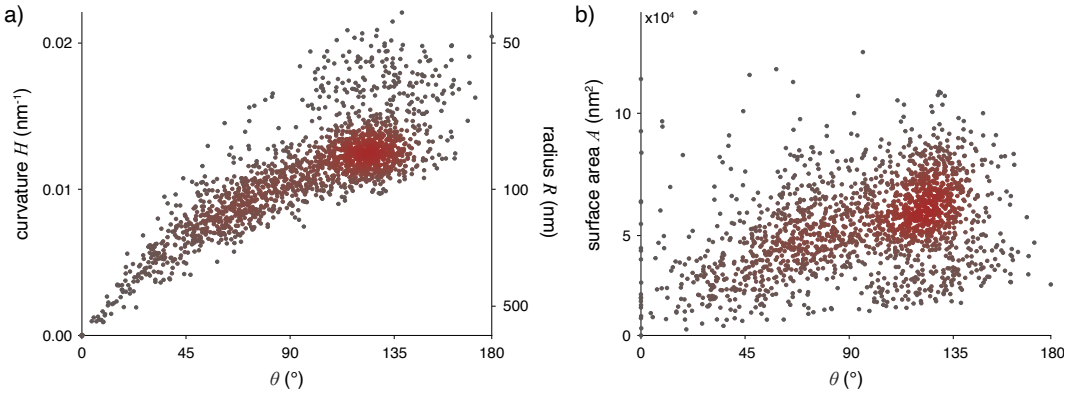


Figure 3.12 | Changes in curvature and surface area of clathrin coats during endocytosis. Every point represents an individual clathrin coat, for which the **a)** curvature H and **b)** surface area A have been calculated. Plotting these quantities over the closing angle θ allowed me to investigate the changes in coat geometries during endocytic progression. In both cases, there was a clear increase detectable, indicating that the clathrin coat simultaneously bends and grows during endocytosis. $N = 13$ cells, $n = 1798$ structures. *Data generated by Dr. Markus Mund, Dr. Johanna L. Mehl, and Aline Tschanz, analysis and figure generated by Aline Tschanz.*

3.2.5 Additional parameters that reflect changes in clathrin coat geometry

According to the analysis results, both the curvature H as well as the surface area A of clathrin-coated structures simultaneously increase during endocytosis. As discussed in Section 1.4 & 1.3, there is a vast source of studies investigating the remodeling of the clathrin coat, employing various methodological approaches. Some of these approaches rely on the interpretation of the area of the top view projection (also known as 'footprint') (Willy *et al.*, 2021) or the length of the edge of the clathrin coat opening (Frey and Schwarz, 2020).

Therefore, I additionally calculated the projected area $A_p = \pi(\sin\theta R)^2$ and edge length $\varepsilon = 2\pi R \sin\theta$. Figure 3.13 shows the distributions of these parameters in the data and their characteristic propagation during endocytic progression.

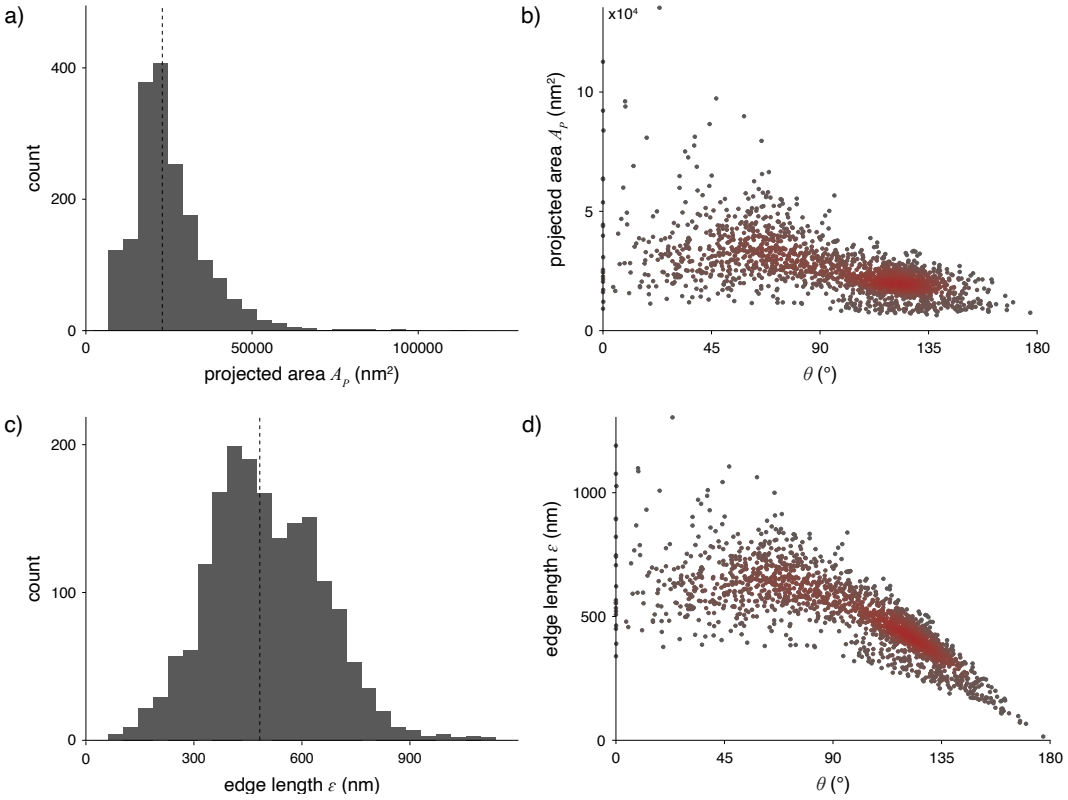


Figure 3.13 | Distribution and propagation of the projected area A_p and edge length ε of clathrin coats. In this data set, n = 1798 clathrin-coated structures, imaged in N = 13 SK-MEL-2 cells were segmented and analyzed using LocMoFit to determine their geometries. **a)** The projected area A_p is distributed within a range of A_p = 6,439 nm^2 to A_p = 135,338 nm^2, with a median of A_p = 22,987 nm^2 (dotted line). **b)** Plotting the projected area A_P against the closing angle θ for each coat indicates a continuous decrease of this parameter during endocytosis (color scale indicates point density). **c)** The edge length ε is distributed within a range of ε = 15 nm to ε = 13,000 nm, with a median of ε = 483 nm (dotted line). **d)** Plotting the edge length ε against the closing angle θ for each coat indicates a continuous decrease of this parameter during endocytosis (color scale indicates point density). *Data generated by Dr. Markus Mund, Dr. Johanna L. Mehl, and Aline Tschanz, analysis and figure generated by Aline Tschanz.*

3.2.6 Golgi-originated clathrin coats grow distinct from endocytic sites

So far, I assumed all the clathrin-coated structures detected and quantified with the pipeline are part of the same endocytic pathway. This notion was further supported by the strong correlation between curvature H and closing angles θ (see Figure 3.12a), which suggested that most of these structures follow the same underlying mechanism.

However, taking a closer look at Figure 3.12a, a sub-population of structures that exhibited a weaker correlation between H and θ becomes apparent. These small, highly curved coats ($H > 0.016\,\text{nm}^{-1}$) appeared at closing angles of $\theta > 90°$, and represented 8.5% of all detected structures (see Figure 3.14).

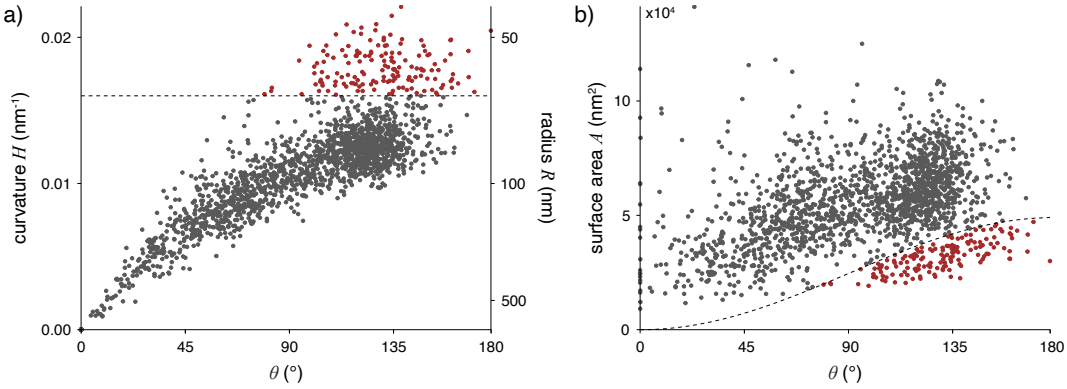


Figure 3.14 | Population of non-endocytic clathrin-coated structures. Here, the same data as in Figure 3.12 are shown, highlighting in red a sub-population of structures that appeared disconnected from the general trajectory of **a)** curvature H and **b)** surface area A. These small, highly curved structures appear above a curvature cut-off of $H > 0.016\,\mathrm{nm}^{-1}$, corresponding to a radius $R < 62.5$ nm, indicated by the dotted line. $N = 13$ cells, $n = 1798$ structures, $n_{\mathrm{red}} = 153$ structures, $n_{\mathrm{grey}} = 1645$ structures. *Data generated by Dr. Markus Mund, Dr. Johanna L. Mehl, and Aline Tschanz, analysis and figure generated by Aline Tschanz.*

Their disconnect indicated that these structures were formed following a different mechanism, and might not have originated via the same endocytic pathway as the rest. I set out to test this hypothesis by adding an endocytosis-specific marker to my imaging pipeline, that allowed the categorization of all clathrin coats as endocytosis, or non-endocytosis-originated structures.

To this end, I generated transiently expressing AP2-GFP cells, with AP-2 being a protein complex specific for endocytosis at the plasma membrane. The GFP signal can then be used to take a diffraction-limited image of AP2-GFP in the cell, which can be overlapped with a superresolved image of clathrin-coated structures generated at the same region-of-interest (see Figure 3.15a-c). Applying the model-fitting pipeline to the clathrin channel allowed the reconstruction of the propagation of curvature H over θ, and the identification of the sub-population of disconnected sites. With the additional annotation from the GFP channel, I then tested whether these structures were truly absent of any endocytic marker (see Figure 3.15d). Indeed, there were no AP2-GFP positive clathrin coats in the disconnected sub-population, and I could thus assume that they originated from a distinct pathway. A possible alternative pathway is the formation of vesicles from the Golgi apparatus. As mentioned in Section 3.1.2, my approach also generates clathrin-specific signals at the Golgi. Thus, some of the structures captured in the data likely originated from this organelle. These findings highlighted that most (91.5%) of the structures present in the data originated from the same endocytic pathway, and highlight the sensitivity of the approach to mechanistically distinct pathways.

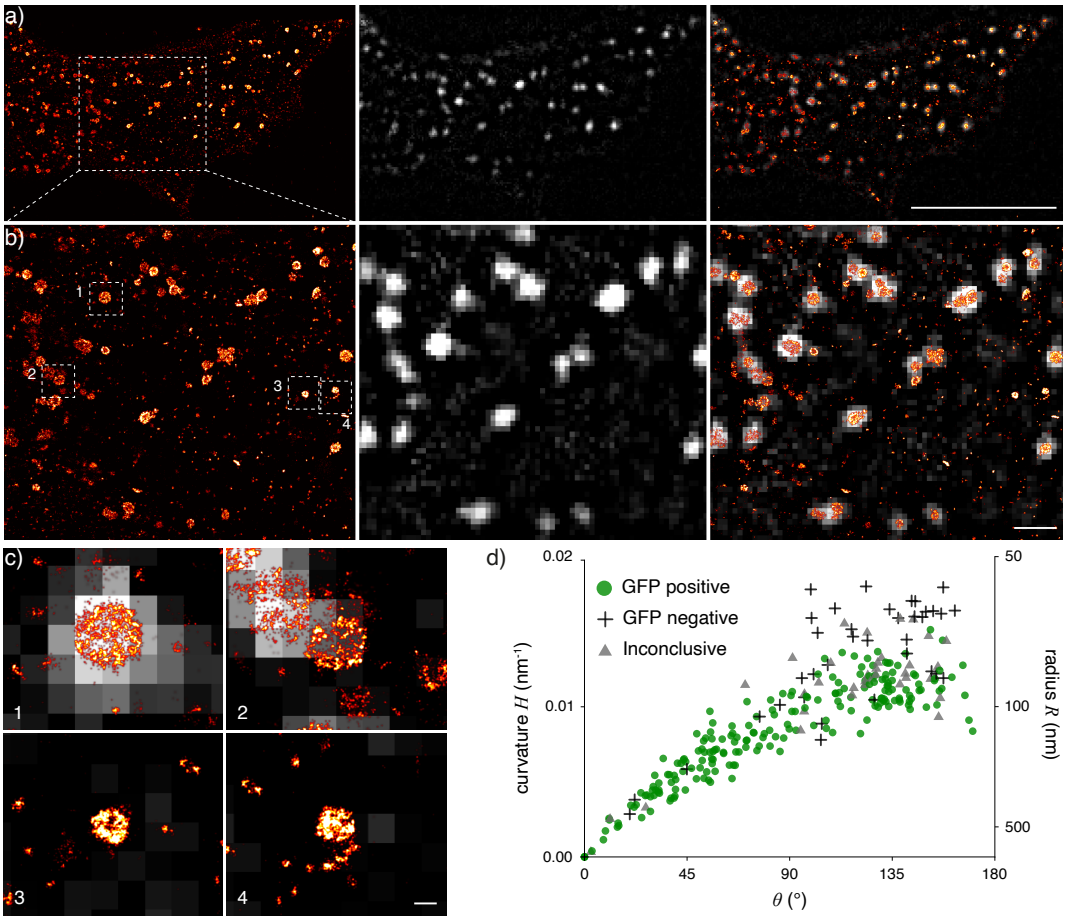


Figure 3.15 | Population of non-endocytic clathrin-coated structures. 3T3 mouse fibroblasts were used to transiently express the endocytic marker AP2-GFP. **a)** Resolving clathrin-coated structures at the bottom membrane of cells allowed me to determine their geometries and measure the parameters curvature H and closing angle θ. The same cell is shown in the middle panel, where AP2-GFP has been visualized as a diffraction-limited image. An overlay of both images can be seen in the right panel, indicating a strong correlation between AP-2 and most clathrin-coated structures. **b)** Enlarged regions as indicated in a). **c)** Example structures for GFP positive (1), inconclusive (2), and GFP negative (3 & 4) annotated structures. **d)** Quantification of the clathrin-coated structures resulted in a curvature H trajectory over closing angle θ similar to results shown in Figure 3.12 and 3.14. The annotation highlighted the absence of AP2-GFP positive clathrin coats in the subpopulation of disconnected structures. $N = 3$ cells and $n = 277$ structures. Scale bars: a), 10 µm; b), 1 µm; c), 100 nm. *Data, analysis, and figure generated by Aline Tschanz.*

3.2.7 Comparing current clathrin coat growth models with experimental data

The two most commonly discussed models to approximate the mechanism of clathrin coat remodeling are the constant area and the constant curvature model. Each of these models comes with its own assumption on how specifically curvature and surface area are propagated during endocytosis (see Figure 1.4). As the same parameters are also quantified for the presented data, the observed changes in curvature H and surface area A could be compared with the expected changes based on the two models. To do so, I fit the constant curvature model $H(\theta) = H_{\mathrm{CCM}}$ defined by the constant curvature H_{CCM},

and the constant area model $H(\theta) = \sqrt{2\pi(1-\cos\theta)/A_{\mathrm{CAM}}}$, defined by the constant area A_{CAM} to my experimental data (see Figure 3.16).

Table 3.1 summarizes the mathematical relationship between the different clathrin coat geometries and closing angle θ. Table 3.3 summarizes the parameters resulting from the clathrin coat growth model fits.

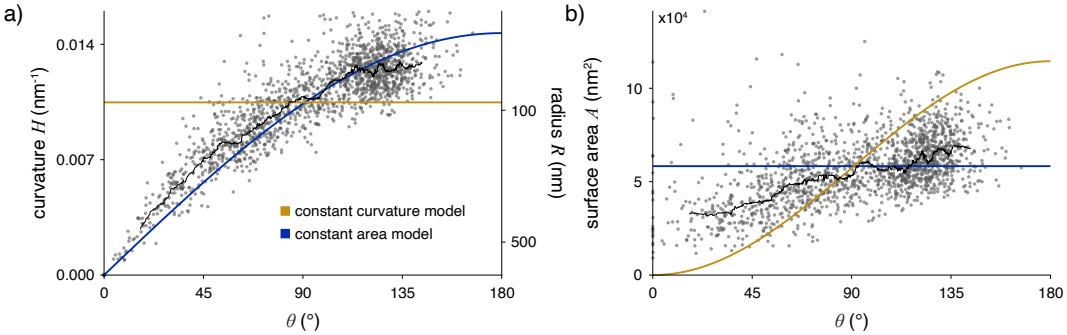


Figure 3.16 | Contradiction of current models with geometric data on clathrin coats. The fit of current clathrin coat growth models to my experimental data (gray), excluding non-endocytic structures (see Section 3.2.6). Rolling median is calculated with an averaging window of 5% of the number of structures (black line). **a)** The observed increase of curvature H over closing angle θ contradicts the constant curvature model (orange) and is better approximated by the constant area model (blue). **b)** Using the same fitting parameters estimated in a), I can determine that neither model describes the increase in surface area A observed. N = 13 cells, n = 1645 structures. *Data generated by Dr. Markus Mund, Dr. Johanna L. Mehl, and Aline Tschanz, analysis and figure generated by Aline Tschanz.*

A constant coat curvature was clearly insufficient to approximate the curvature increase in the data, and fitting a constant coat area described this trajectory much better (see Figure 3.16a). However, the constant area model was not an appropriate assumption to describe the observed surface area increase (see Figure 3.16b). In the end, neither the constant area nor the constant curvature model described the continuous bending and growth of the coat. In the next section, I, therefore, discuss the formulation of a new mechanistic model to approximate these observations and gain insight into the mechanics of clathrin coat remodeling.

	Model		
	Constant curvature	Constant area	Cooperative curvature
$H(\theta)$	H_{CCM}	$\sqrt{\frac{2\pi(1-\cos\theta)}{A_{\mathrm{CAM}}}}$	$H_0 \tanh \frac{\gamma\theta}{H_0}$
$A(\theta)$	$2\pi \frac{1}{H_{\mathrm{CCM}}}^2 (1-\cos\theta)$	A_{CAM}	$2\pi \frac{1}{H_{\mathrm{CoopCM}}}^2 (1-\cos\theta)$
$A_p(\theta)$	$\begin{cases} \pi(\frac{\sin\theta}{H_{\mathrm{CCM}}})^2 & \theta < 90° \\ \pi \frac{1}{H_{\mathrm{CCM}}}^2 & \theta \geq 90° \end{cases}$	$\begin{cases} \pi(\frac{\sin\theta}{H_{\mathrm{CAM}}})^2 & \theta < 90° \\ \pi \frac{1}{H_{\mathrm{CAM}}}^2 & \theta \geq 90° \end{cases}$	$\begin{cases} \pi(\frac{\sin\theta}{H_{\mathrm{CoopCM}}})^2 & \theta < 90° \\ \pi \frac{1}{H_{\mathrm{CoopCM}}}^2 & \theta \geq 90° \end{cases}$
$\varepsilon(\theta)$	$2\pi \frac{1}{H_{\mathrm{CCM}}} \sin\theta$	$2\pi \frac{1}{H_{\mathrm{CAM}}} \sin\theta$	$2\pi \frac{1}{H_{\mathrm{CoopCM}}} \sin\theta$

Table 3.1 | Equations to describe clathrin coat growth according to distinct models. The constant curvature model (CCM) suggests no change in coat curvature during endocytosis, which is expressed as $H(\theta) = H_{\mathrm{CCM}}$. The constant area model (CAM) suggests no change in coat surface area during endocytosis, which is expressed as $A(\theta) = A_{\mathrm{CAM}}$. The cooperative curvature model described the change in coat curvature during endocytosis based on the curvature increase rate γ and the preferred curvature H_0, which is expressed as $H(\theta) = H_0 \tanh \frac{\gamma\theta}{H_0}$. Equations derived from these dependencies are shown for the curvature H, surface area A, projected area A_p, and edge length ε.

3.3 Cooperative curvature model: an updated model for clathrin coat remodeling

The results described in the previous section made it clear that current clathrin coat growth models were insufficient to approximate the data presented in this work. To understand the complex nature of clathrin coat remodeling more mechanistically, Prof. Dr. Ulrich S. Schwarz and Dr. Felix Frey, formulated a new growth model based on the here described experimental findings.

3.3.1 Model assumptions, analytical solution and fit to data

The experimental data clearly showed the simultaneous increase of curvature H and surface area A of the clathrin coat during endocytic progression (see Figure 3.12 & 3.16). Prof. Dr. Ulrich S. Schwarz and Dr. Felix Frey thus aimed to describe this relationship as a physical model.

To this end, they first assumed that clathrin coats start growing on a flat membrane, as this agrees with the observation of shallow coats with small curvatures (see Section 3.2.4).

Next, they assumed that the clathrin coat as a whole prefers to adopt a spherical conformation. This assumption was based on the observation of intrinsic pucker angles in individual clathrin triskelia, their capability of spontaneously generating spherical vesicles *in vitro*, and their preference for curved membranes (Fotin *et al.*, 2004; Woodward and Roth, 1978; Zaremba and Keen, 1983; Pearse and Robinson, 1984). However, early flat

structures observed in the data described in this work suggested that this preference for curvature cannot be realized in an immature coat. It has been suggested that cooperativity between individual clathrin molecules is required to promote the bending of the plasma membrane (Zeno *et al.*, 2021; Sochacki *et al.*, 2021).

Therefore, we hypothesized that the coat curvature H increases at an initial rate γ and asymptotically approaches a preferred curvature H_0. This described a saturation effect, with curvature increasing more drastically at the beginning of the process, and then slowing down the closer the entire structure approaches the preferred curvature H_0. To represent this cooperativity, Prof. Dr. Ulrich S. Schwarz and Dr. Felix Frey chose a quadratic dependency of the curvature change rate on curvature (Equation 3.1).

$$\frac{d}{d\theta}H = \gamma(1 - \frac{H^2}{H_0^2}) \tag{3.1}$$

Equation 3.1 can be solved analytically under the condition of $H(\theta = 0) = 0$ to yield Equation 3.2.

$$H(\theta) = H_0 \tanh \frac{\gamma\theta}{H_0} \tag{3.2}$$

I next fitted this expression to the propagation of curvature H over closing angle θ, to approximate the average trajectory of curvature generation using the cooperative curvature model (see Figure 3.17a). This fit showed good agreement with the experimental data, and I was able to extract two main parameters, the rate of curvature increase γ and the preferred curvature H_0. These further enabled the description of coat surface area A, projected area A_p, and edge length ε during endocytic progression (see Figure 3.17b-d and Table 3.3).

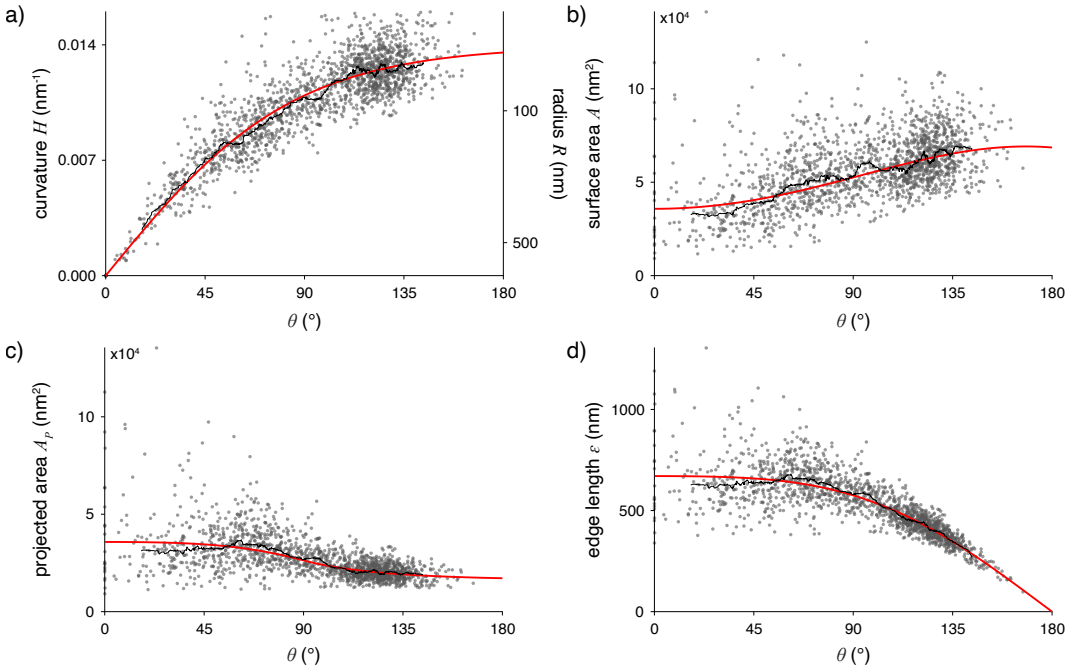


Figure 3.17 | The cooperative curvature model describes clathrin coat remodeling during endocytosis. Fit of the cooperative curvature models to my experimental data (gray), excluding non-endocytic structures (see Section 3.2.6). Rolling median was calculated with an averaging window of 5% of the number of structures (black line). **a)** The cooperative curvature model (red) fit to this data set well approximates the trajectory of curvature generation during endocytic progression. The fit parameters extracted from a) mapped to the clathrin coat surface area A **b);** projected area A_p **c);** and edge length ε **d)** resulted in a good fit of the model to the underlying data. N = 13 cells, n = 1645 structures. Mathematical expression and extracted fit parameters are summarized in Table 3.1 & 3.3 respectively. *Data generated by Dr. Markus Mund, Dr. Johanna L. Mehl, and Aline Tschanz, analysis and figure generated by Aline Tschanz, Model expression developed by Prof. Dr. Ulrich S. Schwarz and Dr. Felix Frey.*

The cooperative curvature model describes the trajectory of my data equally well for curvature $H(\theta)$, surface area $A(\theta)$, projected area $A_P(\theta)$, and edge length $\varepsilon(\theta)$, and results in little variation for these four features of the data (see Table 3.3). This new clathrin coat growth model, based on parameters H_0 and γ, results in an improved fit compared to the constant area or constant curvature model, based on parameters A_{CAM} and H_{CCM}, respectively. To ensure this observation is not just attributed to the additional model parameter in the cooperative curvature model, Prof. Dr. Ulrich S. Schwarz and Dr. Felix Frey calculated the Bayesian information criterion (BIC) for each model. This evaluates the relative likelihood for each model given my data while penalizing additional fitting parameters. The BIC can be formulated by Equation 3.3.

$$BIC = N \ln \frac{RSS}{N-k} + k \ln N \approx N \ln \frac{RSS}{N} + k \ln N \tag{3.3}$$

where N is the number of data points, k is the number of free parameters and RSS is the residual sum of squares $RSS = \sum_i^N (f(x_i) - y_i)^2$ with x_i and y_i being the measured data points and $f(x_i)$ the fitted data. Table 3.2 shows the results of this calculation. Note that

3.3 can be simplified because $N \gg k$. As generally the model with the lowest BIC value is preferred, it can be concluded that the cooperative curvature model is statistically the more likely model given the experimental data.

	Model		
	Constant curvature	Constant area	Cooperative curvature
SK-MEL-2 cells	−19,079	−21,218	−21,670
3T3 cells	−8,119	−9,179	−9,498
U-2 OS cells	−2,784	−3,097	−3,190

Table 3.2 | Bayesian information criterion (BIC) to compare different clathrin coat growth model fits. The BIC was calculated according to Equation 3.3, comparing the fit of the constant curvature, constant area, and cooperative curvature model in $H(\theta)$. Results for data from three different cell lines (SK-MEL-2; 3T3; and U-2 OS) show the superior fit of the cooperative curvature model, despite an additional fitting parameter included. *Analysis performed by Prof. Dr. Ulrich S. Schwarz and Dr. Felix Frey.*

Prof. Dr. Ulrich S. Schwarz and Dr. Felix Frey further compared the quadratic dependency between the curvature change rate on curvature described in Equation 3.1 with a linear model (Mund *et al.*, 2023). Analytical solutions and fit to the experimental data showed a poor agreement of this model given the data. This confirmed the reasoning behind the quadratic relationship chosen for the cooperative curvature model.

With these considerations, we were confident in having developed a robust approximation of clathrin coat growth during mammalian endocytosis. According to the extracted fit parameters, clathrin coats in SK-MEL-2 cell lines approach an average preferred curvature of $H_0 = 0.014\,\mathrm{nm}^{-1}$. This corresponds to a preferred radius of $R_0 = 72\,\mathrm{nm}$. These values represent a more accurate estimation for the average size of a vesicular structure than what was calculated previously (see Section 3.2.4) and agree well with the literature (REF publication and measured radii).

Further, the fraction of surface area A_0 accumulated as a flat structure at the point of coat-curvature initiation $\theta = 0.01^\circ$ can be calculated according to Equation 3.4.

$$A_0 = A(\theta = 0.01)/A(\theta = 180 \tag{3.4}$$

According to the data, approximately half of the final surface area ($A_0 = 0.51$) has to be acquired before the clathrin coat can start to bend. This partial pre-assembly into flat structures has been reported previously using a complementary imaging and analysis approach (Bucher *et al.*, 2018). However, their determined pre-assembled area at $A_0 \approx 0.70$ differs from the observations described here. While this could be due to different imaging modalities and parameter estimation errors, a more probable explanation is that they performed their study in BSC-1 cells. It is well known that different cell

types produce differently sized clathrin-coated structures, likely due to distinct cellular requirements and cell-surface properties (McMahon and Boucrot, 2011). This structural variability could result from mechanistic differences in clathrin-mediated endocytosis between different cell types. Therefore, I asked next to what extent the cooperative curvature model represents a universal mechanism for membrane invagination and to what extent it allows us to quantify cell-type specific variations.

		Fit result			
		Curvature $H(\theta)$	Surface area $A(\theta)$	Projected area $A_p(\theta)$	Edge length $\varepsilon(\theta)$
Constant area model	A_{CAM}	58,300 ± 400 nm^2	56,600 ± 400 nm^2	48,800 ± 500 nm^2	49,400 ± 500 nm^2
Constant curvature model	R_{CCM}	94.5 ± 0.7 nm	84.8 ± 0.4 nm	97.3 ± 0.8 nm	92.8 ± 0.7 nm
Cooperative curvature model	γ	(9.4 ± 0.1) 10^{-3} nm^{-1}	(9.0 ± 0.1) 10^{-3} nm^{-1}	(9.1 ± 0.1) 10^{-3} nm^{-1}	(9.4 ± 0.1) 10^{-3} nm^{-1}
	H_0	(13.9 ± 0.1) 10^{-3} nm^{-1}	(13.8 ± 0.1) 10^{-3} nm^{-1}	(13.6 ± 0.1) 10^{-3} nm^{-1}	(13.4 ± 0.1) 10^{-3} nm^{-1}
	R_0	72.0 ± 0.6 nm	72.2 ± 0.6 nm	73.4 ± 0.9 nm	74.0 ± 0.8 nm
	A_0	0.51	0.55	0.52	0.49
	k_{on}	78.1 nm$\tilde{s}^{-1}$	72.2 nm$\tilde{s}^{-1}$	78.0 nm$\tilde{s}^{-1}$	83.4 nm$\tilde{s}^{-1}$

Table 3.3 | Summary of clathrin coat growth model fits in SK-MEL-2 cells. The constant area, constant curvature, and cooperative curvature model parameters are fitted to four different features of the data: The curvature $H(\theta)$, surface area $A(\theta)$, projected area $A_p(\theta)$, and edge length $\varepsilon(\theta)$ calculated for all clathrin coats of endocytic origin (N = 13 cells, n = 1645 structures). Fitting parameters include the constant area A_{CAM}; constant curvature H_{CCM}; curvature increase rate γ; preferred curvature H_0; preferred radius R_0; fraction of surface area grown flat A_0; and net clathrin coat growth rate k_{on} measured in nm per pseudotime units $\tilde{s}$. Model-fit equations are summarized in Table 3.1. *Data generated by Dr. Markus Mund, Dr. Johanna L. Mehl, and Aline Tschanz, analysis performed by Aline Tschanz, Model expression developed by Prof. Dr. Ulrich S. Schwarz and Dr. Felix Frey.*

3.3.2 Linkage error and potential effects on model fit

As previously discussed (see Section 1.5.5), the displacement between the label or fluorophore, and the biological structure of interest called 'linkage error' can cause a decrease in resolution. If the linkage error is equally distributed, this would result in a homogenous blurring of the underlying structure. In the case of the clathrin coat, it would increase the thickness visible in xz slices (see Figure 3.1).

For our geometric model fit, this results in minimal consequences, as LocMoFit will place the spherical cap model in the middle of this distribution, accurately estimating the original position of the structure. Such a homogenous linkage error was assumed for the simulations shown in Figure 3.8, thus confirming the robustness of the theta estimation approach.

However, a biased distribution of the linkage error could lead to inaccuracies in the model fit (see Figure 3.18). Should antibodies preferably bind to the cytosolic side of the clathrin coat (e.g. due to the membrane-oriented side being too crowded through cargo and adaptor proteins), this would result in overestimation of the model radius R_{M} compared to the true coat radius R_{C} (see Figure 3.18c). Conversely, membrane permeabilization could result in easier access for antibody binding, resulting in linkage error biased towards the lumen of the budding vesicle (see Figure 3.18c). This bias would result in an underestimation of the model radius R_{M} compared to the true coat radius R_{C}.

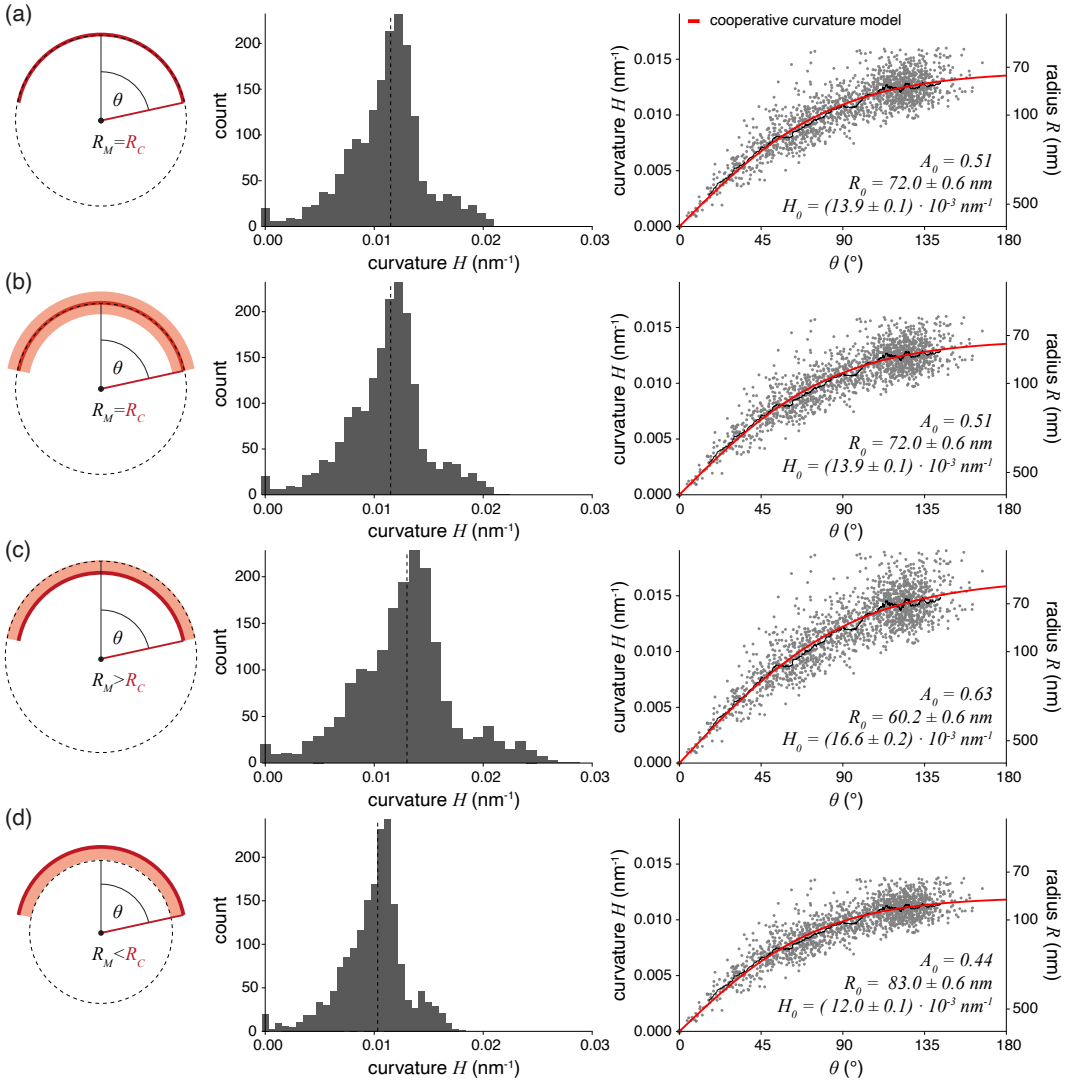


Figure 3.18 | Impact of linkage error on geometric model fit. Indirect immunolabeling displaces the label from the target molecule by two antibodies. This generates a linkage error of on average ± 10 nm, and resulting localizations might not accurately and precisely represent the underlying structure of interest (see Section 1.5.5). **a)** An ideal case of no linkage error, where the model (dotted black line) with radius RM accurately represents the underlying clathrin coat *(red)* with a radius R_C *(left)*. Median curvature of 0.011 nm^{-1} was determined for these structures *(middle, dotted line)* and the cooperative curvature model *(red)* well approximate the data. Resulting fit parameters are shown *(right)*. **b)** Uniform displacement of localizations (*light red*, ± 10 nm) due to unbiased labeling by the antibodies. The radius R_M still accurately represents the true radius R_C. Median curvature of 0.011 nm^{-1} was determined for these structures *(middle, dotted line)* and the cooperative curvature model *(red)* well approximate the data. **c)** Biased labeling of the antibodies (*light red*, + 10 nm) could result in an overestimation of R_M by 10 nm. Median curvature: 0.013 nm^{-1} *dotted line*. The cooperative curvature still approximates the data well, albeit resulting in slightly different parameter values. **c)** Biased labeling could result in an underestimation of R_M by 10 nm. Median: 0.010 nm^{-1}. The cooperative curvature still approximates the data well, albeit resulting in slightly different parameter values. Fitting parameters are A_0: Fraction of surface area growing as a flat lattice before curvature initiation, defined as A_0; R_0: Preferred radius; H_0: Preferred curvature. N = 13 cells, n = 1,645 sites. While the fitting parameters scale with the error in radius estimation, the relationships among the parameters and thus our mechanistic interpretation by the cooperative curvature model still holds true. *Data generated by Dr. Markus Mund, Dr. Johanna L. Mehl, and Aline Tschanz, analysis and figure generated by Aline Tschanz. Published previously in Mund* et al., *2023*.

I, therefore, tested the effect of such inaccuracies in radius estimation on the cooperative curvature model fit. By rescaling the radii of all structures in the data depending on an over or underestimation of the radius by 10 nm, the effect on the model fit could be evaluated. The results show that while biases in linkage error would result in slightly different model fit parameters, the cooperative curvature still approximates the underlying data well. Linkage error bias, therefore, does not result in any changes in the mechanistic interpretation of the results presented here.

3.3.3 Cell-line specific adaptations of the clathrin coat remodeling mechanism

To understand the generalizability of the newly developed cooperative curvature model, I expanded the above-described microscopy and analysis pipeline to additional cell types, including 3T3 mouse fibroblasts (see Figure 3.19) and U-2 OS human bone osteosarcoma (see Figure 3.20).

Slight differences between these cell lines could already be observed during the initial imaging, confirming previous morphological descriptions (3T3, ATCC CRL-1658; U-2 OS, ATCC HTB-96, SK-MEL-2, ATCC HTB-68). While the 3T3 fibroblasts grew flat and irregular, with long, star-like protrusions, U-2 OS cells tended to form elongated, spindle-like shapes. This contrasted the SK-MEL-2, which formed less elongated, but similarly irregular, protrusions to 3T3 cells. Additionally, while 3T3 and SK-MEL-2 cells tended to exhibit many well-isolated clathrin-coated structures, U-2 OS exhibited more clusters and large flat clathrin-coated structures (see Figure 3.20b).

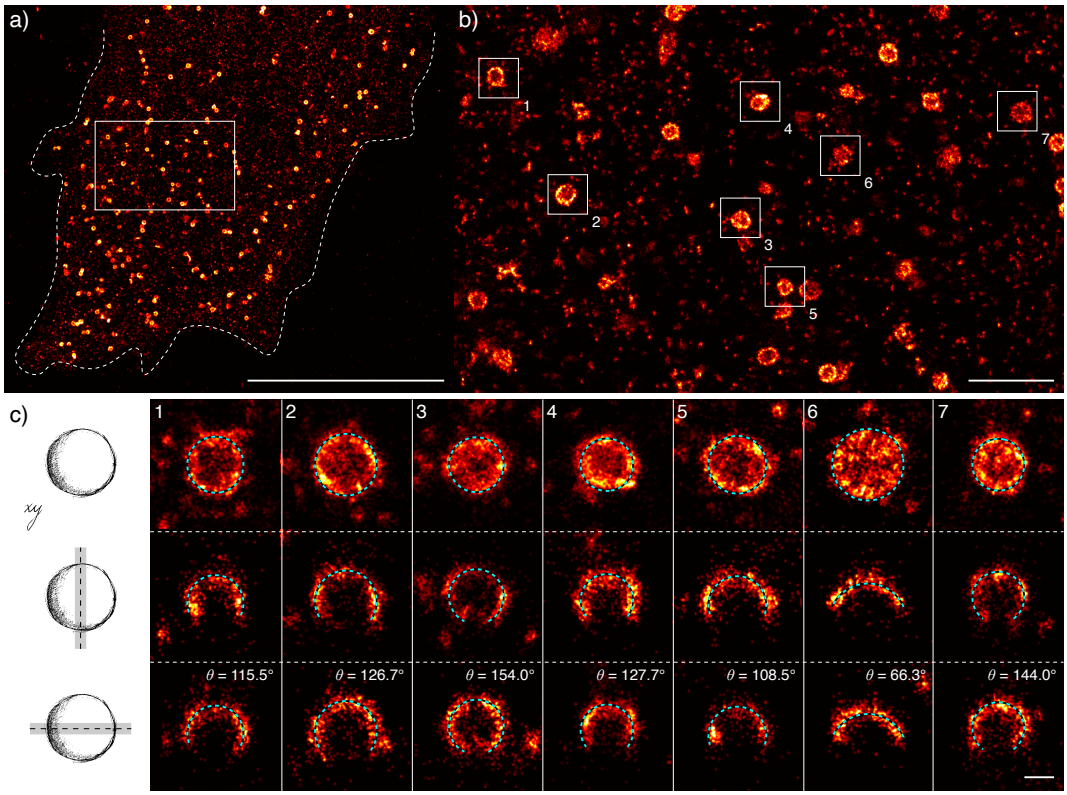


Figure 3.19 | Clathrin-coated structures imaged in 3T3 mouse fibroblasts. a) Clathrin, labeled with AF647 in an exemplary 3T3 cell. **b)** Enlarged region indicated in a) shows well-isolated structures. **c)** Example structures selected in b) are shown as xy-projections, or z-slices, as indicated in the illustrations on the left. The geometric model fit result is plotted as a dotted cyan line, with the corresponding estimated closing angle θ. Scale bars: a), 10 µm; b), 1 µm; c), 100 nm. *Data, analysis, and figure generated by Aline Tschanz.*

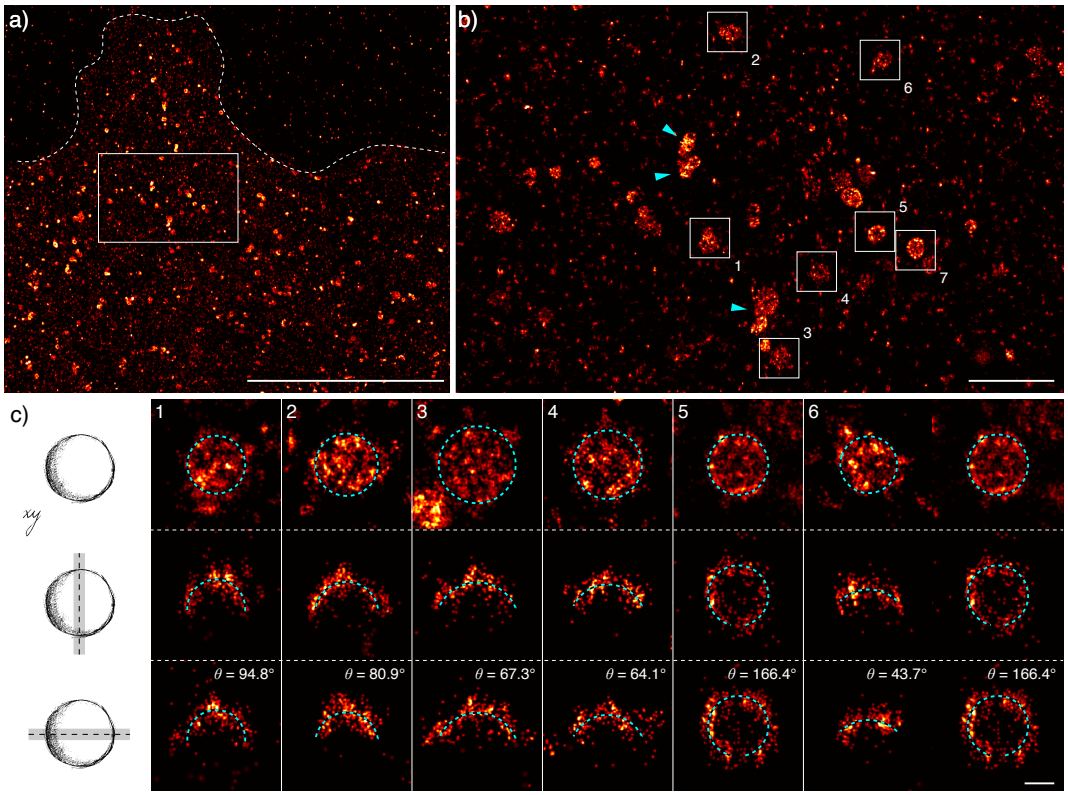


Figure 3.20 | Clathrin-coated structures imaged in U-2 OS human bone osteosarcoma. a) Clathrin, labeled with AF647 in an exemplary U-2 OS cell. **b)** Enlarged region indicated in a) shows well-isolated structures. U-2 OS exhibited more clusters than other cell lines, as indicated by blue arrows. **c)** Example structures selected in b) are shown as xy-projections, or z-slices, as indicated in the illustrations on the left. The geometric model fit result is plotted as a dotted cyan line, with the corresponding estimated closing angle θ. Scale bars: a), 10 µm; b), 1 µm; c), 100 nm. *Data, analysis, and figure generated by Aline Tschanz.*

To understand potential cell-type specific variations in clathrin coat geometry, I quantified all structures as described in Section 3.2. The distributions were within a similar range of values for all three cell lines (see Figure 3.21).

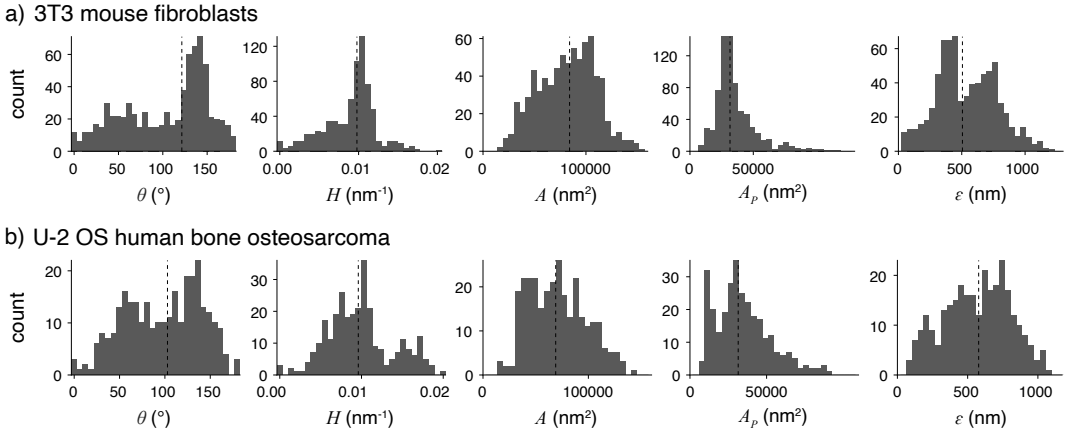


Figure 3.21 | Distributions of clathrin coat geometries in different cell lines. Geometric quantification of clathrin coats was performed according to Section 3.2. Closing angle θ; curvature H; surface area A; projected area A_p; and edge length ε were determined for all clathrin coats, and the median value for each quantity is depicted as a dotted line. **a)** Imaging in 3T3 mouse fibroblast cells resulted in $N = 7$ cells and $n = 739$ structures analyzed. Medians calculated for each quantity are: $\theta = 121°$; $H = 0.010\,\text{nm}^{-1}$; $A = 84{,}104\,\text{nm}^2$; $A_p = 31{,}613\,\text{nm}^2$; and $\varepsilon = 505\,\text{nm}$. **b)** Imaging in U-2 OS bone osteosarcoma cells resulted in $N = 3$ cells and $n = 294$ structures analyzed. Medians calculated for each quantity are: $\theta = 103°$; $H = 0.010\,\text{nm}^{-1}$; $A = 68{,}988\,\text{nm}^2$; $A_p = 31{,}475\,\text{nm}^2$; and $\varepsilon = 578\,\text{nm}$. *Data, analysis, and figure generated by Aline Tschanz.*

I further investigated the characteristic propagation of all geometric quantities during endocytosis by plotting them against the closing angle θ (see Figure 3.22). All trajectories exhibited similar patterns to the data collected from SK-MEL-2 cells, with curvature H and surface area A increasing simultaneously during the process. To quantify these trajectories and compare them between different cell lines, the cooperative curvature model was fit to describe the propagation of curvature $H(\theta)$ (see Section 3.3). In agreement with what was described for SK-MEL-2, the cooperative curvature model approximated the data more accurately than the constant curvature or constant area model could. This held true for both, data extracted from 3T3 fibroblasts (see Figure 3.22a) as well as U-2 OS bone osteosarcoma cells (see Figure 3.22b).

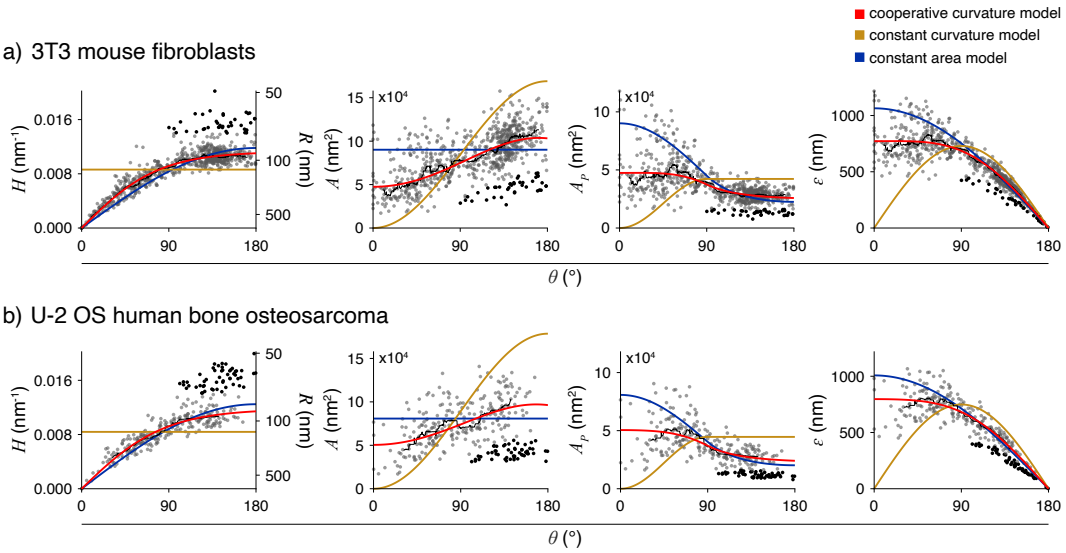


Figure 3.22 | Clathrin coat remodeling in different cell lines. Fit of the cooperative curvature model *(red)* to experimental data *(gray)*. Non-endocytic structures (see Section 3.2.6) excluded from the model fit are shown in black. The rolling median was calculated with an averaging window of 5% of the number of structures (black line). **a)** Curvature H calculated for clathrin coats imaged in 3T3 mouse fibroblasts can be more accurately approximated by the cooperative curvature model. The curvature cut-off for non-endocytic structures is set at $H_C = 0.014$ nm. The same curvature cut-off H_C and model parameter H_0 and γ are used to depict and model the surface area A; projected area A_p; and edge length ε propagation in 3T3 cells. **b)** The same analysis as shown in a), performed on clathrin-coated structures imaged in U-2 OS bone osteosarcoma cells. The same curvature cut-off $H_c = 0.014$ nm was applied. $N_{3T3} = 7$ cells; $n_{3T3} = 739$ structures, of which $n_{3T3} = 40$ structures are of non-endocytic origin. $N_{U2OS} = 3$ cells, $n_{U2OS} = 294$ structures, of which $n_{U2OS} = 53$ structures are of non-endocytic origin. Mathematical expression and extracted fitting parameters for 3T3 and U-2 OS cells are summarized in Table 3.1; 3.4; & 3.5, respectively. *Data, analysis, and figure generated by Aline Tschanz.*

The overlap between the cooperative curvature model and the experimental data of either cell line showed that this model indeed describes a generalizable mechanism of clathrin coat remodeling. Comparing the fit parameters between the different cell lines further showed that, while the trajectory of curvature and surface area is very similar, there are size differences in the structures that are thus produced. In the SK-MEL-2 data set, I observed a preferred curvature of $H_0 = 0.014\,\text{nm}^{-1}$ (corresponding to a radius of $R_0 = 72$ nm). 3T3 cells on the other hand approached a preferred curvature of $H_0 = 0.011\,\text{nm}^{-1}$ (radius $R_0 = 89$ nm), generating larger structures in comparison to SK-MEL-2. Similarly, the U-2 OS cells also produced larger structures of a preferred curvature of $H_0 = 0.012\,\text{nm}^{-1}$ (radius $R_0 = 85$ nm). The point of curvature initiation was similar across all three cell lines. The fraction of flat assembled surface area A_0 for SK-MEL-2 was $A_0 = 0.51$, while for U-2 OS cells a fraction of $A_0 = 0.52$ and for 3T3 cells of $A_0 = 0.45$ was calculated. For a summary of all fit parameters, see Table 3.4 and 3.5

		Fit result			
		Curvature $H(\theta)$	Surface area $A(\theta)$	Projected area $A_p(\theta)$	Edge length $\varepsilon(\theta)$
Constant area model	A_{CAM}	90,100 ± 1,000 nm^2	83,700 ± 1,000 nm^2	66,200 ± 1,000 nm^2	65,800 ± 1,000 nm^2
Constant curvature model	R_{CCM}	115.8 ± 1.5 nm	98.3 ± 0.7 nm	121.1 ± 2 nm	108.5 ± 1.5 nm
Cooperative curvature model	γ	(8.2 ± 0.1) 10^{-3} nm^{-1}	(7.8 ± 0.1) 10^{-3} nm^{-1}	(7.8 ± 0.1) 10^{-3} nm^{-1}	(7.9 ± 0.1) 10^{-3} nm^{-1}
	H_0	(11.3 ± 0.1) 10^{-3} nm^{-1}	(11.2 ± 0.1) 10^{-3} nm^{-1}	(11.2 ± 0.2) 10^{-3} nm^{-1}	(11.2 ± 0.2) 10^{-3} nm^{-1}
	R_0	88.8 ± 0.7 nm	89.3 ± 0.7 nm	89.5 ± 1.3 nm	89.1 ± 1.4 nm
	A_0	0.45	0.49	0.47	0.49
	k_{on}	89.3 nm$\tilde{s}^{-1}$	91.5 nm$\tilde{s}^{-1}$	105.5 nm$\tilde{s}^{-1}$	110.3 nm$\tilde{s}^{-1}$

Table 3.4 | Summary of clathrin coat growth model fits in 3T3 cells. The constant area, constant curvature, and cooperative curvature model parameters are fitted to four different features of the data: The curvature $H(\theta)$, surface area $A(\theta)$, projected area $A_P(\theta)$, and edge length $\varepsilon(\theta)$ calculated for all clathrin coats of endocytic origin (N = 7 cells, n = 699 structures). Fitting parameters include the constant area A_{CAM}; constant curvature H_{CCM}; curvature increase rate γ; preferred curvature H_0; preferred radius R_0; fraction of surface area grown flat A_0; and net clathrin coat growth rate k_{on} measured in nm per pseudotime units $\tilde{s}$. Model-fit equations are summarized in Table 3.1. *Data generated by Aline Tschanz, analysis performed by Aline Tschanz. Model expression developed by Prof. Dr. Ulrich S. Schwarz and Dr. Felix Frey.*

		Fit result			
		Curvature $H(\theta)$	Surface area $A(\theta)$	Projected area $A_p(\theta)$	Edge length $\varepsilon(\theta)$
Constant area model	A_{CAM}	80,800 ± 1,600 nm^2	76,900 ± 1,700 nm^2	65,400 ± 1,600 nm^2	65,900 ± 1,600 nm^2
Constant curvature model	R_{CCM}	119.1 ± 2.5 nm	101.6 ± 1.5 nm	122.8 ± 2.7 nm	115 ± 2.4 nm
Cooperative curvature model	γ	(7.9 ± 0.2) 10^{-3} nm^{-1}	(7.7 ± 0.2) 10^{-3} nm^{-1}	(7.9 ± 0.2) 10^{-3} nm^{-1}	(8.1 ± 0.2) 10^{-3} nm^{-1}
	H_0	(11.8 ± 0.2) 10^{-3} nm^{-1}	(11.5 ± 0.2) 10^{-3} nm^{-1}	(11.1 ± 0.3) 10^{-3} nm^{-1}	(11.0 ± 0.3) 10^{-3} nm^{-1}
	R_0	85.0 ± 1.8 nm	87.1 ± 1.7 nm	90.2 ± 2.6 nm	90.5 ± 2.7 nm
	A_0	0.52	0.52	0.47	0.45
	k_{on}	89.3 nm$\tilde{s}^{-1}$	91.5 nm$\tilde{s}^{-1}$	105.5 nm$\tilde{s}^{-1}$	110.3 nm$\tilde{s}^{-1}$

Table 3.5 | Summary of clathrin coat growth model fits in U-2 OS cells. The constant area, constant curvature, and cooperative curvature model parameters are fitted to four different features of the data: The curvature $H(\theta)$, surface area $A(\theta)$, projected area $A_P(\theta)$, and edge length $\varepsilon(\theta)$ calculated for all clathrin coats of endocytic origin (N = 3 cells, n = 241 structures). Fitting parameters include the constant area A_{CAM}; constant curvature H_{CCM}; curvature increase rate γ; preferred curvature H_0; preferred radius R_0; fraction of surface area grown flat A_0; and net clathrin coat growth rate k_{on} measured in nm per pseudotime units $\tilde{s}$. Model-fit equations are summarized in Table 3.1. *Data generated by Aline Tschanz, analysis performed by Aline Tschanz. Model expression developed by Prof. Dr. Ulrich S. Schwarz and Dr. Felix Frey.*

3.4 Clathrin coat remodeling over pseudotime

The entire analysis I presented so far relied on interpreting the closing angle θ as a proxy for endocytic progression. However, this parameter is not uniformly distributed in my data set (see Section 3.2.3). Instead, the data showed an enrichment at $\theta \approx 70°$ and an even stronger enrichment at $\theta \approx 135°$ (see Figure 3.21).

Due to the high throughput of the superresolution microscopy approach, a large data set of clathrin coats was obtained. Since I systematically collected all structures within each individual cell, I could confidently assume these irregularities to represent the dynamic variabilities of the process. Slowly progressing stages of endocytosis are over-represented in the data, while transient, short-lived structures are less frequently captured. This information could be used to reconstruct clathrin coat remodeling over pseudotime, asking the question of whether curvature is generated in a linear fashion, or if certain transitions require more time than others.

3.4.1 Reconstructing the pseudo-timeline of clathrin coat remodeling

To interpret the density of endocytic stages as clathrin coat lifetimes, I sorted all structures along their closing angle θ, with the rank of each structure corresponding to an arbitrary unit of time $\tilde{s}$. I chose a range of 0 to 1 and thus placed each structure at its relative time point in pseudotime. This, in effect, corresponds to a flattening out of the θ histogram into a uniform distribution of pseudotime (see Figure 3.23a).

With the help of Prof. Dr. Ulrich S. Schwarz and Dr. Felix Frey, the cooperative curvature model was further extended to incorporate this dynamic information. To this end, we assumed the net growth of the clathrin coat to occur via the edge of the lattice ε at a constant growth rate k_{on}. Thus, area growth depends on the edge length, and we could formulate Equation 3.5.

$$\frac{d}{dt}A = \dot{A} = k_{on}\varepsilon \tag{3.5}$$

This equation was solved to derive an expression for θ over time t, with a coat that starts out flat and then increases in curvature. (Equation 3.6)

$$\theta(t) = \sqrt{\frac{24\gamma k_{on}}{8\gamma^2 H_0^{-2} - 1}t} \tag{3.6}$$

As the clathrin coat approaches its preferred curvature, curvature generation is slowed down, represented by the square-root dependence of θ on time t. To fit this model to our data and determine k_{on}, I used the extracted values for H_0 and γ determined during the previous fit in θ (see Table 3.3 & 3.4). This resulted in a good approximation of the

θ trajectory over pseudotime, confirming the non-linear, cooperative effect underlying the mechanism of curvature generation during endocytosis (see Figure 3.23b).

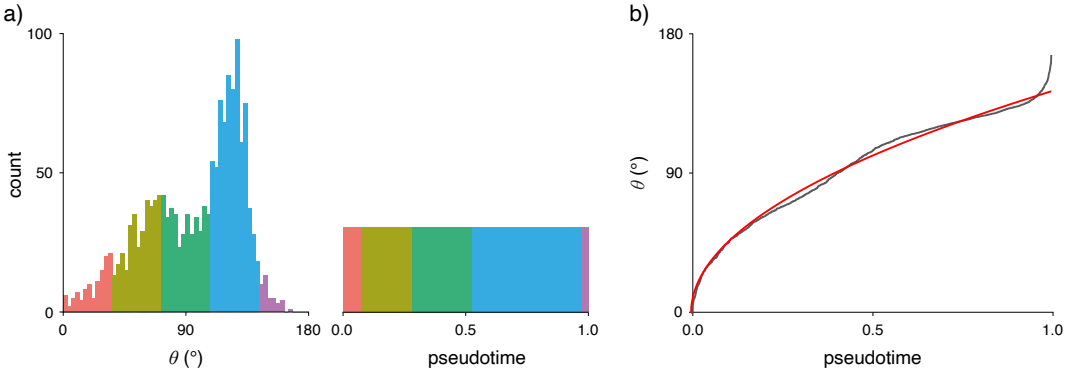


Figure 3.23 | Dynamic interpretation of the clathrin coat closing angle θ in SK-MEL-2 cells. **a)** To interpret the density of the closing angle θ in the data, I ranked all structures sorted in θ and assigned a pseudotime based on this rank ranging from 0 to 1 $\tilde{s}$. The pseudotime is now uniformly distributed in the data. **b)** Plotting the closing angle θ against pseudotime (gray) shows a non-linear correlation, indicative of dynamic variability in endocytic progression. This relationship can be approximated by the cooperative curvature model (red, see Equation 3.6), highlighting the square-root dependence of θ on time t. Fit parameters H_0 and γ were extracted from the fit in curvature $H(\theta)$, and all parameters are summarized in Table 3.3. $N = 13$ cells, $n = 1645$ structures. *Data generated by Dr. Markus Mund, Dr. Johanna L. Mehl, and Aline Tschanz, analysis and figure generated by Aline Tschanz.*

Plotting the coat geometries over their rank allowed me to visualize the trajectory of curvature H, surface area A, projected area A_p, and edge length ε over pseudotime (see Figure 3.24). The cooperative curvature model approximated these geometries well, and I could investigate the coat remodeling dynamics. These results showed that the curvature is acquired quickly within the first $\approx 10\%$ of the timeline (increase from $H(t = 0) \approx 0\,\mathrm{nm}^{-1}$ to $H(t = 0.1) \approx 0.007\,\mathrm{nm}^{-1}$), after which it increases at a slower rate, and almost comes to a halt for the last $\approx 40\%$ of the timeline towards vesicle scission at $H(t = 0) \approx 0.013\,\mathrm{nm}^{-1}$. During this time, the surface area increases almost linearly, doubling between the point of curvature initiation and vesicle scission, which reflected the previously mentioned fraction of flat area growth of $A_0 = 0.51$.

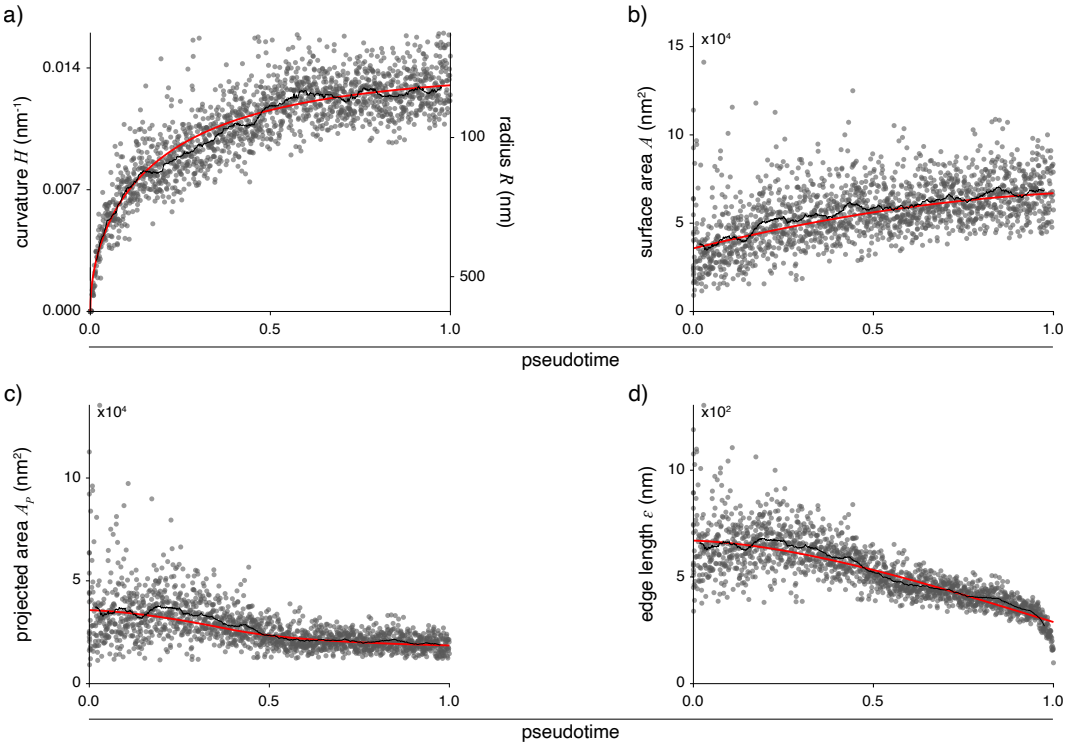


Figure 3.24 | Clathrin coat remodeling over pseudotime in SK-MEL-2 cells. The pseudotime was determined by ranking all structures sorted in θ from 0 to 1 and has an arbitrary unit of $\tilde{s}$. **a)** Curvature H is acquired quickly at the beginning of the process. The closer the clathrin coat curvature approaches the preferred curvature H_0 of the coat, the slower its increase until it almost plateaus towards the end of the process. **b)** Surface area A almost linearly increases until vesicle formation. **c)** Projected area A_p and **d)** edge length decrease during endocytosis. For all geometries, the cooperative curvature model (red) well explains the underlying data (gray). The rolling median is calculated with an averaging window of 5% of the number of structures (black line). For model fitting, the parameters H_0, γ and k_{on} were determined using the fit in curvature $H(\theta)$ and $H(t)$, as summarized in Table 3.3. $N = 13$ cells, $n = 1645$ structures. *Data generated by Dr. Markus Mund, Dr. Johanna L. Mehl, and Aline Tschanz, analysis and figure generated by Aline Tschanz. Model expression developed by Prof. Dr. Ulrich S. Schwarz and Dr. Felix Frey.*

I repeated this analysis also for the cell lines 3T3 and U-2 OS, to investigate potential cell-type specific differences. In Figure 3.25, the result of the pseudotime assignment and cooperative curvature model fit is shown (fit results summarized in Table 3.4 and 3.5). While the cooperative curvature model explains the trajectory of coat geometries over pseudotime well in each cell line, there are also some cell-type-specific differences in coat remodeling dynamics. These become most apparent when looking at the closing angle θ distribution for each cell line. We have discussed the two enrichments at $\theta \approx 70°$ and $\theta \approx 135°$ visible in SK-MEL-2 derived structures. A similar almost bimodal distribution is visible for 3T3 and U-2 OS. However, the positions of these enrichments vary. For 3T3 cells, they occur at $\theta \approx 50°$ and $\theta \approx 135°$, and for U-2 OS at $\theta \approx 60°$ and $\theta \approx 135°$.

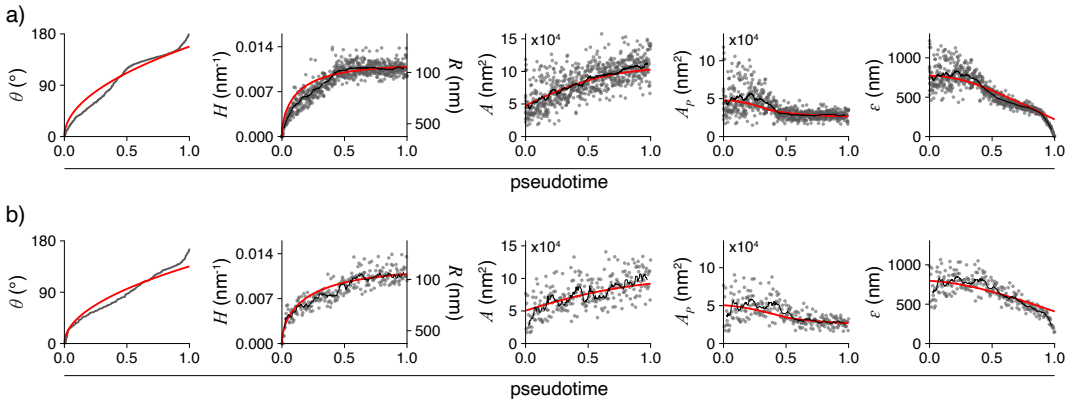


Figure 3.25 | Clathrin coat remodeling over pseudotime in 3T3 and U2OS cells. The pseudotime was determined by ranking all structures sorted in θ from 0 to 1 and has an arbitrary unit of $\tilde{s}$. The cooperative curvature model (red) well explains the relationship between θ and pseudotime, as described by Equation 3.6. Curvature H, Radius R, projected area A_p, and edge length ε are plotted over pseudotime. The rolling median is calculated with an averaging window of 5% of the number of structures (black line). **a)** Pseudotime analysis for 3T3 mouse fibroblasts. $N = 7$ cells, $n = 699$ structures. For model fitting, the parameters H_0, γ and k_{on} were determined using the fit in curvature $H(\theta$ and $H(t)$, as summarized in Table 3.4. **b)** Pseudotime analysis for U-2 OS human bone osteosarcoma. $N = 3$ cells, $n = 241$ structures. For model fitting, the parameters H_0, γ and k_{on} were determined using the fit in curvature $H(\theta$ and $H(t)$, as summarized in Table 3.5. *Data, analysis, and figure generated by Aline Tschanz. Model expression developed by Prof. Dr. Ulrich S. Schwarz and Dr. Felix Frey.*

As discussed at the beginning of this section, enrichments in θ indicate the slow progression of the overall process. The enrichment at $\theta \approx 135°$, consistent between all cell lines tested, indicated a stalling that occurs right before scission. At this stage, the curvature H of the clathrin coat was almost plateauing. The surface area, on the other hand, almost linearly increased until the very end of the process.

As this stalling represents a discrepancy from the square-root dependence on time assumed by the cooperative curvature model (see Equation 3.6), this stage is likely regulated by further, clathrin-independent factors. This could include the recruitment of dynamic, which is required to perform scission at the neck of the budding vesicle. Similarly, the second enrichment at lower closing angles θ could indicate an endocytic stage where additional factors need to be recruited, forming a checkpoint for endocytic progression.

3.4.2 Generating high-resolution averages of clathrin coats at distinct endocytic stages

To understand systematic changes in clathrin coat geometries, it can be useful to look at the average distribution of clathrin at distinct endocytic stages. By generating such high-resolution averages, random noise and labeling artifacts can be averaged out. Thus, I return to the original imaging data, using extracted model fit parameters to align and rescale structures at distinct pseudo-timepoints.

This approach shares certain similarities with the idea behind sub-tomogram averaging used in electron microscopy. Here, multiple orientations of the same image are aligned

and averaged to inform a high-resolution 3D reconstruction of the original structure. The difference in the here presented approach is that direct 3D information is already contained in the data. Additionally, rather than comprised of discrete categories of structures, the process of clathrin coat remodeling is dynamic. Thus we can directly align our 3D structures in space while considering their relationship over pseudotime.

To generate high-resolution averages from single-molecule localization data, all snapshots have to first be sorted along their closing angle θ. The data is then split into 10 equally sized bins, to generate 10 distinct averages, each average containing 164 structures. In each bin, all structures are rescaled to their mean radius and aligned in regards to their central coordinate as well as rotational angle. For each bin, a rotational average is then generated (see Section 6.2.6.4).

This workflow was computationally implemented by Dr. Yu-Le Wu and allowed the generation of rotationally symmetric averages for each bin, avoiding any artifacts from inhomogeneous labeling and deformed coats. The resulting image in Figure 3.26 shows the projected top views in xy and xz-slices of the developing clathrin coat, with each structure representing a highly-resolved average of the clathrin coat at distinct endocytic stages.

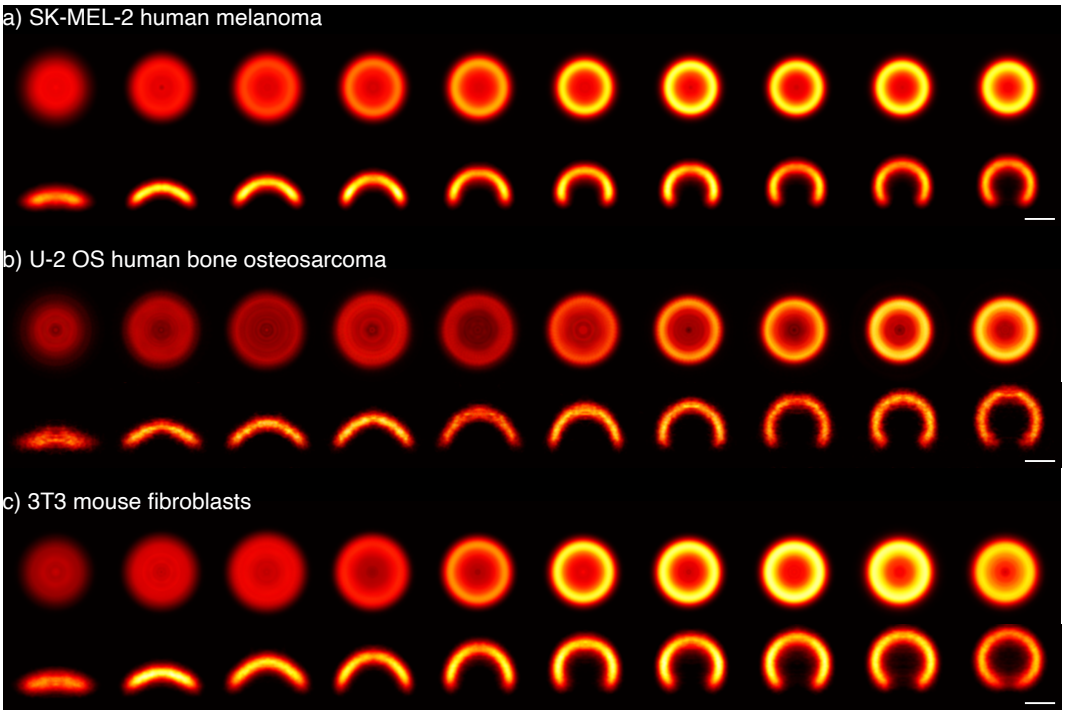


Figure 3.26 | High-resolution averages of clathrin coat remodeling in three different cell lines. **a)** Clathrin coat snapshots imaged in $N = 13$ SK-MEL-2 cells were sorted along their closing angle θ, and equally sized bins containing $n = 163$ structures were rescaled to their mean radius, aligned, and rotationally averaged. **b)** Clathrin coat snapshots imaged in $N = 3$ U-2 OS cells were sorted along their closing angle θ, and equally sized bins containing $n = 24$ structures were rescaled to their mean radius, aligned, and rotationally averaged. **c)** Clathrin coat snapshots imaged in $N = 7$ 3T3 cells were sorted along their closing angle θ, and equally sized bins containing $n = 68$ structures were rescaled to their mean radius, aligned, and rotationally averaged. Scale bars: 100 nm. *Data generated by Dr. Markus Mund, Dr. Johanna L. Mehl, and Aline Tschanz, analysis and figure generated by Aline Tschanz.*

The strong differences between the first five averaged structures indicated the fast initial curvature generation in the data. In comparison, the structures towards the final stages of the process do not differ much in curvature anymore. Instead, the coat is finalized by the addition of clathrin triskelia, visible as an increase in surface area A.

U-shaped clathrin coats have been previously described in the literature (Avinoam *et al.*, 2015; Akamatsu *et al.*, 2020). Should these structures be enriched at a certain endocytic stage, this should also be preserved in our data, as a U-shape is symmetric along the rotational axis over which we average. To ensure that my approach indeed preserves such geometries, Dr. Yu-Le Wu simulated a data set of U-shaped structures to analyze with our spherical cap model (see Figure 3.27a-c). While using a spherical model to describe a U-shaped structure created some additional errors in surface area A and radius R estimation (see Figure 3.27d), the overall geometry was preserved in the resulting average. As such shapes were absent in the data, and the microscopy averages appeared spherical at all stages, these structures were either absent or not frequent enough to manifest themselves in this analysis. In Section 5 I discuss further possibilities to quantify such structural deviations of the data from the spherical model.

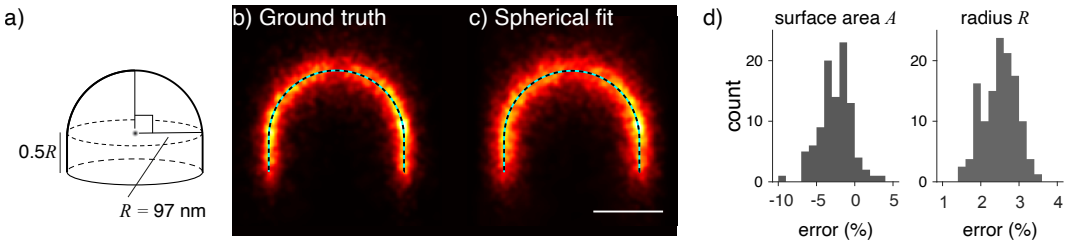


Figure 3.27 | Simulation and analysis of U-shaped clathrin coats. U-shaped geometries are preserved in high-resolution averaging based on a spherical model fit. **a)** The model for simulation is defined by a hemisphere with a specific radius of R = 97 nm. This was combined with a cylindrical model of the same radius R, with a height of $0.5R$. **b)** The simulated data of n = 100 structures were averaged based on the ground-truth model (cyan, dotted line). **c)** The same data analyzed and averaged based on a spherical model preserves the structure of the original U-shaped model (cyan, dotted line). **d)** Distribution of the normalized errors for surface area A (mean value of -2.6%) and radius R (mean value of 2.5%) estimation. Scale bar: 100 nm. *Data, analysis, and figure generated by Dr. Yu-Le Wu, adapted by Aline Tschanz.*

3.5 Towards a reconstruction of the entire endocytic machinery

As previously discussed, the non-uniform distribution of endocytic stages indicates a dynamic variability in the process of clathrin coat remodeling (see Section 3.2.3 & 3.4). Enrichment of certain stages during endocytosis seemed to require the recruitment of additional factors for their progression. This discovery was not surprising, as it is known that over 50 other endocytic components are involved in regulating and promoting this process (see Section 1.3.3). The adaptor protein 2 (AP-2) and dynamin-2 (DNM2) are two prominent and essential players during vesicle formation. AP-2 functions as a linker between clathrin triskelia, plasma membrane, and cargo molecules and is known to be present throughout the endocytic process. DNM2 is the scission protein that releases budding vesicles into the cytosol. It is therefore expected to be recruited towards the end of the process, while certain reports on DNM2 also have a regulatory function during earlier time points (Bhave *et al.*, 2020).

In this section, preliminary data showcases the potential of the here presented approach in investigating the recruitment of these additional proteins to the developing clathrin coat. Such investigations can provide insights into the molecular dynamics and functional aspects of such key players during endocytosis.

3.5.1 Using the clathrin coat as a structural and temporal reference

To understand when and where proteins are recruited to the developing clathrin coat, these targets need to be brought into the same spatial and temporal coordinate system.

To this end, I acquired dual-color superresolution images of clathrin together with the target of interest. By labeling clathrin with AF647 and the target protein with CF680, a ratiometric approach can be applied to assign the correct color to each localized fluorophore (see Section 1.5.2). After generating a sufficiently large data set, all clathrin coats were analyzed using the quantification pipeline described earlier (see Section 3.2). Thus, a

closing angle θ can be assigned to each dual-color snapshot. This allows the reconstruction of the target protein recruitment to the developing clathrin coat in pseudotime. Next, the geometric and spatial information extracted from the model fit can be used to align and rescale all structures and generate a high-resolution rotational average (see Section 3.4.2). This results in the reconstruction of the temporal and spatial recruitment pattern of the target protein to the developing clathrin coat. An additional advantage of this approach is the increased labeling efficiency in the averages. Getting a structure as densely labeled as the clathrin coat takes a lot of optimization, and is sometimes not possible due to the lack of appropriate dye combinations and delivery systems. However, as the model fit is not applied to the target protein, sparse labeling is not an analysis issue and can be improved by increasing the number of structures in the data over which averages are generated.

3.5.2 Dynamin-2 recruitment to the developing clathrin coat

As discussed in Section 3.4.1, the enrichment of at the closing angle $\theta = 135°$ most probably coincides with the recruitment of dynamin to the neck of the budding vesicle (Antonny *et al.*, 2016). When I reconstruct the high-resolution rotational averages of DNM2-GFP-CF680, the concentration of DNM2 at the vesicle towards the later stage of the process agrees with this hypothesis. However, some DNM2 specific signal is also detected during the earliest structures, as is visible from plotting the detected number of localizations for the DNM2 channel against the respective θ value (see Figure 3.29). While some of this signal can be the result of non-specific nanobody binding, it could further indicate the presence of this protein at all endocytic stages. This is an exciting confirmation of previous suggestions of DNM2 having a regulatory role already during early endocytosis (Bhave *et al.*, 2020). Despite these findings having to be further confirmed through the addition of careful controls, they further highlight the potential of this approach to infer the functions of proteins due to their structural and temporal organization within the endocytic machinery.

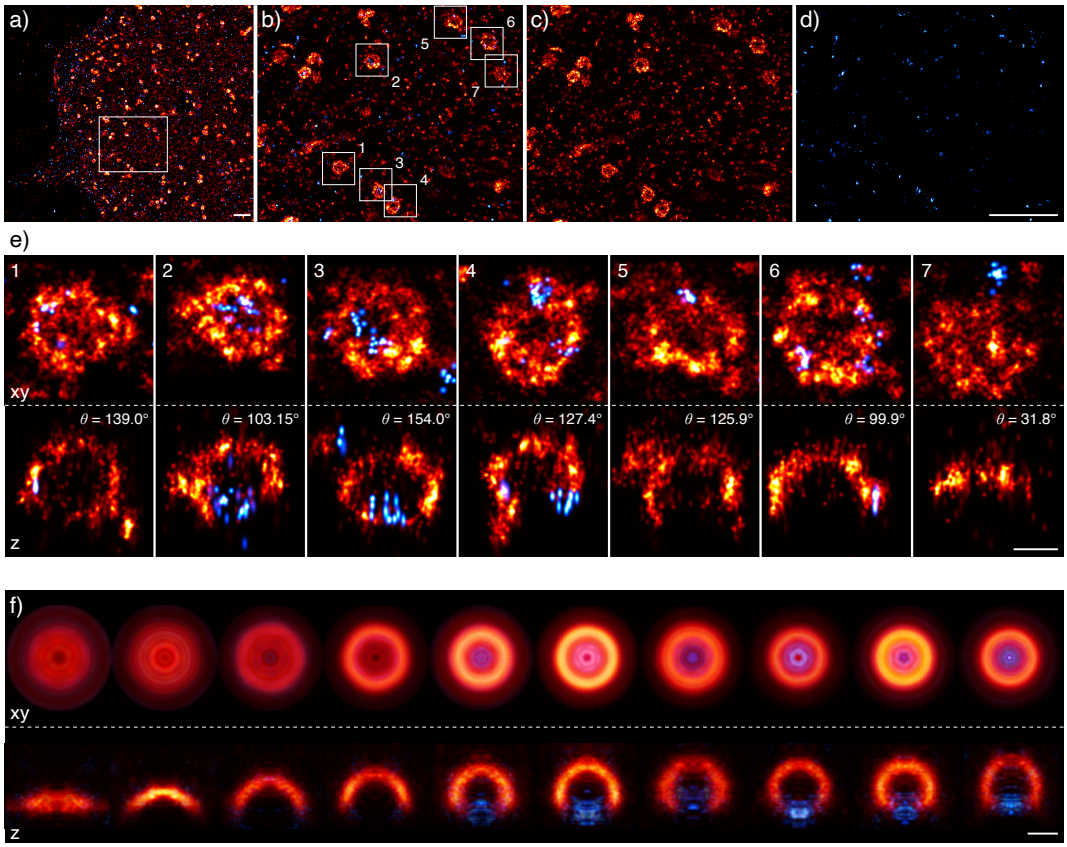


Figure 3.28 | Analysis of dynamin-2 recruitment to the developing clathrin coat. a) Dual-color image of clathrin immunolabeled with AF647 and dynamin-2-GFP labeled anti-GFP nanobodies conjugated to CF680. **b)** Enlarged region as indicated in a). **c)** Enlarged region as indicated in a), only showing clathrin signal. **d)** Enlarged region as indicated in a) only showing dynamin-2 signal. **e)** Selected structures as indicated in b), shown as xy projections or a 50 nm wide z-slice. Results for the closing angle θ, as extracted from the geometric model fit with LocMoFit are shown. **f** Rotational averages generated for distinct endocytic sites show recruitment of dynamin-2 to the developing neck of the clathrin coat. N = 1 SK-MEL-2 cell, n = 72 structures. Scale bars: a), 1 µm; d), 1 µm; e), 100 nm; f), 100 nm. *Data, analysis, and figure generated by Aline Tschanz*

.

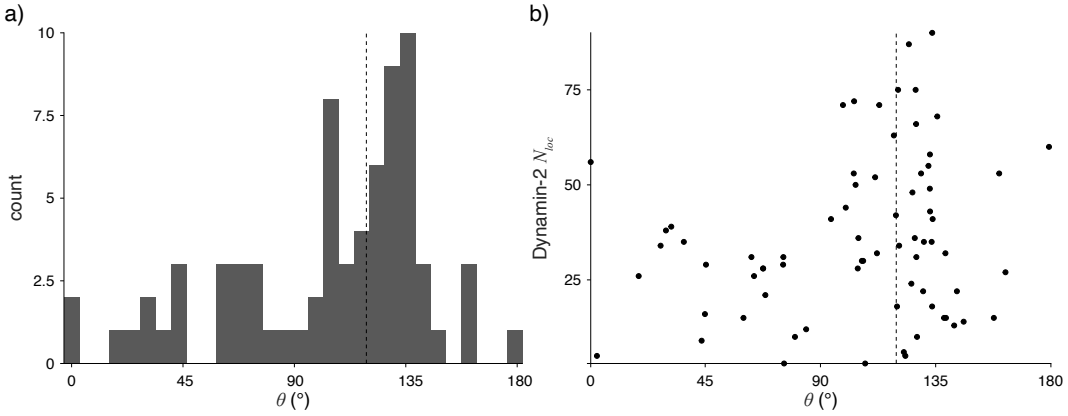


Figure 3.29 | Dynamin-2 is increasingly recruited at enriched endocytic stages. a) Distribution of closing angle θ extracted from clathrin coats imaged together with dynamin-2. Enrichment at 135° can be seen as described previously (see Section 3.2.3). Median is calculated at 119° (dotted line). **b)** For each structure, the number of localizations retrieved from the dynamin-2 channel is plotted against their respective closing angle θ values. For reference, the median at 119° is shown again (dotted line). A constant level of dynamin-2 is detected for all structures. Around the enrichment at 135°, an increased number of sites show an increased number of dynamin-2 specific localizations. This indicates that the enrichment represents a stalling during which clathrin coats accumulate dynamin-2. N = 1 SK-MEL-2 cell, n = 72 structures. *Data, analysis, and figure generated by Aline Tschanz*

.

3.5.3 AP-2 recruitment to the developing clathrin coat

As AP-2 is an essential nucleator of the endocytic process, linking clathrin to the relevant cargo and membrane (structure resolved in Kovtun *et al.*, 2020). It is thus expected to be present throughout the endocytic process, forming a layer just below the clathrin coat. By labeling the β-subunit of AP-2 with CF680 using indirect immunolabeling, this could be confirmed as AP-2-specific signals could be detected at each endocytic stage.

In single snapshots, the AP-2 signal appears more sparse in comparison to the dense clathrin labeling. This can mainly be attributed to the labeling approach applied. While clathrin was redundantly labeled with polyclonal antibodies for both subunits, AP-2 was labeled with a monoclonal antibody against a single epitope on the σ-subunit. Together with imperfect labeling efficiency, this leads to a smaller fraction of AP-2 being detected compared to clathrin. When averaging these structures based on the model fit in the clathrin channel, this decreased labeling should average out and the distribution of AP-2 at a layer just below the clathrin coat should still be visible.

However, when looking at these averages, the AP-2 signal appears more diffuse than the clear coat visualized for clathrin. This can have multiple reasons: First of all, for CF680 we observe lower localization precision than AF647 (see Figure 3.30), leading to a lower resolution when imaging this structure (see Section 1.5.3). Second, applying the model fit directly to the clathrin data leads to an optimal alignment of different clathrin coats, which might not be ideal for the AP-2 structure. Slight registration errors between the two color channels could result in a misalignment of the two structures. Future investigations

could resolve this by applying a spherical fit to highly resolved AP-2 structures, possibly labeled with AF647 to increase resolution. Lastly, the AP-2 β-subunit is recognized at an epitope located at the appendage of this structure. This appendage is connected to the body of the AP-2 complex via a flexible linker, which could introduce sufficient variability to blur the averaged structure of the AP-2 coat. This could be improved in future studies by directly tagging an AP-2 subunit, such as σ-subunit located at the core of the complex.

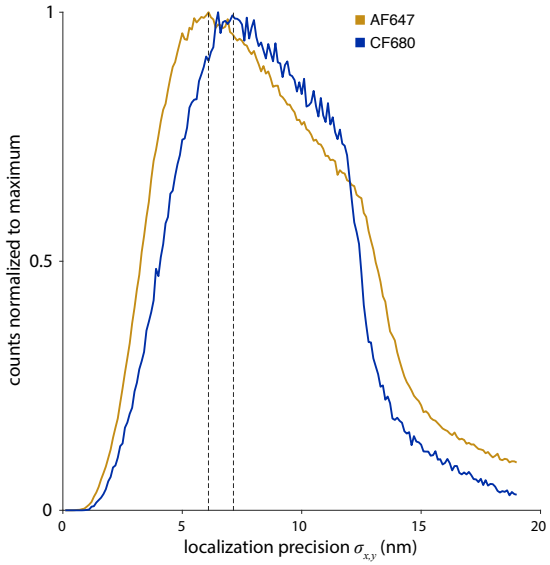


Figure 3.30 | Localization precision determined for AF647 and CF680. SK-MEL-2 cells were immunolabeled for clathrin with AF647, and for the *sigma*-subunit of AP-2 was with CF680. Statistical analysis of these dual-color images shows an improved localization precision σ for AF647 compared to CF680. N = 4 SK-MEL-2 cells, n = 183 structures. *Data, analysis, and figure generated by Aline Tschanz*

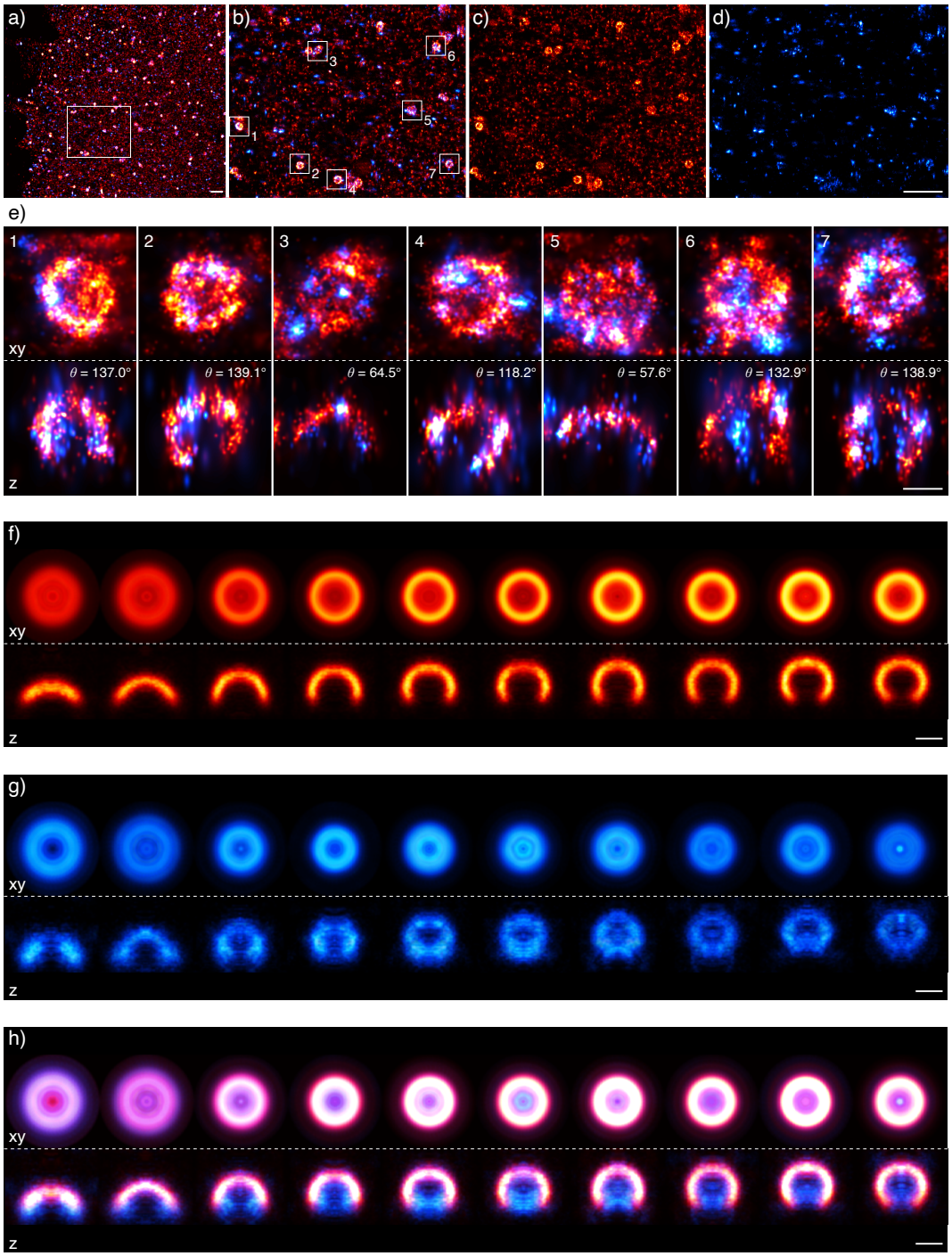


Figure 3.31 | Analysis of AP-2 recruitment to the developing clathrin coat. a) Dual-color image of clathrin immunolabeled with AF647 and the σ-subunit of AP-2 immunolabeled with CF680. **b)** Enlarged region as indicated in a). **c)** Enlarged region as indicated in a), only showing clathrin signal. **d)** Enlarged region as indicated in a) only showing AP-2 signal. **e)** Selected structures as indicated in b), shown as xy projections or a 50 nm wide z-slice. Results for the closing angle θ, as extracted from the geometric model fit with LocMoFit are shown. **f-h** Rotational averages generated for distinct endocytic sites show recruitment of AP-2 throughout the endocytic process. While clathrin forms a clear coat (f), AP-2 resutls in a more blurred structure (g). Overlap of both signals can be seen in h). N = 4 SK-MEL-2 cell, n = 183 structures. Scale bars: a), 1 µm; d), 1 µm; e), 100 nm; f-h), 100 nm. .

3.6 Contributions

The data presented here are the result of fruitful collaborative efforts. As it might be difficult to tease apart the individual contributions, they are listed here again.

The project was originally conceived by Dr. Markus Mund and Dr. Ori Avinoam in 2017, affiliated at the time with EMBL Heidelberg, under the guidance of Dr. Jonas Ries and Dr. Marko Kaksonen. Dr. Markus Mund and Dr. Johanna L. Mehl performed initial experiments and provided proof-of-principle for studying the ultrastructure of clathrin in mammalian cells using SMLM.

My contribution to the project started in 2019. By re-curating and reproducing the previously acquired data under various conditions, I helped optimize the robustness of sample preparation and data acquisition. An essential part of this work was the development of an accurate and robust quantification pipeline. The model-fitting framework LocMoFit, developed by Dr. Jonas Ries and Dr. Yu-Le Wu, enabled this analysis. I applied this framework, using a spherical cap model postulated by Dr. Jonas Ries and Dr. Yu-Le Wu, to data generated by Dr. Markus Mund, Dr. Johanna L. Mehl, and myself. I provided 6 imaged SK-MEL-2 cells, while Dr. Johanna L. Mehl under the supervision of Dr. Markus Mund provided 7 to the final data set. Through repeated application and testing of LocMoFit on this final data set, I helped Dr. Yu-Le Wu in his optimization of this pipeline to SMLM clathrin data. This resulted in numerous iterations for model fit optimization between me and Dr. Yu-Le Wu.

Dr. Yu-Le Wu further performed all simulations to ensure the robustness of LocMoFit.

I performed all data acquisition, curation, and analyses of clathrin-coated structures in U-2 OS and 3T3 cell lines.

The cooperative curvature model was developed by Prof. Dr. Ulrich S. Schwarz (Heidelberg University) and Dr. Felix Frey (Institute of Science and Technology, Klosterneuburg), with conceptual input by Dr. Markus Mund, Dr. Jonas Ries, and me. The Bayesian information criterion was calculated by Prof. Dr. Ulrich S. Schwarz and Dr. Felix Frey.

I used R to fit all clathrin coat growth models to the SMLM data, according to suggestions by Dr. Felix Frey.

All dual-color images were generated, curated, and analyzed by me.

Throughout the entire project, I received input from Dr. Markus Mund.

The study was supervised by Dr. Jonas Ries.

4 | Discussion

In this study, I set out to investigate how the protein assembly created during clathrin-mediated endocytosis can reshape the underlying membrane into a spherical vesicle. While we have a thorough understanding of the components involved in this process and the sequential order of their recruitment, the underlying mechanism by which the deformation of the plasma membrane is achieved remains elusive. Contradictory interpretations of *in situ* and *in vitro* findings result in different geometric conceptualizations of the process, which suggest different mechanistic consequences. The reason why it has been difficult to converge on a single, experimentally well-supported model of clathrin coat growth can be found in the small size of the generated structures (≈80 nm), and the fast dynamics at which structural changes occur (≈80 s). To this day, no imaging tool provides sufficient spatial and temporal resolution to directly visualize the nanoscale dynamics of clathrin-mediated endocytosis.

While an ideally suited microscopy method does not yet exist, generating a large data set at high spatial resolution offers the possibility of reliably reconstructing the coat dynamics from static images, under the assumption that all images represent snapshots of the same pathway. To do so requires an imaging approach that offers high spatial resolution at high throughput, directly visualizing the 3D organization of clathrin-coated structures. In this study, I propose a superresolution microscopy approach that fulfills these requirements. Single-molecule localization microscopy is capable of resolving the geometries of clathrin coats while retaining important advantages inherent to fluorescence microscopy. These advantages include high throughput, molecular specificity, and signal contrast.

Importantly, SMLM provides direct 3D information, which can be used to accurately estimate the geometric properties of the coat. To do so, I helped to develop LocMoFit, a computational tool to robustly fit geometric models directly to 3D pointillist localization data. This analysis approach allowed us to robustly estimate the geometric parameters of the clathrin coats by approximating these structures as a spherical cap, fully described by its radius r and closing angle θ.

4.1 Investigating geometric changes of the clathrin coat

In this work, I visualized the 3D architecture of 1798 clathrin-coated structures *in situ* using SMLM. This approach allowed me to densely sample the endocytic timeline with randomly arrested snapshots of clathrin coats. By precisely resolving the 3D architecture, I could robustly estimate the geometric parameters of the imaged structures using LocMoFit (Wu *et al.*, 2023), and subsequently sort them along the endocytic progression.

Similar to previous reports, I observed a diverse set of coat curvatures within the SMLM data set, ranging from shallow, to domed, to completely spherical structures (Heuser, 1980; Avinoam *et al.*, 2015; Sochacki *et al.*, 2021). The crucial addition of my results to the current literature lies in the comparably large data set combined with direct 3D information. This methodological advantage allowed me to perform a detailed investigation of geometric changes in the clathrin coat during endocytic progression.

Thus this data enables the testing of different clathrin coat growth models currently discussed in the literature.

4.2 Clathrin coat growth models

Conventionally, there are two main clathrin coat growth models discussed: The constant curvature and the constant area model (Kaksonen and Roux, 2018; Chen and Schmid, 2020).

According to the constant curvature model, our data is expected to show no correlation between curvature and endocytic progression (closing angle θ). The mechanistic basis of this model is that the polymerization of intrinsically curved triskelia suffices to provide the necessary energy for membrane bending. This observation was initially supported by *in vitro* studies which observed the spontaneous curvature generation by a minimal endocytic machinery (Woodward and Roth, 1978; Zaremba and Keen, 1983; Pearse and Robinson, 1984). To arrange into a flat lattice, clathrin triskelia form hexagonal faces. Curved structures, however, were shown to be enriched for pentagonal faces. It was thus argued that it is energetically much more favorable for clathrin to directly arrange itself into pentagonal faces within a curved structure, instead of transforming hexagons into pentagons (Kirchhausen, 1993). As the data presented here clearly show an increase in curvature during endocytic progression, the polymerization of clathrin into a pre-bent coat seems to be an unlikely approximation of the mechanism as it occurs within a cellular context.

According to the constant area model, a clathrin coat has to grow to its final surface area A value to be able to initiate and increase curvature. The mechanistic basis is that curvature acquisition of the coat drives membrane bending through structural remodeling. This structural remodeling was initially suggested to cause the transformation of hexagons to pentagonal faces (Kanaseki, 1969; Heuser, 1980). The constant area model agrees well

with the observed increase of curvature, as it suggests a remodeling of flat to curved coats. However, the puristic interpretation of this approximation requires flat assembly to the very final coat area, which disagrees with the observed increase in surface area A reported here.

Taken together, neither of these conventionally discussed models is fully able to explain the data I presented in this study. Instead, the observed geometric behavior can be described as an initial flat pre-assembly, followed by a flat-to-curved transition and subsequent curvature increase. This agrees well with recent findings, which report an alternative interpretation of the constant area model where clathrin polymerization and curvature increase can occur simultaneously (Bucher *et al.*, 2018; Scott *et al.*, 2018; Nawara *et al.*, 2022).

4.3 Membrane bending according to the cooperative curvature model

To explain our observation on the geometric behavior of clathrin coats, we formulated a new clathrin coat growth model called the cooperative curvature model (see Section 3.3.

This model considers the transition from an initially flat to an increasingly curved coat and assumes changes in curvature to occur over the entire coat area. Curvature initiation is interpreted as a consequence of the cooperative behavior of multiple triskelia, with the tendency of the coat to bend increasing with the number of molecules assembled into a flat structure. Once initiated, the curvature is then assumed to increase asymptotically towards a preferred curvature H_0.

Once coat curvature H approaches H_0, curvature saturates, while the surface area keeps increasing to finalize the vesicular structure. It can thus be argued that H_0 sets the final size of clathrin-coated vesicles. There are various factors that could influence this parameter. Firstly, the ultrastructure of clathrin triskelia reveals a pucker angle at the vertex of the complex. It has thus been speculated that, due to their intrinsic curvature, triskelia exhibit a preference to position themselves into a curved structure. Indeed, *in vitro* assays have shown that clathrin spontaneously arranges itself into spherical barrels, with comparably little size variation. The homogeneity of the structures formed further suggests an intrinsic preference for a specific curvature value by these molecules (Wood and Smith, 2021).

When comparing clathrin coats generated *in vitro* and *in situ*, it becomes apparent that in a cellular context, clathrin can form more diverse and larger structures (Saleem, 2015). H_0 *in vivo* is thus not only determined by the intrinsic curvature of clathrin triskelia themselves but modified by further factors such as additional endocytic proteins and mechanical cell surface properties. This notion is further supported by the variable values extracted for H_0 for different cell lines (see Table 3.3; 3.4; & 3.5). Different cell types are known to express variable cell surface properties and membrane composition, thus explaining the variable sizes and H_0 determined for clathrin-coated structures.

4.4 Flat clathrin pre-assembly

Using the imaging and analysis pipeline presented in this work, I was able to image hundreds to thousands of clathrin-coated structures in an automated and minimally biased fashion. This resulted in a dense and homogenous sampling of the endocytic trajectory. I then used the closing angle θ as an indicator of endocytic progression to sort clathrin coats in increasing order of maturity. Because of the uniform sampling of the process, the speed of vesicle maturation at each endocytic stage can be assumed to be inversely proportional to the number of samples that are present at each θ angle (see Section 3.4). Transient stages are assumed to be observed less frequently, while slowly progressing stages resulted in an enrichment in the θ distribution.

While this approach works well for later stages of clathrin-mediated endocytosis, the early stages where clathrin coats are smaller and nearly flat are harder to sort along the endocytic progression. Here, the model would assign a closing angle θ close to zero to all flat structures irrespective of their size, sorting them close to the same time point. A more appropriate parameter to reconstruct flat assembly would thus be the increasing surface area. However, this would neglect the size variability across clathrin-coated structures *in vivo* and represent an unreliable proxy for endocytic progression.

In practice, however, it turned out that there was a very low prevalence of flat structures (<1%) in the data, indicating that any sorting errors are negligible. Additionally, I observed that even the earliest coats already measured already half the surface area of the final vesicles ($A_0 = 0.51$). I am thus likely not capturing the earliest flat assembly during clathrin-mediated endocytosis with my approach.

There are various reasons why flat assembly seems to evade detection by SMLM. One explanation is that the initial accumulation of clathrin to half the surface area happens so quickly that there are simply no representative structures in our dataset. However, there could also be several technical reasons to explain this phenomenon.

Firstly, early flat structures might be simply too small to be reliably distinguished from unspecific antibody clusters which are routinely observed in SMLM images of immuno-labeled structures (see Figure 3.3). Additional imperfect, sub-stoichiometric labeling (see Figure 3.10) could further limit the detectability of already small structures.

Further, initial assemblies might comprise a loose network of triskelia, that are not tightly interacting, with vacancies and defects within the lattice (Frey *et al.*, 2020; Sochacki *et al.*, 2021). These interactions might be less well stabilized by chemical fixation and could thus be lost during sample preparation. However, small flat structures are also rarely observed in electron microscopy images (Avinoam *et al.*, 2015; Bucher *et al.*, 2018; Sochacki *et al.*, 2021), which employ a different fixation process. As these approaches do not suffer the same technical limitations, reduced fixation efficiency seems a more unlikely explanation for the rarity of small flat structures.

However, coat defects and vacancies could also result in flat lattices containing a smaller density of triskelia and thus result in even more sparse labeling. The lower number of target molecules within the flat structures would explain why it is more difficult to observe them, both in electron microscopy (lower protein density) and SMLM (less signal per coat area). Interestingly, the loose assembly of clathrin has been proposed as a structural requirement for flat sites. As soon as clathrin organizes into a more dense and rigid conformation, coat stiffening could lead to the induction of curvature since it is energetically more stable. This has been previously proposed as a mechanism underlying the flat-to-curved transition (Frey and Schwarz, 2020).

While we might miss smaller flat structures due to their transient nature and potential technical limitations, also larger completely flat structures are rare. This agrees with the observations made by Heuser using electron microscopy (Heuser, 1980), where he described even the most shallow structures to already contain small degrees of curvature. This suggests that curvature acquisition is a fast process, and flat clathrin coats represent a meta-stable structure with the built-in capacity to generate curvature. This agrees with recent findings that report flat structures store elastic energy, and relaxation thereof drives initial coat bending (Tagiltsev *et al.*, 2021). This flat-to-curved transition has been observed to occur spontaneously, without the need for additional energy sources or the recruitment of other endocytic factors (Sochacki *et al.*, 2021).

4.5 Abortive events

Previous studies have identified the generation of curvature to be a critical factor for coat maturation, as failure to do so results in abortive events (Aguet *et al.*, 2013; Loerke, 2009; Mettlen, 2009; Bucher *et al.*, 2018). These abortive events are characterized by live-cell fluorescence imaging as shorter-lived sites (<20 s) than what would be expected to successfully internalize cargo. Additionally, they never become as bright as mature coats detected right before scission (Taylor *et al.*, 2011; Liu *et al.*, 2010a), thus likely failing to recruit sufficient coat material to mature and undergo scission.

Under the assumption that abortive events do not differ mechanistically from *bone fide* clathrin structures, my analysis approach does not allow for the detection of these events. However, as abortive events can be considered short-lived, small, and never acquiring significant curvature, it is likely that I capture them only rarely in the data set (see Section 4.4). The earliest structures in the data are already half the final area size, and only a very small number of them are completely flat (<1%). Thus, abortive events are likely to have a negligible impact on my analysis.

4.6 Further mechanistic interpretations of the cooperative curvature model

The data presented here strongly suggest a transition from flat lattices to increasingly curved coats. While this has been observed previously, with orthogonal methods (Bucher *et al.*, 2018; Avinoam *et al.*, 2015; Sochacki *et al.*, 2021; Scott *et al.*, 2018; Nawara *et al.*, 2022), it is curious to speculate on the underlying mechanism that drives this structural rearrangement.

It was initially suggested that a transformation of hexagonal to pentagonal faces results in structural changes that generate local curvatures which then propagate over the entire coat area (Heuser, 1980; Kanaseki, 1969). This transformation requires the breaking and re-forming of existing bonds between triskelia, a process that is considered energetically costly and thus unfavorable (Nossal, 2001; Kirchhausen, 1993). However, this hypothesis describes flat clathrin coats as tightly interwoven, strictly hexagonal structures. Instead, if flat coats represent flexible structures, with loosely bound triskelia, the energetic barrier for structural remodeling into a curved coat could be significantly decreased. As a consequence, loosely bound triskelia have the possibility to orient themselves more freely within the lattice, potentially forming pentagons also in flat coats. This notion is supported by findings by electron microscopy that report the presence of vacancies and disordered connections within flat clathrin coats (Sochacki *et al.*, 2021; Frey *et al.*, 2020).

There are additional factors that might contribute to a flat-to-curved transition *in vivo*. These include the removal of flattening forces (Sochacki *et al.*, 2021), relaxation of elastic energy within the coat (Tagiltsev *et al.*, 2021), conformational changes of triskelia upon clathrin light chain binding (Obashi *et al.*, 2023; Dannhauser, 2015), and filling up vacancies and mending the clathrin lattice (Frey *et al.*, 2020; Sochacki *et al.*, 2021). If we consider very low energetic barriers for structural re-arrangements, curvature could also be a stochastic effect of a few triskelia arranging themselves spontaneously into pentagonal structures, nucleating local curvature. As clathrin has been shown to exhibit a preference for curvature, local curvature could allow triskelia to relax into an energetically more favorable geometry and form tighter interactions. This could lead to a cascade of solidification of triskelia interactions throughout the lattice, resulting in a stiffening of the coat and propagation of curvature (Frey and Schwarz, 2020).

This hypothesis is consistent with our observation of a rapid initial increase in curvature, followed by a plateauing. As soon as the curvature is initiated, it becomes increasingly favorable for triskelia to establish strong bonds within the increasingly curved coat. This drives the entire coat towards its preferred curvature, overcoming any force that resists deformation, such as membrane tension or other flattening forces. During this process, it can be assumed that more and more coat vacancies are filled up, and more and more tight interactions are realized until no clathrin-clathrin binding site remains available and

the coat becomes saturated. Once it is saturated and the preferred curvature is achieved, other energetic factors might come into play in completing the structure.

Such factors could comprise other endocytic components being recruited to the endocytic site (see Section 4.8.1). Proteins of the BAR domain family, for example, have been shown to preferably arrange themselves at the edge of the coat, where they are thought to stabilize curvature generated by the coat or recruit necessary regulatory and force-generating proteins to the endocytic site. Actin is known to be a significant force contributor in yeast, and recent studies suggest that it also plays a crucial role in finalizing clathrin-mediated endocytosis in mammalian cells (Akamatsu *et al.*, 2019; Kaplan *et al.*, 2022).

Additionally, while curvature eventually saturates over pseudotime, the coat area almost linearly increases towards the very end of the process (see Figure 3.24 & 3.25). Thus, while clathrin polymerization might not suffice to bend the plasma membrane from the beginning, as suggested by the constant area model, it could provide the relevant energy to finalize the vesicular structure.

Further experiments are necessary to test the here listed speculations on force generation during endocytosis (see Section 5).

4.7 Cellular consequences of the cooperative curvature model

As mentioned previously (see Section 1.3 & 1.3.3), the clathrin-mediated endocytosis machinery is highly conserved across cell types, tissues, species, and mechanical environments. Even within a single cell, it has to have the ability to adapt to changing membrane properties during for example migration (Tsygankova and Keen, 2019; Rappoport and Simon, 2003). Equipped with new mechanistic insights generated in this work, it is interesting to hypothesize on the structural consequences of this adaptability.

Ultimately, the clathrin-mediated endocytosis machinery has to provide the necessary energy to counteract the resistance of the membrane to deformation. As discussed above, this energy seems to be initially provided by the acquisition of curvature by the clathrin coat through a cooperatively generated flat-to-curved transition. It has been suggested that an increase in membrane tension may cause endocytosis to stall at the stage of curvature generation (Bucher *et al.*, 2018), indicating that there may be structural consequences if the membrane's resistance to deformation were to increase.

While the membrane-tension increase might stall curvature generation, the ability to polymerize into a flat lattice should be unaffected. Thus, clathrin might continue to assemble into a flat lattice. Thus, the continued polymerization of clathrin could represent an adaptive mechanism that allows the endocytic site to recruit sufficient material to overcome the increased membrane tension by increasing the cooperative effect within the lattice. Once curvature is initiated, it will follow the same trajectory as for smaller membrane tension. As a consequence, the flat-to-curved transition would occur in a larger area. Following the same mechanism of curvature increase and saturation, this

might result in a larger final vesicle. This would explain the size variability observed across cell types, as described above (see Section 4.3).

4.8 Limitations of the cooperative curvature model

The cooperative curvature model describes our SMLM data better than both previously proposed models (see Section 3.3.1). It suggests cooperativity between triskelia to be the driving factor behind curvature generation, leading to a flat-to-curved transition at approximately half the final coat area.

While the good fit of the model to the underlying data is encouraging, it exhibits certain limitations worth mentioning.

4.8.1 Other endocytic components

The cooperative curvature model suggests a monotonous increase of curvature during endocytosis, which is solely promoted by increasingly many triskelia cooperatively interacting. It hereby considers geometric changes within the clathrin coat, and how they propagate over pseudotime but does not necessarily reflect the multitude of different factors involved in the process.

Apart from triskelia themselves, clathrin-mediated endocytosis can be modulated by various other proteins as well as the mechanical environment of the cell. Over 50 proteins have been found to participate in this process (cite). When comparing the results between different cell lines (see Table 3.3; 3.4; & 3.5), I observe cell-type specific differences in the fitted parameters, such as the preferred curvature H_0. While the cooperative curvature model can capture these differences, it does not allow further mechanistic insights into the possible causes thereof.

There are various possibilities by which other endocytic proteins could influence the dynamics of membrane bending by the clathrin coat. These include proteins of the BAR domain family, which are known to be recruited to the endocytic site (Daumke *et al.*, 2014). BAR proteins are of crescent shape, with an affinity for membranes with similar curvatures, and are known to function as curvature sensors, stabilizers, and initiators (Qualmann *et al.*, 2011). At high concentrations, these proteins are capable of inducing curvature and creating membrane tubules (Mim, 2012). At more physiological levels, they show an affinity for curved membranes and were suggested to function as a recruiter for other components, such as dynamin, delivering them to the various degrees of membrane curvature generated during endocytosis (Itoh, 2005; Neumann and Schmid, 2013).

Dynamin itself provides the mechanical function for vesicle scission towards the end of the endocytic process (Antonny *et al.*, 2016). Dual-color data of dynamin and clathrin shows that the enrichment of dynamin coincides with enrichment in closing angle θ (see Figure 3.29). This suggests that stalling of endocytosis at $\approx 135^\circ$ is regulated by dynamin recruitment, and only once sufficient dynamin has been collected can the

process proceed. However, the dual-color data further suggest the presence of dynamin at lower concentrations throughout the entire endocytic process. While this observation has to still be validated, and controlled for unspecific signals, it supports the previously proposed regulatory role of dynamin during early endocytosis (Bhave *et al.*, 2020).

Collectively, these factors may account for the discrepancies between the simplified cooperative curvature model and the experimental findings. It is believed that dynamin rapidly catalyzes scission and the subsequent release of the budding vesicle once it has accumulated at the vesicle neck. This idea is consistent with the observed deviation between the cooperative curvature model and the experimental data at the final stage of the process (refer to Figure 3.23). Additionally, the model does not anticipate the observed enrichment.

Taken together, these considerations highlight the complex nature of the endocytic machinery. While clathrin coat growth models allow for the conceptualization of this process, and enable targeted hypothesis generation and testing, they still greatly simplify the process of membrane bending by the clathrin coat.

4.8.2 Assumption of a single endocytic pathway

My imaging and analysis approach does not capture any direct temporal information on clathrin-mediated endocytosis. Instead, I infer the dynamics of this process from the static snapshots of clathrin coats, reconstructed along their closing angle θ. Thus, the reconstruction over endocytic progression represents the average trajectory of clathrin coat remodeling, generated from many individual endocytic snapshots.

Previous studies have reported the co-existence of multiple distinct mechanistic pathways within a single cell (Scott *et al.*, 2018; Nawara *et al.*, 2022). As I am generating a single average trajectory for clathrin coat remodeling, it is possible that pathways with distinct mechanisms are averaged out. However, distinct pathways such as the constant curvature and constant area model are expected to show different geometric behaviors, which could result in the presence of subpopulations following separate geometric trajectories. This is not the case for most structures in the data set, where a strong correlation between θ and H suggests a single, stereotypic pathway. Our data can therefore not be explained by simply mixing the two previously proposed models.

However, I do observe a small number of relatively small structures that are disconnected from the stereotypical trajectory of curvature generation during endocytosis. Further experiments suggested that this point cloud is formed by structures generated through endocytosis-independent mechanisms (see Section 3.2.6). This provides evidence that mechanistically distinct pathways are discernable within our data.

Live-cell data from mammalian cells suggests a high degree of stochasticity in clathrin-mediated endocytosis, with single events strongly varying in their duration. Also in the

data here, the variation of curvature $H(\theta)$ indicates a structural diversity of the process, even within single cells of the same tissue origin.

While the approach I present in this work might be sensitive enough to distinguish between endocytic and non-endocytic clathrin coats, it still represents an averaged view of a heterogenous process. Thus, more subtle mechanistic differences between individual endocytic events cannot be explored with this pipeline.

4.9 Comparison with live-cell data

Clathrin-mediated endocytosis has been extensively studied using live-cell microscopy, resolving the dynamic characteristics of the process and the sequential recruitment of additional endocytic components to the clathrin-coated site (Cocucci *et al.*, 2012; Aguet *et al.*, 2013; Doyon *et al.*, 2011; Loerke, 2009; Mettlen, 2009; Saffarian *et al.*, 2009; Taylor *et al.*, 2011; He *et al.*, 2017; Schöneberg *et al.*, 2018; Jin *et al.*, 2022).

While these reports show heterogeneity in the duration or 'lifetime' of individual endocytic events, they describe a characteristic behavior of the endocytosis-specific signal. Generally, upon nucleation fluorescence intensity rapidly increases, followed by a plateau or maturation phase, which sharply decreases again upon vesicle scission.

As I interpret the dynamics of clathrin coat remodeling over a pseudotime, it would be curious to speculate on the correlation of this pseudotime with real-time clathrin dynamics. The correlation between these vastly different types of data is difficult. While the number of clathrin localization correlates with surface area A, immunolabeling is not always quantitative, and a direct comparison between the number of localizations, and fluorescence intensity could be misleading. Nevertheless, as mentioned previously (see Section 3.4), initial flat assembly likely happens fast, which would correspond to the initial steep increase in fluorescence intensity measured live. As we are describing the second half of clathrin coat assembly, respective to the surface area, we are likely capturing the slower fluorescence increase and subsequent plateauing. Thus, the plateau detected in live-cell microscopy likely coincides with curvature generation and the final addition of triskelion at the clathrin coat edge. This is a curious suggestion, as the duration of the plateau is reported to be a principal source of lifetime heterogeneity in endocytic events (Loerke, 2009; Aguet *et al.*, 2013).

Ultimately, to reliably correlate structural changes at the nanoscale with dynamic consequences, we would require a method that captures both information at sufficiently high resolution. Superresolution microscopy promises to increase spatial resolution while retaining many advantages inherent to fluorescence microscopy, which include theoretical live-cell compatibility. While this did not apply to SMLM, other superresolution methods promise direct dynamic information at a decreased spatial resolution, albeit still at greater structural detail than conventional fluorescence microscopy.

Along these lines, a recent study employed structured illumination microscopy (SIM) in total internal reflection fluorescence mode (TIRF) to address clathrin coat maturation *in vivo*. The structural resolution of this approach enabled the authors to quantify the 2D projected area of developing clathrin coats. According to the constant area and constant curvature model, the projected area is expected to follow a different trajectory. According to the author's interpretation of the constant area model, the projected area is expected to increase up until the point of curvature generation. At the point of curvature initiation, the projected area is expected to abruptly jump to the much smaller projected area of a curved and finalized vesicle. Conversely, according to the constant curvature model, the projected area is expected to increase constantly, until a closing angle of 90% is reached, where any decrease of the area is expected to occur due to an increasing distance between the substrate and the developing vesicle, owing to the evanescent profile of the TIRF illumination. In their study, the authors report a monotonous increase in the projected area, thus concluding that curvature is generated from the beginning of the endocytic event. While this interpretation of the data indeed supports the constant curvature model, it does not necessarily contradict my findings. Instead of a completely flat assembly of the clathrin coat, which then almost instantly acquires the final curvature of a vesicle, I find that curvature is acquired continuously throughout the process. This suggests that the puristic interpretation of a flat-to-curved transition tested by the work performed by Willy et al. might be misleading. Indeed, Figure 3.13b shows a monotonous decrease of the projected area A_p. Using SIM-TIRF, endocytic events are likely captured much earlier than in the SMLM approach. Indeed, the earliest structures detected in this pipeline are already accumulated to $\approx$ half their final size. It is therefore difficult to compare the trajectory of the projected area over pseudotime, with the real-time information reported by Willy et al.. However, the decrease in projected area A_p is subtle and could fall below the detection limit of SIM-TIRF. Thus, the decrease in projected area A_p might not be captured, but be detected as a plateau in A_p, as is reported for the later stage of endocytosis by Willy et al.. While careful calibration between the two approaches would be required to test this hypothesis, the discrepancies between these two studies could be due to technical limitations and an overly strict interpretation of the flat-to-curved transition.

It becomes apparent that direct 3D information is essential to understand the dynamic 3D organization of clathrin coats during endocytosis. While providing essential information on the process (see Section 1.4.2), inferring curvature from changes in the projected area (Willy *et al.*, 2021), changes in fluorescence intensity ratios (Scott *et al.*, 2018; Nawara *et al.*, 2022), or greyscale values of 2D high-resolution images (Bucher *et al.*, 2018; Sochacki *et al.*, 2021) is insufficient to probe the continuous and potentially subtle changes in clathrin coat curvature.

5 | Future outlook

Clathrin-mediated endocytosis is a complex and dynamic process, mediated by a network of over 50 components (Merrifield and Kaksonen, 2014). The pipeline I described in this work focused on the geometric consequences of this network on the clathrin coat architecture. By visualizing clathrin, and reconstructing its remodeling during endocytic progression, I was able to gain insights into the force-generating mechanisms behind membrane bending.

Together with recent studies, findings reported in this work suggest the convergence towards a single, geometric conceptualization of clathrin coat growth. It is reasonable to assume that clathrin pre-assembles on plasma membranes, followed by a flat-to-curved transition into a vesicular coat. However, while these observations allow for new mechanistic speculations, we still have a limited understanding of the precise coordination and activity of other endocytic components, and how they work together to promote the production of vesicles in a highly regular and robust manner.

To further dissect the individual contributions of endocytic components on membrane remodeling, it would thus be essential to resolve their recruitment to the developing clathrin coat. By locating the exact position and timing of these factors, we could provide the basis for further, more targeted research.

I have therefore extended the presented pipeline to dual-color imaging to demonstrate how it can be used to investigate the spatiotemporal recruitment of other endocytic components (see Section 3.5). Theoretically, this approach can be extended to any target of interest, as long as it can be efficiently targeted with a fluorescent label. The mechanical role of actin, for example, promises an interesting candidate for further research. Actin has been shown to be an essential force provider in yeast endocytosis (Aghamohammadzadeh and Ayscough, 2009; Basu *et al.*, 2014), but its role in mammalian cells is less well understood, and a common topic of research (Kaplan *et al.*, 2022; Akamatsu *et al.*, 2020; Jin *et al.*, 2022; Yang *et al.*, 2022, see Section 1.3). In mammalian cells, has been suggested to be recruited to endocytic sites to overcome increased force requirements, caused by for example higher membrane tension (Bucher *et al.*, 2018). However, it is unclear how or when the actin network exerts force on the clathrin-coated structures. The dual-color imaging and analysis approach would allow us to study the spatiotemporal interactions

between the clathrin coat and the actin network under different environmental conditions, further elucidating its mechanical role in the process (see Figure 5.1).

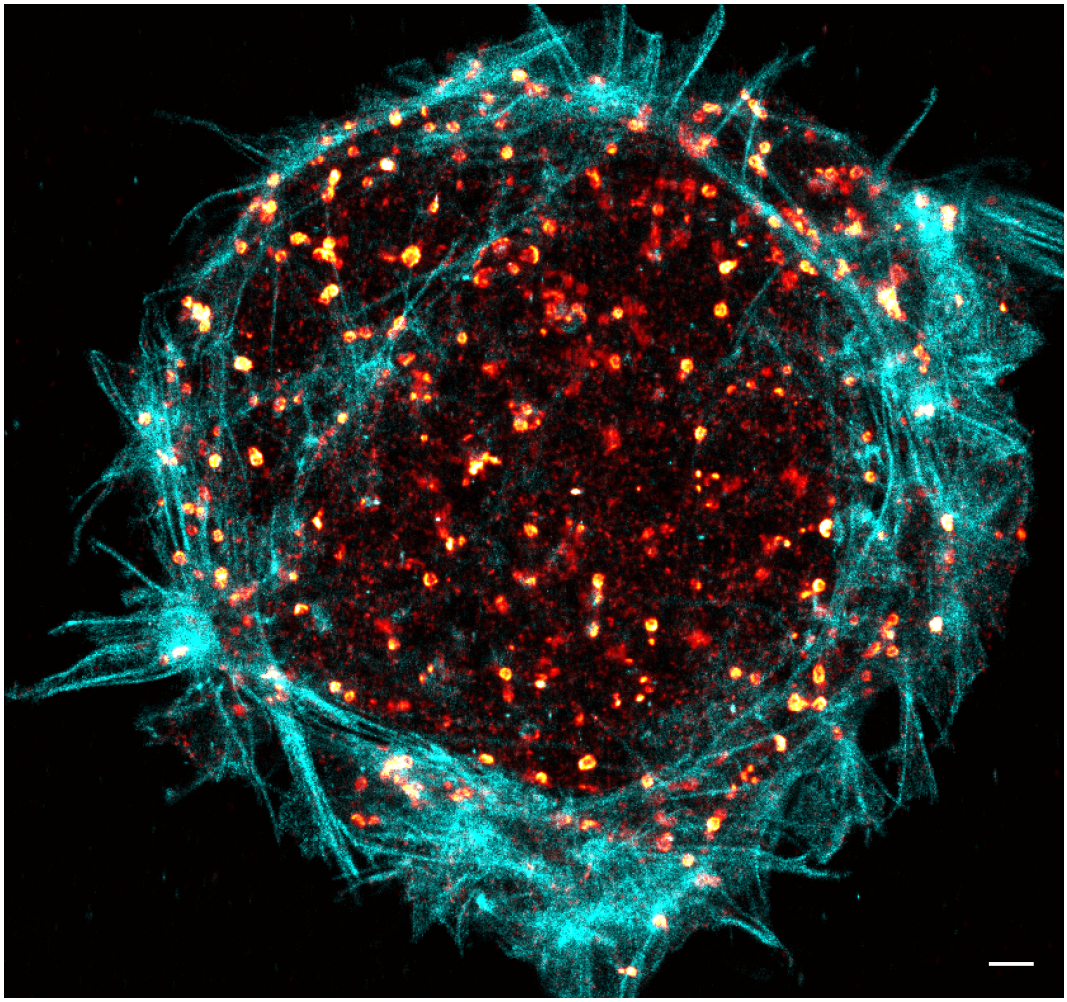


Figure 5.1 | Dual-color imaging of clathrin and actin. Clathrin immunolabeled with CF680 *(red)* was imaged together with actin labeled with phalloidin conjugated to AF647 (*blue*). Scale bar: 1 µm *Data and figure generated by Aline Tschanz*.

The here presented approach could further be used to study the structural adaptation of the endocytic machinery to changing environmental conditions. While the results of this study showed that the general mechanism of clathrin coat remodeling is consistent across three cultured cell lines, they also showed slight variations sizes of vesicles generated (see Section 3.3.3). This is indicative of the capability of the endocytic machinery to adapt to varying demands in force generation, as different cell types exhibit varying membrane composition and tension.

To explore the adaptive mechanisms of the endocytic machinery, it would thus be curious to manipulate the force requirements and investigate the structural adaptations at the nanoscale (Ferguson *et al.*, 2017). Depending on these adaptations, novel insight into the force generation mechanism could be gained. An exciting model system regards the changes in cell surface properties during cell spreading and migration (Wood and Smith,

2021). Here, I have collected preliminary data which suggests an increase of flat endocytic sites in spread cells, compared to cells freshly seeded. Correlating mechanical changes in cell surface properties during cell spreading with structural and dynamic changes in the clathrin coat is a promising endeavor to investigate adaptive mechanisms by the endocytic machinery.

Lastly, in this study, I used a spherical cap model, which closely matched the large majority of structures within the data (see Section 3.2.2). However, certain clathrin coats appear to be asymmetric, ellipsoidal, or otherwise deformed irregularly (see Figure 3.6). So far, I did not explore these asymmetries in this work. However, they could have some mechanistic implications that would be curious to investigate. By extending LocMoFit to incorporate more complex geometric models, such as ellipsoidal caps, I could quantify any systematic deviations from the original spherical cap model.

In the more distant future, the approach presented in this thesis could also be applied to other cellular processes that cannot be easily studied with conventional fluorescence microscopy approaches. For example, there are a number of other membrane-bending and vesicle-forming mechanisms in the cell (e.g. membrane tubulation by BAR domain or ESCRT (endosomal sorting complex required for transport) proteins) that present attractive targets for superresolution microscopy paired with geometric modeling.

6 | Materials & Methods

6.1 Materials

6.1.1 Chemicals

Table 6.1 | List of chemicals used in this work

Name	Supplier	Catalog number
AF647 NHS	Thermo Fisher Scientific, Waltham, MA USA	A37573
anti-β-adaptin antibody	Santa Cruz Biotechnology, Inc. Dallas, TX USA	sc-74423
anti-CHC antibody	Abcam, Cambridge, UK	ab21679
anti-CLC antibody	Santa Cruz Biotechnology, Inc. Dallas, TX USA	sc28276
anti-GFP nanobody	NanoTag Biotechnologies GmbH, Göttingen, Germany	N0304
anti-mouse antibody (CF680)	Merck, Darmstadt, Germany	SAB4600394
anti-rabbit antibody	Jackson ImmunoResearch Europe Ltd, Cambridgeshire, UK	711-005-152
BSA (bovine serum albumin)	Sigma-Aldrich, St. Louisie, MO USA	A7030
Catalase	Sigma-Aldrich, St. Louisie, MO USA	C3155
D-glucose	Sigma-Aldrich, St. Louisie, MO USA	D3179
Digitonin	Sigma-Aldrich, St. Louisie, MO USA	D141
DMEM (Gibco, phenol red)	Thermo Fisher Scientific, Waltham, MA USA	10565-018
DMEM (Gibco, w/o phenol red)	Thermo Fisher Scientific, Waltham, MA USA	11880-028
DMEM (Media kitchen, 4.5 g L^{-1} D-glucose, phenol red)	EMBL Media Kitchen	
DMSO (cell culture)	Merck, Darmstadt, Germany	102950
EGTA	Sigma-Aldrich, St. Louisie, MO USA	E4378
Ethanol	Merck, Darmstadt, Germany	100983
FBS (fetal bovine serum)	Thermo Fisher Scientific, Waltham, MA USA	10270-106
Glucose oxidase	Sigma-Aldrich, St. Louisie, MO USA	49180
GlutaMAX (Gibco)	Thermo Fisher Scientific, Waltham, MA USA	51985026
HCl (hydrochloric acid)	Merck, Darmstadt, Germany	100317
Image-iT FX™	Thermo Fisher Scientific, Waltham, MA USA	I36933
Kcl (Potassium chloride)	Merck, Darmstadt, Germany	104936
Lipofectamine	Thermo Fisher Scientific, Waltham, MA USA	11668019

Table 6.1 | List of chemicals used in this work (continued)

Name	Supplier	Catalog number
MEA (β-mercaptoethylamine or cysteamine)	Merck, Darmstadt, Germany	30070
MEM NEAA (Gibco, non-essential amino acids)	Thermo Fisher Scientific, Waltham, MA USA	11140-035
MES pH 6 (2-(N-morpholino)ethane sulfonic acid)	EMBL Media Kitchen	
methanol	Merck, Darmstadt, Germany	106009
$MgCl_2$ (Magnesium chloride, 1 M)	EMBL Media Kitchen	
$NaBH_4$ (Sodium borohydride)		
NaCl (Sodium chloride)	Merck, Darmstadt, Germany	106404
OptiMEM I (Gibco)	Thermo Fisher Scientific, Waltham, MA USA	51985026
Paraformaldehyde (PFA, 16 %)	SElectron Microscopy Science, Hatfield, PA, USA	RT15710
Tetraspeck (fluorescent bead stock solution)	Thermo Fisher Scientific, Waltham, MA USA	T7279
Tris-HCl pH 8, 1 M	EMBL media kitchen	
TrypLE (Gibco)	Thermo Fisher Scientific, Waltham, MA USA	12604-013
Zellshield™	Minerva Biolabs, Berlin, Germany	13-0050

6.1.2 Consumables

Table 6.2 | List of consumables used in this work

Name	Supplier	Catalog number
6-Well cell culture plates	Thermo Fisher Scientific, Waltham, MA USA	140675
Coverslips No. 1.5H, ⌀24 mm	Marienfeld, Lauda-Königshofen, Germany	117640
Coverslips, ⌀16 mm	Marienfeld, Lauda-Königshofen, Germany	0111560
Millex-GP membrane filters, 0.22 µm	Merck, Darmstadt, Germany	SLGP033RS
Culture flask CellStar™, 25 cm^2	Greiner Bio-One GmbH, Frickenhausen, Germany	690160
Culture flask CellStar™, 75 cm^2	Greiner Bio-One GmbH, Frickenhausen, Germany	690160
Culture flask CellStar™, 175 cm^2	Greiner Bio-One GmbH, Frickenhausen, Germany	690160
Zeba™Micro Spin columns, 7K MWCO	Thermo Fisher, Waltham, MA, USA	89882
Falcon tubes, 50 mL	Sarstedt AG & Co. KG, Numbrecht, Germany	1071821
Falcon tubes, 15 mL	Sarstedt AG & Co. KG, Numbrecht, Germany	00U0423
KIMTECH Precision wipes	Roswell, GE USA	7552

6.1.3 Buffers, solutions, and media

All buffers and solutions were prepared with dH_2O (Mili-Q®ultrapure water). When indicated, filtering was performed using 0.22 µm membrane filters.

Growth medium for SK-MEL-2	
DMEM (Gibco, phelol red)	500 mL
FBS	50 mL
ZellShield™	5 mL

Growth medium for 3T3	
DMEM (Media kitchen, 4.5 g L^{-1} D-glucose, phenol red)	500 mL
FBS	50 mL
ZellShield™	5 mL

Growth medium for U-2 OS	
DMEM (Gibco, w/o phenol red)	500 mL
FBS	50 mL
MEM NEAA	50 mL
GlutaMAX	50 mL
ZellShield™	5 mL

Freezing medium	
FBS	50 mL
DMSO (cell culture)	10 % [w/v]

PBS	
KCl	2.7 mM
KH_2PO_4	1.5 mM
Na_2HPO_4	8.1 mM
NaCl	137 mM
prepared by EMBL media kitchen	

Paraformaldehyde (PFA) fixation solution	
Paraformaldehyde (16 %)	3 % [w/v]
MES	10 mM
NaCl	150 mM
$MgCl_2$	5 mM
EGTA	5 mM
D-glucose	5 mM

Quenching buffer	
$NaBH_4$	0.1 % [w/v]
in PBS	

Permeabilization solution	
Digitonin	0.01 % [w/v]
in PBS	

Blocking solution	
BSA	2 % [w/v]
in PBS, filtered	

Clathrin staining solution	
anti-CHC antibody	1:300 dilution
anti-CLC antibody	1:100 dilution
Image-iT FX™	50 % [v/v]
BSA	1 % [w/v]
in PBS	

Clathrin and dynamin-2 labeling solution	
anti-CHC antibody	1:300 dilution
anti-CLC antibody	1:100 dilution
anti-GFP nanobody	1:100 dilution
Image-iT FX™	50 % [v/v]
BSA	1 % [w/v]
in PBS	

Clathrin and AP-2 labeling solution	
anti-CHC antibody	1:300 dilution
anti-CLC antibody	1:100 dilution
anti-β-adaptin antibody	1:100 dilution
Image-iT FX™	50 % [v/v]
BSA	1 % [w/v]
in PBS	

Anti-rabbit labeling solution	
anti-rabbit AF647 antibody	1:300 dilution
Image-iT FX™	50 % [v/v]
BSA	1 % [w/v]
in PBS	

Anti-rabbit and anti-mouse labeling solution	
anti-rabbit AF647 antibody	1:300 dilution
anti-mouse CF680 antibody	1:300 dilution
Image-iT FX™	50 % [v/v]
BSA	1 % [w/v]
in PBS	

GLOX imaging buffer	
Tris/HCl pH 8	50 mM
NaCl	10 mM
D-glucose	10 % [v/v]
Glucose oxidase	500 µg mL^{-1}
Catalase	40 µg mL^{-1}
MEA	35 mM
in dH_2O	

6.1.4 Equipment

6.1.4.1 Microscope for localization microscopy

A custom-built microscope was used for all single-molecule localization microscopy (SMLM) presented in this work. This setup was originally developed by Dr. Joran Deschamps and Dr. Jonas Ries (Deschamps *et al.*, 2016) and applied and further developed by multiple users in the Laboratory of Dr. Jonas Ries (Mund, 2016; Deschamps, 2017; Cieslinski, 2018; Thevathasan, 2019; Höß, 2021; Wu, 2022).

Excitation light path. The output light from the laser box was coupled to either a single-mode (fluorescent bead imaging) or a multi-mode fiber (biological sample imaging). An additional booster laser was further coupled into the excitation beam path using a polarization beam splitter and then to the multi-mode fiber.

To achieve homogenous illumination intensity from the multi-mode fiber, the 2 m long multi-mode fiber was coiled, and intertwined with elastic rubber bands. These bands, in turn, were suspended in an aluminum box. A motor with an unbalanced weight was attached, whose vibrations resulted in mode scrambling, reducing the speckles resulting from interference between modes. The aluminum box was further insulated to reduce the noise caused by the motor.

The fiber output was guided through a laser clean-up filter, removing fiber-generated fluorescence. A square iris constricts the beam width to adjust the illumination area size in the image plane. The laser beam was reflected into the objective lens using a first dichroic mirror.

Emission light path. The emitted light was collected by the objective lens, reflected by a second dichroic mirror, and focused onto the camera chip by a tube lens. The resulting effective pixel size was measured at 127 nm. In single-color mode, the emission path was further filtered using a selection of bandpass filters on filter wheel 1. In 3D mode, a cylindrical lens was inserted to the emission path to introduce astigmatic aberration. In multi-color mode, a dichroic mirror/beamsplitter was manually placed in the emission path, transmitting wavelengths above 665 nm, while reflecting those below. In this study, CF680 and AF647 were used. Most of their emission spectra were thus transmitted (almost all of CF680, and most of AF647), while a small amount was reflected. The transmitted light (channel 1) was used for localization of signal resulting from both fluorescent species, while the small portion as reflected light (channel 2) was only used for color assignment (see Section 6.2.5.6). Individual bandpass filters were placed into both emission paths. The two channels were focused side-by-side onto the camera chip.

Perfect focus. To ensure a stable focus during imaging, an infrared laser (785 nm) was coupled into the objective at a total internal reflecting angle. The reflected light was detected on a quadrant photodiode (QPD) to monitor the sample position, and axial sample drift was automatically corrected to maintain the focus via a direct feedback loop with the objective piezo positioner.

Back focal plane (BFP). To assess the homogeneity of the illumination and assure minimal aberrations, a lens can be introduced into the emission path to image the back-focal plane onto the camera.

Microscope operation. The control of all automated microscope components was performed by a custom-written plugin for μManager (Edelstein *et al.*, 2014; Edelstein *et al.*, 2010) called Easier microscope user-interface or short, EMU (Deschamps and Ries, 2020, available at https://github.com/jdeschamps/EMU).

In addition to the general control of the microscope components, EMU allows for automated activation of fluorophores, controlling the density of blinks per frame, and adjusting the pulse length of the 405 laser accordingly. It further enabled the automated acquisition of multiple positions on the coverslip.

Table 6.3 | Microscope components

Component	Specification	Manufacturer
Laserbox	LightHub equipped with Luxx 405, 488, 638 and Cobolt 561 laser	Omicron-laserage Laserprodukte, Rodgau, Germany
Booster laser	640 nm, iBeam Smart	Toptica, Solna, Germany
Single-mode fiber	LightHub	Omicron-laserage Laserprodukte, Rodgau, Germany
Multi-mode fiber	M103L05	Thorlabs, Newton, NJ, USA
Laser clean-up filter	390/482/563/640 HC Quad	AHF, Tübingen, Germany
Quad-Notch filter	400-410/488/561/631-640 F40-072	Semrock, Rochester, NY, USA
Dichroic mirror, objective	TIRF Quad Line Beamsplitter zt405/488/561/640rpc	Chroma, Bellows Falls, VT, USA
Objective	HCX PL APO 160×/1.43 NA	Leica, Wetzlar, Germany
Piezo objective positioner	P-726	Physik Instrumente, Karlsruhe, Germany
Sample stage	HCU-3D	SmarAct, Oldenburg, Germany
Bandpass filters, wheel 1	525/50 (FF03-525/50-25) 600/60 (NC458462) 700/100 (ET700/100m)	Semrock, Rochester, NY, USA Chroma, Bellows Falls, VT, USA Chroma, Bellows Falls, VT, USA
Dichroic mirror/beamsplitter	665LP (ET665lp)	Chroma, Bellows Falls, VT, USA
Bandpass filter, dual-color mode	Transmitted path: 685/70 (ET685/70m) Reflected path: 676/37 (FF01-676/37-25)	Chroma, Bellows Falls, VT, USA Semrock, Rochester, NY, USA
Camera, EMCCD	Evolve512D	Photometrics, Tucson, AZ, USA
785 nm focus lock laser	iBeam Smart 785	Toptica, Solna, Germany
Dichroic mirror, focus lock laser	SP beam splitter T750SPXRXT	Chroma, Bellows Falls, VT, USA
Filter, focus lock laser	SP75, FESH0750	Thorlabs, Newton, NJ, USA
Quadrant photodiode (QPD)	SD197-23-21-041	Laser Components, Olching, Germany
Fiel-programmable gate array	Mojo	Alchitry (former: Embedded Micro), Littleton, CO, USA

Table 6.4 | Equipment used in this work

Item	Supplier
Water bath, 37 °C	GFL Gesellschaft für Labortechnik mbH, Burgwedel , Germany
Heraeus HERAsafe™, Laminar flow hood	Thermo Fisher Scientific, Waltham, MA USA
Nanodrop 1000 microvolume spectrophotometer	peqLab Biotechnologie GmbH, Erlangen, Germany
Heraeus Megafuge 1.0R centrifuge	Thermo Fisher Scientific, Waltham, MA USA
MIDI 40 CO_2 Incubator	Thermo Fisher Scientific, Waltham, MA USA
Leica DM IL LED inverse microscope	Leica Microsystems, Wetzlar, Germany
Vortex-Genie 2	Scientific Industries Inc., Bohemia, NY USA
Centrifuge 5418	Eppendorf, Hamburg, Germany
ROCKER 3D digital	IKA®-Werke GmbH & Co. KG, Staufen, Germany

6.2 Methods

6.2.1 Antibody conjugation

Clathrin-labeled data were generated using a secondary anti-rabbit antibody, conjugated in-house to AF647. The first step of this conjugation is to adjust the pH of the antibody storage solution to pH 8.2 using 0.2 M $NaCO_3$. Thus, 1.4 µL of $NaCO_3$ pH 8.2 were added to 5 µL of antibody solution. AF647 NHS was then added at 5-fold excess compared to the molar antibody concentration. The solution was incubated at RT for 2 h.

After incubation, the non-conjugated dye was removed using Zeba™Micro Spin columns according to the manufacturer's instructions. The degree of labeling (DOL) is calculated as the ratio between the dye concentration n_{AF647} and the antibody (IgG) concentration n_{IgG}. These concentrations are determined from the absorption A_{280} measured at 280 nm and A_{647} measured at 647 nm using a Nanodrop microvolume spectrophotometer. The contribution of the dye to the absorption at 280 nm is assumed to be 0.03 A_{647}. The molar extinction coefficient of IgG ε_{IgG} is ≈210,000 M^{-1} cm^{-1}, while ε_{AF647} is ≈239,000 M^{-1} cm^{-1}. DOL is calculated according to Equation 6.1.

$$\mathrm{DOL} = \frac{n_{AF647}}{n_{IgG}} = \frac{\frac{A_{647}}{\varepsilon_{AF647}}}{\frac{A_{280}-0.03A_{647}}{\varepsilon_{IgG}}} \tag{6.1}$$

The DOL of the secondary antibody used here was 1.8.

6.2.2 Cell culture

Three adherent cell lines were cultured for this study. Aliquots of all cell lines were stored in liquid nitrogen. Cells were thawed rapidly (<3 min) in a water bath at 37 °C. Using proper aseptic technique and working in a laminar flow hood, cells were then slowly re-suspended in 6 mL growth medium pre-warmed to RT, using a 15 mL falcon tube. To remove the toxic cryoprotectant (DMSO), cells were centrifuged at 700 rpm for 5 min. The supernatant was then aspirated, and the pellet was re-suspended in 6 mL pre-warmed growth medium (RT). The cell suspension was next transferred to a 25 cm^2 culture flask. As these cells form adherent monolayers on the flask surface, the flask was gently shaken to ensure an even distribution of cells and avoid clustered growth. Adhesions form within 30 min to 2 h. Cells were cultured at their preferred confluency in an incubator at 37 °C and 5 % CO_2.

To keep cells in their log growth phase, they were split when their cell-type specific confluency maximum was reached. To this end, the growth medium was aspirated and replaced with PBS, which was again aspirated. After this washing step, 1 mL of TrypLE was added to trypsinize and release the cells into suspension. Gently rocking the culture flask ensures even distribution of TrypLe, covering the entire cell layer. After the cell-type

specific incubation time at 37 °C and 5 % CO_2, trypsinization was quenched by adding 5 mL of growth medium (RT). The appropriate cell suspension volume was removed to ensure the minimal cell confluency preferred for each cell type. The removed volume was replaced by an equal volume of the fresh growth medium (RT), and cells were returned to the incubator (37 °C; 5 % CO_2) after gently rocking the flask. Cells were cultured for an average of 3 months, after which a fresh aliquot was thawed.

To properly maintain and restock frozen cell stock, freshly thawed cells were expanded and frozen down in aliquots to preserve for long-term storage. To this end, cell suspension after the first trypsinization was transferred into increasingly large culture flasks (75 cm^2; 175 cm^2), and let to grow to the cell-type specific maximum confluency. Cells are then trypsinized, transferred to a 50 mL falcon tube and centrifuged at 800 rpm for 3 min. The pellet is resuspended in 7 mL of freezing medium, and aliquoted into 7 cryovials.

6.2.2.1 SK-MEL-2 human melanoma cells

SK-MEL-2 cells were used to generate the majority of data discussed in this study. They were generously gifted to us by the Drubin Laboratory, UC Berkeley, USA, as described in Doyon *et al.*, 2011. They additionally contain endogenously tagged clathrin-light chain A-RFP (CLTA-RFP) and dynamin-2-GFP (DNM2-GFP).

The cells were kept at a range of 60 to 80% confluency. The growth medium composition is summarized in Section 6.1.3. Trypsinization was performed for 6 min, and cells were split Monday, Wednesday, and Friday to ensure the correct confluency.

6.2.2.2 3T3 mouse fibroblasts

3T3 cells were generously gifted to us by the Diz-Muñoz Laboratory, EMBL Heidelberg, Germany.

The cells were kept at a range of 60 to 80% confluency. The growth medium composition is summarized in Section 6.1.3. Trypsinization was performed for 3 min, and cells were split Monday, Wednesday, and Friday to ensure the correct confluency.

6.2.2.3 U-2 OS human bone osteosarcoma

U2OS cells (no. 300174; Cell Line Services) were cultured as described in Thevathasan *et al.*, 2019.

The cells were kept at a range of 80 to almost 100% confluency. The growth medium composition is summarized in Section 6.1.3. Trypsinization was performed for 12 min, and cells were split Monday, Wednesday, and Friday to ensure the correct confluency.

6.2.2.4 Transfection of 3T3 mouse fibroblasts

To generate the data shown in Figure 3.15, 3T3 cells were transiently transfected with a plasmid encoding the sigma-2 subunit of the adaptor protein complex 2 fused to GFP.

The plasmid (no. 53610, Addgene) was a gift by the Boulant Laboratory, University of Florida, USA. The following workflow was performed underneath a laminar flow hood, with cells previously seeded onto glass coverslips (see Section 6.2.3).

The transfection was performed using Lipofectamine, according to the manufacturer's recommendations: 1 µg DNA was mixed with 50 µL OptiMEM I. The same was done for 3 µL Lipofectamin in 50 µL OptiMEM I. Both solutions were incubated for 5 min and then mixed together and incubated for an additional 10 min at RT. The growth medium of cells was exchanged to OptiMEM I (RT). The DNA-Lipofectamin solution (100 µL) was then dropwise added to the cells. After overnight incubation (≈24 h) the medium was exchanged with fresh growth medium (RT). After additional incubation for ≈16 hour, cells were ready for further sample preparation (see Sections 6.2.3).

6.2.3 Sample preparation

6.2.3.1 Coverslip preparation

High-precision ⌀24 mm round glass coverslips were used for all samples (bead sample, dye sandwich, biological sample). Before biological samples can be prepared, the coverslips had to be cleaned to remove any contamination. To this end, coverslips were separated into a mini-rack that can withstand strong acids. The entire rack is next placed into a methanol:hydrochloric acid (50:50 v/v) mixture. Overnight incubation (16 to 24 h) using a magnetic stirrer ensured thorough cleaning. To remove the acid, the coverslips were rinsed with dH_2O until a neutral pH was reached. To air dry the coverslips without risk of further contamination, they were placed in the laminar flow hood. The entire process was finalized by irradiating the coverslips inside the laminar flow hood with ultraviolet (UV) light for 30 min.

6.2.3.2 Fluorescent bead sample preparation

To generate an experimental PSF model, align the microscope, or check the setup for any vibrations, fluorescent beads are used. To prepare such a sample, 40 µL of 1 M magnesium chloride ($MgCl_2$) is added to the center of a glass coverslip (no need to clean before). The glass coverslip is already placed on the sample holder. Next, 0.8 µL of the bead stock solution is diluted in 360 µL dH_2O, and vortexed for 30 s to avoid aggregation. This bead solution is next added to the $MgCl_2$, and thoroughly mixed by pipetting up and down. After 3 min, the beads were adherent to the glass, and the solution could be exchanged with pure dH_2O.

The immersion of the beads in dH_2O is important, as it ensures the proper photophysical behavior of the water-soluble fluorescent molecules, and it creates an environment for the signal similar to biological samples.

6.2.3.3 Fluorescent dye sandwich preparation

To optimize the uniformity of the illumination field, a fluorescent dye sandwich was used. To this end, 1 µL of AF647 was placed on a glass coverslip. A second, smaller ⌀16 mm glass coverslip was then placed on top of the droplet and gently pressed down until all the volume is spread evenly. This 'sandwich' is then sealed up using clear nail polish to connect the two coverslips.

6.2.3.4 Biological sample preparation

The preparation of biological samples can be categorized as follows: Cell seeding; cell fixation; cell permeabilization; staining.

SK-MEL-2 cells were seeded in the laminar flow hood ≈7 h before fixation. 3T3 cells were seeded ≈16 h, and U-2 OS ≈72 h before fixation. To this end, a 6-well plate was prepared under the laminar flow hood by adding a cleaned glass coverslip to each well. Cells were then trypsinized, and 500 µL of cell suspension was added to each coverslip. This volume was adjusted depending on the confluency before trypsinization. Each well was then filled up to 2 mL of growth medium (RT). After gently rocking the 6-well plate, it was transferred back to the incubator until sample fixation.

To perform cell fixation a 6-well plate was prepared by adding 2 mL of fixation buffer to each well. The coverslips on which cells were previously seeded were then transferred to each well. After 7 min incubation on a shaker, fixation was stopped using quenching buffer. to this end, 2 mL quenching buffer was added to a fresh 6-well plate (or fresh, un-used wells of the same plate), and coverslips of fixed cells were transferred to the quenching solution. Quenching was performed for 7 min on the shaker. The quenching solution was then aspirated, and replaced with PBS. After 5 min incubation of the sample on the shaker, the solution in each well was exchanged with 2 mL fresh PBS. This washing step was repeated a total of 3 times.

Permeabilization of the cell membrane was achieved using digitonin. 120 µL of permeabilization solution was added to clean parafilm for each coverslip. The coverslips were then inverted and placed on top of these droplets, with the cell growth surface facing downward, ensuring contact between cells and the permeabilization solution. After 15 min permeabilization, the coverslips are transferred back into a 6-well plate, with each well containing 2 mL fresh PBS. A total of two washing steps in PBS for 5 min on the shaker are then performed.

Next, for blocking of the sample 120 µL droplets of Image-iT FX™Signal Enhancer are prepared on a fresh parafilm. Coverslips are again inverted and placed onto these droplets with the cell growth surface facing downward. After 30 min incubation, the coverslips are transferred onto prepared 120 µL droplets of blocking solution, again with the cell growth surface facing downward, incubating for another 30 min. Staining was then performed by transferring the coverslips to 120 µL droplets of clathirn labeling solution. The sample

was incubated at 4 °C in the dark, over night (≈16 h). To avoid drying out of the sample, a KIMTECH wipe was soaked with dH_2O and placed next to the sample underneath a protective plastic cover. After incubation, the coverslips were thoroughly washed in PBS 5 times, at RT on a shaker, for 5 min per washing step. Secondary staining was achieved by placing the inverted coverslips onto 120 µL anti-rabbit labeling solution. Incubation was performed at RT in the dark, for 2 h. After this, the sample was washed 3 more times using PBS, each washing step at a duration of 5 min. The sample was then ready for imaging

Dual-color staining of clathrin and dynamin-2 was performed in SK-MEL-2 cells, which additionally contain endogenously tagged CLTA-RFP and DNM2-GFP. A clathrin and dynamin-2 labeling solution additionally containing anti-GFP nanobodies was used to target the GFP of dynamin-2. All other sample preparation steps were kept the same.

Dual-color imaging of AP-2 and clathrin was performed by additionally targeting the beta-subunit of AP-2. To this end, a primary clathrin and AP-2 labeling solution and a secondary anti-rabbit and anti-mouse labeling solution were used. All other sample preparation steps were kept the same.

Correlative imaging of super-resolved clathrin and diffraction-limited AP-2 was performed in 3T3 cells transiently expressing the endocytosis specific sigma-2 subunit of AP-2 fused to GFP. Sample preparation steps were kept the same.

6.2.4 Microscopy

6.2.4.1 Sample mounting

All samples described above use the same custom-made sample holder setup. A metal plate with a hole in its center serves as a base for the sample coverslip. By placing a ring magnet on top, the coverslip is fixed in place, and a chamber is formed that can be filled with imaging solution. The imaging solution for fluorescent beads is dH_2O, for biological samples it is GLOX imaging buffer, and for fluorescent dye sandwiches, no imaging solution is needed.

The magnet ring is encased in a hard PVC casing, and to ensure thorough sealing, an O-ring is installed in a corresponding groove in the underside of the magnet casing. Since the ring magnet is in direct contact with the sample and the sample buffer, it must be wrapped in fresh parafilm to avoid the carryover of fluorescent particles between experiments. To wrap the magnet, a square piece of parafilm is placed on the underside of the ring magnet (clean side facing outward). The edges of the square piece of parafilm are then folded over the outside of the ring and fixed on top. Using a 1 mL pipette tip, the parafilm is pushed through the center of the ring from below. The edges of the resulting tube can then be pulled over the top using the same pipette tip. The magnet should now be completely wrapped by parafilm.

To mount a sample, the sample coverslip is placed onto the metal plate, and fixed in place by the ring magnet, completely wrapped in parafilm. An imaging solution is then added to the chamber. For high-throughput experiments, automated acquisitions were often performed overnight. To avoid acidification of the GLOX imaging buffer, the chamber is filled up to the top (corresponding to a volume of 1.2 mL) with imaging solution, and sealed with a small square piece of parafilm to decrease diffusion of oxygen into the buffer. This measure prolonged imaging time from 1 to 2 h to 1 to 2 days.

After preparing the sample on the sample holder, the coverslip was cleaned from below using 70% ethanol (v/v). This removed any dust or debris at the immersion oil/glass interface. Before mounting the sample holder, a drop of immersion oil was applied to the objective. Care had to be taken when placing the sample onto the microscope to avoid air bubbles getting introduced into the immersion oil.

6.2.4.2 Biological sample image acquisition in single-color

For single-color imaging of clathrin-AF647, a multimode fiber, and scrambler were used to ensure homogenous illumination across the entire field of view using a 638 nm laser for excitation. The emitted light was filtered using a 676/37 bandpass filter. After placing the sample onto the objective, this laser was turned on at the lowest intensity to focus on the sample. To focus on clathrin-coated structures at the bottom membrane of mammalian cells, it was advised to first focus on the coverslip itself, and then move the focus up by 200 to 300 nm. Once the focus has been set, it can be locked using the perfect-focus feature. Next, the BFP lens was placed into the light path to check for air bubbles in the immersion oil. A cut-off in the BFP image indicates a non-homogenous light distribution and aberrations, which could be caused by air bubbles in the immersion oil. In those instances, the sample had to be re-mounted. For 3D imaging, the cylindrical lens was introduced into the emission path.

After setting the right laser wavelength, emission filters, and focus lock, the sample is ready to be imaged at the chosen region of interest (ROI). For a single ROI, the laser power of the 638 nm laser was set to 100%. For the field illumination of ≈630 µm^2, this resulted in a laser intensity of ≈15 kW cm^{-2}.

To achieve optimal blinking density, a UV laser at 405 nm wavelength was adjusted automatically by changing pulse duration to ensure a constant number of emitter detections per frame (≈12 detections per frame).

Acquisition was terminated after 200,000 to 300,000 frames were acquired at an exposure time of 15 - 30 ms.

For the automated acquisition of multiple ROIs in one acquisition step, a selection of ROIs was first defined using the stage position list in μManager. To acquire localization data for each position, the main parameters as described above were also defined in the configuration file for automated acquisition in EMU. After the set maximum of frames

was acquired for one position, the stage was moved to the next ROI, where it started a new acquisition after 3 s settling time. This time would be especially necessary if certain hardware configuration changes occurred between each position.

6.2.4.3 Biological sample image acquisition in dual-color

For dual-color imaging of clathrin-AF647 and DNM2-CF680 or AP-2-CF680, a 665LP beamsplitter was introduced into the emission path. The transmitted light was filtered by a 685/70BP filter, while the reflected path was filtered by a 676/37BP filter. Emitted light from both paths was imaged side by side on the camera chip, resulting in two distinct camera channels.

6.2.4.4 Acquisition of 3D bead stacks

3D bead stacks are required to generate an experimental PSF model. To this end, the microscope is set up similarly to the configuration used during the biological data acquisition. After mounting the bead sample, locking the focus, and checking the BFP for air bubbles, the same filters, lenses, and laser wavelengths were used. To decrease the flickering of signal intensities, fluorescent beads were imaged in single-mode. 15 ROIs were selected, containing 3 to 5 beads per region. Compared to biological data acquisition, the default camera settings were changed from EM200 to conventional gain. The automated configuration file in EMU was then adjusted to generate z-stacks, starting 1.2 µm below the focal point. The focus was then moved up at 10 nm steps, until 1.2 µm above the focal point. Thus, the PSF generated by the fluorescent beads were sampled in a range of 2.4 µm, at 10 nm step sizes.

For dual-color imaging, bead stacks were acquired according to the same criteria. The only adjustment needed here is the insertion of the same beamsplitter and filters as are used in the biological data acquisition.

6.2.4.5 Imaging of a dye sandwich

A dye sandwich was used to assess the uniformity of the illumination field and to overlay the illumination area onto the image area. To this end, the dye sandwich was placed on the sample holder, and fixed in place using the ring magnet. No imaging solution was needed, and all irises in the beam path were fully opened. Using low laser power, the uniformity of the illumination field was optimized and the highest-intensity regions from single-mode and multi-mode fibers were aligned by iteratively adjusting the mirror angles to the area imaged by the camera.

6.2.5 Processing of microscope images

All analyses of microscopy images described below were performed in a modular super-resolution microscopy analysis platform for SMLM data called SMAP, developed by Dr. Jonas Ries. The source code of SMAP, implemented in MATLAB (Inc., 2022)

can be found at http://www.github.com/jries/SMAP. A standalone version, as well as documentation, test data, and updated versions, can be downloaded at http://www.rieslab.de.

6.2.5.1 Localization of fluorescence signal

Single-color localization was performed using the default localize workflow 'fit_fastsimple' in SMAP. When loading the raw Tagged Image File Format (TIFF) files the acquisition parameters are automatically set based on the extracted metadata and the camera added to the Camera Manager.

The first step of the localization pipeline is called 'peak finder'. Here, signals corresponding to individual molecules are selected. To this end, each image was convoluted applying a difference-of-Gaussian filter set to 1.2. Next, a dynamic cut-off (dynamic factor: 1.5) was chosen to select the specific signal corresponding to a molecule. Regions of interest (13 x 13 pixels) centered on the detected peaks were then cut out from the raw images.

To localize the coordinate of each peak, a maximum-likelihood estimation (MLE) based algorithm was used (Li *et al.*, 2018). This returned the table of localization coordinates in xy, together with the corresponding photon counts, background estimations, sizes of the PSF (FWHM), the relative log-likelihoods, the frames of detection, and the localization precision.

It was possible to perform localization in parallel to raw image acquisition, to ensure the possibility of immediate troubleshooting. To this end, intermediate images were reconstructed from the localization data, to visualize the super-resolved data being acquired. Here, localizations that likely originated from the same fluorescent molecule were grouped into one localization. This was based on the criterion of localizations being closer than 35 nm of another, with a maximum of one dark frame in between. The new xy-coordinates were calculated from the average coordinate, weighted by their localization precision. The number of peaks and background photons was summed up.

In the above-described localization pipeline, each peak is fitted with a symmetric Gaussian, assuming a Gaussian-distributed PSF ('PSFfree' in the fitter tab). To determine the axial position of a molecule in 3D imaging, an experimental PSF model derived from fluorescent bead stacks was used for fitting (free fitting parameters: x, y, z, photons per localization, background per pixel). This bead calibration could be loaded in by changing the PSF model from 'PSFfree' to 'Spline' in the fitter tab.

Due to distortions caused by the cylindrical lens, pixel sizes were adjusted to 0.127 in x and 0.117 in y. A correction factor of 0.8 was applied to z, to correct for refractive index mismatches between the immersion oil and the imaging solution (movement of the objective during z-stack acquisition results in smaller movement in the focal plane, Huang *et al.*, 2008).

6.2.5.2 Generation of an experimental PSF model

To generate an experimental model of a 3D PSF, z-stacks of fluorescent bead samples are acquired as described above. Here, each bead represents a single PSF, and by taking z-stacks over a range of 2.4 µm, at a step size of 10 nm, the 3D distribution of the PSF is sampled. In order to build a 3D model, a calibration is performed using the SMAP plugin 'Analyze:sr3D:calibrate3DSplinePSF'. This plugin generates a cSpline model for experimental PSFs.

6.2.5.3 Rendering and filtering

After all peaks were localized, the final super-resolved image could be reconstructed. This was done for grouped localizations, as mentioned above. Their coordinates were superimposed, and rendered with a Gaussian blur, scaled to the σ of their respective localization precision. The red hot color map used represents the density of localizations per pixel and is scaled in a way that 0.03% of the pixel values are saturated.

Localizations were further filtered based on their localization precision < 20 nm in xy, and < 30 nm in z. The relative log-likelihood was also adjusted for each acquisition, removing outliers identifiable as the tail of the log-likelihood distribution.

6.2.5.4 Drift correction

The x, y, and z positions of all localizations were corrected for residual drift. This was achieved through a custom algorithm based on redundant cross-correlations. Here, the data were distributed into 10 time bins of equal length. A superresolution image was then reconstructed for each bin. Cross-correlations among all superresolution images were then calculated to extract the relative displacements in x and y. These displacements between maxima of cross-correlated images were then plotted and interpolated by a smoothed spline function, which further allowed the correction of all xy coordinates. Z-drift was determined in a second step, analogous to the xy-drift correction, using intensity profiles in z instead of images for cross-correlation.

6.2.5.5 Image resolution

To determine the resolution of superresolved images, the modal values of localization precision were used. These modal values corresponded to σ_{xy} = 3.9 nm in the lateral, and σ_z = 12 nm in the axial direction. The corresponding resolution was estimated at 9.2 nm in xy and 29.4 nm in z, using the full-width at half maximum (FWHM) criterium according to Equation 6.2.

$$\mathrm{FWHM} = 2\sqrt{2\ln 2}\sigma \tag{6.2}$$

These values were determined for a representative image.

6.2.5.6 Color assigmnent

For dual-color imaging, a ratiometric approach was applied, imaging two targets labeled with spectrally closely related dyes (AF647 and CF680). As described previously, their emission is split into two distinct regions on the same camera, resulting in two camera channels. The same localization will thus result in a signal in both channels. To identify what fluorescent species this specific localization belongs to, the signal intensity ratio between the two channels has to be determined. Therefore, the number of photons measured in channel 1 was plotted against the number of photons measured in channel 2. By doing so for all detected localizations, two distinct clusters of localizations could be determined, which allows the distinct assignment of color to localizations belonging to either of them.

To achieve this assignment of color, first, a calibration file has to be generated, describing both the experimental PSF as well as the transformation between the two channels. This transformation is required to identify the same localization in both camera channels. The same plugin 'Analyze:sr3D:calibrate3DSplinePSF' is used to generate this calibration file. Instead of the default 'arbitrary' 3D modality, 'global 2 Channel' was used. Generally, only one of the two channels is used to determine the coordinates of the molecule. As localization precision scales with the number of photons detected, the brighter of the two channels is defined as the main channel for localizations, which can be adjusted in the 'Global fit parameters' and was set to 'd/r' (down-right) and 'up-down mirror'. Localizations detected in the second channel were linked to allow for color assignment, but not used to determine the coordinates and localization precision (see Li *et al.*, 2022).

To fit dual-color data using the calibration file described above, the fitting workflow in the localization plugin was changed to 'fit_global_dualchannel'. While the same parameters were used in the peak finder tab, the region for localization was specified using the 'ROI include' and 'ROI exclude' buttons. The calibration file has to be specified in both, the peak finder tab as well as the fitter tab.

The color assignment was performed using the plugin 'Process:Assign2C:Intensity2ManzChannels'. Here, the photon count for each localization detected in channel 1 can be plotted against the photon count detected for the same localization in channel 2. Using 'ROI 1' and 'ROI 2', the region of interest could be manually defined around the clustered localizations.

To render dual-color images, a second layer could be added in the render tab. By adjusting the channel 'Ch' to 1 for 'ROI 1' in 'Layer 1', and to 2 for 'ROI 2' in 'Layer 2', the two fluorescent species are separated, allowing the user to define the look-up table (LUT) specific for each species. Red hot LUT is always chosen for the clathrin specific AF647 signal, and cyan cold for the second target, labeled with CF680.

6.2.6 Geometric model fitting

6.2.6.1 Segmentation

Segmentation was performed using the 'ROI Manager' integrated into SMAP. During segmentation, an individual image, or 'file', is subdivided into multiple square regions, or 'cells'. Each cell is in turn subdivided into segmented structures, or 'sites'.

In ROI manager, a preview of each 'file', 'cell', and 'site' is shown. The size and rendering parameters for each cell and site can be defined in the ROIs:Settings tab. For data presented in this work, the 'Pixelsize' was set to 5 nm; the 'FoV' was set to 700 nm; the 'ROI' was set to 500 nm for all sites. For cells, the 'Pixelsize' was set to 15 nm; and the 'FoV' was set to 5,000 nm. The pixel size defines the rendering of the images shown in the ROI manager. The FoV (field of view) defines the area rendered for each cell or site. The ROI is specified for each site and defines the localizations to which any subsequent analysis has been applied to.

To subdivide a file into cells, the plugin 'Segment:makeCellGrid' in the ROI tab was used. To then further identify the sites of interest, in this case, clathrin-coated structures, the plugin 'Segment:SegmentNPC' was applied. The parameters for site segmentation were set to a 'cutoff' of 0.8; a 'diameterNPC' of 120 nm; and a 'rim' of 5 nm. The nomenclature is a remnant of the analysis of NPCs, for which this plugin was originally developed. During segmentation, the images were first blurred using a Gaussian filter with a sigma of 100 nm. Peaks were detected based on the manually defined cut-off at 0.8.

6.2.6.2 Curation

After segmentation, an initial curation step was applied, in which certain structures were excluded from further analysis. These excluded structures were non-endocytic structures such as antibody clusters or large flat plaques, or endocytic structures originating from the upper plasma membrane, showing an upside-down orientation. The curation was performed manually.

6.2.6.3 LocMoFit analysis

Geometric model fitting was performed using LocMoFit, a maximum-likelihood estimation (MLE) based model fitting approach described in detail in Wu *et al.*, 2023; Wu, 2022.

LocMoFit uses the spatial coordinates $\vec{x}_k$ within a defined region of interest, and their respective localization precision $\vec{\sigma}_k$ as well as a parametrized model $f(p)$ as input. This input data is then used to construct a probability density function (PDF). Next, the log-likelihood L of the model describing the data is calculated according to Equation 6.3.

$$L(p) = \sum_k M(\vec{x_k}, \vec{\sigma_k}|p) \tag{6.3}$$

The MLE (see Equation 6.4) then iteratively explores the parameter space until the maximal log-likelihood $\hat{L}$ is reached, containing the parameter set $\hat{p}$ that best describes the data.

$$[\hat{L}, \hat{p}] = \arg\max_p L(p) \tag{6.4}$$

The model applied to SMLM data of clathrin was defined as a hollow spherical cap, parameterized by the surface area A and the closing angle θ between the top and the edge of the sphere. Additional parameters include the center of the model x_0, y_0, z_0 (center of mass), and the orientation of the sphere opening. To approximate an even distribution of points on a sphere, the spherical cap was discretized by placing spiral points on the sphere surface (Saff and Kuijlaars, 1997). These points were treated as discrete localization coordinates when constructing the PDF. During fitting, extra weight for uncertainty in addition to localization precision and background was applied to the PDF. The radius R can be derived as $R = A/2\pi(1 - \cos\theta)$ (see Table 6.5).

Manual curation of the model fit results was performed using the SMAP plugin 'ROIManager:Analyze:siteGallery_mCME', which depicts each structure in a top view, as well as xz-slices at 0°, 45°, 90°, 135°, relative to the x-axis. The model itself was plotted on top of each reconstructed structure, which allowed curation. Sites were excluded for the same categories as in the initial first curation step, or in the case of poor overlap between the model and data. This curation step was an essential part of the analysis pipeline optimization, as it allowed the investigation of potential obvious biases of the model fit. After repeated iterations of curation and parameter optimization, the model fit was optimized to approximate almost all structures well, and the number of excluded structures was negligible.

6.2.6.4 Rotational averages over pseudotime

To generate the rotational averages of distinct endocytic structures over pseudotime, the data set was first filtered according to the cell-type specific curvature cut-off ($0.016\,\mathrm{nm}^{-1}$ for SK-MEL-2; $0.014\,\mathrm{nm}^{-1}$ for U-2 OS and 3T3) to exclude non-endocytic structures (see Section 3.2.6). Next, all structures were sorted along their closing angle θ, and split into 10 equal-sized bins resulting in $n = 163$ structures per bin for SK-MEL-2; $n = 24$ structures per bin for U-2 OS; and $n = 68$ structures per bin for 3T3.

These sites were then spatially and rotationally aligned and re-scaled to the average radius of all sites within the same bin. To visualize the average distribution of clathrin at distinct endocytic stages, rotational averaging was performed. To this end, 72 duplicates of each structure were generated and rotated by 5° with respect to each other.

Instead of generating averages for 10 distinct bins, the dynamic remodeling of the clathrin coat can also be visualized using a sliding window of 30 sites per frame, in a 20-site frame-to-frame increment. The resulting movie is available on BioStudies (https://www.ebi.ac.uk/biostudies/) under accession number S-BIAD566.

6.2.6.5 Simulations

The LocMoFit simulation engine implemented in SMAP was derived from the version first described in Thevathasan *et al.*, 2019. Simulation parameters including the number of photons per localization, background photons, and fluorophore on-time $t_(frame)$, were extracted directly from our experimental data. A two-state fluorophore model (on and off state), including bleaching was assumed (Sage *et al.*, 2019).

An equal distribution of closing angle θ from 0 to 100° was sampled, and the respective surface area was calculated according to the cooperative curvature model as $A(\theta) = 2\pi(1 - \cos\theta)/H(\theta)^2$. $H(\theta)$ is defined by Equation 3.3, and fitting parameters were determined based on $H(\theta)$ in Table 3.3.

Next, protein coordinates for each simulated structure were generated. To this end, randomly drawn samples were taken ($N_{\text{sample}} \propto A$) from the PDF of the hollow spherical cap with no uncertainty.

A fluorescent label was then generated at that protein position, at a probability $p_{\text{label}} = 0.6$.

Linkage errors in x, y, and z were assumed to be normally distributed variables with a variance corresponding to a displacement by 5 nm and added to the fluorescent label. The fluorophores were assumed to randomly rotate in 3D space between blinks.

Each fluorophore was assumed to appear at random time points, staying in the on-state for t_{frame}, which was determined as a random variable from an exponential distribution (mean = 1.6 frames).

The reactivation probability was estimated at $p_{\text{react}} = 0.5$. Non-reactivated fluorophores were considered bleached and did not appear again at any time point.

The brightness of a fluorophore was considered constant, and thus proportional to the fraction of time the fluorophore was in its on-state per frame.

The number of emitted photons was estimated as a random Poisson distributed variable with a mean value corresponding to the average brightness per frame.

A Cramér-Rao lower bound (CRLB) was calculated in x, y, and z for each frame based on the theoretical Gaussian PSF (Mortensen *et al.*, 2010). A mean number of 11,000 Photons and 130 background photons per pixel were used. Alternatively, a 3D cSpline PSF model derived from bead calibrations was used (Li *et al.*, 2018) for error estimation. This error was added to the true x, y, and z positions of the fluorophore as normally distributed random values with a variance corresponding to the calculated CRLB.

6.2.7 Further data analysis

Using the plugin 'ROIManager:Analyze:SMLMModelFit_saveResults', parameters determined from the MLE-based model fitting could be saved as a text file. The saved parameters included 'ID' (unique identifier per structure or site); 'filenumber' (specifying the image from which a certain site originated); 'projectionArea' (referred to as A_p in this work); 'radius' (referred to as R in this work); 'realCloseAngle' (referred to as θ in this work); 'curvature' (referred to as H in this work); and 'realSurfaceArea' (referred to as A in this work).

These data were further analyzed using R (R Core Team, 2022) for summary, plotting, and clathrin growth model fitting.

6.2.7.1 Data manipulation

Completely flat structures were generally fitted with negative curvature. Thus, these sites were assigned a closing angle $\theta = 0.000,1°$ and curvature $H = 0\,\mathrm{nm}^{-1}$ to approximate them as truly flat structures, corresponding to the earliest detectable endocytic stages. $\theta = 0.000,1°$ was chosen instead of $\theta = 0°$ to avoid division by 0 at a later analysis step. Additionally, the edge length ε was calculated, according to the Equations summarized in Table 6.5. Cell-type specific cut-offs ensure the exclusion of the non-endocytic population of clathrin-coated structures (see Section 3.2.6) For SK-MEL-2 a cut-off of $0.016\,\mathrm{nm}^{-1}$ was chosen. Structures extracted from U-2 OS and 3T3 cells were cut-off at a curvature of $0.014\,\mathrm{nm}^{-1}$.

$R = A/2\pi(1-\cos\theta)$
$H = 1/R$
$A = 2\pi R^2(1-\cos\theta)$
$A_p \begin{cases} \pi(R\sin\theta)^2 & \theta < 90° \\ \pi R^2 & \theta \geq 90° \end{cases}$
$\varepsilon = 2\pi R\sin\theta$

Table 6.5 | Geometric descriptions of a spherical cap. These equations were used to derive the following geometries from the extracted LocMoFit model parameters (surface area A and closing angle θ): Radius R; curvature H; projected area A_p; and edge length ε.

Next, a pseudotime was assigned to each structure. To this end, the data sets sorted in θ were first filtered by the cell-type specific cut-off. Next, each site was assigned a rank index. Flat sites were assigned the same pseudo-temporal index of 0.

6.2.7.2 Clathrin coat growth model fitting

To fit the different growth models according to the Equations summarized in Table 3.1, a Nonlinear Least Squares (NLS) estimation was used. The fit was performed for curvature over closing angle $H(\theta)$. The extracted fit parameters for all fits in curvature $H(\theta)$ were mapped to the surface area $A(\theta)$; projected area $A_p(\theta)$; or edge length $\varepsilon(\theta)$, to generate Figures 1.8, 3.17, & 3.22. Fit results for all growth models, fitted directly for all geometric quantities are summarized in Tables 3.3, 3.4, & 3.5.

6.2.8 Data availability

Data presented in this work is available on BioStudies(https://www.ebi.ac.uk/biostudies/) under accession number S-BIAD566. Data includes a pseudo-temporal movie; localization data; LocMoFit analysis results; a gallery of all sites; and rotating movies of all sites.

File descriptions below are citations from the pre-print of the here presented work published on BioRxiv, and the file descriptions as presented on BioStudies.

Pseudo-temporal movie (mp4 format, 1 file) Pseudo-temporal movie of clathrin coat remodeling during endocytosis in SK-MEL-2 cells. Each frame corresponds to a sliding window average of 30 sites, with a frame-to-frame increment of 20 sites. The median pseudotime of those 30 sites is indicated.

Localization data (csv format, 23 files) Localization coordinates for all superresolution images, grouped by cell line (SK-MEL-2, 13 files; U2OS, 3 files; 3T3, 7 files). The localizations were grouped (localizations that persisted over several adjacent frames and thus resulted from the same single fluorophore were combined into one localization) and filtered with a maximum localization precision of 20 nm in xy, and 30 nm in z. The first 2000 frames of each acquisition are excluded since the blinking density is too high for reliable localization. Each file contains the columns xnm (x coordinate in nm); ynm (y coordinate in nm); znm (z coordinate in nm); locprecnm (localization precision in xy in nm); locpreczнm (localization precision in z in nm); frame; site_ID (marks all localizations belonging to the respective segmented clathrin structure; localizations outside of analyzed sites are put to 0); filenumber (identifier for acquisition file, unique for each cell line). Identifiers for acquisition files and clathrin-coated structures are kept consistent between all supplementary data.

Model fit results (CSV format, 23 files) Results from LocMoFit analysis of individual clathrin-coated structures, grouped by cell line. Columns are ID (identifier for individual structures); file_number (identifier for each acquisition file); cell_line; disconnected_sites (true for non-endocytic sites). Model fit parameters calculated for each structure using LocMoFit include theta θ; radius R; curvature H; surface_area A; rim_length ε; and projected_area A_p. Further included in the table are the corrected values theta_corrected

and curvature corrected, where each structure fitted with a negative radius was manually put to θ =0.000,1° and curvature = 0 nm^{-1}.

Site gallery (PDF format, 3 files) Snapshots of all analyzed clathrin-coated structures and their respective model fit results. For each structure, shown are the top view (left), as well as 50 nm side-view cross-sections through the structure at angles 0°, 45°, 90°, and 135° (left to right). Shown are site number, theta θ, surface area A, and radius R. Scale bar is 100 nm.

Rotating movies of all sites, (mp4 format, 49 files) Rotating movies of the 3D SMLM data (left) and renderings of the corresponding models (right) of all clathrin-coated structures in SK-MEL-2 cells. Shown are site identifiers and model fit results (theta, surface area A, and radius R). Scale bar is 100 nm.

Bibliography

Abbe, E. 1873. Beiträge zur Theorie des Mikroskops und der mikroskopischen Wahrnehmung. *Archiv für Mikroskopische Anatomie* **9(1)**: 413–468. DOI: 10.1007/BF02956173.

Aghamohammadzadeh, S. and K. R. Ayscough. 2009. Differential requirements for actin during yeast and mammalian endocytosis. *Nature Cell Biology* **11(8)**: 1039–1042. DOI: 10.1038/ncb1918.

Aguet, F., C. N. Antonescu, M. Mettlen, S. L. Schmid, and G. Danuser. 2013. Advances in Analysis of Low Signal-to-Noise Images Link Dynamin and AP2 to the Functions of an Endocytic Checkpoint. *Developmental Cell* **26(3)**: 279–291. DOI: 10.1016/j.devcel.2013.06.019.

Airy, G. B. 1835. On the Diffraction of an Object-glass with Circular Aperture. *Transactions of the Cambridge Philosophical Society* **5** 283.

Aitken, C. E., R. A. Marshall, and J. D. Puglisi. 2008. An Oxygen Scavenging System for Improvement of Dye Stability in Single-Molecule Fluorescence Experiments. *Biophysical Journal* **94(5)**: 1826–1835. DOI: 10.1529/biophysj.107.117689.

Akamatsu, M., R. Vasan, D. Serwas, M. Ferrin, P. Rangamani, and D. G. Drubin. 2019. Principles of self-organization and load adaptation by the actin cytoskeleton during clathrin-mediated endocytosis. *bioRxiv*: 678797. DOI: 10.1101/678797.

Akamatsu, M., R. Vasan, D. Serwas, M. A. Ferrin, P. Rangamani, and D. G. Drubin. 2020. Principles of self-organization and load adaptation by the actin cytoskeleton during clathrin-mediated endocytosis. *eLife* **9** e49840. DOI: 10.7554/eLife.49840.

Alberts, B., J. Wilson, and T. Hunt. 2008. Molecular biology of the cell. 5th ed. New York: Garland Science. ISBN: 978-0-8153-4105-5.

Almeida-Souza, L., R. A. W. Frank, J. García-Nafría, A. Colussi, N. Gunawardana, C. M. Johnson, M. Yu, G. Howard, B. Andrews, Y. Vallis, and H. T. McMahon. 2018. A Flat BAR Protein Promotes Actin Polymerization at the Base of Clathrin-Coated Pits. *Cell* **174(2)**: 325–337.e14. DOI: 10.1016/j.cell.2018.05.020.

Anderson, R. G. W., J. L. Goldstein, and M. S. Brown. 1977. A mutation that impairs the ability of lipoprotein receptors to localise in coated pits on the cell surface of human fibroblasts. *Nature* **270(5639)**: 695–699. DOI: 10.1038/270695a0.

Ando, R., H. Mizuno, and A. Miyawaki. 2004. Regulated fast nucleocytoplasmic shuttling observed by reversible protein highlighting. *Science (New York, N.Y.)* **306(5700)**: 1370–1373. DOI: 10.1126/science.1102506.

Antonny, B., C. Burd, P. D. Camilli, E. Chen, O. Daumke, K. Faelber, M. Ford, V. A. Frolov, A. Frost, J. E. Hinshaw, T. Kirchhausen, M. M. Kozlov, M. Lenz, H. H. Low, H. McMahon, C. Merrifield, T. D. Pollard, P. J. Robinson, A. Roux, and S. Schmid. 2016. Membrane fission by dynamin: what we know and what we need to know. *The EMBO Journal* **35(21)**: 2270–2284. DOI: 10.15252/embj.201694613.

Aquino, D., A. Schönle, C. Geisler, C. v. Middendorff, C. A. Wurm, Y. Okamura, T. Lang, S. W. Hell, and A. Egner. 2011. Two-color nanoscopy of three-dimensional volumes by 4Pi detection of stochastically switched fluorophores. *Nature Methods* **8(4)**: 353–359. DOI: 10.1038/nmeth.1583.

Arasada, R., W. A. Sayyad, J. Berro, and T. D. Pollard. 2018. High-speed superresolution imaging of the proteins in fission yeast clathrin-mediated endocytic actin patches. *Molecular Biology of the Cell* **29(3)**: 295–303. DOI: 10.1091/mbc.E17-06-0415.

Avinoam, O., M. Schorb, C. J. Beese, J. A. G. Briggs, and M. Kaksonen. 2015. Endocytic sites mature by continuous bending and remodeling of the clathrin coat. *Science* **348(6241)**: 1369–1372. DOI: 10.1126/science.aaa9555.

Axelrod, D. 2001. Total Internal Reflection Fluorescence Microscopy in Cell Biology. *Traffic* **2(11)**: 764–774. DOI: 10.1034/j.1600-0854.2001.21104.x.

Baddeley, D. and J. Bewersdorf. 2018. Biological Insight from Super-Resolution Microscopy: What We Can Learn from Localization-Based Images. *Annual Review of Biochemistry* **87(1)**: 965–989. DOI: 10.1146/annurev-biochem-060815-014801.

Baddeley, D., M. B. Cannell, and C. Soeller. 2010. Visualization of Localization Microscopy Data. *Microscopy and Microanalysis* **16(1)**: 64–72. DOI: 10.1017/S143192760999122X.

Baddeley, D., M. B. Cannell, and C. Soeller. 2011. Three-dimensional sub-100 nm super-resolution imaging of biological samples using a phase ramp in the objective pupil. *Nano Research* **4(6)**: 589–598. DOI: 10.1007/s12274-011-0115-z.

Bai, X.-c., G. McMullan, and S. H. W. Scheres. 2015. How cryo-EM is revolutionizing structural biology. *Trends in Biochemical Sciences* **40(1)**: 49–57. DOI: 10.1016/j.tibs.2014.10.005.

Barasoain, I., J. F. Díaz, and J. M. Andreu. 2010. Chapter 19 - Fluorescent Taxoid Probes for Microtubule Research. *Methods in Cell Biology*. **95** Microtubules, in vitro. Academic Press: 353–372. DOI: 10.1016/S0091-679X(10)95019-X.

Basu, R., E. L. Munteanu, and F. Chang. 2014. Role of turgor pressure in endocytosis in fission yeast. *Molecular Biology of the Cell* **25(5)**: 679–687. DOI: 10.1091/mbc.e13-10-0618.

Bates, M., T. R. Blosser, and X. Zhuang. 2005. Short-Range Spectroscopic Ruler Based on a Single-Molecule Optical Switch. *Physical Review Letters* **94(10)**: 108101. DOI: 10.1103/PhysRevLett.94.108101.

Beckers, J. M. 1993. Adaptive Optics for Astronomy: Principles, Performance, and Applications. *Annual Review of Astronomy and Astrophysics* **31(1)**: 13–62. DOI: 10.1146/annurev.aa.31.090193.000305.

Betzig, E. 1995. Proposed method for molecular optical imaging. *Optics Letters* **20(3)**: 237–239. DOI: 10.1364/OL.20.000237.

Betzig, E., G. H. Patterson, R. Sougrat, O. W. Lindwasser, S. Olenych, J. S. Bonifacino, M. W. Davidson, J. Lippincott-Schwartz, and H. F. Hess. 2006. Imaging Intracellular Fluorescent Proteins at Nanometer Resolution. *Science* **313(5793)**: 1642–1645. DOI: 10.1126/science.1127344.

Bhave, M., M. Mettlen, X. Wang, and S. L. Schmid. 2020. Early and non-redundant functions of dynamin isoforms in clathrin-mediated endocytosis. *Molecular Biology of the Cell*: mbc.E20–06–0363. DOI: 10.1091/mbc.E20-06-0363.

Booth, M. J. 2014. Adaptive optical microscopy: the ongoing quest for a perfect image. *Light: Science & Applications* **3(4)**: e165–e165. DOI: 10.1038/lsa.2014.46.

Boulant, S., C. Kural, J.-C. Zeeh, F. Ubelmann, and T. Kirchhausen. 2011. Actin dynamics counteract membrane tension during clathrin-mediated endocytosis. *Nature Cell Biology* **13(9)**: 1124–1131. DOI: 10.1038/ncb2307.

Bourg, N., C. Mayet, G. Dupuis, T. Barroca, P. Bon, S. Lécart, E. Fort, and S. Lévêque-Fort. 2015. Direct optical nanoscopy with axially localized detection. *Nature Photonics* **9(9)**: 587–593. DOI: 10.1038/nphoton.2015.132.

Bretscher, M. S., J. N. Thomson, and B. M. Pearse. 1980. Coated pits act as molecular filters. *Proceedings of the National Academy of Sciences* **77(7)**: 4156–4159. DOI: 10.1073/pnas.77.7.4156.

Brown, M. S. and J. L. Goldstein. 1976. Analysis of a mutant strain of human fibroblasts with a defect in the internalization of receptor-bound low density lipoprotein. *Cell* **9(4 PT 2)**: 663–674. DOI: 10.1016/0092-8674(76)90130-6.

Bucher, D., F. Frey, K. A. Sochacki, S. Kummer, J.-P. Bergeest, W. J. Godinez, H.-G. Kräusslich, K. Rohr, J. W. Taraska, U. S. Schwarz, and S. Boulant. 2018. Clathrin-adaptor ratio and membrane tension regulate the flat-to-curved transition of the clathrin coat during endocytosis. *Nature Communications* **9(1)**: 1109. DOI: 10.1038/s41467-018-03533-0.

Carrington, G., D. Tomlinson, and M. Peckham. 2019. Exploiting nanobodies and Affimers for superresolution imaging in light microscopy. *Molecular Biology of the Cell* **30(22)**: 2737–2740. DOI: 10.1091/mbc.E18-11-0694.

Chen, Z. and S. L. Schmid. 2020. Evolving models for assembling and shaping clathrin-coated pits. *Journal of Cell Biology* **219(9)**: e202005126. DOI: 10.1083/jcb.202005126.

Cheng, Y., W. Boll, T. Kirchhausen, S. C. Harrison, and T. Walz. 2007. Cryo-electron Tomography of Clathrin-coated Vesicles: Structural Implications for Coat Assembly. *Journal of Molecular Biology* **365(3)**: 892–899. DOI: 10.1016/j.jmb.2006.10.036.

Cieslinski, K. 2018. Structural studies of the budding yeast kinetochore using single molecule localization microscopy. PhD thesis. Duisburg-Essen.

Cocucci, E., F. Aguet, S. Boulant, and T. Kirchhausen. 2012. The First Five Seconds in the Life of a Clathrin-Coated Pit. *Cell* **150(3)**: 495–507. DOI: 10.1016/j.cell.2012.05.047.

Collins, A., A. Warrington, K. A. Taylor, and T. Svitkina. 2011. Structural organization of the actin cytoskeleton at sites of clathrin-mediated endocytosis. *Curr. Biol.* **21** DOI: 10.1016/j.cub.2011.05.048.

Combs, C. A. and H. Shroff. 2017. Fluorescence Microscopy: A Concise Guide to Current Imaging Methods. *Current Protocols in Neuroscience* **79(1)**: 2.1.1–2.1.25. DOI: 10.1002/cpns.29.

Curd, A. P., J. Leng, R. E. Hughes, A. J. Cleasby, B. Rogers, C. H. Trinh, M. A. Baird, Y. Takagi, C. Tiede, C. Sieben, S. Manley, T. Schlichthaerle, R. Jungmann, J. Ries, H. Shroff, and M. Peckham. 2021. Nanoscale Pattern Extraction from Relative Positions of Sparse 3D Localizations. *Nano Letters* **21(3)**: 1213–1220. DOI: 10.1021/acs.nanolett.0c03332.

Dannhauser, P. N. 2015. Effect of clathrin light chains on the stiffness of clathrin lattices and membrane budding. *Traffic* **16** DOI: 10.1111/tra.12263.

Dannhauser, P. N. and E. J. Ungewickell. 2012. Reconstitution of clathrin-coated bud and vesicle formation with minimal components. *Nat. Cell Biol.* **14** DOI: 10.1038/ncb2478.

Dasgupta, A., J. Deschamps, U. Matti, U. Hübner, J. Becker, S. Strauss, R. Jungmann, R. Heintzmann, and J. Ries. 2021. Direct supercritical angle localization microscopy for nanometer 3D superresolution. *Nature Communications* **12(1)**: 1180. DOI: 10.1038/s41467-021-21333-x.

Daumke, O., A. Roux, and V. Haucke. 2014. BAR Domain Scaffolds in Dynamin-Mediated Membrane Fission. *Cell* **156(5)**: 882–892. DOI: 10.1016/j.cell.2014.02.017.

Dempsey, G. T., M. Bates, W. E. Kowtoniuk, D. R. Liu, R. Y. Tsien, and X. Zhuang. 2009. Photoswitching Mechanism of Cyanine Dyes. *Journal of the American Chemical Society* **131(51)**: 18192–18193. DOI: 10.1021/ja904588g.

Dempsey, G. T., J. C. Vaughan, K. H. Chen, M. Bates, and X. Zhuang. 2011. Evaluation of fluorophores for optimal performance in localization-based super-resolution imaging. *Nature Methods* **8(12)**: 1027–1036. DOI: 10.1038/nmeth.1768.

Deschamps, J. 2017. Towards quantitative high-throughput 3D localization microscopy. PhD thesis. Ruprecht-Karls-Universität Heidelberg.

Deschamps, J., M. Mund, and J. Ries. 2014. 3D superresolution microscopy by supercritical angle detection. *Optics Express* **22(23)**: 29081–29091. DOI: 10.1364/OE.22.029081.

Deschamps, J. and J. Ries. 2020. EMU: reconfigurable graphical user interfaces for Micro-Manager. *BMC Bioinformatics* **21(1)**: 456. DOI: 10.1186/s12859-020-03727-8.

Deschamps, J., A. Rowald, and J. Ries. 2016. Efficient homogeneous illumination and optical sectioning for quantitative single-molecule localization microscopy. *Optics Express* **24(24)**: 28080. DOI: 10.1364/OE.24.028080.

Dickson, R. M., A. B. Cubitt, R. Y. Tsien, and W. E. Moerner. 1997. On/off blinking and switching behaviour of single molecules of green fluorescent protein. *Nature* **388(6640)**: 355–358. DOI: 10.1038/41048.

Doyon, J. B., B. Zeitler, J. Cheng, A. T. Cheng, J. M. Cherone, Y. Santiago, A. H. Lee, T. D. Vo, Y. Doyon, J. C. Miller, D. E. Paschon, L. Zhang, E. J. Rebar, P. D. Gregory, F. D. Urnov, and D. G. Drubin. 2011. Rapid and efficient clathrin-mediated endocytosis revealed in genome-edited mammalian cells. *Nature Cell Biology* **13(3)**: 331–337. DOI: 10.1038/ncb2175.

Edeling, M. A., C. Smith, and D. Owen. 2006. Life of a clathrin coat: insights from clathrin and AP structures. *Nature Reviews Molecular Cell Biology* **7(1)**: 32–44. DOI: 10.1038/nrm1786.

Edelstein, A., N. Amodaj, K. Hoover, R. Vale, and N. Stuurman. 2010. Computer Control of Microscopes Using μManager. *Current Protocols in Molecular Biology* **92(1)**. DOI: 10.1002/0471142727.mb1420s92.

Edelstein, A. D., M. A. Tsuchida, N. Amodaj, H. Pinkard, R. D. Vale, and N. Stuurman. 2014. Advanced methods of microscope control using μManager software. *Journal of Biological Methods* **1(2)**: e10. DOI: 10.14440/jbm.2014.36.

Ehrlich, M. 2004. Endocytosis by random initiation and stabilization of clathrin-coated pits. *Cell* **118** DOI: 10.1016/j.cell.2004.08.017.

Endesfelder, U., K. Finan, S. J. Holden, P. R. Cook, A. N. Kapanidis, and M. Heilemann. 2013. Multiscale Spatial Organization of RNA Polymerase in Escherichia coli. *Biophysical Journal* **105(1)**: 172–181. DOI: 10.1016/j.bpj.2013.05.048.

Engqvist-Goldstein, Å. E., R. A. Warren, M. M. Kessels, J. H. Keen, J. Heuser, and D. G. Drubin. 2001. The actin-binding protein Hip1R associates with clathrin during early stages of endocytosis and promotes clathrin assembly in vitro. *Journal of Cell Biology* **154(6)**: 1209–1224. DOI: 10.1083/jcb.200106089.

Ferguson, J. P., S. D. Huber, N. M. Willy, E. Aygün, S. Goker, T. Atabey, and C. Kural. 2017. Mechanoregulation of clathrin-mediated endocytosis. *Journal of Cell Science* **130(21)**: 3631–3636. DOI: 10.1242/jcs.205930.

Ford, M. G. 2001. Simultaneous binding of PtdIns(4,5) P2 and clathrin by AP180 in the nucleation of clathrin lattices on membranes. *Science* **291** DOI: 10.1126/science.291.5506.1051.

Fotin, A., Y. Cheng, P. Sliz, N. Grigorieff, S. C. Harrison, T. Kirchhausen, and T. Walz. 2004. Molecular model for a complete clathrin lattice from electron cryomicroscopy. *Nature* **432(7017)**: 573–579. DOI: 10.1038/nature03079.

Frey, F., D. Bucher, K. A. Sochacki, J. Taraska, S. Boulant, and U. S. Schwarz. 2020. Eden growth models for flat clathrin lattices with vacancies. *New Journal of Physics*. DOI: 10.1088/1367-2630/ab99e1.

Frey, F. and U. S. Schwarz. 2020. Competing pathways for the invagination of clathrin-coated membranes. *Soft Matter* **16(47)**: 10723–10733. DOI: 10.1039/D0SM01375G.

Früh, S. M., U. Matti, P. R. Spycher, M. Rubini, S. Lickert, T. Schlichthaerle, R. Jungmann, V. Vogel, J. Ries, and I. Schoen. 2021. Site-Specifically-Labeled Antibodies for Super-Resolution Microscopy Reveal *In Situ* Linkage Errors. *ACS Nano* **15(7)**: 12161–12170. DOI: 10.1021/acsnano.1c03677.

Fujimoto, L. M., R. Roth, J. E. Heuser, and S. L. Schmid. 2000. Actin assembly plays a variable, but not obligatory role in receptor-mediated endocytosis in mammalian cells. *Traffic* **1** DOI: 10.1034/j.1600-0854.2000.010208.x.

Gaidarov, I., F. Santini, R. A. Warren, and J. H. Keen. 1999. Spatial control of coated-pit dynamics in living cells. *Nature Cell Biology* **1(1)**: 1–7. DOI: 10.1038/8971.

Gautier, A., A. Juillerat, C. Heinis, I. R. Corrêa, M. Kindermann, F. Beaufils, and K. Johnsson. 2008. An Engineered Protein Tag for Multiprotein Labeling in Living Cells. *Chemistry & Biology* **15(2)**: 128–136. DOI: 10.1016/j.chembiol.2008.01.007.

Giepmans, B. N. G., S. R. Adams, M. H. Ellisman, and R. Y. Tsien. 2006. The Fluorescent Toolbox for Assessing Protein Location and Function. *Science* **312(5771)**: 217–224. DOI: 10.1126/science.1124618.

Götzke, H., M. Kilisch, M. Martínez-Carranza, S. Sograte-Idrissi, A. Rajavel, T. Schlichthaerle, N. Engels, R. Jungmann, P. Stenmark, F. Opazo, and S. Frey. 2019. The ALFA-tag is a highly versatile tool for nanobody-based bioscience applications. *Nature Communications* **10(1)**: 4403. DOI: 10.1038/s41467-019-12301-7.

Haar, E. ter, A. Musacchio, S. C. Harrison, and T. Kirchhausen. 1998. Atomic Structure of Clathrin: A β Propeller Terminal Domain Joins an α Zigzag Linker. *Cell* **95(4)**: 563–573. DOI: 10.1016/S0092-8674(00)81623-2.

Hassinger, J. E., G. Oster, D. G. Drubin, and P. Rangamani. 2017. Design principles for robust vesiculation in clathrin-mediated endocytosis. *Proceedings of the National Academy of Sciences of the United States of America* **114(7)**: E1118–E1127. DOI: 10.1073/pnas.1617705114.

He, K., R. Marsland III, S. Upadhyayula, E. Song, S. Dang, B. R. Capraro, W. Wang, W. Skillern, R. Gaudin, M. Ma, and T. Kirchhausen. 2017. Dynamics of phosphoinositide conversion in clathrin-mediated endocytic traffic. *Nature* **552(7685)**: 410–414. DOI: 10.1038/nature25146.

Heilemann, M., S. van de Linde, A. Mukherjee, and M. Sauer. 2009. Super-Resolution Imaging with Small Organic Fluorophores. *Angewandte Chemie International Edition* **48(37)**: 6903–6908. DOI: 10.1002/anie.200902073.

Heilemann, M., S. van de Linde, M. Schüttpelz, R. Kasper, B. Seefeldt, A. Mukherjee, P. Tinnefeld, and M. Sauer. 2008. Subdiffraction-Resolution Fluorescence Imaging with Conventional Fluorescent Probes. *Angewandte Chemie International Edition* **47(33)**: 6172–6176. DOI: 10.1002/anie.200802376.

Heilemann, M., E. Margeat, R. Kasper, M. Sauer, and P. Tinnefeld. 2005. Carbocyanine Dyes as Efficient Reversible Single-Molecule Optical Switch. *Journal of the American Chemical Society* **127(11)**: 3801–3806. DOI: 10.1021/ja044686x.

Heuser, J. 1980. Three-dimensional visualization of coated vesicle formation in fibroblasts. *The Journal of Cell Biology* **84(3)**: 560–583. DOI: 10.1083/jcb.84.3.560.

Holliger, P. and P. J. Hudson. 2005. Engineered antibody fragments and the rise of single domains. *Nature Biotechnology* **23(9)**: 1126–1136. DOI: 10.1038/nbt1142.

Hooke, R. and Jo. Martyn and Ja. Allestry. 1665. Micrographia, or, Some physiological descriptions of minute bodies made by magnifying glasses :with observations and inquiries thereupon /by R. Hooke ... London : Printed by Jo. Martyn and Ja. Allestry, printers to the Royal Society ... , DOI: 10.5962/bhl.title.904.

Höß, P. 2021. Towards a dynamic reconstruction of the endocytic machinery by dual-color localization microscopy. DOI: 10.11588/HEIDOK.00029646.

Huang, B., W. Wang, M. Bates, and X. Zhuang. 2008. Three-Dimensional Super-Resolution Imaging by Stochastic Optical Reconstruction Microscopy. *Science* **319(5864)**: 810–813. DOI: 10.1126/science.1153529.

Huang, F., G. Sirinakis, E. S. Allgeyer, L. K. Schroeder, W. C. Duim, E. B. Kromann, T. Phan, F. E. Rivera-Molina, J. R. Myers, I. Irnov, M. Lessard, Y. Zhang, M. A. Handel, C. Jacobs-Wagner, C. P. Lusk, J. E. Rothman, D. Toomre, M. J. Booth, and J. Bewersdorf. 2016. Ultra-High Resolution 3D Imaging of Whole Cells. *Cell* **166(4)**: 1028–1040. DOI: 10.1016/j.cell.2016.06.016.

Inc., T. M. 2022. MATLAB. Natick, Massachusett.

Itoh, T. 2005. Dynamin and the actin cytoskeleton cooperatively regulate plasma membrane invagination by BAR and F-BAR proteins. *Dev. Cell* **9** DOI: 10.1016/j.devcel.2005.11.005.

Jin, M., C. Shirazinejad, B. Wang, A. Yan, J. Schöneberg, S. Upadhyayula, K. Xu, and D. G. Drubin. 2022. Branched actin networks are organized for asymmetric force production during clathrin-mediated endocytosis in mammalian cells. *Nature Communications* **13(1)**: 3578. DOI: 10.1038/s41467-022-31207-5.

Juette, M. F., T. J. Gould, M. D. Lessard, M. J. Mlodzianoski, B. S. Nagpure, B. T. Bennett, S. T. Hess, and J. Bewersdorf. 2008. Three-dimensional sub–100 nm resolution fluorescence microscopy of thick samples. *Nature Methods* **5(6)**: 527–529. DOI: 10.1038/nmeth.1211.

Kaksonen, M., Y. Sun, and D. G. Drubin. 2003. A pathway for association of receptors, adaptors, and actin during endocytic internalization. *Cell* **115** DOI: 10.1016/S0092-8674(03)00883-3.

Kaksonen, M. and A. Roux. 2018. Mechanisms of clathrin-mediated endocytosis. *Nature Reviews Molecular Cell Biology* **19(5)**: 313–326. DOI: 10.1038/nrm.2017.132.

Kanaseki, T. 1969. THE "VESICLE IN A BASKET": A Morphological Study of the Coated Vesicle Isolated from the Nerve Endings of the Guinea Pig Brain, with Special Reference to the Mechanism of Membrane Movements. *The Journal of Cell Biology* **42(1)**: 202–220. DOI: 10.1083/jcb.42.1.202.

Kaplan, C., S. J. Kenny, X. Chen, J. Schöneberg, E. Sitarska, A. Diz-Muñoz, M. Akamatsu, K. Xu, and D. G. Drubin. 2022. Load adaptation by endocytic actin networks. *Molecular Biology of the Cell* **33(6)**: ar50. DOI: 10.1091/mbc.E21-11-0589.

Keppler, A., H. Pick, C. Arrivoli, H. Vogel, and K. Johnsson. 2004. Labeling of fusion proteins with synthetic fluorophores in live cells. *Proceedings of the National Academy of Sciences* **101(27)**: 9955–9959. DOI: 10.1073/pnas.0401923101.

Kessels, M. M. and B. Qualmann. 2021. Interplay between membrane curvature and the actin cytoskeleton. *Current Opinion in Cell Biology*. Cell Architecture **68** 10–19. DOI: 10.1016/j.ceb.2020.08.008.

Keyel, P. A., S. C. Watkins, and L. M. Traub. 2004. Endocytic Adaptor Molecules Reveal an Endosomal Population of Clathrin by Total Internal Reflection Fluorescence Microscopy * [boxs]. *Journal of Biological Chemistry* **279(13)**: 13190–13204. DOI: 10.1074/jbc.M312717200.

Kirchhausen, T. 1993. Coated pits and coated vesicles — sorting it all out. *Curr. Opin. Struct. Biol.* **3** DOI: 10.1016/S0959-440X(05)80150-2.

Kovtun, O., V. K. Dickson, B. T. Kelly, D. J. Owen, and J. A. G. Briggs. 2020. Architecture of the AP2/clathrin coat on the membranes of clathrin-coated vesicles. *Science Advances* **6(30)**: eaba8381. DOI: 10.1126/sciadv.aba8381.

Kukulski, W., M. Schorb, M. Kaksonen, and J. A. Briggs. 2012. Plasma membrane reshaping during endocytosis is revealed by time-resolved electron tomography. *Cell* **150** DOI: 10.1016/j.cell.2012.05.046.

Lackner, R. M., C. L. Johnny, and D. M. Chenoweth. 2020. Chapter Seventeen - Photoconvertible diazaxanthilidene dyes for live cell imaging. *Methods in Enzymology*. **639** Chemical Tools for Imaging, Manipulating, and Tracking Biological Systems: Diverse Methods for Optical Imaging and Conjugation. Academic Press: 379–388. DOI: 10.1016/bs.mie.2020.04.024.

Lacy, M. M., R. Ma, N. G. Ravindra, and J. Berro. 2018. Molecular mechanisms of force production in clathrin-mediated endocytosis. *FEBS Letters* **592(21)**: 3586–3605. DOI: 10.1002/1873-3468.13192.

Lambert, T. J. 2019. FPbase: a community-editable fluorescent protein database. *Nature Methods* **16(4)**: 277–278. DOI: 10.1038/s41592-019-0352-8.

Lardon, N., L. Wang, A. Tschanz, P. Hoess, M. Tran, E. D'Este, J. Ries, and K. Johnsson. 2021. Systematic Tuning of Rhodamine Spirocyclization for Super-resolution Microscopy. *Journal of the American Chemical Society* **143(36)**: 14592–14600. DOI: 10.1021/jacs.1c05004.

Legant, W. R., L. Shao, J. B. Grimm, T. A. Brown, D. E. Milkie, B. B. Avants, L. D. Lavis, and E. Betzig. 2016. High-density three-dimensional localization microscopy across large volumes. *Nature Methods* **13(4)**: 359–365. DOI: 10.1038/nmeth.3797.

Lelek, M., M. T. Gyparaki, G. Beliu, F. Schueder, J. Griffié, S. Manley, R. Jungmann, M. Sauer, M. Lakadamyali, and C. Zimmer. 2021. Single-molecule localization microscopy. *Nature Reviews Methods Primers* **1(1)**: 1–27. DOI: 10.1038/s43586-021-00038-x.

Lewis, W. H. 1937. Pinocytosis by Malignant Cells. *The American Journal of Cancer* **29(4)**: 666–679. DOI: 10.1158/ajc.1937.666.

Leyton-Puig, D., T. Isogai, E. Argenzio, B. van den Broek, J. Klarenbeek, H. Janssen, K. Jalink, and M. Innocenti. 2017. Flat clathrin lattices are dynamic actin-controlled hubs for clathrin-mediated endocytosis and signalling of specific receptors. *Nature Communications* **8** 16068. DOI: 10.1038/ncomms16068.

Li, H. and J. C. Vaughan. 2018. Switchable Fluorophores for Single-Molecule Localization Microscopy. *Chemical Reviews* **118(18)**: 9412–9454. DOI: 10.1021/acs.chemrev.7b00767.

Li, Y., M. Mund, P. Hoess, J. Deschamps, U. Matti, B. Nijmeijer, V. J. Sabinina, J. Ellenberg, I. Schoen, and J. Ries. 2018. Real-time 3D single-molecule localization using experimental point spread functions. *Nature Methods* **15(5)**: 367–369. DOI: 10.1038/nmeth.4661.

Li, Y., W. Shi, S. Liu, I. Cavka, Y.-L. Wu, U. Matti, D. Wu, S. Koehler, and J. Ries. 2022. Global fitting for high-accuracy multi-channel single-molecule localization. *Nature Communications* **13(1)**: 3133. DOI: 10.1038/s41467-022-30719-4.

Linde, S. van de, S. Wolter, M. Heilemann, and M. Sauer. 2010. The effect of photoswitching kinetics and labeling densities on super-resolution fluorescence imaging. *Journal of Biotechnology*. BioImaging - Contributions from Biology, Physics and Informatics **149(4)**: 260–266. DOI: 10.1016/j.jbiotec.2010.02.010.

Liu, A. P., F. Aguet, G. Danuser, and S. L. Schmid. 2010a. Local clustering of transferrin receptors promotes clathrin-coated pit initiation. *J. Cell Biol.* **191** DOI: 10.1083/jcb.201008117.

Liu, J., Y. Sun, G. F. Oster, and D. G. Drubin. 2010b. Mechanochemical crosstalk during endocytic vesicle formation. *Current opinion in cell biology* **22(1)**: 36. DOI: 10.1016/j.ceb.2009.11.009.

Liu, S., P. Hoess, and J. Ries. 2022. Super-Resolution Microscopy for Structural Cell Biology. *Annual Review of Biophysics* **51(1)**: 301–326. DOI: 10.1146/annurev-biophys-102521-112912.

Lizarrondo, J., D. P. Klebl, S. Niebling, M. Abella, M. A. Schroer, H. D. T. Mertens, K. Veith, R. Thuenauer, D. I. Svergun, M. Skruzny, F. Sobott, S. P. Muench, and M. M. Garcia-Alai. 2021. Structure of the endocytic adaptor complex reveals the basis for efficient membrane anchoring during clathrin-mediated endocytosis. *Nature Communications* **12(1)**: 2889. DOI: 10.1038/s41467-021-23151-7.

Loerke, D. 2009. Cargo and dynamin regulate clathrin-coated pit maturation. *PLoS Biol.* **7** DOI: 10.1371/journal.pbio.1000057.

Loerke, D., M. Wienisch, O. Kochubey, and J. Klingauf. 2005. Differential control of clathrin subunit dynamics measured with EW-FRAP microscopy. *Traffic* **6** DOI: 10.1111/j.1600-0854.2005.00329.x.

Loerke, D., M. Mettlen, S. L. Schmid, and G. Danuser. 2011. Measuring the Hierarchy of Molecular Events During Clathrin-Mediated Endocytosis. *Traffic* **12(7)**: 815–825. DOI: 10.1111/j.1600-0854.2011.01197.x.

Los, G. V., L. P. Encell, M. G. McDougall, D. D. Hartzell, N. Karassina, C. Zimprich, M. G. Wood, R. Learish, R. F. Ohana, M. Urh, D. Simpson, J. Mendez, K. Zimmerman, P. Otto, G. Vidugiris, J. Zhu, A. Darzins, D. H. Klaubert, R. F. Bulleit, and K. V. Wood. 2008. HaloTag: A Novel Protein Labeling Technology for Cell Imaging and Protein Analysis. *ACS Chemical Biology* **3(6)**: 373–382. DOI: 10.1021/cb800025k.

Maib, H., F. Ferreira, S. Vassilopoulos, and E. Smythe. 2018. Cargo regulates clathrin-coated pit invagination via clathrin light chain phosphorylation. *The Journal of Cell Biology* **217(12)**: 4253–4266. DOI: 10.1083/jcb.201805005.

Mayor, S. and R. E. Pagano. 2007. Pathways of clathrin-independent endocytosis. *Nature Reviews Molecular Cell Biology* **8(8)**: 603–612. DOI: 10.1038/nrm2216.

McKinney, S. A., C. S. Murphy, K. L. Hazelwood, M. W. Davidson, and L. L. Looger. 2009. A bright and photostable photoconvertible fluorescent protein. *Nature Methods* **6(2)**: 131–133. DOI: 10.1038/nmeth.1296.

McMahon, H. T. and E. Boucrot. 2011. Molecular mechanism and physiological functions of clathrin-mediated endocytosis. *Nat. Rev. Mol. Cell Biol.* **12** DOI: 10.1038/nrm3151.

Merrifield, C. J., M. E. Feldman, L. Wan, and W. Almers. 2002. Imaging actin and dynamin recruitment during invagination of single clathrin-coated pits. *Nat. Cell Biol.* **4** DOI: 10.1038/ncb837.

Merrifield, C. J. and M. Kaksonen. 2014. Endocytic Accessory Factors and Regulation of Clathrin-Mediated Endocytosis. *Cold Spring Harbor Perspectives in Biology* **6(11)**: a016733–a016733. DOI: 10.1101/cshperspect.a016733.

Merrifield, C. J., D. Perrais, and D. Zenisek. 2005. Coupling between clathrin-coated-pit invagination, cortactin recruitment, and membrane scission observed in live cells. *Cell* **121** DOI: 10.1016/j.cell.2005.03.015.

Metchnikoff, E. 1883. Untersuchungen über die mesodermalen Phagocyten einiger Wirbeltiere. *Biol Zentralbl* **3** 560–5.

Metschnikoff, E. 1887. Ueber den Kampf der Zellen gegen Erysipel-kokken. *Archiv für pathologische Anatomie und Physiologie und für klinische Medicin* **107(2)**: 209–249. DOI: 10.1007/BF01926053.

Mettlen, M. 2009. Endocytic accessory proteins are functionally distinguished by their differential effects on the maturation of clathrin-coated pits. *Mol. Biol. Cell* **20** DOI: 10.1091/mbc.e09-03-0256.

Mettlen, M., D. Loerke, D. Yarar, G. Danuser, and S. L. Schmid. 2010. Cargo- and adaptor-specific mechanisms regulate clathrin-mediated endocytosis. *J. Cell Biol.* **188** DOI: 10.1083/jcb.200908078.

Mettlen, M., P.-H. Chen, S. Srinivasan, G. Danuser, and S. L. Schmid. 2018. Regulation of Clathrin-Mediated Endocytosis. *Annual Review of Biochemistry* **87(1)**: 871–896. DOI: 10.1146/annurev-biochem-062917-012644.

Michie, M. S., R. Götz, C. Franke, M. Bowler, N. Kumari, V. Magidson, M. Levitus, J. Loncarek, M. Sauer, and M. J. Schnermann. 2017. Cyanine Conformational Restraint in the Far-Red Range. *Journal of the American Chemical Society* **139(36)**: 12406–12409. DOI: 10.1021/jacs.7b07272.

Miller, S. E. 2015. CALM regulates clathrin-coated vesicle size and maturation by directly sensing and driving membrane curvature. *Dev. Cell* **33** DOI: 10.1016/j.devcel.2015.03.002.

Mim, C. 2012. Structural basis of membrane bending by the N-BAR protein endophilin. *Cell* **149** DOI: 10.1016/j.cell.2012.01.048.

Moerner, W. E. and L. Kador. 1989. Optical detection and spectroscopy of single molecules in a solid. *Physical Review Letters* **62(21)**: 2535–2538. DOI: 10.1103/PhysRevLett.62.2535.

Morris, J. D. and C. K. Payne. 2019. Microscopy and Cell Biology: New Methods and New Questions. *Annual Review of Physical Chemistry* **70(1)**: 199–218. DOI: 10.1146/annurev-physchem-042018-052527.

Mortensen, K. I., L. S. Churchman, J. A. Spudich, and H. Flyvbjerg. 2010. Optimized localization analysis for single-molecule tracking and super-resolution microscopy. *Nature Methods* **7(5)**: 377–381. DOI: 10.1038/nmeth.1447.

Moulay, G., J. Lainé, M. Lemaître, M. Nakamori, I. Nishino, G. Caillol, K. Mamchaoui, L. Julien, F. Dingli, D. Loew, M. Bitoun, C. Leterrier, D. Furling, and S. Vassilopoulos. 2020. Alternative splicing of clathrin heavy chain contributes to the switch from coated pits to plaques. *Journal of Cell Biology* **219(9)**: e201912061. DOI: 10.1083/jcb.201912061.

Mund, M. 2016. Superresolution imaging of clathrin-mediated endocytosis in yeast.

Mund, M., J. A. van der Beek, J. Deschamps, S. Dmitrieff, P. Hoess, J. L. Monster, A. Picco, F. Nédélec, M. Kaksonen, and J. Ries. 2018. Systematic Nanoscale Analysis of Endocytosis Links Efficient Vesicle Formation to Patterned Actin Nucleation. *Cell* **174(4)**: 884–896.e17. DOI: 10.1016/j.cell.2018.06.032.

Mund, M., A. Tschanz, Y.-L. Wu, F. Frey, J. L. Mehl, M. Kaksonen, O. Avinoam, U. S. Schwarz, and J. Ries. 2023. Clathrin coats partially preassemble and subsequently bend during endocytosis. *Journal of Cell Biology* **222(3)**: e202206038. DOI: 10.1083/jcb.202206038.

Nahidiazar, L., A. V. Agronskaia, J. Broertjes, B. v. d. Broek, and K. Jalink. 2016. Optimizing Imaging Conditions for Demanding Multi-Color Super Resolution Localization Microscopy. *PLOS ONE* **11(7)**: e0158884. DOI: 10.1371/journal.pone.0158884.

Nawara, T. J., Y. D. Williams, T. C. Rao, Y. Hu, E. Sztul, K. Salaita, and A. L. Mattheyses. 2022. Imaging vesicle formation dynamics supports the flexible model of clathrin-mediated endocytosis. *Nature Communications* **13(1)**: 1732. DOI: 10.1038/s41467-022-29317-1.

Neumann, S. and S. L. Schmid. 2013. Dual role of BAR domain-containing proteins in regulating vesicle release catalyzed by the GTPase, dynamin-2. *The Journal of Biological Chemistry* **288(35)**: 25119–25128. DOI: 10.1074/jbc.M113.490474.

Nossal, R. 2001. Energetics of clathrin basket assembly. *Traffic* **2** DOI: 10.1034/j.1600-0854.2001.020208.x.

Obashi, K., K. A. Sochacki, M.-P. Strub, and J. W. Taraska. 2023. A conformational switch in clathrin light chain regulates lattice structure and endocytosis at the plasma membrane of mammalian cells. *Nature Communications* **14(1)**: 732. DOI: 10.1038/s41467-023-36304-7.

Opazo, F., M. Levy, M. Byrom, C. Schäfer, C. Geisler, T. W. Groemer, A. D. Ellington, and S. O. Rizzoli. 2012. Aptamers as potential tools for super-resolution microscopy. *Nature Methods* **9(10)**: 938–939. DOI: 10.1038/nmeth.2179.

Owen, D. M., C. Rentero, J. Rossy, A. Magenau, D. Williamson, M. Rodriguez, and K. Gaus. 2010. PALM imaging and cluster analysis of protein heterogeneity at the cell surface. *Journal of Biophotonics* **3(7)**: 446–454. DOI: 10.1002/jbio.200900089.

Pageon, S. V., T. Tabarin, Y. Yamamoto, Y. Ma, P. R. Nicovich, J. S. Bridgeman, A. Cohnen, C. Benzing, Y. Gao, M. D. Crowther, K. Tungatt, G. Dolton, A. K. Sewell, D. A. Price, O. Acuto, R. G. Parton, J. J. Gooding, J. Rossy, J. Rossjohn, and K. Gaus. 2016. Functional role of T-cell receptor nanoclusters in signal initiation and antigen discrimination. *Proceedings of the National Academy of Sciences* **113(37)**: E5454–E5463. DOI: 10.1073/pnas.1607436113.

Paraan, M., J. Mendez, S. Sharum, D. Kurtin, H. He, and S. M. Stagg. 2020. The structures of natively assembled clathrin-coated vesicles. *Science Advances* **6(30)**: eaba8397. DOI: 10.1126/sciadv.aba8397.

Patterson, G. H. and J. Lippincott-Schwartz. 2002. A photoactivatable GFP for selective photolabeling of proteins and cells. *Science (New York, N.Y.)* **297(5588)**: 1873–1877. DOI: 10.1126/science.1074952.

Pavani, S. R. P., M. A. Thompson, J. S. Biteen, S. J. Lord, N. Liu, R. J. Twieg, R. Piestun, and W. E. Moerner. 2009. Three-dimensional, single-molecule fluorescence imaging beyond the diffraction limit by using a double-helix point spread function. *Proceedings of the National Academy of Sciences* **106(9)**: 2995–2999. DOI: 10.1073/pnas.0900245106.

Pearse, B. M. and M. S. Robinson. 1984. Purification and properties of 100-kd proteins from coated vesicles and their reconstitution with clathrin. *The EMBO Journal* **3(9)**: 1951–1957.

Pearse, B. M. 1975. Coated vesicles from pig brain: purification and biochemical characterization. *J. Mol. Biol.* **97** DOI: 10.1016/S0022-2836(75)80024-6.

Pechstein, A., J. Bacetic, A. Vahedi-Faridi, K. Gromova, A. Sundborger, N. Tomlin, G. Krainer, O. Vorontsova, J. G. Schäfer, S. G. Owe, M. A. Cousin, W. Saenger, O. Shupliakov, and V. Haucke. 2010. Regulation of synaptic vesicle recycling by complex formation between

intersectin 1 and the clathrin adaptor complex AP2. *Proceedings of the National Academy of Sciences* **107(9)**: 4206–4211. DOI: 10.1073/pnas.0911073107.

Picco, A. and M. Kaksonen. 2018. Quantitative imaging of clathrin-mediated endocytosis. *Current Opinion in Cell Biology*. Membrane Trafficking **53** 105–110. DOI: 10.1016/j.ceb.2018.06.005.

Popova, N., I. Deyev, and A. Petrenko. 2013. Clathrin-Mediated Endocytosis and Adaptor Proteins. *Acta Naturae* **5(3)**: 62–73.

Qualmann, B., D. Koch, and M. M. Kessels. 2011. Let's go bananas: revisiting the endocytic BAR code. *The EMBO Journal* **30(17)**: 3501–3515. DOI: 10.1038/emboj.2011.266.

R Core Team. 2022. R: A Language and Environment for Statistical Computing. Vienna, Austria.

Rappoport, J. Z. and S. M. Simon. 2003. Real-time analysis of clathrin-mediated endocytosis during cell migration. *Journal of Cell Science* **116(5)**: 847–855. DOI: 10.1242/jcs.00289.

Rayleigh. 1879. XXXI. *Investigations in optics, with special reference to the spectroscope. The London, Edinburgh, and Dublin Philosophical Magazine and Journal of Science* **8(49)**: 261–274. DOI: 10.1080/14786447908639684.

Remington, S. J. 2011. Green fluorescent protein: A perspective. *Protein Science* **20(9)**: 1509–1519. DOI: 10.1002/pro.684.

Ries, J., C. Kaplan, E. Platonova, H. Eghlidi, and H. Ewers. 2012. A simple, versatile method for GFP-based super-resolution microscopy via nanobodies. *Nature Methods* **9(6)**: 582–584. DOI: 10.1038/nmeth.1991.

Robinson, M. S. 2015. Forty Years of Clathrin-coated Vesicles. *Traffic* **16(12)**: 1210–1238. DOI: 10.1111/tra.12335.

Rodriguez, E. A., R. E. Campbell, J. Y. Lin, M. Z. Lin, A. Miyawaki, A. E. Palmer, X. Shu, J. Zhang, and R. Y. Tsien. 2017. The growing and glowing toolbox of fluorescent and photoactive proteins. *Trends in biochemical sciences* **42(2)**: 111–129. DOI: 10.1016/j.tibs.2016.09.010.

Roth, T. F. and K. R. Porter. 1964. Yolk protein uptake in the oocyte of the mosquito Aedes aegypti. L. *J. Cell Biol.* **20** DOI: 10.1083/jcb.20.2.313.

Royle, S. J. 2006. The cellular functions of clathrin. *Cellular and molecular life sciences : CMLS* **63(16)**: 1823–1832. DOI: 10.1007/s00018-005-5587-0.

Rust, M. J., M. Bates, and X. Zhuang. 2006. Sub-diffraction-limit imaging by stochastic optical reconstruction microscopy (STORM). *Nature Methods* **3(10)**: 793–796. DOI: 10.1038/nmeth929.

Saff, E. B. and A. B. J. Kuijlaars. 1997. Distributing many points on a sphere. *The Mathematical Intelligencer* **19(1)**: 5–11. DOI: 10.1007/BF03024331.

Saffarian, S., E. Cocucci, and T. Kirchhausen. 2009. Distinct Dynamics of Endocytic Clathrin-Coated Pits and Coated Plaques. *PLOS Biology* **7(9)**: e1000191. DOI: 10.1371/journal.pbio.1000191.

Sage, D., T.-A. Pham, H. Babcock, T. Lukes, T. Pengo, J. Chao, R. Velmurugan, A. Herbert, A. Agrawal, S. Colabrese, A. Wheeler, A. Archetti, B. Rieger, R. Ober, G. M. Hagen, J.-B. Sibarita, J. Ries, R. Henriques, M. Unser, and S. Holden. 2019. Super-resolution fight club: assessment of 2D and 3D single-molecule localization microscopy software. *Nature Methods* **16(5)**: 387–395. DOI: 10.1038/s41592-019-0364-4.

Saleem, M. 2015. A balance between membrane elasticity and polymerization energy sets the shape of spherical clathrin coats. *Nat. Commun.* **6** DOI: 10.1038/ncomms7249.

Schermelleh, L., A. Ferrand, T. Huser, C. Eggeling, M. Sauer, O. Biehlmaier, and G. P. C. Drummen. 2019. Super-resolution microscopy demystified. *Nature Cell Biology* **21(1)**: 72–84. DOI: 10.1038/s41556-018-0251-8.

Schmid, S. L., A. Sorkin, and M. Zerial. 2014. Endocytosis: Past, Present, and Future. *Cold Spring Harbor Perspectives in Biology* **6(12)**: a022509. DOI: 10.1101/cshperspect.a022509.

Schnitzbauer, J., M. T. Strauss, T. Schlichthaerle, F. Schueder, and R. Jungmann. 2017. Super-resolution microscopy with DNA-PAINT. *Nature Protocols* **12(6)**: 1198–1228. DOI: 10.1038/nprot.2017.024.

Schoen, I., L. Aires, J. Ries, and V. Vogel. 2017. Nanoscale invaginations of the nuclear envelope: Shedding new light on wormholes with elusive function. *Nucleus* **8(5)**: 506–514. DOI: 10.1080/19491034.2017.1337621.

Schöneberg, J., D. Dambournet, T.-L. Liu, R. Forster, D. Hockemeyer, E. Betzig, and D. G. Drubin. 2018. 4D cell biology: big data image analytics and lattice light-sheet imaging reveal dynamics of clathrin-mediated endocytosis in stem cell–derived intestinal organoids. *Molecular Biology of the Cell* **29(24)**: 2959–2968. DOI: 10.1091/mbc.E18-06-0375.

Scott, B. L., K. A. Sochacki, S. T. Low-Nam, E. M. Bailey, Q. Luu, A. Hor, A. M. Dickey, S. Smith, J. G. Kerkvliet, J. W. Taraska, and A. D. Hoppe. 2018. Membrane bending occurs at all stages of clathrin-coat assembly and defines endocytic dynamics. *Nature Communications* **9(1)**: 1–9. DOI: 10.1038/s41467-018-02818-8.

Sengupta, P., T. Jovanovic-Talisman, D. Skoko, M. Renz, S. L. Veatch, and J. Lippincott-Schwartz. 2011. Probing protein heterogeneity in the plasma membrane using PALM and pair correlation analysis. *Nature Methods* **8(11)**: 969–975. DOI: 10.1038/nmeth.1704.

Shannon, C. 1949. Communication in the Presence of Noise. *Proceedings of the IRE* **37(1)**: 10–21. DOI: 10.1109/JRPROC.1949.232969.

Shechtman, Y., S. J. Sahl, A. S. Backer, and W. E. Moerner. 2014. Optimal Point Spread Function Design for 3D Imaging. *Physical Review Letters* **113(13)**: 133902. DOI: 10.1103/PhysRevLett.113.133902.

Shim, S.-H., C. Xia, G. Zhong, H. P. Babcock, J. C. Vaughan, B. Huang, X. Wang, C. Xu, G.-Q. Bi, and X. Zhuang. 2012. Super-resolution fluorescence imaging of organelles in live cells with photoswitchable membrane probes. *Proceedings of the National Academy of Sciences* **109(35)**: 13978–13983. DOI: 10.1073/pnas.1201882109.

Shivanandan, A., H. Deschout, M. Scarselli, and A. Radenovic. 2014. Challenges in quantitative single molecule localization microscopy. *FEBS Letters*. SI: Single molecule techniques - Applications in biology **588(19)**: 3595–3602. DOI: 10.1016/j.febslet.2014.06.014.

Shroff, H., H. White, and E. Betzig. 2008. Photoactivated localization microscopy (PALM) of adhesion complexes. *Current Protocols in Cell Biology* **Chapter 4** Unit 4.21. DOI: 10.1002/0471143030.cb0421s41.

Shtengel, G., J. A. Galbraith, C. G. Galbraith, J. Lippincott-Schwartz, J. M. Gillette, S. Manley, R. Sougrat, C. M. Waterman, P. Kanchanawong, M. W. Davidson, R. D. Fetter, and H. F. Hess. 2009. Interferometric fluorescent super-resolution microscopy resolves 3D cellular ultrastructure. *Proceedings of the National Academy of Sciences* **106(9)**: 3125–3130. DOI: 10.1073/pnas.0813131106.

Sirotkin, V., J. Berro, K. Macmillan, L. Zhao, and T. D. Pollard. 2010. Quantitative analysis of the mechanism of endocytic actin patch assembly and disassembly in fission yeast. *Mol. Biol. Cell* **21** DOI: 10.1091/mbc.e10-02-0157.

Sitarska, E. and A. Diz-Muñoz. 2020. Pay attention to membrane tension: Mechanobiology of the cell surface. *Current Opinion in Cell Biology* **66** 11–18. DOI: 10.1016/j.ceb.2020.04.001.

Skruzny, M. 2022. The endocytic protein machinery as an actin-driven membrane-remodeling machine. *European Journal of Cell Biology* **101(4)**: 151267. DOI: 10.1016/j.ejcb.2022.151267.

Smith, C. J., N. Grigorieff, and B. M. Pearse. 1998. Clathrin coats at 21 Å resolution: a cellular assembly designed to recycle multiple membrane receptors. *The EMBO Journal* **17(17)**: 4943–4953. DOI: 10.1093/emboj/17.17.4943.

Smith, S. M. and C. J. Smith. 2022. Capturing the mechanics of clathrin-mediated endocytosis. *Current Opinion in Structural Biology* **75** 102427. DOI: 10.1016/j.sbi.2022.102427.

Sochacki, K. A., A. M. Dickey, M.-P. Strub, and J. W. Taraska. 2017. Endocytic proteins are partitioned at the edge of the clathrin lattice in mammalian cells. *Nature Cell Biology* **19(4)**: 352–361. DOI: 10.1038/ncb3498.

Sochacki, K. A., B. L. Heine, G. J. Haber, J. R. Jimah, B. Prasai, M. A. Alfonzo-Méndez, A. D. Roberts, A. Somasundaram, J. E. Hinshaw, and J. W. Taraska. 2021. The structure and spontaneous curvature of clathrin lattices at the plasma membrane. *Developmental Cell* **56(8)**: 1131–1146.e3. DOI: 10.1016/j.devcel.2021.03.017.

Speiser, A., L.-R. Müller, P. Hoess, U. Matti, C. J. Obara, W. R. Legant, A. Kreshuk, J. H. Macke, J. Ries, and S. C. Turaga. 2021. Deep learning enables fast and dense single-molecule localization with high accuracy. *Nature Methods* **18(9)**: 1082–1090. DOI: 10.1038/s41592-021-01236-x.

Stabley, D. R., T. Oh, S. M. Simon, A. L. Mattheyses, and K. Salaita. 2015. Real-time fluorescence imaging with 20 nm axial resolution. *Nature Communications* **6(1)**: 8307. DOI: 10.1038/ncomms9307.

Swoboda, M., J. Henig, H.-M. Cheng, D. Brugger, D. Haltrich, N. Plumeré, and M. Schlierf. 2012. Enzymatic Oxygen Scavenging for Photostability without pH Drop in Single-Molecule Experiments. *ACS Nano* **6(7)**: 6364–6369. DOI: 10.1021/nn301895c.

Tagiltsev, G., C. A. Haselwandter, and S. Scheuring. 2021. Nanodissected elastically loaded clathrin lattices relax to increased curvature. *Science Advances* **7(33)**: eabg9934. DOI: 10.1126/sciadv.abg9934.

Tauber, A. I. 2003. Metchnikoff and the phagocytosis theory. *Nature Reviews Molecular Cell Biology* **4(11)**: 897–901. DOI: 10.1038/nrm1244.

Taylor, M. J., D. Perrais, and C. J. Merrifield. 2011. A High Precision Survey of the Molecular Dynamics of Mammalian Clathrin-Mediated Endocytosis. *PLoS Biology* **9(3)**: e1000604. DOI: 10.1371/journal.pbio.1000604.

Thevathasan, J. V. 2019. Establishing single-molecule localization microscopy as a quantitative tool towards structural cell biology. DOI: 10.11588/HEIDOK.00027336.

Thevathasan, J. V., M. Kahnwald, K. Cieśliński, P. Hoess, S. K. Peneti, M. Reitberger, D. Heid, K. C. Kasuba, S. J. Hoerner, Y. Li, Y.-L. Wu, M. Mund, U. Matti, P. M. Pereira, R. Henriques, B. Nijmeijer, M. Kueblbeck, V. J. Sabinina, J. Ellenberg, and J. Ries. 2019. Nuclear pores as versatile reference standards for quantitative superresolution microscopy. *Nature Methods* **16(10)**: 1045–1053. DOI: 10.1038/s41592-019-0574-9.

Thompson, R. E., D. R. Larson, and W. W. Webb. 2002. Precise Nanometer Localization Analysis for Individual Fluorescent Probes. *Biophysical Journal* **82(5)**: 2775–2783. DOI: 10.1016/S0006-3495(02)75618-X.

Thottacherry, J. J., M. Sathe, C. Prabhakara, and S. Mayor. 2019. Spoiled for Choice: Diverse Endocytic Pathways Function at the Cell Surface. *Annual Review of Cell and Developmental Biology* **35(1)**: 55–84. DOI: 10.1146/annurev-cellbio-100617-062710.

Traub, L. M. 2009. Tickets to ride: selecting cargo for clathrin-regulated internalization. *Nat. Rev. Mol. Cell Biol.* **10** DOI: 10.1038/nrm2751.

Traub, L. M. and J. S. Bonifacino. 2013. Cargo recognition in clathrin-mediated endocytosis. *Cold Spring Harb. Perspect. Biol.* **5** DOI: 10.1101/cshperspect.a016790.

Traub, L. M. 2011. Regarding the Amazing Choreography of Clathrin Coats. *PLOS Biology* **9(3)**: e1001037. DOI: 10.1371/journal.pbio.1001037.

Tsien, R. Y. 1998. The Green Fluorescent Protein. *Annual Review of Biochemistry* **67(1)**: 509–544. DOI: 10.1146/annurev.biochem.67.1.509.

Tsygankova, O. M. and J. H. Keen. 2019. A unique role for clathrin light chain A in cell spreading and migration. *Journal of Cell Science* **132(10)**: jcs224030. DOI: 10.1242/jcs.224030.

Ungewickell, E. and D. Branton. 1981. Assembly units of clathrin coats. *Nature* **289(5796)**: 420–422. DOI: 10.1038/289420a0.

Van Noorden, R. 2014. Nobel for microscopy that reveals inner world of cells. *Nature* **514(7522)**: 286–286. DOI: 10.1038/nature.2014.16097.

Vigers, G., R. Crowther, and B. Pearse. 1986. Three-dimensional structure of clathrin cages in ice. *The EMBO Journal* **5(3)**: 529–534. DOI: 10.1002/j.1460-2075.1986.tb04242.x.

Virant, D., B. Traenkle, J. Maier, P. D. Kaiser, M. Bodenhöfer, C. Schmees, I. Vojnovic, B. Pisak-Lukáts, U. Endesfelder, and U. Rothbauer. 2018. A peptide tag-specific nanobody enables high-quality labeling for dSTORM imaging. *Nature Communications* **9(1)**: 930. DOI: 10.1038/s41467-018-03191-2.

Weinberg, J. and D. G. Drubin. 2012. Clathrin-mediated endocytosis in budding yeast. *Trends Cell Biol.* **22** DOI: 10.1016/j.tcb.2011.09.001.

Willy, N. M., J. P. Ferguson, A. Akatay, S. Huber, U. Djakbarova, S. Silahli, C. Cakez, F. Hasan, H. C. Chang, A. Travesset, S. Li, R. Zandi, D. Li, E. Betzig, E. Cocucci, and C. Kural. 2021. De novo endocytic clathrin coats develop curvature at early stages of their formation. *Developmental Cell* **56(22)**: 3146–3159.e5. DOI: 10.1016/j.devcel.2021.10.019.

Wood, K. M. and C. J. Smith. 2021. Clathrin: the molecular shape shifter. *Biochemical Journal* **478(16)**: 3099–3123. DOI: 10.1042/BCJ20200740.

Woodward, M. P. and T. F. Roth. 1978. Coated vesicles: characterization, selective dissociation, and reassembly. *Proceedings of the National Academy of Sciences of the United States of America* **75(9)**: 4394–4398.

Wu, Y.-L. 2022. Maximum-likelihood model fitting for quantitative analysis of SMLM data. DOI: 10.11588/HEIDOK.00031920.

Wu, Y.-L., P. Hoess, A. Tschanz, U. Matti, M. Mund, and J. Ries. 2023. Maximum-likelihood model fitting for quantitative analysis of SMLM data. *Nature Methods* **20(1)**: 139–148. DOI: 10.1038/s41592-022-01676-z.

Wu, Y.-L., A. Tschanz, L. Krupnik, and J. Ries. 2020. Quantitative Data Analysis in Single-Molecule Localization Microscopy. *Trends in Cell Biology* **30(11)**: 837–851. DOI: 10.1016/j.tcb.2020.07.005.

Wu, X. 2001. Clathrin exchange during clathrin-mediated endocytosis. *J. Cell Biol.* **155** DOI: 10.1083/jcb.200104085.

Wulf, E., A. Deboben, F. A. Bautz, H. Faulstich, and T. Wieland. 1979. Fluorescent phallotoxin, a tool for the visualization of cellular actin. *Proceedings of the National Academy of Sciences* **76(9)**: 4498–4502. DOI: 10.1073/pnas.76.9.4498.

Yang, C., P. Colosi, S. Hugelier, D. Zabezhinsky, M. Lakadamyali, and T. Svitkina. 2022. Actin polymerization promotes invagination of flat clathrin-coated lattices in mammalian cells by pushing at lattice edges. *Nature Communications* **13(1)**: 6127. DOI: 10.1038/s41467-022-33852-2.

Ybe, J. A., F. M. Brodsky, K. Hofmann, K. Lin, S.-H. Liu, L. Chen, T. N. Earnest, R. J. Fletterick, and P. K. Hwang. 1999. Clathrin self-assembly is mediated by a tandemly repeated superhelix. *Nature* **399(6734)**: 371–375. DOI: 10.1038/20708.

Yoshida, A., N. Sakai, Y. Uekusa, Y. Imaoka, Y. Itagaki, Y. Suzuki, and S. H. Yoshimura. 2018. Morphological changes of plasma membrane and protein assembly during clathrin-mediated endocytosis. *PLOS Biology* **16(5)**: e2004786. DOI: 10.1371/journal.pbio.2004786.

Zaremba, S. and J. H. Keen. 1983. Assembly polypeptides from coated vesicles mediate reassembly of unique clathrin coats. *Journal of Cell Biology* **97(5)**: 1339–1347. DOI: 10.1083/jcb.97.5.1339.

Zeno, W. F., J. B. Hochfelder, A. S. Thatte, L. Wang, A. K. Gadok, C. C. Hayden, E. M. Lafer, and J. C. Stachowiak. 2021. Clathrin senses membrane curvature. *Biophysical Journal* **120(5)**: 818–828. DOI: 10.1016/j.bpj.2020.12.035.

Zhang, Y., L. K. Schroeder, M. D. Lessard, P. Kidd, J. Chung, Y. Song, L. Benedetti, Y. Li, J. Ries, J. B. Grimm, L. D. Lavis, P. De Camilli, J. E. Rothman, D. Baddeley, and J. Bewersdorf. 2020. Nanoscale subcellular architecture revealed by multicolor three-dimensional salvaged fluorescence imaging. *Nature Methods* **17(2)**: 225–231. DOI: 10.1038/s41592-019-0676-4.

Zuylen, J. v. 1981. The microscopes of Antoni van Leeuwenhoek. *Journal of Microscopy* **121(3)**: 309–328. DOI: 10.1111/j.1365-2818.1981.tb01227.x.

LaTeX

I composed this thesis with Overleaf, and used a custom document structure based on the 'Masters/Doctoral Thesis' LaTeXtemplate (www.latextemplates.com, authors Steve Gunn, Sunil Patel, vel@latextemplates), modified by Dr. Markus Mund, Dr. Jervis Vermal Thevathasan, Dr. Philipp Hoess, & Dr. Yu-Le Wu, which is available under CC BY-NC-SA 3.0.

Licenses used in this thesis

- CC BY-NC-SA 3.0: http://creativecommons.org/licenses/by-nc-sa/3.0/
- CC BY 4.0: https://creativecommons.org/licenses/by/4.0/

